THE UNIVERSITY *of* EDINBURGH

Transition Metal Fluorides:

From Superconductors to Multiferroics.

Christina Drathen

For the Degree of Doctor of Philosophy
School of Chemistry
The University of Edinburgh

2012

"… l' étude des composés fluorés réserve encore bien des surprises."

H. Moissan

Le Fluor et ses Composés, 1900

Declaration

I do hereby declare, that this thesis has been composed by myself alone, and that the work detailed herein is my own, except where otherwise stated. Further, I confirm that no part of this thesis has been submitted for any other degree or professional qualification than this doctorate.

Christina Drathen

Acknowledgements

This thesis, and the research it is based on, would not have been possible without the help of many people. Foremost, I am indebted to my supervisor, Serena Margadonna, for all the discussions and corrections of the last weeks, for guidance and support and for everything she taught me during the past years. I was lucky to have the opportunity to visit and use synchrotron facilities around the world, and to get to know and live in two countries, Scotland and Norway. Lastly, for giving me access to the 'fluoride' goldmine!

At Edinburgh University, I would like to thank Paul Attfield and Neil Robertson, for help and advice; to Anna Kusmartseva and Gaetan Giriat for invaluable assistance with the PPMS and SQUID, regardless of the hour; to Takeshi Nakagawa, for preparing a beautiful $K_{0.6}CrF_3$ sample and for showing me Japan; to the girls in the office, past and present members of CSEC and those at Oslo University for all the little bits and pieces, useful discussions and good times. I am grateful for Lorenzo Malavasi at University of Pavia for introducing me to total scattering techniques. The scientists at central facilities for support: Andy Fitch, Caroline Curfs, Adrian Hill and Yves Watier at ID31; Wilson Crichton for the diffraction measurements at ID06 and ID11; Thomas Hansen at D20 and Yasuo Ohishi at BL10XU. The School of Chemistry, University of Edinburgh, for the provision of a studentship, and the University of Oslo for financial support.

Many thanks to friends and family near and far; in particular to Jennie and Gemma, for being amazing flatmates and patiently spelling new English words for me, also for proofreading parts of this thesis. To Simon, for bearing with me during the past month and for making my time in Oslo infinitely more enjoyable: thank you.

Last, but by no means least: thanks to my sister, Anne, as she talks the same language as me; to my brother, Vitus, for showing me how to carry on under the most difficult circumstances, I wish you would still be with us. And to Mama and Papa, for you made me the person that I am and gave me the confidence to go my own path.

Abstract

Transition metal fluorides represent an important family of complex solids displaying a variety of different properties and interesting phenomena. Despite their remarkable behaviour, these classes of materials have not received much attention and the rationalization of their behaviour is still lacking a systematic approach. This thesis aims to contribute to the field by examining previously unknown or understudied complex fluorides. The compounds were selected for their intriguing physical properties that range from superconductivity to multiferroism.

The discovery of superconductivity in the iron pnictides sparked new interest in materials with layered ZrCuSiAs-type structure. Herein the properties of one of these systems, namely SrFeAsF, will be discussed. We have found that it behaves as a poor metal and undergoes a tetragonal (*P*4/*nmm*) to orthorhombic (*Cmma*) structural transition at $T = 180$ K, accompanied by a spin density wave in magnetic susceptibility and electrical resistivity. Below $T < 150$ K, the Fe moments order in antiferromagnetic spin-stripes. Electron doping with La^{3+} is a successful route to obtain superconducting phases, with maximum $T_c = 27$ K ($x = 0.2$). The isostructural *Ae*Mn*Pn*F series (*Ae* = Sr, Ba; *Pn* = P, As, Sb) was also investigated to elucidate the influence of transition metal *d*-electrons and size effects of *Ae* and *Pn* on the physical properties. The isoelectronic replacement of *Ae* and *Pn* leads to a significant distortion in the tetragonal building blocks. All d^5 Mn fluorides investigated here are insulating antiferromagnets with $T_N \sim 350$ K.

Due to the coexistence of electronic and magnetic ordering, the tetragonal tungsten bronze (TTB) materials $K_xM^{2+}{}_xM^{3+}{}_{1-x}F_3$ ($x = 0.4 – 0.6$; M = transition metal) are potential multiferroics. The type of structural distortion adopted by these systems is strongly dependant on the M^{2+}/M^{3+} ratio. For instance, our high-resolution diffraction study on $K_{0.5}Mn_{0.5}Cr_{0.5}F_3$ has revealed a small orthorhombic distortion, which indicates full chemical order of Mn^{2+} and Cr^{3+} on all crystallographic sites. $K_{0.5}Mn_{0.5}Cr_{0.5}F_3$ remains orthorhombic *Ccc*2 on cooling through the ferromagnetic transition at $T_N = 23$ K. On heating, the structure is acentric up to $T = 373$ K, where a change to tetragonal $P4_2/mbc$ symmetry marks the transition from ferroelectric (polar) to paraelectric (apolar) states. High-pressure diffraction experiments have shown that the *Ccc*2 structure is robust upon pressurization with anisotropic axial compressibility up to the maximum pressure applied $p = 18$ GPa.

The crystal structure of related mixed-valence TTB fluoride $K_{0.6}Cr^{2+}_{0.6}Cr^{3+}_{0.4}F_3$ is influenced by the presence of Jahn-Teller active Cr^{2+}. The structural analysis described here revealed the presence of a small polar monoclinic distortion (*P*112) providing a clear signature of full charge order (CO). On heating, the gradual loss of CO leads to two consecutive structural phase transitions to orthorhombic (*Pba*2, T = 423 K) and then tetragonal ($P4_2/mbc$, T = 823 K) lattices, the latter is the signature of the ferro- to paraelectric transition. Below T = 150 K, increased X-ray exposure time leads to CO-melting and the stabilization of a new, charge-disordered orthorhombic phase (*Cmm*2), with a phenomenology similar to the CO manganites. In high-pressure diffraction experiments, a further transition to tetragonal *P*4*bm* symmetry is found at p = 6 GPa. The magnetic susceptibility points towards a complex spin arrangement, with two transitions at T_N = 33 K and 6 K.

The results presented herein show the richness of the structural, electronic and magnetic phase diagrams of transition metal fluorides and clearly demonstrate that systematic studies on these systems will greatly enhance our current understanding of the underlying mechanisms of important phenomena such as superconductivity and ferroelectricity.

Table of Contents

List of Figures

List of Tables

List of Common Abbreviations

A	alkali metal
AC	alternating current
Ae	alkaline-earth metal
AFM	antiferromagnetic
APS	Advanced Photon Lightsource
BCS	Bardeen Cooper and Schrieffer
BM	bending magnet
BM	Birch Murnaghan
BNN	$Ba_2NaNb_5O_{15}$
C	Curie constant
CCD	charge coupled device
Ch	chalcogenide
CN	coordination number
CO	charge order
COS	charge ordered structure
DAC	diamond anvil cell
DC	direct current
DM	diamagnetic
E	electrical field
E	energy
ED	electron diffraction
EoS	Equation of States
EPR	electron paramagnetic resonance
ESRF	European Synchrotron Radiation Facility
e_s	spontaneous strain
F	Helmholtz free energy
FC	field-cooled
FES	ferroelastic structure
FM	ferromagnetic
FWHM	full width at half maximum
H	applied magnetic field
HS	high-spin
HTB	hexagonal tungsten bronze
I	intensity
ICSD	inorganic crystal structure database
ID	insertion device
ILL	Institute Laue Langevin
IP	image plate
J	total angular momentum
JT	Jahn-Teller
KK	Kugel-Khmoskii
L	orbital angular momentum
M	(transition) metal
M	magnetisation

MPMS	magnetic properties measurement system
MR	magnetoresistance
NMR	nuclear magnetic resonance
NPD	neutron powder diffraction
O	orthorhombic
OO	orbital order
p	pressure
P	polarisation
P_s	spontaneous polarization
PDF	pair distribution function
PM	paramagnetic
Pn	pnictide
PPMS	physical properties measurement system
PSD	position sensitive device
PTB	perovskite tungsten bronze
R	resistance
Re	rare-earth metal
R_{H}	Hall coefficient
RMC	Reverse Monte Carlo
RT	room temperature
S	spin angular momentum
SC	superconductivity
SNS	Spallation Neutron Source
SDW	spin density wave
Spring-8	Super Photon Ring – 8 GeV
SQUID	superconducting quantum interference device
(S)XRD	(synchrotron) X-ray diffraction
T	temperature
T_c	critical temperature
T_C	Curie temperature
T_M	transition metal
T_N	Néel temperature
T	tetragonal
TTB	tetragonal tungsten bronze
U	internal energy
V	voltage
V	volume
X	halogen or oxygen
XPS	X-ray photoelectron spectroscopy
Z	atomic number
ZFC	zero-field-cooled
ε	electrical polarisability
θ	angle (of diffraction)
θ	Weiss constant
ρ	electrical resistivity
μ	magnetic moment
χ	magnetic susceptibility
χ_{m}	molar magnetic susceptibility

Chapter 1

Solid-State Oxides and Fluorides

1.1 Introduction to Oxides and Fluorides

1.1.1 Examples of Oxides

On of the most abundant elements in the earth's crust is oxygen and its inorganic compounds are ubiquitous. Solid-state oxide materials are present in all areas of life: in form of ordinary cement ($CaO \cdot SiO_2$) they hold buildings together, as ferrites (e.g. $BaFe_2O_4$) they store information in magnetic-core memories, and they are used as electrolytes (e.g. ZrO_2-Y_2O_3) in solid oxide fuel cells, to mention only a few examples.

It may appear somewhat surprising to start a thesis dedicated to fluoride-based materials with a paragraph on the fascinating world of oxides. This is driven by the consideration that fluorides and oxides are closely related and show many similarities in their structure and properties. Yet the fluoride materials are less studied and it is worthwhile to briefly visit some inorganic oxide materials, before moving to the class of fluoride materials. During the past decades, research efforts towards new transition-metal oxides have lead to some of the most important discoveries in materials chemistry. This includes the high-T_c superconductivity in the cuprates, the colossal magneto resistance of the manganites and the ferroelectric properties of the niobates and the titanates.

a) The High-T_C Superconducting Cuprates

Since the discovery of superconductivity in mercury by H. K. Onnes a century ago, superconducting materials have intrigued scientists [1]. For several decades, the state of zero resistance was observed predominantly in metals and simple alloys and only below $T = 30$ K. This changed with Bednorz and Müller's report of superconductivity with a critical temperature $T_c = 35$ K in the Ba-La-Cu-O system [2]. Very quickly the T_c surpassed the boiling point of liquid nitrogen (Figure 1.1). These findings revolutionised materials science research, not only because the high T_c brought technological applications within reach, but also because the existing theory could not explain the observed properties [3]. To date, the theoretical description of unconventional superconductivity remains a challenge [4].

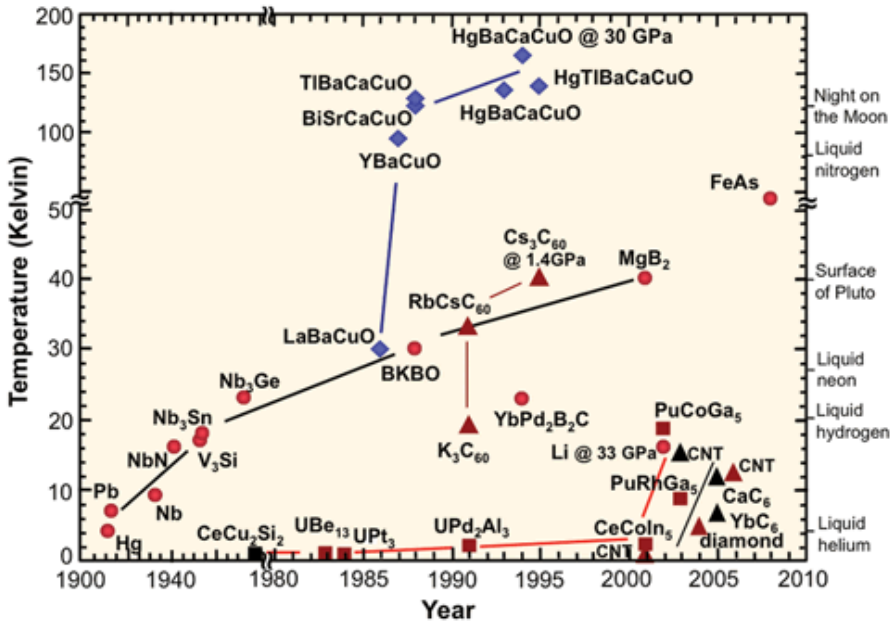

Figure 1.1: The discoveries of selected superconducting compounds over the past century [5]. The discovery of the cuprate high-T_c superconductors (blue) marked a revolution of the field, as for the first time superconducting phases could be reached with liquid nitrogen cooling rather than using the more expensive liquid helium.

b) Colossal Magnetoresistance in Manganites

The perovskite manganites have attracted much attention due to their colossal magnetoresistance [6]. The parent material $Re\mathrm{MnO_3}$ (Re = rare earth metal) are semiconducting antiferromagnets, but upon doping on the Re-site with a divalent metal $Re_{1-x}M_x\mathrm{MnO_3}$ ($0.13 < x < 0.45$), they become ferromagnetic metals below their Curie temperature T_c and the Jahn Teller distortion of Mn^{3+} vanishes. The half-doped manganites ($x \sim 0.5$) show Mn^{3+}/Mn^{4+} charge order and are insulating. The electrical transport properties of $Re_{1-x}M_x\mathrm{MnO_3}$ can be greatly enhanced by the application of an external magnetic field, see Figure 1.2. This was firstly explained in terms of the double-exchange mechanism, which principally states that the hopping of electrons is facilitated when the spins of neighbouring metals centres are aligned parallel [7]. But the double exchange mechanism alone was not sufficient to explain the observed properties. The formation of lattice polarons was proposed, which is enhanced by the Jahn-Teller effect, but should diminish with increasing doping level [8]. The case could be clarified through a local structure investigation of the low doped regime of $La_{1-x}Sr_x\mathrm{MnO_3}$: it revealed that the Jahn-Teller distortions of Mn^{3+} are not suppressed, but preserved locally [9]. Additional local structure studies reported the observation of the formation of small lattice polarons [10].

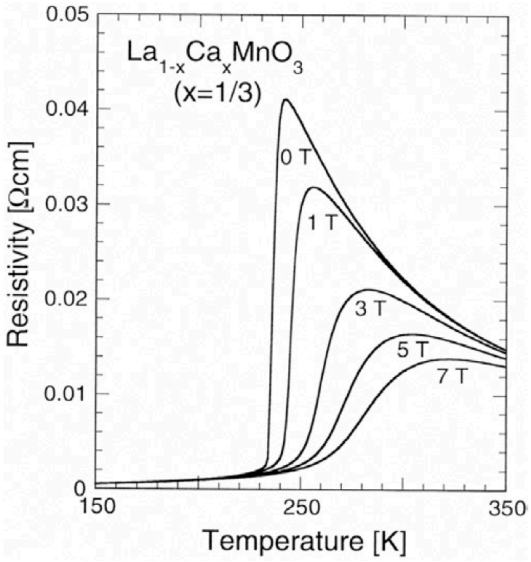

Figure 1.2: The effect of an applied magnetic field on the electrical transport properties of $La_{1-x}Ca_xMnO_3$. The resistivity drops significantly as the magnetic field strength increases [11].

c) Ferroelectric Titanates and Niobates

The last example of a perovskite oxide to be mentioned here is the lead titanate $PbTiO_3$, which is ferroelectric. Ferroelectric materials are of great interest for technological applications, for example as capacitors or transducers. A more detailed description of another ferroelectric material, the tetragonal tungsten bronze type $Ba_2NaNb_5O_{15}$, is given below.

1.1.2 Examples of Fluorides

Fluorides show a range of fascinating phenomena, arising from the interdependence of structure, electronic and physical properties. The investigation of such systems is interesting from both a fundamental as well as a technological point of view. Due to the comparable size of the F^- and O^{2-} anions, the structures involving fluorine show similarities to those involving oxide, but differ from the other halogenides, which often resemble sulphides and selenides [12]. The radius ratio of most transition metals with the fluorine ligand is $r(T_M)/r(F) = 0.41 - 0.73$, which supports a six-fold octahedral coordination (coordination number CN = 6). Also common is tetrahedral coordination (CN = 4), adopted for example by the binary alkali-earth fluorides. Both polyhedra, MF_6 and MF_4 can be corner-, edge- or face-sharing to form infinite structures containing chains, layers or three-dimensional networks.

The numerous structure types adopted by fluorides give rise to a wide spectrum of properties. Similar to the oxide-perovskites, the structural and magnetic phase diagrams of the isostructural fluorides are determined by the interplay of charge-, orbital- and spin degrees of freedom. A number of compounds shall be reviewed here, selected either for their exceptional physical properties or fundamental importance.

a) Cooperative Jahn-Teller Effect in $KCrF_3$

At room temperature $KCrF_3$ adopts an orthorhombic distorted perovskite-type structure (space group *I*4/*mcm*) [13]. The Jahn-Teller active Cr^{2+} ($3d^4$) leads to elongated coordination octahedra, which order cooperatively. The long and short Cr-F bonds alternate in the *ab* plane, and are rotated by 90° along the *c*-axis. In $KCrF_3$, orbital ordering is strongly coupled to the lattice, and a spin-reorientation below $T = 250$ K triggers a phase transition to monoclinic symmetry (non-conventional space group setting *I*112/*m*) [13]. The orbital ordering patterns of both phases are shown in Figure 1.3. On heating, the lattice expands linearly up to $T = 973$ K, when a structure change to cubic symmetry (space group *Pm*-3*m*) occurs, indicating an orbital liquid state (see Figure 1.4) [14].

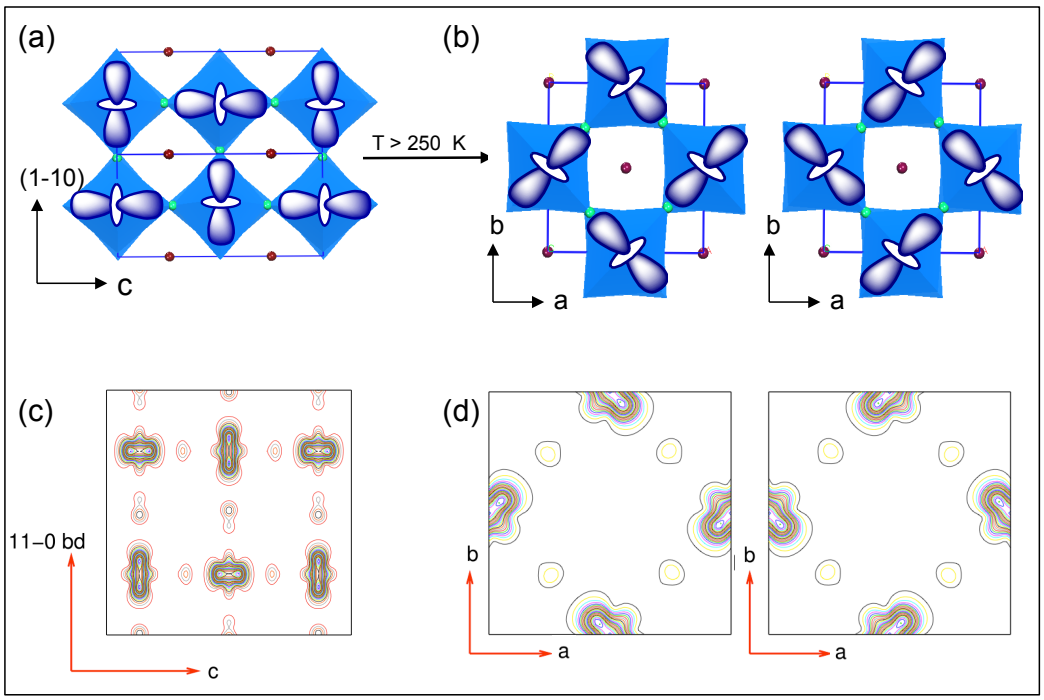

Figure 1.3: The orbital ordering pattern of $KCrF_3$ (a) in its monoclinic phase (*I*112/*m*) and (b) in its orthorhombic phase (*I*4/*mcm*). The calculated electron density (c, d) is in excellent agreement with the results from high-resolution powder diffraction analysis [13], [15].

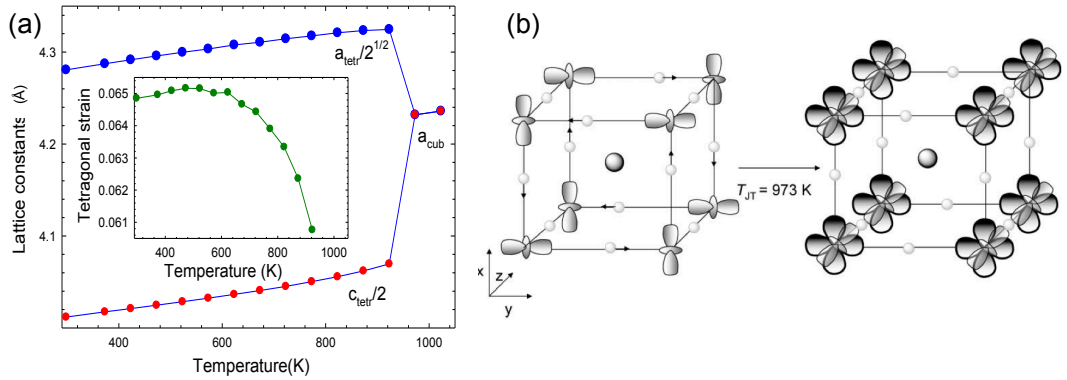

Figure 1.4: (a) The temperature dependence of the lattice constants of $KCrF_3$ above room temperature. (b) At the structural transition to cubic symmetry (*Pm*-3*m*) at T = 973 K, the orbital ordered state changes to an orbital liquid state [14].

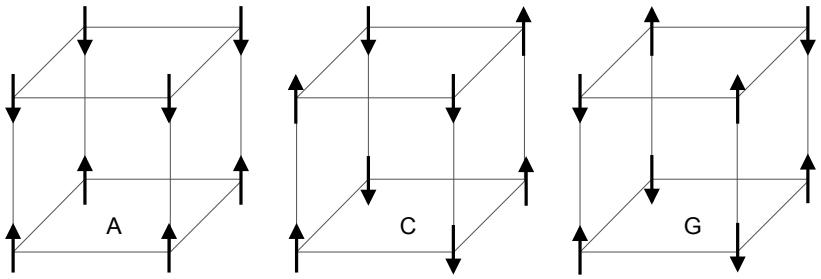

Figure 1.5: Schematic illustration of different types of magnetic or orbital ordering patterns.

The magnetic structure was reported to be A-type antiferromagnetic [16], [17], see also Figure 1.6. Magnetic susceptibility measurements determined the magnetic ordering temperature (Néel temperature) as T_N = 46 K and revealed two further transitions at T = 11 K and 4 K [13]. Recently, Xiao *et al.* reported a detailed neutron diffraction study and showed that $KCrF_3$ is an incommensurate antiferromagnet below T = 79.5 K; commensurate long-range antiferromagnetic order is observed at T = 45.8 K [18]. Consistent with magnetic susceptibility measurements, additional transitions were observed at T = 9.5 K and 3.2 K, and connected to more complex spin structures involving weak ferromagnetic and canted antiferromagnetic configurations [13], [18].

A number of theoretical calculations on $KCrF_3$ have confirmed the G-type orbital- and A-type antiferromagnetic ordering patterns [15], [19], [20]. Figure 1.3 shows the contour plots of the charge density from the filled e_g orbitals for the monoclinic and tetragonal phases, highlighting the excellent agreement between theory and experiment [15].

The introduction of potassium vacancies (i.e. generating Cr^{3+}) suppresses the long-range orbital order. The potassium-deficient $K_{0.9}CrF_3$ adopts a cubic structure (space group *Pm*-3*m*) and shows no structural transitions on cooling to $T = 5$ K. The change in crystal structure is accompanied by different magnetic properties: $K_{0.9}CrF_3$ is paramagnetic. The application of hydrostatic pressure induces two consecutive phase transitions to tetragonal and orthorhombic lattices, at $p = 7$ GPa and 18 GPa, respectively. While the tetragonal phase is orbitally-ordered, the Jahn-Teller effect is quenched in the orthorhombic phase.

The use of total scattering techniques solved the puzzle of the cubic structure observed crystallographically. The analysis of the pair distribution function revealed the presence of 80 % tetragonal and 20 % cubic phase, related to Cr^{2+} and Cr^{3+}, respectively. Although Cr^{2+} is still Jahn-Teller active, the crystallographic cell becomes cubic. This is because the presence of cubic Cr^{3+} 'islands' disturbs the cooperative ordering of the tetragonal Cr^{2+} domains.

b) Metal – Insulator Transition of $KAgF_3$

The metallic and superconducting properties of AgF_2 have stimulated research in materials containing AgF_2 sheets, in particular perovskite type $KAgF_3$ [21], [22], [23]. Ultra-high resolution X-ray photoelectron spectroscopy suggested strong hybridisation of the Ag(*4d*) and F(*2p*) orbitals, which may lead to metallic behaviour [24]. Yet, the strongly oxidizing, air- and moisture sensitive properties of the fluroargentates prevented the experimental assessment of their electrical resistivity [25]. Using a microwave cavity perturbation technique, Grochala demonstrated that $KAgF_3$ does indeed become metallic above $T = 50$ K [26]. The metal – insulator transition occurs in the same temperature region as the onset of antiferromagnetic order [27], [26]. The fascinating family of fluoro-argentates has been reviewed in reference [28].

Another interesting members of the fluoro-argentate family is Cs_2AgF_4, that represents a rare example of a strongly correlated, orbitally-orderd two-dimensional ferromagnet [30], [31]. The layered material is structurally related to K_2NiF_4 and La_2CuO_4, the parent compound of the cuprate high-T_c-superconductors, see Figure 1.6. Encouraged by the reported drop in magnetisation in the Be-Ag-F system (resembling the Meissner-Ochsenfeld effect) compounds containing $Ag^{II}F_2$ sheets were recently suggested as potential superconductors [32], [33], [28].

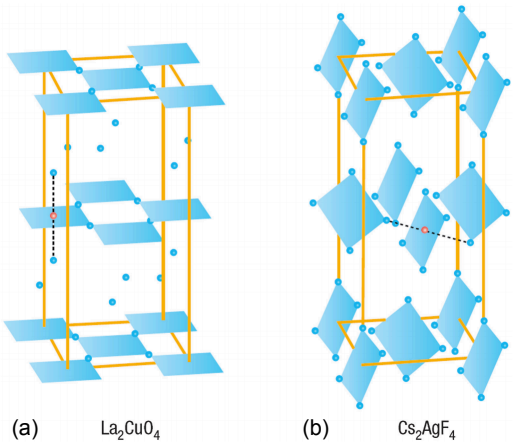

Figure 1.6: Schematic crystal structures of (a) La_2CuO_4, the parent materials of the high T_c - superconducting cuprates, and (b) Cs_2AgF_4, a potential fluoride based superconductor [29].

c) Orbital Ordering in $KCuF_3$

The perovskite $KCuF_3$ has attracted constant interest since the 1960s, as it is considered to be a prototype orbital ordered system. The presence of Jahn-Teller active Cu^{2+} distorts the cubic perovskite structure to tetragonal [34]. $KCuF_3$ is described as a one-dimensional S = ½ Heisenberg antiferromagnet, which orders at T_N = 38 K [35]. Based on the results of temperature dependent resonant X-ray scattering experiments, orbital ordering (OO) is believed to occur below T_{OO} ~ 800 K [36]. Within the Kugel-Khmoskii (KK) model, orbital ordering of $KCuF_3$ is induced by superexchange interactions only, but the accordingly calculated transition temperature is only T_{KK} ~ 350 K [37], [38]. In addition to the superexchange effect, it was suggested that the Jahn-Teller distortions of Cu^{2+} stabilise the orbital order at high temperatures (electron-phonon coupling) [38]. The experimental confirmation of the melting of orbital order at or above T_{OO} ~ 800 K is complicated by the decomposition of the material at this temperature range. A variable temperature diffraction study used the series $KCu_{1-x}Mg_xF_3$ as model for the (experimentally inaccessible) orbitally melted high temperature $KCuF_3$ structure and support the importance of electron-phonon stabilisation of the orbitally ordered state [39].

d) Lower Dimensional Fluoride Structures

The fluoride materials $KCrF_3$, $KCuF_3$ and $KAgF_3$ described above adopt the perovskite structure. Pyrochlores and rutiles are also formed from interlinked fluoride polyhedra. Although their structures are three-dimensional, the physical properties can be of lower dimension, as exemplified in $KCuF_3$. However, the

structures of fluorine compounds are by no means limited to three-dimensional networks. In a comprehensive review, Massa and Babel describe and group the variety of structural motifs that solid-state fluoride materials adopt [40]. For instance (i) isolated [MF_6] fluoride groups can be found among the Cryolites and Elpasolites, (ii) chain structures can be formed by Na_2CuF_4, $CsNiF_3$ and $CsCrF_4$ and (iii) $BaZnF_4$ and the Cs-Ni-F systems can form layered structures. A collection of structural motifs found in fluoride materials is shown in Figure 1.7. Also inorganic-organic hybrid fluoride materials display a wide range of structural types, ranging from zero- to three-dimensional structures [41].

Although fluorine networks often resemble those of oxides, and their structural variety is indeed in no way inferior to oxides, the number of pure[*] compounds known to date vary hugely: ~ 70,000 oxides but only ~ 4,000 fluorides are listed in the inorganic crystal structure database (ICSD), Figure 1.8. Given the high reactivity of fluorine – it forms compounds with almost every other element in the periodic table – this strikes a rather big discrepancy. On the other hand, its reactivity is also an obstacle during synthetic procedures and presents a challenge in the analysis of the products formed. Hence, the field of solid-state fluoride materials is much less explored than that of the oxides – both in terms of systematics and the number of known compounds.

[*] Pure with regard to the respective other element, thus the oxyfluorides are excluded form these estimates.

[†] $T_C = (K/2k_B)(d_z/2)^2$; where K = force constant, k_B = Boltzmann's constant; $K/2k$ =

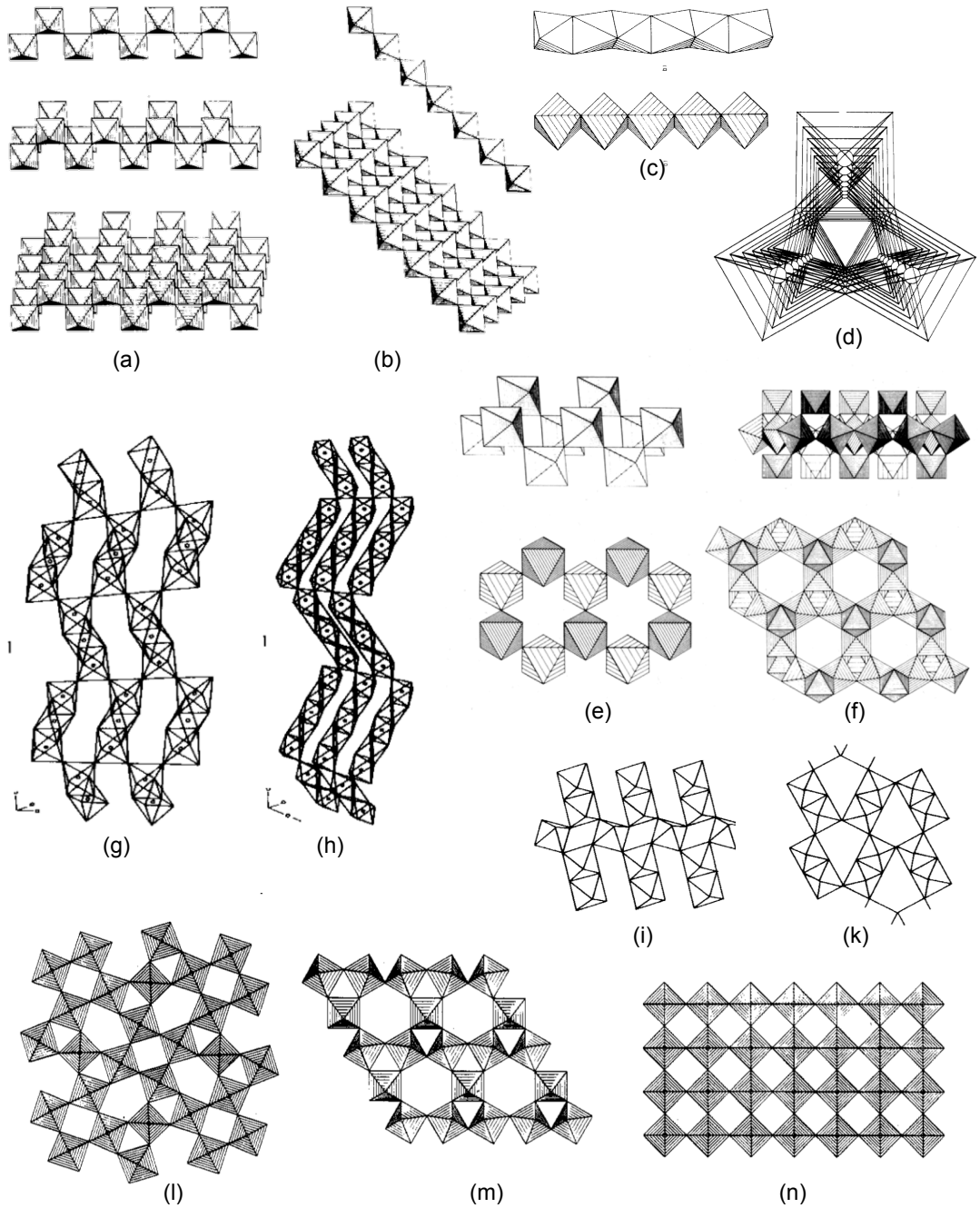

Figure 1.7: Examples of structures adopted by fluorine based materials in the solid state [40]. (a) Cis connected chains, double chains and layers of A_mMF_5, $A_mM_2F_9$ and A_mMF_4. (b) Same as (a), but trans connected chains. (c) Chains of edge- and face-sharing MF_6 units, found in Na_2CuF_4 and $CsNiF_3$. (d) Triple chains of $CsCrF_4$. (e) Puckered layer of $CsBa_2Ni_2F_9$ adopting a rhombohedral structure. (f) Triple layer of Cs_4CoCrF_{18}, derived from the pyrochlore structure. (g) Tri- and (h) pentanuclear groups of face sharing octahedra found in CsF-NiF_2 compounds. (i) Binuclear edge sharing motif in NH_4MnFeF_6. (k) Edge-sharing layers of $Ba_2CuV_2F_{12}$. (l) Layer of tetragonal tungsten bronze, (m) hexagonal tungsten bronze and (n) perovskite structure that are staked along the *c*-axis.

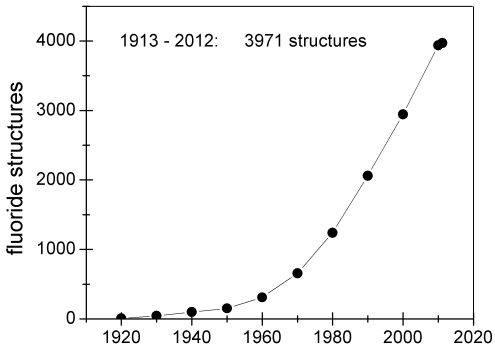

Figure 1.8: Number of fluoride structures reported in the inorganic crystal structure database.

The different oxidation state, and the more ionic character of fluorine allow modification of the physical properties, such as electrical transport. Electron itinerancy, which may prevent the observation of metal – insulator transitions in oxides, is reduced in fluoride materials. Furthermore, the electrons in F^- are more tightly bound than those of O^{2-} making F^- a very rigid and ionic ligand. As a result, covalency effects have less influence on the transition metal interactions involved in magnetism. Different oxidation states can be accessed using the fluoride ion instead of the oxide. As an example, this allows the combination of ferroelectric and magnetic properties in the same sublattice in the AMX_3 perovskites – a feature deemed 'mutually exclusive' in the oxide perovskites [42]. The special electrophilic characteristics of fluorine open the way to a wide range of physical and chemical properties, including electro-optical phenomena and multiferroicity. Fluoride materials include for instance the laser material Nd:$LiYF_4$ and ferroelectric $BaMnF_4$ [43], [44]. In recent years, fluorides have also emerged as a new class of layered superconductors, such as the so-called '1111'-type *Ae*FeAsF (*Ae* = Ca, Sr) [45], [46].

e) Two-Dimensional AeT_MPnF and Three-Dimensional $K_xMM'F_6$

Given the advantages of fluorine, we have set out to explore fluoride-based materials and to determine their complex structural and magnetic phase diagrams. This thesis focuses on two classes of materials of varying dimensionality: firstly, in chapter 3, on the two dimensional AeT_MPnF (*Ae* = alkaline earth metal, T_M = transition metal, *Pn* = pnictide) materials of ZrCuSiAs structure that comprise fluorine in a tetrahedral coordination environment. Secondly, in chapters 4 and 5, on the three-dimensional tetragonal tungsten bronzes A_xMF_3 (*A* = alkali metal, *M* = metal) that are three-dimensional networks build from fluoride octahedra (see Figure 1.9).

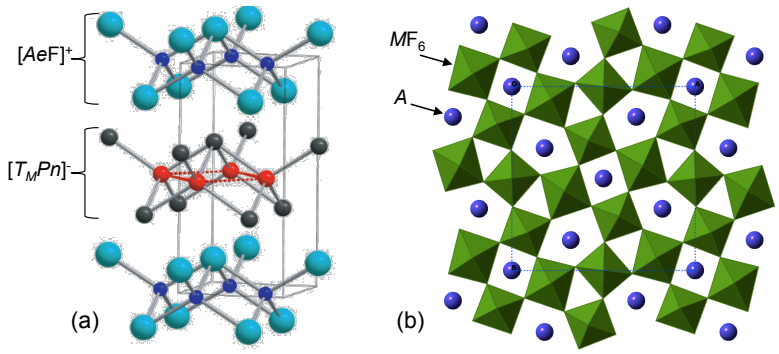

Figure 1.9: (a) The layered structure of the 1111 type AeT_MPnF materials. (b) A single layer of the tetragonal tungsten bronze structure of the AMF_3 materials, seen along the *c*-axis.

The layered '1111'-type fluorides are related to the oxypnictides ReT_MPnO (*Re* = rare earth metal, T_M = Ni, Fe, *Pn* = P, As), which are renown for their superconducting properties. In general, the physical properties of the fluoride materials resemble those of the oxide materials, and superconducting phases can be achieved via electron doping.

The investigation of the tetragonal tungsten bronze fluorides was triggered by the isostructural oxides, which display a range of physical properties of important technological application, including electro-optic and ferroelectric. In particular the latter is of interest herein, because some empirical relationships have been established that link ferroelectricity to structural features.

1.2 Layered ZrCuSiAs-type materials

Layered structures are particularly appealing to a solid-state chemist, as the building blocks can be modified and combined in an infinite number of ways. Structural flexibility opens the way for a multitude of elemental combinations, which modify the distances within and between the layers and serve as a tool to tune the physical properties.

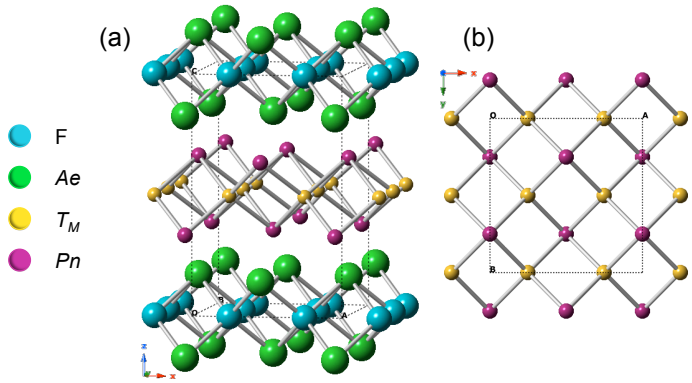

Figure 1.10: (a) The ZrCuSiAs-type structure adopted by the AeT_MPnF materials (Ae = Sr, Ba; T_M = Fe, Mn; Pn = P, As, Sb). The $[Ae\text{F}]^+$ and $[T_MPn]^-$ layers are build from edge-sharing FAe_4 and T_MPn_4 tetrahedra, respectively. (b) The $[T_MPn]^-$ layer seen along c-direction. The Pn caps the square T_M net alternating above and below the plane.

Metal pnictide compounds adopting the tetragonal ZrCuSiAs structure, Figure 1.10, have been intensely studied in the 1990s due to their optoelectronic properties and potential for application (e.g. in light emitting diodes) [47], [48]. To date, the two broadest classes of materials are the p-type transparent semiconductors, such as LaCuSO and the superconducting iron (and nickel) pnictides [49]. The discoveries in 2006/07 of superconducting LaFePO and LaNiPO with T_c = 3.2 K and 4.3 K, respectively, sparked new interest in this structural type [50], [51]. This exploded into a frenzy of research activity after Hosono reported a remarkable T_c = 26 K in $LaFeAsO_{1-x}F_x$ in 2008 [52].

1.2.1 The '1111'-Type Iron Superconductors

The iron-pnictides are commonly formulated as $Re^{3+}T_M^{2+}Pn^{3-}O^{2-}$ (Re = rare earth, T_M = transition metal, Pn = pnictide), and consist of two alternating slabs. The atomic arrangement in these layers is related to the fluorite structure, in which the cations are face centred cubic packed, and the anions occupy the cubic holes. In the

anti-fluorite structure, the positions of cations and anions are exchanged. Here, the $[T_MPn]^-$ layer is fluorite-type and the $[ReO]^+$ layer is anti-fluorite-type. In the $[T_MPn]^-$ layer, the transition metal forms a square planar net, which is capped by the pnictide, alternating above and below the plane. This results in a T_MPn_4 tetrahedral coordination environment for the transition metal, and a PnT_{M4} square pyramidal coordination for the pnictide. The tetrahedra share edges on four sites to form planar sheets. The $[ReO]^+$ (fluorite) layer shows the same arrangement of atoms, with the oxygen taking the place of the transition metal and the rare earth taking that of the pnictide. The characteristics of the $[T_MPn]^-$ (anti-fluorite) layer are predominantly determining the properties of the compounds, e.g. the superconductivity is related to the FeAs layers and can be considered as two-dimensional. The T_M-Pn bond distances (e.g. $d_{\text{Fe-As}}$ ~ 2.4 Å) are slightly longer than the sum of their covalent radii (2.37 Å), indicating that the T_M-Pn bonds have covalent character, which is also supported by calculations [53]. The interlayer forces between the fluorite and anti-fluorite layers are of ionic character.

Superconductors related to LaFePO, are often referred to as '1111'-type, according to their stoichiometry. Fluoride based materials are obtained through replacement of the $[ReO]^+$ layer with an isoelectronic $[AeF]^+$ (Ae^{2+} = alkaline earth metal) layer. Other structure types of the iron-based superconducting materials are obtained by replacing the $[ReO]^+$ slab with A^+ or Ae^{2+} ions (A = Li, Ae = Ba), which gives the so called "111" and "122" materials, adopting PbFCl and $ThCr_2Si_2$ structures, or with perovskite-type layers to give the "42622" materials, such as e.g. $(Sr_4Sc_2O_6)Fe_2P_2$, adopting the K_2NiF_4 structure [54], [55], [56]. Together with the superconducting "11" type binary compound FeCh, (Ch = Se, Te), which adopts an anti-PbO structure, these materials have been the topic of more than 2000 publications and have been extensively reviewed [57], [58], [59], [60], [61]. The materials described in chapter 3 of this thesis adopt the '1111' structure, which will therefore be discussed here in detail. The 11, 111, 122 and 42622 materials do not contain fluoride, and their detailed description is outside the scope of this work.

1.2.2 The Oxide-Pnictides *Re*FeAsO

A typical phase diagram of the superconducting phases of $ReFeAsO_{1-x}F_x$ is shown in Figure 1.11. The parent materials are characterised by the presence of a spin density wave anomaly, which coincides with a structural transition from tetragonal $P4/nmm$ to orthorhombic $Cmma$ ($T \rightarrow O$ transition). Magnetic long-range order occurs at lower

temperatures. Through doping, the $T \rightarrow O$ transition, spin density wave and magnetic order can be suppressed, and superconductivity emerges below the critical temperature T_c. The phase diagrams vary slightly for different compounds: $CeFeAsO_{1-x}F_x$ and $SmFeAsO_{1-x}F_x$, for instance, show coexistence of magnetic and superconducting phases below the optimum doping level.

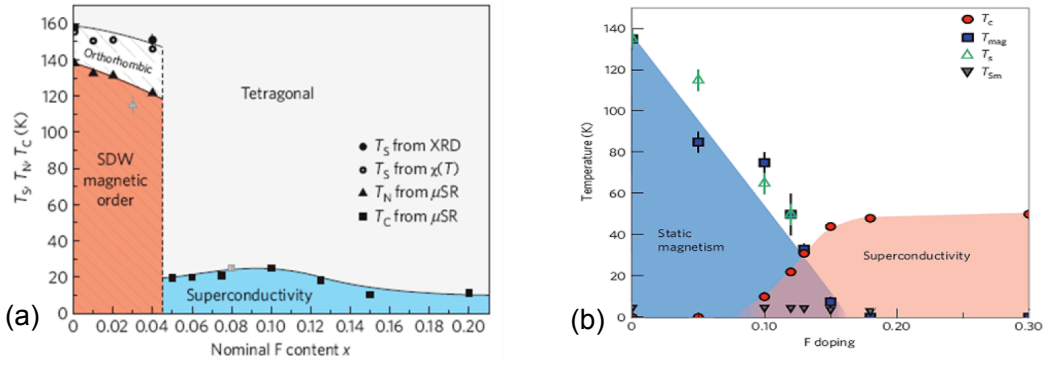

Figure 1.11: Typical phase diagram of the 1111-type iron-pnictide superconductors. (a) $LaFeAsO_{1-x}F_x$ [62] and (b) $SmFeAsO_{1-x}F_x$ [63].

In the iron-pnictides, the hybridisation of Fe *3d* and As *4p* states influences the electronic structure near the Fermi surface. The height of the pnictide h_{Pn} above the Fe plane plays a crucial role and acts as a switch between high-T_c nodeless and low-T_c nodal pairings [64], [65], [66]. The sensitivity to h_{Pn} is related to the Fe-As-Fe angle, which determines the in-plane hopping integral. In this respect, isoelectronic replacement of As with P and Sb has been explored as a means to modify the properties of the *Re*FeAsO parent material without affecting the charge carrier density, and to induce superconducting phases.

Pn-Site Doping in $ReFeAs_{1-x}Pn_xO$

Phosphorus substitution in the *Re*$FeAs_{1-x}P_xO$ group (*Re* = La, Sm) does not affect the carrier concentration, but supresses the $T \rightarrow O$ transition and spin density wave anomaly [67], [68], [69]. In $LaFeAs_{1-x}P_xO$, superconductivity with $T_c \sim 10$ K is induced for $x = 0.25 - 0.3$, whereas $SmFeAs_{1-x}P_xO$ becomes superconducting below $T_c = 4.1$ K at $x = 0.565$ [67], [68]. The stoichiometric end members of the series LaFePO and SmFePO are nonmagnetic and metallic [70], [69]. Superconductivity reported in LaFePO is likely related to the presence of impurities ($LaFe_4P_{12}$, La) or oxygen deficiency [70]. Zhidalgo *et al.* investigated the influence of phosphorus doping, oxygen vacancies and synthesis technique (ambient *vs.* high-pressure) [69]. The study revealed that superconductivity in *Re*$FeAs_{1-x}P_xO$ arises only after heat

treatment under high-pressure, and is probably related to modifications of the intralayer distance [69].

On the other hand, phosphorus doping in $CeFeAs_{1-x}P_xO$ ($0 < x < 1$) supresses the antiferromagnetic order and spin density wave of its parent compound CeFeAsO for $x \sim 0.4$ but does not lead to superconducting phases down to $T = 2$ K [71]. The low temperature antiferromagnetic order of Ce changes to ferromagnetic order for $x \sim 0.45$, and the material becomes metallic but not superconducting [71], [72]. It was later demonstrated that superconductivity in $CeFeAs_{1-x}P_xO_{0.95}F_{0.05}$ can coexist with Ce-antiferromagnetic order ($0 < x < 0.55$), but strongly competes with ferromagnetic order [73].

In contrast to phosphorus doping, antimony doping in $LaFeAs_{1-x}Sb_xO$ ($x < 0.5$) does not supress the spin density wave or superconductivity [74]. This was related to the opposite structural response of the lattice upon Sb substitution compared to P: Sb-doping elongates the Fe-*Pn* bond, increases the [Fe*Pn*] layer thickness and the intralayer distance [74]. Whilst the structure approaches the ideal As-Fe-As angle, the magnetic moments are slightly enhanced and prevent the formation of superconducting phases [74]. In analogy to *Re*FePO materials, superconducting phases were realised in co-doped $LaFeAs_{1-x}Sb_xO_{1-y}F_y$ [75], [76]. The critical temperature of $LaFeAs_{1-x}Sb_xO_{0.8}F_{0.2}$ is slightly enhanced for small doping levels of Sb, from $T_c = 28.5$ K for $x = 0$, to $T_c = 30.1$ K for $x = 0.05$ [75], similar to results obtained in reference [76].

Fe-Site Doping in $ReFe_{1-x}M_xAsO$

Isovalent substitution on the Fe site has been explored for example via Ru and Ir doping. $PrFe_{1-x}Ru_xAsO$ ($x = 0 - 0.75$) does not become superconducting although spin density wave, structural transition and magnetic order of Pr are suppressed [77]. On the other hand, isoelectronic substitution of Fe with Ir in $SmFe_{1-x}Ir_xAsO$ leads to superconducting phases for $x = 0.06 - 0.16$ with a plateau like behaviour of $T_c \sim 18$ K [78]. The end members of the series, *Re*RuAsO (*Re* = La, Nd, Sm, Gd) are metallic and show antiferromagnetic order of the *Re* (except La), whilst Ru magnetism is not observed [79]. The co-doped compounds $SmFe_{1-x}Ru_xAsO_{0.85}F_{0.15}$ and $NdFe_{1-x}Ru_xAsO_{0.89}F_{0.11}$ were studied in [80], [81]. Chemical pressure (via *Re* replacement) was compared to hydrostatic pressure in the series $ReFe_{0.85}Ir_{0.15}AsF$ (*Re* = Gd, Sm, Nd, La). The T_c decreases with decreasing *Re* size, whilst hydrostatic

pressure diminishes T_c for the largest member of the series (Gd) and enhances T_c for the smallest member (La) [82].

1.2.3 The Fluoro-Pnictides *Ae*FeAsF

The fluoride based iron-pnictide parent materials have the general formula *Ae*FeAsF, where *Ae* = Ca, Sr, Eu. All materials adopt the tetragonal *P*4/*nmm* structure at room temperature, and show a structural transition to orthorhombic *Cmma* symmetry on cooling to T = 134(3) K and 180 K for *Ae* = Ca, Sr, respectively [45], [83]. The parent materials have been investigated at high pressure and low temperature (T = 40 K). CaFeAsF undergoes a structural phase transition to monoclinic symmetry at p = 14 GPa, whereas this transition occurs over a broad pressure range (p = 9 GPa to 39 GPa) in SrFeAsF [84].

The structural transition coincides with a spin-density wave anomaly at $T \approx$ 118 K, 173 K and 153 K (*Ae* = Ca, Sr, Eu, respectively) in magnetic susceptibility, electrical resistivity and heat capacity data [85], [86], [83]. Interestingly, antiferromagnetic long-range magnetic order occurs at lower temperatures, T_N = 114(3) K and 133(3) K in *Ae* = Ca and Sr, respectively [45], [87]. Both materials, CaFeAsF and SrFeAsF, were described as quasi two-dimensional Ising systems [87], [88]. The low temperature Fe spin structure of CaFeAsF is shown in Figure 1.12. The magnetic moments align parallel to the *a*-axis and are ordered antiferromagnetically along the *a*- and *c*-directions, and ferromagnetically along the *b*-direction, giving a spin-striped pattern [45], [87]. The effective magnetic moment at T = 2 K is μ_{eff}(Ca) = 0.49(5) μ_B and μ_{eff}(Sr) = 0.58(6) μ_B [45], [87].

Muon spin relaxation and neutron diffraction studies indicate that the magnetic intralayer exchange is weaker in the fluorides than the oxides and confirmed that three-dimensional magnetic long-range order occurs about ΔT = 50 K below the structural transition, which is considerably larger as compared to the isostructural oxides [88]. The transport properties of the 1111-fluoride compounds are characterised by positive Hall coefficients R_H, in contrast to the 1111-oxides that have negative R_H coefficients [85].

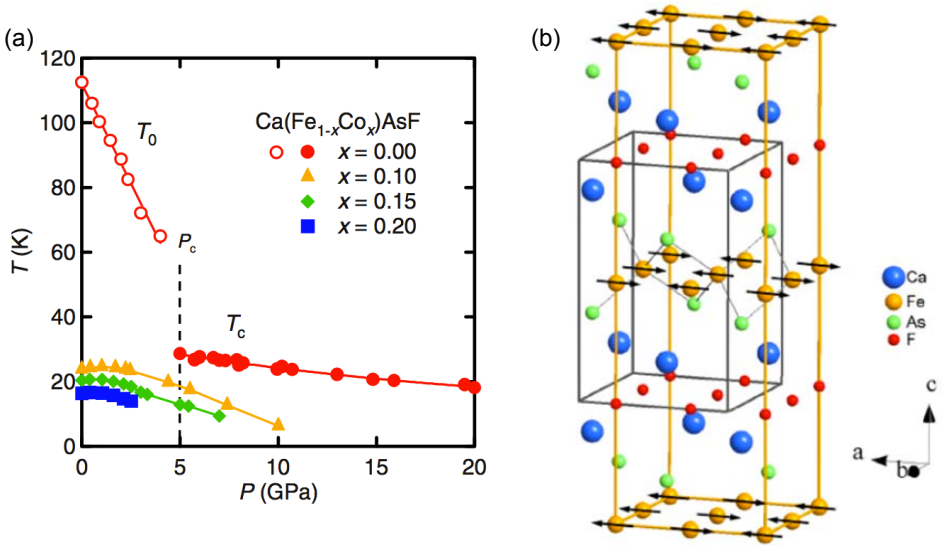

Figure 1.12: (a) The phase diagram of $CaFe_{1-x}Co_xAsF$. (b) The nuclear (black box) and magnetic (orange box) unit cell of CaFeAsF determined by neutron powder diffraction [45].

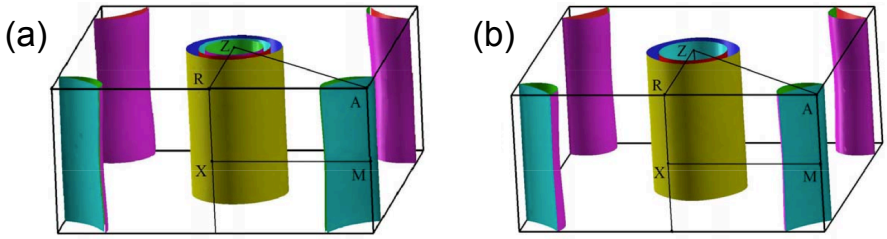

Figure 1.13: The Fermi surfaces of the fluoride based parent materials (a) CaFeAsF and (b) SrFeAsF [89].

Band structure calculations clarified the nature of bonding: the Fe-As bonds are a combination of covalent (hybridisation of Fe *3d* and As *4p* orbitals) and ionic bonds. Furthermore, there are Fe-Fe metal bonds and predominantly covalent *Ae*-F interactions in the antifluorite layer [89]. The Fermi surface of the fluoride compounds, shown in Figure 1.13, resembles those of the oxide *Re*FeAsO materials [89]. The interlayer charge transport was calculated to be 0.280e and 0.309e for *Ae* = Ca and Sr, respectively, indicating ionic bonds between layers [89]. The charge transfer is smaller as compared as compared to LaFeAsO, where it is 0.391e [89].

a) Ae- and Fe- Site Doping in the Fluoro-Pnictides

The parent materials are poor metals, but through doping the spin density wave (SDW) anomaly and magnetic order are suppressed, and superconductivity emerges (in the paramagnetic phase) [45], [90]. Doping on the *Ae*-site with *Re* = La,

Nd, Pr, or on the Fe-site with T_M = Co, Ni induces superconductivity [85], [86], [91]. *Ae*-site doping gives the maximum reported T_c = 54 K in both (impure) $Nd_{0.7}Sr_{0.3}FeAsF$ and $Nd_{0.6}Ca_{0.4}FeAsF$ whereas a lower T_c ~ 22 K was achieved in 10% Co-doped CaFeAsF [45], [85], [90], [91], [92]. The phase diagram of the $CaFe_{1-x}Co_xAsF$ system is shown in Figure 1.12. Replacing Co with Ni also affords superconducting phases and doubles the effective carrier concentration [93]. On the other hand, Cr, Mn and Cu act as scattering centres and do not lead to superconducting phases, which is believed to be due to the increased interlayer distance [94].

1.2.4 The '1111'-Type Manganese Pnictides

Certainly the iron containing materials are in the focus of current research of ZrCuSiAs type materials. In this context, chemical doping has been explored to obtain superconducting phases. Furthermore, Fe and As have been completely substituted with other transition metals and pnictides (or chalcogenides), respectively. In fact, the fully substituted materials had been already investigated before 2006's discovery of LaFePO. The number of such fluorides-based materials reported is small, and only few structural details are known. The pnictides BaZnPF, BaZnSbF, BaMnPF, SrZnPF are semiconducting – insulating and of brown-blackish colour [95]; whereas the chalcogenides *Ae*Cu*Ch*F (*Ae* = Sr, Ba, Eu; *Ch* = S, Se) are known as p-type transparent conductors [96], [97], [98].

The manganese-based '1111'-type materials were studied more intensely after the discovery of the superconducting iron compounds. Compared to Fe^{2+} (d^6, $S = 2$), the odd *d*-electron number of Mn^{2+} (d^5, $S = 5/2$) results in different properties and hence complements the understanding of the structure-property relationships of the iron-pnictides. In this context, LaMnSeO, was suggested as a potential candidate for new superconducting materials, because its electronic structure is similar to that of LaFeAsO [99].

Other manganite pnictides, as *Re*MnAsO (*Re* = Nd, La) (space group *P*4/*nmm*) were reported to show magnetoresistance [100], [101]. The Mn spins order antiferromagnetically but parallel to the *c*-axis, and realign in the *ab*- plane below the magnetic ordering temperature of the *Re* ion. A similar *Re*-induced spin-reorientation accompanied by a structural transition to orthorhombic symmetry (space group *Pnmm*) was observed in metallic PrMnSbO [102].

The modular structure and flexibility of the layered '1111'-type compounds offers a playground for solid-state chemists: a wide range of chemical substitutions is supported that gives rise to intriguing physical properties, including for instance magnetoresistance and superconductivity. Elemental substitutions have not been exhaustively probed yet, in particular not in the fluorine based materials. Further modifications via replacement of entire building blocks may give rise to completely new structures and unexpected functionalities.

1.3 Three-Dimensional Networks: A_xMX_3

Most structures adopted by ternary A_xMX_3 systems can be derived from the perovskite structure, where corner-sharing MX_6 octahedra are arranged in a cubic net and the A ions fills the 12-fold cages. The A-site counter ion primarily acts to balance the negative charge of the MX_3 framework, but depending on the radius ratio it may also deform the surrounding framework. The non-stoichiometric compounds A_xMX_3 are referred to as bronzes. These can be broadly classified into three crystallographic families, (i) the perovskite tungsten bronzes (PTB) or framework bronzes ($x > 0.6$), (ii) the tetragonal tungsten bronzes (TTB) ($0.6 < x < 0.4$), and (iii) the hexagonal tungsten bronzes (HTB) ($x < 0.4$) [103]. All bronze structures consist of three dimensional networks of corner sharing MX_6 octahedra, but – depending on the type of linking – the geometry of the resulting tunnels hosting the A-site cation varies. The channels are square in PTB; pentagonal, square and trigonal in TTB; hexagonal and trigonal in HTB. The materials described in chapter 4 and 5 of this thesis adopt the TTB structure, which will therefore be discussed in detail here. For more extensive description of the perovskites and structures derived thereof, see for example reference [103].

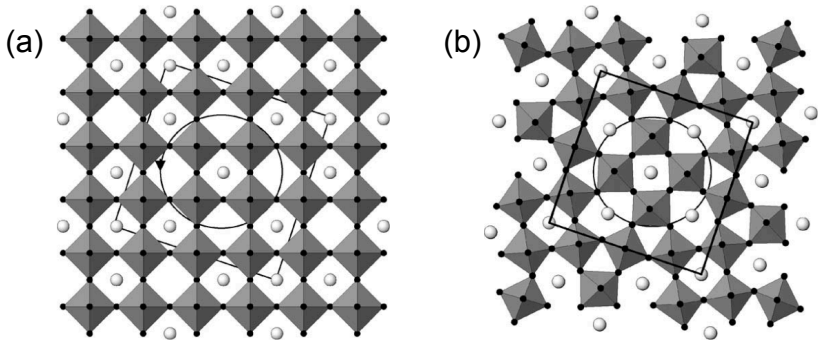

Figure 1.14: Conversion from the perovskite to the TTB structure, taken from reference [104]. (a) Perovskite structure A_xMX_3 ($x = 0.6$), seen in direction of the c-axis. The square marks the outline of the new unit cell; the circle and arrow indicate the column to be rotated. (b) The completed 45° rotation gives rise to the TTB cell. Two different structural subunits are present, a square and trigonal arrangement of MX_6 octahedra, which give rise to trigonal (**C** site), square (**B** site) and pentagonal (**A** site) channels.

The prototype TTB structure can be derived from the perovskite structure by a 45° rotation of a square group of four corner-sharing octahedra (see Figure 1.14 and reference [105]). The resulting three-dimensional network contains pentagonal

(**A** site; CN = 15), square (**B** site; CN = 12) and triangular (**C** site; CN = 9) channels running parallel to the *c*-axis. The **A** and **B** sites are occupied by large mono- or divalent ions, whereas the **C**-site remains vacant for all but small ions (e.g. Li^+). The stoichiometry varies between $A_{0.6}MX_3$ (vacant **C** sites) and $A_{0.4}MX_3$ (**C** and **B** site vacant); the filling of the pentagonal cages appears to be important for the stabilization of the TTB structure and defines the lower limit. Two structural units are present: a perovskite type M_4X_{20} unit and a hexagonal M_3X_{15} unit (herein referred to as extra-perovskite site) in which the ions *M* have a square and trigonal arrangement, respectively. The irregular shape of the pentagonal channels is a result of the combination of these structural motives: two angles are close to 90° and three angles close to 120°.

The beauty of the TTB structure is its flexibility that supports a large variety of elemental combinations on the various crystallographic sites, which allows for tuning of properties of the material. Some selectivity arises from the different sized channels. In addition, it is an ideal system to study magnetic interactions, because the angles between adjacent MX_6 units are close to 180°. Furthermore, some degree of frustration of magnetically active ions arises from the triangular connectivity of the hexagonal M_3X_{15} unit where two nearest neighbours have a common nearest neighbour.

1.3.1 Tetragonal Tungsten Bronzes

The structure of the 'original' TTB compound K_xWO_3 was determined to be tetragonal *P*4/*mbm*, with a_{TTB} ~ 12 Å and c_{TTB} ~ 4 Å by Magnéli in 1949 [106], [107]. Since then, TTB materials have been intensely studied due to their structural complexity and their technological importance [44]. In particular, TTB materials are known for their ferroelectric or relaxor ferroelectric behaviour. A prominent example of this family of materials is $Ba_2NaNb_5O_{15}$ (BNN), which undergoes a series of phase transitions, the exact nature of which is still under debate [108], [109].

BNN is one of the most-studied systems adopting the TTB structure and is believed to adopt tetragonal *P*4/*mbm* symmetry with a unit cell size of $a \approx b \approx 12$ Å and $c \approx 4$ Å at high temperatures. On cooling, the tilting of the NbO_6 octahedra, leads to symmetry decreasing modulations of pseudo-tetragonal character. Twinning due to the pseudo-symmetry further complicates the analysis of the ambient temperature structure; ferroelectric domains arise from two possible orientations of the polar *c*-axis whereas the interchange of *a*- and *b*- axis results in ferroelastic domains.

The initial description of the room temperature structure of BNN (space group *Cmm*2) by Jamieson *et al.* involved a shearing of the NbO_6 octahedra. In *Cmm*2, the *a*- and *b*- lattice parameters are rotated by 45° around the *c*-axis, ($a \approx b \approx 17.6$ Å, $c \approx 4$ Å), doubling the unit cell volume [110]. A consecutive study by Labbé *et al.* on detwinned single crystals showed that the *a*- and *c*-vectors are in fact doubled ($a \approx 2 \cdot a_{TTB} \cdot \sqrt{2} \approx 35.2$ Å, $b \approx a_{TTB} \cdot \sqrt{2} \approx 17.6$ Å, $c \approx 2 \cdot c_{TTB} \approx 8$ Å). The space group *Bbm*2 is employed to describe the quasi-commensurate modulations arsing from a combination of tilting (predominantly) and shearing of the NbO_6 units [111].

The number of detailed structural studies of TTB fluorides are still scarce, although a number of compositions of varying M^{2+}/M^{3+} has been prepared (M^{2+} = Fe, Mn, Cr, Zn, V, Mg, Co, …; M^{3+} = Fe, Cr, Ti, V, Sc, In, …) [112], [113], [114], [115], [116]. The structure and (charge) ordering patterns are intimately linked to the precise composition and stoichiometry, which further complicates any generalization of structure property relationships. The case of K_xFeF_3 highlights the importance of careful structure determination: small changes in potassium content induce modifications of the charge order pattern, structural changeovers, and different physical properties [117], [118], [119], [120].

1.3.2 The tetragonal tungsten bronze fluoride K_xFeF_3

Although detailed studies of TTB fluorides are rare, the series $K_xFe^{2+}_{1-x}Fe^{3+}_xF_3$ ($0.6 < x < 0.5$) is the exception from the rule and hence shall be described here in more detail. K_xFeF_3 ($x = 0.6$) was initially synthesised in 1965 [112], and its crystal structure was described as orthorhombic distorted tetragonal tungsten bronze type, (space group *Pba*2), with $a = 12.750(2)$ Å, $b = 12.637(2)$ Å and $c = 3.986(2)$ Å by Hardy *et al.* in 1973 [121].

Structural criteria[†] to predict ferroelectric – paraelectric transition temperatures (Curie temperature, T_C) had been developed earlier [122], [123]. In 1989, Abrahams employed these criteria to the fractional coordinates published by Hardy *et al.* to predict the ferroelectric $T_C = 535$ K of $K_{0.6}FeF_3$ [121], [124]. Experimental confirmation of the estimated T_C would not be long in coming. In the same year that $K_{0.6}FeF_3$ was predicted to be ferrelectric, measurements carried out by Ravez *et al.* revealed a λ-type anomaly in the heat capacity at $T_C = 490(10)$ K and a maximum in

[†] $T_C = (K/2k_B)(d_z/2)^2$; where K = force constant, k_B = Boltzmann's constant; $K/2k = 2.0 \times 10^4$ K Å^{-2}, d_z = atomic displacement in Å. T_C is obtained in Kelvin [K].

the dielectric permittivity at T_C = 495(10) K [125]. Examination of single crystals of $K_{0.6}FeF_3$ in polarised light indicated the loss of ferroelastic domains at T_C = 490(10) K (on heating)[‡]. This suggested a symmetry change from *mm*2 – 4/*mmm* connected to an Fe^{2+}/Fe^{3+} order – disorder transition at the transition temperature [125]. This study proved the proposed ferroelectric properties, but also showed that ferroelectricity and ferroelasticity are strongly coupled.

Furthermore, the dielectric properties were linked to the orthorhombic distortion of the structure. In 1990, Mössbauer measurements confirmed the Fe^{2+}/Fe^{3+} order – disorder transition at T_C suggested by Ravez [125], [126]. At T_C, the temperature dependence of the quadrupolar splitting and the isomer shifts of Fe^{3+} change sharply [126]. Simultaneously, the proportion of Fe^{2+} decreases, which was connected to the transfer of one *3d* electron of Fe^{2+} to the conduction band in agreement with the observed increase in electrical conductivity at T_C [125], [126]. In the same year, Ravez *et al.* studied the connection between the stoichiometry, crystal structure and dielectric properties [117]. They found that the ferroelectric transition temperature of the series K_xFeF_3 is dramatically reduced for small changes in potassium content, from T_C = 490 K (x = 0.6) to T_C = 340 K (x = 0.59) and T_C = 230 K (x = 0.56) [117].

After this burst of research activity in the late 1980s, which was initiated by the prediction of ferroelectricity based on the crystal structure, the topic remained almost untouched except for two polarised light studies by Ishihara in 1993 and 1994 [127], [128]. The first study established the correlations between refractive indices, extinction coefficients and cell parameters at room temperature, whereas the latter revealed the presence of two additional transitions on cooling [127], [128]. These transitions observed at T = 290 K and 120 K are related to a second order structural change to monoclinic symmetry, and a magnetic transition with ferromagnetic component, respectively [128].

More recently, in 2004, Fabbrici *et al*. investigated the structure of K_xFeF_3 by electron diffraction [119]. The underlying unit cell for compositions close to $K_{0.5}FeF_3$ is tetragonal *P*4*bm*, with $a = b \approx a_{TTB} \approx$ 12.634(1) Å and $c \approx c_{TTB} \approx$ 3.9515(3) Å. The modulation satellites observed at room temperature were connected to the cooperative tilting of the FeF_6 octahedra, which gives rise to the so-called 'ferroelastic superstructure' (FES) [119]. In analogy to BNN, the FES structure was

[‡] T_C = 480(10) K on cooling.

described as monoclinic *Bbm*2, with $a \approx 2\cdot\sqrt{2}\cdot a_{TTB} \approx 35.7$ Å, $b \approx \sqrt{2}\cdot a_{TTB} \approx 17.9$ Å, $c \approx 2\cdot c_{TTB} \approx 8$ Å) (see Figure 1.15.b) [119], [129]. In addition to the FES satellite peaks, different, composition-dependent reflections were found and related to a charge-ordered structure (COS, space group $P4_2bc$) where charge order results in *c*-axis doubling ($a_{COS} \approx b_{COS} \approx a_{TTB} \approx 12$ Å, $c_{COS} \approx 2\cdot c_{TTB} \approx 8$ Å) [119]. The origin of the COS satellites was related to the size difference between the cations M^{2+} and M^{3+}, rather than electrostatic interactions [119]. This was because the COS satellites disappeared when the ions M^{2+} and M^{3+} were of similar size, as for instance in $K_{0.4}Fe_{0.4}In_{0.6}F_3$ [119]. It was also pointed out by Fabbrici, that the COS and FES modulations coexist independently, both with a different periodicity compared to the conventional TTB cell [119].

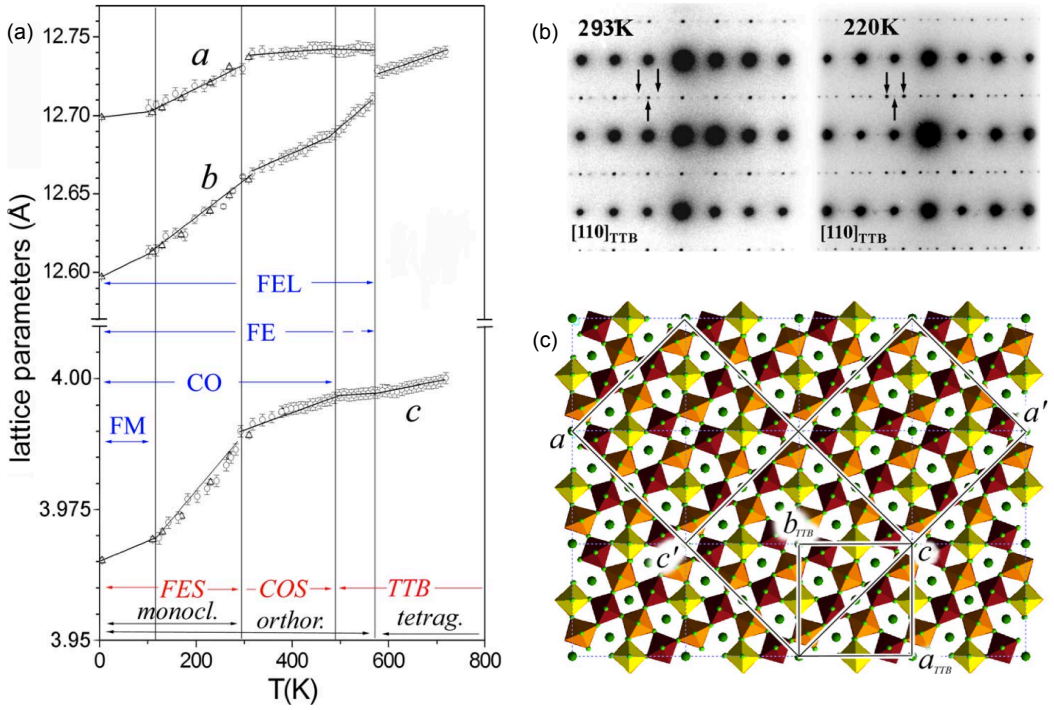

Figure 1.15: (a) The phase diagram of $K_{0.6}FeF_3$ [120]. The blue FM, CO, FE and FEL refer to ferromagnetic, charge-ordered, ferroelectric and ferroelastic regions, respectively. The red FES, COS and TTB correspond to the ferroelastic supercell, charge-ordered supercell and tetragonal tungsten bronze cell observed by diffraction experiments. (b) Electron diffraction patterns of $K_{0.6}FeF_3$. The arrows highlight the FES (T = 293 K) and COS (T = 220 K) modulation satellites. (c) The relationship between fundamental TTB cell (a_{TTB}, b_{TTB}) and the twinning variants of the FES structure (*a*, *c*; *a′*, *c′*).

In 2008, the same group studied a single crystal of the potassium rich, orthorhombic $K_{0.593}FeF_3$ [120]. They confirmed the orthorhombic *Pba*2 structure ($a \approx 12.751(1)$ Å, $b \approx$

12.660(1) Å and $c \approx 7.975(1)$ Å), and determined the charge-ordering pattern that leads to the doubling of the *c*-axis (Figure 1.16). At room temperature, Fe^{3+} and Fe^{2+} alternate along the *c*-axis on the extra-perovskite sites (2*c*) and around the perovskite cage (*4b* sites) at $z = 0.25$, whereas the *4b* site at $z = 0.75$ is disordered (nominally occupied by $Fe^{2.5+}$). The structural phase diagram (Figure 1.15) provided located the orthorhombic to tetragonal transition at a higher temperature ($T = 570$ K) than earlier reports [120]. This might be either related to the loss of ferroelastic properties, as suggested by the authors, or to the varying stoichiometry of the sample investigated. Neutron diffraction and magnetisation measurements revealed the ferrimagnetic behaviour of $K_{0.6}FeF_3$ below $T = 120$ K [120] and demonstrated that K_xFeF_3 ($x \sim 0.6$) is multiferroic below its magnetic ordering temperature. Later on, in 2011, the magnetic properties were studied in more detail, and the magnetic structure was found to resemble the antiferromagnetic triangular spin structure of $KMnFeF_6$ (space group *Pb′a*2′) [130], [131]. Most recently, $K_{0.58}FeF_3$ was studied by high-resolution powder diffraction, and an additional phase transition to orthorhombic symmetry (related to space group *Cmmm*) was observed below room temperature [132]. Unfortunately, the sample contained multiple phases K_xFeF_3 and the space group and atomic coordinates were not determined more closely [132].

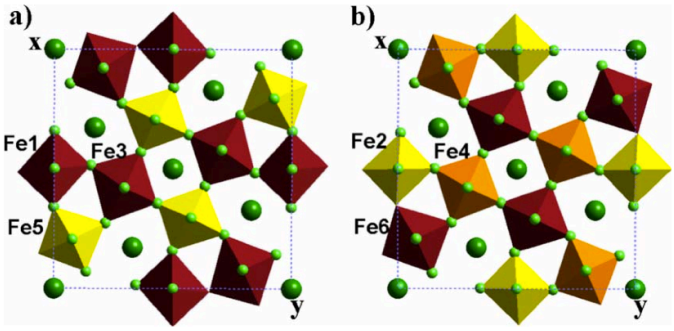

Figure 1.16: The charge ordering pattern of Fe^{2+} (dark red) and Fe^{3+} (yellow) in $K_{0.6}FeF_3$ at (a) $z = 0.25$ and (b) $z = 0.75$. One perovskite type (*4c*) site at $z = 0.75$ is occupied by both, Fe^{2+} and Fe^{3+} (orange) [120].

Over the past five years, a number of studies on the physical properties of $K_{0.6}FeF_3$ have been published. No anomalies were observed at $T_C = 490$ K in the X-band of electron paramagnetic resonance (EPR) and in ^{39}K-NMR measurements [133]. From this, Blinc *et al.* concluded that the ferroelectric – paraelectric transition is of phonon type, as in the classical oxides, rather than of electronic origin [133]. The authors remark further that there is no deviation from the Curie-Weiss behaviour in the

temperature dependent X-band EPR susceptibility at T_C, as would be expected for a ferroelectric transition with an electronic contribution [133]. From a combination of magnetic susceptibility measurements and Mössbauer spectroscopy Blinc *et al*. found that an anomaly in the dielectric constant, and the low conductivity near T_N = 122 K are typical for an intrinsic magnetoelectric effect [134]. Levstik investigated the transport mechanism of $K_{0.6}FeF_3$, and find that the tunnelling of small polarons is governing below T < 80 K, whereas a thermally activated process is dominating at high temperatures [135]. Magnetisation and muon spin relaxation measurements showed of a second magnetic transition at T = 80 K and indicated inhomogeneous static magnetic fields below T_N = 125 K, which may be connected to a spin-glass or incommensurate magnetic structure [136].

Despite these research efforts, the origin of the ferroelectric properties of the TTB fluoride $K_{0.6}FeF_3$ is still under debate. Initially, ferroelectricity was assumed to be of displacive origin, connected to the orthorhombic distortion of the structure, and the cooperative displacement of the Fe ions. A different ferroelectric mechanism was put forward in a recent theoretical study by Yamauchi *et al*. [137]. They proposed that strong electron correlations in a fully charge ordered $K_{0.6}FeF_3$ give rise to improper ferroelectricity. The complete order of Fe^{2+} and Fe^{3+} should result into to a small monoclinic distortion of the crystal, which may be related to ferroelastic properties [137]. But the current experimental description of $K_{0.6}FeF_3$ in space group *Pba*2 does not support full charge order: there are 10 Fe^{2+}, 6 Fe^{3+} and 4 $Fe^{2.5+}$ per unit cell, distributed over four *4b* and two *2c* sites (Figure 1.16) [120]. The mixed valence state points towards metallic properties, which contradicts the experimentally observed ferroelectricity (requires insulating behaviour to maintain polarization). In addition, the contribution to the ferroelectric polarization of the proposed charge order pattern cancel each other out [137]. Clearly, more experimental studies are required to clarify the nature of charge order in $K_{0.6}FeF_3$.

In summary, the extensive studies carried out in the past decades have revealed the complex phase diagram of $K_{0.6}FeF_3$. It is ferroelectric below T_C = 490 K and ferromagnetic below T = 120 K. The dielectric and magnetic properties originate from the same Fe-sublattice and make $K_{0.6}FeF_3$ a fluoride based multiferroic material [138].

1.3.3 The Bronze Structures of A_xCrF_3

In 1972, Dumora reported the preparation of the series A_xCrF_3 (A = K, Rb, Cs) [139]. The materials adopt a hexagonal tungsten bronze structure type (for $0.2 < x < 0.3$). For higher values of x, the Rb and Cs materials crystallise in structures related to pyrochlore, whereas the K compound adopts a structure related to hexagonal $BaTa_2O_6$ ($x \sim 0.5$) [139]. In 1984, a more detailed investigation Rb_xCrF_3 ($0.18 < x < 0.29$) revealed composition dependent modulations of the hexagonal tungsten bronze structure, related to ½, ⅔ and ¾ filled Rb^+ sites [140]. In the following years, the tetragonal tungsten bronze structures of other transition metal fluorides were reported. Curiously, Dumora had not reported the tetragonal bronze structure and it was believed initially that the Jahn-Teller active Cr^{2+} prevents its formation. However, when Hong *et al.* revisited the K_xCrF_3 series in 1990, they found that K_xCrF_3 ($0.51 < x < 0.59$) adopts indeed the tetragonal tungsten bronze structure [141]. The room temperature structure was indexed as orthorhombic *Pba*2, with a = 13.127 Å, b = 12.563 Å and c = 7.838 Å for x = 0.58. The doubled c-axis was related to Cr^{2+}/Cr^{3+} ordering around the perovskite cage. Magnetic susceptibility measurements showed a maximum at T_N = 10 K, with a Weiss constant θ = - 60 K [141].

1.3.4 The Tetragonal Tungsten Bronze $KMnFeF_6$

$KMnFeF_6$, firstly synthesised in 1979, crystallises in the tetragonal space group $P4_2bc$ ($a \approx 12$ Å, $c \approx 8$ Å) and shows partial order of Mn^{2+} and Fe^{3+} around the perovskite cage, whilst the extra-perovskite site appears disordered [113]. This system has received much attention, because Mn^{2+} and Fe^{3+} are expected to couple antiferromagnetically through 180° superexchange interactions, but magnetic frustration arises from the triangular connectivity of the extra-perovskite site and spin canting leads to the observed ferrimagnetic behaviour. In 1983, Banks measured the temperature dependence of magnetisation of the series $K_xMn_xFe_{1-x}F_3$, which indeed pointed towards a spin-canted antiferromagnetic order. The Néel temperature was determined as T_N = 148 K for x = 0.5 [142]. The magnetic structure was solved from neutron diffraction experiments by Lacorre in 1991 [130]. The moments of the star-like spin arrangement (space group *Pb′a*2′) are predominantly confined to the *ab*-plane and couple antiparallel between consecutive planes (see Figure 1.17) [130].

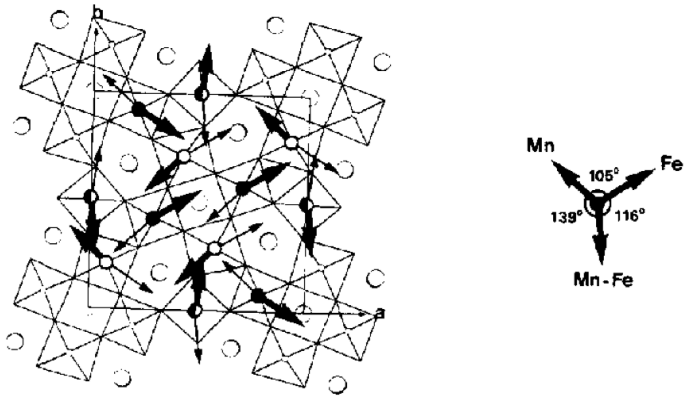

Figure 1.17: The star-like spin arrangement of $KMnFeF_6$ (space group *Pb′a*2′) derived from neutron diffraction experiments [130]. The thick and thin arrows indicate the direction of magnetic moments on two consecutive layers.

During the following years, the majority of studies aimed to unravel the magnetic properties in detail. In 1994, Giri *et al.* suggested a spin-glass transition around T = 108 K from alternating current (AC) magnetic susceptibility measurements, but Yusuf disproved this later with neutron depolarization experiments [143], [144]. ^{19}F-NMR measurements confirmed the frustrated nature of the $KMnFeF_6$ system, and further indicated the development of short-range antiferromagnetic and ferromagnetic (related to spin canting) correlations at $T < 200$ K well above the magnetic ordering temperature [145], [146]. Most recently, $KMnFeF_6$ was suggested as a multiferroic compound, based on its polar crystal structure (evoking ferroelectricity) and magnetic space group (*Pb′a*2′) by Nénert and Palstra [147]. They predicted that the application of a magnetic field switches the direction of polarization [147].

1.3.5 Mixed Tetragonal Tungsten Bronzes Fluorides

In connection with the complex magnetic behaviour of $KMnFeF_6$, the isostructural series $KMn_{1-x}Co_xFeF_6$ and $KCoFeF_6$ were studied by magnetisation and ^{19}F-NMR measurements [118], [148], [149]. The degree of magnetic frustration present in $KMn_{1-x}Co_xFeF_6$ can be described in terms of the ratio θ/T_N, and is found to decreases up to x = 0.6, and then increases again [149]. Differently to $KMnFeF_6$, $KCoFeF_6$ shows antiferromagnetic type order below T_N = 110 K, and antiferro- and ferromagnetic short-range correlations occur only in the vicinity of T_N [118], [150].

The multiferroic properties of $K_{0.6}FeF_3$ and the prediction of $KMnFeF_6$ as multiferroic material triggered the investigations of $K_{0.6}Cr_{0.4}Fe_{0.6}F_3$ and $K_{0.6}Fe_{0.4}Cu_{0.6}F_3$, where Fe is in its 2+ and 3+ oxidation state, respectively [151], [152]. Through EPR, Mössbauer and ^{39}K-NMR studies, $K_{0.6}Fe_{0.4}Cu_{0.6}F_3$ was found to show antiferromagnetic behaviour below $T_N = 85$ K, whereas $K_{0.6}Cr_{0.4}Fe_{0.6}F_3$ shows two relaxor-type magnetic transitions at $T = 37$ K and 11 K. The crystal structures of both materials were described in space group *P*4/*mbm*, and with surprisingly identical lattice constants of $a = 12.5925$ Å and $c = 3.9406$ Å [151], [152]. Despite the centrosymmetric space group – that implies disorder of Cr (Cu) and Fe – these TTB fluorides were declared multiferroic [136], [138], [151]. On the other hand, the materials were said to undergo a structural transition to orthorhombic *Pba*2 in their ferroelectric phase, but details of neither structure nor dielectric measurements have been published [136].

Several other transition metal fluoride compounds $KM^{2+}M^{3+}F_6$ adopting the tetragonal tungsten bronze structure have been reported. These materials adopt the same tetragonal $P4_2bc$ structure as $KMnFeF_6$ ($a \approx 12$ Å, $c \approx 8$ Å) and order magnetically below T_N. The combinations studied to date include M^{2+}/M^{3+} (T_N) = Zn/Ti (80 K); Zn/V (50 K); V/Sc (60 K); Cr/Sc (23 K); Mn/Sc (50 K) and Mn/Cr (31 K) [114], [115]. Except for the lattice constants, structural details (e.g. atomic coordinates, occupancies or temperature dependence) are not known. The structural similarities of $KMnCrF_6$ to $KMnFeF_6$ suggest that also the former is a multiferroic compound.

Other notable TTB fluorides include $K_x(Mg_xIn_{1-x})F_3$ ($x = 0.38$), where Mg and In are disordered but a monoclinic distorted cell is adopted as the result of octahedral tilting [153]. Further, $Ba_xSr_{2-x}(NH_4)Mg_5F_{15}$ ($x = 1.8 - 0.6$) crystallises in the tetragonal space group *P*4/*mbm*, and shows yellow-white luminescence and phosphorescence in samples heated to $T = 570$ K [154].

In summary, the TTB fluorides show a wealth of intriguing and potentially technological important properties. They form for a wide range of element combination, which allows tuning of their (magnetic) properties. Detailed structural studies are absolutely necessary to gain a deeper understanding of the connections between structure and properties and to clarify the nature of the ferroelectric transitions observed.

1.4 References

[1] H.K. Onnes, *Communications from the Physical Laboratory at the University of Leiden* Suppl. 29 (Nov. 1911).

[2] J. Bednorz, K. Müller, *Zeitschrift für Physik B: Condensed Matter* 64 (1986) 189.

[3] J. Bardeen, L.N. Cooper, J.R. Schrieffer, *Physical Review* 108 (1957) 1175.

[4] M.R. Norman, *Science* 332 (2011) 196.

[5] Coalition for the Commercial Application of Superconductors (2012). CCAS, Available from: http://www.ccas-web.org/superconductivity/ {Accessed: 05. August 2012]

[6] K. Chahara, T. Ohno, M. Kasai, Y. Kozono, *Applied Physics Letters* 63 (1993) 1990.

[7] C. Zener, *Physical Review* 81 (1951) 440.

[8] A. Millis, P. Littlewood, B. Shraiman, *Physical Review Letters* 74 (1995) 5144.

[9] D. Louca, T. Egami, *Journal of Applied Physics* 81 (1997) 5484.

[10] S. Billinge, R. Difrancesco, G. Kwei, J. Neumeier, J. Thompson, *Physical Review Letters* 77 (1996) 715.

[11] Y. Tokura, *Reports on Progress in Physics* 69 (2006) 797.

[12] O. Glemser, *Journal of Fluorine Chemistry* 33 (1986) 45.

[13] S. Margadonna, G. Karotsis, *Journal of the American Chemical Society* 128 (2006) 16436.

[14] S. Margadonna, G. Karotsis, *Journal of Materials Chemistry* 17 (2007) 2013.

[15] G. Giovannetti, S. Margadonna, J. Van Den Brink, *Physical Review B: Condensed Matter and Materials Physics* 77 (2008) 075113.

[16] V. Scatturin, J. Hastings, L. Corliss, N. Elliott, *Acta Crystallographica* 14 (1961) 19.

[17] S. Yoneyama, K. Hirakawa, *Journal of the Physical Society of Japan* 21 (1966) 183.

[18] Y. Xiao, Y. Su, H.F. Li, C. Kumar, R. Mittal, J. Persson, A. Senyshyn, K. Gross, T. Brueckel, *Physical Review B: Condensed Matter and Materials Physics* 82 (2010) 094437.

[19] Y. Xu, X. Hao, M. Lv, Z. Wu, D. Zhou, J. Meng, *Journal of Chemical Physics* 128 (2008) 164721.

[20] G. Wang, Z. Li, L. Zheng, Z. Yang, *Physical Review B: Condensed Matter and Materials Physics* 84 (2011) 045111.

[21] S. Ido, S. Uchida, K. Kitazawa, S. Tanaka, *Journal of the Physical Society of Japan* 57 (1988) 997.

[22] H. Kawamura, T. Hirooka, M. Fukohira, I. Shirotan, Y. Maruyama, H. Inokuchi, *Chemical Physics Letters* 15 (1972) 594.

[23] K. Andres, N. Kuebler, M. Robin, *Journal of Physics and Chemistry of Solids* 27 (1966) 1747.

[24] W. Grochala, R. Egdell, P. Edwards, Z. Mazej, B. Zemva, *ChemPhysChem* 4 (2003) 997.

[25] C. Shen, B. Zemva, G. Lucier, O. Graudejus, J. Allman, N. Bartlett, *Inorganic Chemistry* 38 (1999) 4570.

[26] W. Grochala, P.P. Edwards, *Physica Status Solidi B: Basic Solid State Physics* 240 (2003) R11.

[27] R.-H. Odenthal, D. Paus, R. Hoppe, *Zeitschrift für Anorganische und Allgemeine Chemie* 407 (1974) 151.

[28] W. Grochala, R. Hoffmann, *Angewandte Chemie* 113 (2001) 2816.

[29] Z. Mazej, E. Goreshnik, Z. Jaglicic, B. Gawel, W. Lasocha, D. Grzybowska, T. Jaron, D. Kurzydlowski, P. Malinowski, W. Kozminski, J. Szydlowska, P. Leszczynski, W. Grochala, *CrystEngComm* 11 (2009) 1702.

[30] S. Mclain, M. Dolgos, D. Tennant, J. Turner, T. Barnes, T. Proffen, B. Sales, R. Bewley, *Nature Materials* 5 (2006) 561.

[31] D.-Y. Liu, F. Lu, L.-J. Zou, *Journal of Physics: Condensed Matter* 21 (2009) 026014.

[32] W. Grochala, A. Porch, P. Edwards, *Solid State Communications* 130 (2004) 137.

[33] W. Grochala, *Journal of Materials Chemistry* 19 (2009) 6949.

[34] A. Okazaki, Y. Suemune, *Journal of the Physical Society of Japan* 16 (1961) 176

[35] M. Hutching, E. Samuelse, G. Shirane, *Physical Review* 188 (1969) 919.

[36] L. Paolasini, R. Caciuffo, A. Sollier, P. Ghigna, M. Altarelli, *Physical Review Letters* 88 (2002) 106403.

[37] K. Kugel, D. Khomskii, *Soviet Physics - JETP* 37 (1973) 725

[38] E. Pavarini, E. Koch, A.I. Lichtenstein, *Physical Review Letters* 101 (2008) 266405.

[39] P. Ghigna, M. Scavini, C. Mazzoli, M. Brunelli, C. Laurenti, C. Ferrero, *Physical Review B: Condensed Matter and Materials Physics* 81 (2010) 073107.

[40] W. Massa, D. Babel, *Chemical Reviews* 88 (1988) 275.

[41] K. Adil, M. Leblanc, V. Maisonneuve, P. Lightfoot, *Dalton Transactions* 39 (2010) 5983.

[42] N.A. Hill, *The Journal of Physical Chemistry B* 104 (2000) 6694.

[43] E. Sharp, D. Horowitz, J. Miller, *Journal of Applied Crystallography* 44 (1973) 5399.

[44] J. Scott, *Reports on Progress in Physics* (1979).

[45] Y. Xiao, Y. Su, R. Mittal, T. Chatterji, T. Hansen, *Physical Review B: Condensed Matter and Materials Physics* 79 (2009) 060504(R).

[46] H. Wen, G. Mu, L. Fang, H. Yang, X. Zhu, *EPL (Europhysics Letters)* 82 (2008) 17009.

[47] V. Johnson, W. Jeitschko, *Journal of Solid State Chemistry* 11 (1974) 161.

[48] R. Pöttgen, D. Johrendt, *Zeitschrift für Naturforschung, B: A Journal of Chemical Sciences* 63 (2008) 1135

[49] H. Hiramatsu, H. Kamioka, K. Ueda, H. Ohta, T. Kamiya, M. Hirano, H. Hosono, *Physica Status Solidi A: Applications and Materials Science* 203 (2006) 2800.

[50] Y. Kamihara, H. Hiramatsu, M. Hirano, R. Kawamura, H. Yanagi, T. Kamiya, H. Hosono, *Journal of the American Chemical Society* 128 (2006) 10012

[51] T. Watanabe, H. Yanagi, T. Kamiya, Y. Kamihara, H. Hiramatsu, M. Hirano, H. Hosono, *Inorganic Chemistry* 46 (2007) 7719

[52] Y. Kamihara, T. Watanabe, M. Hirano, H. Hosono, *Journal of the American Chemical Society* 130 (2008) 3296.

[53] D. Johrendt, H. Hosono, R.-D. Hoffmann, R. Poettgen, *Zeitschrift für Kristallographie* 226 (2011) 435.

[54] J.H. Tapp, Z. Tang, B. Lv, K. Sasmal, B. Lorenz, P.C.W. Chu, A.M. Guloy, *Physical Review B: Condensed Matter and Materials Physics* 78 (2008) 060505.

[55] M. Rotter, M. Tegel, D. Johrendt, *Physical Review Letters* 101 (2008) 107006.

[56] H. Ogino, Y. Matsumura, Y. Katsura, K. Ushiyama, S. Horii, K. Kishio, J.-I. Shimoyama, *Superconductor Science and Technology* 22 (2009) 075008.

[57] K. Ishida, Y. Nakai, H. Hosono, *Journal of the Physical Society of Japan* 78 (2009) 062001.

[58] D.C. Johnston, *Advances in Physics* 59 (2010) 803.

[59] H.-H. Wen, S. Li, *Annual Review of Condensed Matter Physics* 2 (2011) 121.

[60] P.M. Aswathy, J.B. Anooja, P.M. Sarun, U. Syamaprasad, *Superconductor Science and Technology* 23 (2010) 073001.

[61] L. Malavasi, S. Margadonna, *Chemical Society Reviews* 41 (2012) 3897.

[62] H. Luetkens, H.-H. Klauss, M. Kraken, F.J. Litterst, T. Dellmann, R. Klingeler, C. Hess, R. Khasanov, A. Amato, C. Baines, M. Kosmala, O.J. Schumann, M. Braden, J. Hamann-Borrero, N. Leps, A. Kondrat, G. Behr, J. Werner, B. Buechner, *Nature Materials* 8 (2009) 305.

[63] A.J. Drew, C. Niedermayer, P.J. Baker, F.L. Pratt, S.J. Blundell, T. Lancaster, R.H. Liu, G. Wu, X.H. Chen, I. Watanabe, V.K. Malik, A. Dubroka, M. Roessle, K.W. Kim, C. Baines, C. Bernhard, *Nature Materials* 8 (2009) 310.

[64] C.S. Liu, Y.L. Li, Y. Xu, X.L. Wang, Z. Zeng, *Physica B: Condensed Matter* 404 (2009) 3242.

[65] K. Kuroki, H. Usui, S. Onari, R. Arita, H. Aoki, *Physical Review B: Condensed Matter and Materials Physics* 79 (2009) 224511.

[66] Y. Mizuguchi, Y. Hara, K. Deguchi, S. Tsuda, T. Yamaguchi, K. Takeda, H. Kotegawa, H. Tou, Y. Takano, *Superconductor Science and Technology* 23 (2010) 054013.

[67] C. Wang, S. Jiang, Q. Tao, Z. Ren, Y. Li, L. Li, C. Feng, J. Dai, G. Cao, Z.-A. Xu, *EPL (Europhysics Letters)* 86 (2009) 47002.

[68] Y. Li, X. Lin, T. Zhou, J. Shen, Y. Luo, Q. Tao, G. Cao, Z. Xu, *Physica C: Superconductivity and Its Applications* 470 (2010) S493.

[69] N.D. Zhigadlo, S. Katrych, M. Bendele, P.J.W. Moll, M. Tortello, S. Weyeneth, V.Y. Pomjakushin, J. Kanter, R. Puzniak, Z. Bukowski, H. Keller, R.S. Gonnelli, R. Khasanov, J. Karpinski, B. Batlogg, *Physical Review B: Condensed Matter and Materials Physics* 84 (2011) 134526.

[70] T.M. Mcqueen, M. Regulacio, A.J. Williams, Q. Huang, J.W. Lynn, Y.S. Hor, D.V. West, M.A. Green, R.J. Cava, *Physical Review B: Condensed Matter and Materials Physics* 78 (2008) 024521.

[71] C. De La Cruz, W.Z. Hu, S. Li, Q. Huang, J.W. Lynn, M.A. Green, G.F. Chen, N.L. Wang, H.A. Mook, Q. Si, P. Dai, *Physical Review Letters* 104 (2010) 017204.

[72] Y. Luo, Y. Li, S. Jiang, J. Dai, G. Cao, Z.-A. Xu, *Physical Review B: Condensed Matter and Materials Physics* 81 (2010) 134422.

[73] Y. Luo, H. Han, S. Jiang, X. Lin, Y. Li, J. Dai, G. Cao, Z.-A. Xu, *Physical Review B: Condensed Matter and Materials Physics* 83 (2011) 054501.

[74] S.J.E. Carlsson, F. Levy-Bertrand, C. Marcenat, A. Sulpice, J. Marcus, S. Pairis, T. Klein, M. Nunez-Regueiro, G. Garbarino, T. Hansen, V. Nassif, P. Toulemonde, *Physical Review B: Condensed Matter and Materials Physics* 84 (2011) 104523.

[75] S.J. Singh, J. Prakash, S. Patnaik, A.K. Ganguli, *Superconductor Science and Technology* 22 (2009) 045017.

[76] C. Wang, Z. Ma, S. Jiang, Y. Li, Z. Xu, G. Cao, *Science China - Physics, Mechanics and Astronomy* 53 (2010) 1225.

[77] M.A. Mcguire, D.J. Singh, A.S. Sefat, B.C. Sales, D. Mandrus, *Journal of Solid State Chemistry* 182 (2009) 2326.

[78] B. Maroni, L. Malavasi, M.C. Mozzati, M.S. Grandi, A.H. Hill, D. Chermisi, P. Dore, P. Postorino, *Physical Review B: Condensed Matter and Materials Physics* 82 (2010) 104503.

[79] M.A. Mcguire, A.F. May, B.C. Sales, *Journal of Solid State Chemistry* 191 (2012) 71.

[80] M. Tropeano, M.R. Cimberle, C. Ferdeghini, G. Lamura, A. Martinelli, A. Palenzona, I. Pallecchi, A. Sala, I. Sheikin, F. Bernardini, M. Monni, S. Massidda, M. Putti, *Physical Review B: Condensed Matter and Materials Physics* 81 (2010) 184504.

[81] S.C. Lee, E. Satomi, Y. Kobayashi, M. Sato, *Journal of the Physical Society of Japan* 79 (2010) 023702.

[82] B. Maroni, D. Di Castro, M. Hanfland, J. Boby, C. Vercesi, M.C. Mozzati, S. Weyeneth, H. Keller, R. Khasanov, C. Drathen, P. Dore, P. Postorino, L. Malavasi, *Journal of the American Chemical Society* 133 (2011) 3252.

[83] M. Tegel, S. Johansson, V. Weiß, I. Schellenberg, W. Hermes, R. Pottgen, D. Johrendt, E. Germany, *EPL (Europhysics Letters)* 84 (2008) 67007.

[84] S.K. Mishra, R. Mittal, S.L. Chaplot, S.V. Ovsyannikov, D.M. Trots, L. Dubrovinsky, Y. Su, T. Brueckel, S. Matsuishi, H. Hosono, G. Garbarino, *Physical Review B: Condensed Matter and Materials Physics* 84 (2011) 224513.

[85] X. Zhu, F. Han, P. Cheng, G. Mu, B. Shen, B. Zeng, H.H. Wen, *Physica C: Superconductivity and Its Applications* 469 (2009) 381.

[86] X. Zhu, F. Han, P. Cheng, G. Mu, B. Shen, L. Fang, H.-H. Wen, *EPL (Europhysics Letters)* 85 (2009) 17011.

[87] Y. Xiao, Y. Su, R. Mittal, T. Chatterji, T. Hansen, S. Price, C.M.N. Kumar, J. Persson, S. Matsuishi, Y. Inoue, H. Hosono, T. Brueckel, *Physical Review B: Condensed Matter and Materials Physics* 81 (2010) 094523.

[88] P.J. Baker, I. Franke, T. Lancaster, S.J. Blundell, L. Kerslake, S.J. Clarke, *Physical Review B: Condensed Matter and Materials Physics* 79 (2009) 060402.

[89] I.R. Shein, A.L. Ivanovskii, *JETP Letters* 88 (2008) 683.

[90] S. Takeshita, R. Kadono, M. Hiraishi, M. Miyazaki, A. Koda, S. Matsuishi, H. Hosono, *Physical Review Letters* 103 (2009) 027002.

[91] S. Chong, S. Hashimoto, H. Yamaguchi, K. Kadowaki, *Journal of Superconductivity and Novel Magnetism* 23 (2010) 1479

[92] S. Matsuishi, Y. Inoue, T. Nomura, H. Yanagi, M. Hirano, H. Hosono, *Journal of the American Chemical Society* 130 (2008) 14428.

[93] M. Zhang, C. Zhang, Y. Yu, L. Zhang, Z. Qu, L. Ling, C. Xi, S. Tan, Y. Zhang, *New Journal of Physics* 12 (2010) 083050.

[94] S. Matsuishi, Y. Inoue, T. Nomura, Y. Kamihara, M. Hirano, H. Hosono, *New Journal of Physics* 11 (2009) 025012.

[95] H. Kabbour, L. Cario, F. Boucher, *Journal of Materials Chemistry* 15 (2005) 3525.

[96] H. Kabbour, L. Cario, S. Jobic, B. Corraze, *Journal of Materials Chemistry* 16 (2006) 4165.

[97] H. Yanagi, S. Park, A. Draeseke, D. Keszler, J. Tate, *Journal of Solid State Chemistry* 175 (2003) 34.

[98] A. Zakutayev, J. Tate, G. Schneider, *Physical Review B: Condensed Matter and Materials Physics* 82 (2010) 195204.

[99] G. Wang, L. Zheng, M. Zhang, Z. Yang, *Physics Letters A* 374 (2009) 351.

[100] N. Emery, E.J. Wildman, J.M.S. Skakle, G. Giriat, R.I. Smith, A.C. Mclaughlin, *Chemical Communications* 46 (2010) 6777

[101] A. Marcinkova, T. Hansen, C. Curfs, S. Margadonna, J. Bos, *Physical Review B: Condensed Matter and Materials Physics* 82 (2010) 174438.

[102] S. Kimber, A. Hill, Y.-Z. Zhang, H. Jeschke, R. Valentí, C. Ritter, I. Schellenberg, W. Hermes, R. Pöttgen, D. Argyriou, *Physical Review B: Condensed Matter and Materials Physics* 82 (2010) 100412.

[103] R.H. Mitchell (2002) *Perovskites: Modern and Ancient*. Ontario: Almaz Press.

[104] R.H. G. Siebert, *Zeitschrift für Anorganische und Allgemeine Chemie* 391 (1972) 117

[105] M.O.O.K. B.G. Hyde, *Acta Crystallographica, Section A: Foundations of Crystallography* 29 (1973) 243.

[106] A. Magneli, *Arkiv foer Kemi* 1 (1949) 269

[107] A. Magneli, *Arkiv foer Kemi* 1 (1949).

[108] J. Scott, S. Hayward, M. Miyake, *Journal of Physics: Condensed Matter* 17 (2005) 5911.

[109] C. Filipic, Z. Kutnjak, R. Lortz, A. Torres-Pardo, M. Dawber, J.F. Scott, *Journal of Physics: Condensed Matter* 19 (2007) 236206.

[110] A. Jamieson, Bernstein, *Journal of Chemical Physics* 50 (1969) 4352.

[111] P. Labbe, H. Leligny, B. Raveau, J. Schneck, J.C. Toledano, *Journal of Physics: Condensed Matter* 2 (1990) 25.

[112] R. De Pape, *Comptes Rendus de l'Académie des Sciences*. 260 (1965) 4527.

[113] E. Banks, S. Nakajima, G.J.B. Williams, *Acta Crystallographica, Section B: Structural Science* 35 (1979) 46.

[114] E. Banks, M. Shone, Y. Hong, R. Williamson, W. Boo, *Inorganic Chemistry* 21 (1982) 3894.

[115] Y.S. Hong, W.O.J. Boo, D.L. Mattern, *Journal of Solid State Chemistry* 183 (2010) 1805.

[116] A. Caramanian, N. Dupont, P. Gredin, A. De Kozak, *Zeitschrift für Anorganische und Allgemeine Chemie* 625 (1999) 933.

[117] J.A. Ravez, S.C.; Mercier, A.M.; Rabardel, L.; R. De Pape, J*ournal of Applied Physics* 67 (1990) 3.

[118] S. Giri, K. Ghoshray, A. Ghoshray, *Journal of Physics: Condensed Matter* 11 (1999) 4261.

[119] S. Fabbrici, E. Montanari, L. Righi, G. Calestani, A. Migliori, *Chemistry of Materials* 16 (2004) 3007.

[120] F. Mezzadri, S. Fabbrici, E. Montanari, L. Righi, G. Calestani, E. Gilioli, F. Bolzoni, A. Migliori, P*hysical Review B: Condensed Matter and Materials Physics* 78 (2008) 064111.

[121] A. Hardy, A.M. Hardy, G. Ferey, *Acta Crystallographica, Section B: Structural Science* 29 (1973) 1654.

[122] S. Abrahams, S. Kurtz, P. Jamieson, *Physical Review* 172 (1968) 551.

[123] S.C. Abrahams, *Acta Crystallographica, Section B: Structural Science* 44 (1988) 585.

[124] S. Abrahams, *Acta Crystallographica Section B: Structural Science* 45 (1989) 228.

[125] J.A. Ravez, S.C.; R. De Pape, *Journal of Applied Physics* 65 (1989) 4.

[126] Y. Calage, S. Abrahams, J. Ravez, R. De Pape, *Journal of Applied Physics* 67 (1990) 430.

[127] S. Ishihara, Z.G.Ye, H. Rabe, J.-P. Rivera, F. Kubel, H. Schmid, *Ferroelectrics* 140 (1993) 53.

[128] S. Ishihara, J.-P. Rivera, E. Kita, Z.-G. Ye, F. Kubel, H. Schmid, *Ferroelectrics* 162 (1994) 51.

[129] P. Labbe, H. Leligny, B. Raveau, J. Schneck, J. Toledano, *Journal of Physics: Condensed Matter* 2 (1990) 25.

[130] P. Lacorre, J. Pannetier, G. Ferey, *Journal of Magnetism and Magnetic Materials* 94 (1991) 331.

[131] F. Mezzadri, G. Calestani, C. Pernechele, M. Solzi, G. Spina, L. Cianchi, F. Del Giallo, M. Lantieri, M. Buzzi, E. Gilioli, *Physical Review B: Condensed Matter and Materials Physics* 84 (2011) 104418.

[132] S.A. Reisinger, M. Leblanc, A.-M. Mercier, C.C. Tang, J.E. Parker, F.D. Morrison, P. Lightfoot, *Chemistry of Materials* 23 (2011) 5440.

[133] R. Blinc, B. Zalar, P. Cevc, A. Gregorovič, B. Žemva, G. Tavčar, V. Laguta, J. Scott, N. Dalal, *Journal of Physics: Condensed Matter* 21 (2009) 045902.

[134] R. Blinc, G. Tavcar, B. Zemva, D. Hanzel, P. Cevc, C. Filipic, A. Levstik, Z. Jaglicic, Z. Trontelj, N. Dalal, *Journal of Applied Physics* 103 (2008) 074114.

[135] A. Levstik, C. Filipic, V. Bobnar, G. Tavcar, B. Zemva, *EPL (Europhysics Letters)* 83 (2008) 27001.

[136] A. Potočnik, A. Zorko, D. Arčon, E. Goreshnik, B. Žemva, R. Blinc, P. Cevc, Z. Trontelj, Z. Jagličić, J.F. Scott, *Physical Review B: Condensed Matter and Materials* 81 (2010) 214420.

[137] K. Yamauchi, S. Picozzi, *Physical Review Letters* 105 (2010) 107202.

[138] J. Scott, R. Blinc, *Journal of Physics: Condensed Matter* 23 (2011) 113202.

[139] D. Dumora, J. Ravez, P. Hagenmuller, *Journal of Solid State Chemistry* 5 (1972) 35.

[140] Y. Hong, K. Baker, R. Williamson, W. Boo, *Inorganic Chemistry* 23 (1984) 2787.

[141] Y. Hong, K. Baker, A. Shah, R. Williamson, W. Boo, *Inorganic Chemistry* 29 (1990) 3037.

[142] E.S. Banks, M.; Williamson, R.F.; Boo, W.O.J. , *Inorganic Chemistry* (1983) 4.

[143] S. Giri, K. Ghoshray, R. Ranganathan, A. Roy, B. Bal, A. Ghoshray, *Solid State Communications* 91 (1994) 273.

[144] S. Mohammad Yusuf, L. Madhav Rao, R. Mukhopadhyay, S. Giri, K. Ghoshray, A. Ghoshray, *Solid State Communications* 101 (1997) 145.

[145] S. Giri, K. Ghoshray, A. Ghoshray, N. Chatterjee, *Physical Review B: Condensed Matter and Materials Physics* 54 (1996) 411.

[146] S. Giri, K. Ghoshray, A. Ghoshray, N. Chatterjee, *Physical Review B: Condensed Matter and Materials Physics* 56 (1997) 3347.

[147] G. Nénert, T. Palstra, J*ournal of Physics: Condensed Matter* 19 (2007) 406213.

[148] S. Giri, K. Ghoshray, A. Ghoshray, N. Chatterjee, *Physical Review B: Condensed Matter and Materials Physics* 54 (1996) 411.

[149] S. Giri, K. Ghoshray, *Physical Review B: Condensed Matter and Materials Physics* 57 (1998) 5918.

[150] S. Giri, K. Ghoshray, A. Ghoshray, N. Chatterjee, *Journal of Magnetism and Magnetic Materials* 157 (1996) 411.

[151] R. Blinc, P. Cevc, A. Potocnik, B. Zemva, E. Goreshnik, D. Hanzel, A. Gregorovic, Z. Trontelj, Z. Jaglicic, V. Laguta, *Journal of Applied Physics* 107 (2010) 043511.

[152] R. Blinc, G. Tavcar, B. Zemva, E. Goreshnik, D. Hanzel, P. Cevc, A. Potocnik, V. Laguta, Z. Trontelj, Z. Jaglicic, *Journal of Applied Physics* 106 (2009) 023924.

[153] S.C. Abrahams, *Acta Crystallographica, Section B: Structural Science* 55 (1999) 12.

[154] F. Kubel, M. Pantazi, *Zeitschrift für Anorganische und Allgemeine Chemie* 633 (2007) 752.

Chapter 2

Theoretical Concepts

2.1 Diffraction Basics

2.1.1 Crystal Lattices and Symmetry

Crystals are regular and symmetric arrangements of atoms. They can be described as a combination of a three dimensional array of lattice points. To each lattice point is associated a structural motif (i.e. atoms, ions or molecules). The simplest repeating unit in a crystal is the unit cell. There are seven unique ways of connecting lattice points to give primitive unit cells (i.e. containing only one lattice point), which define the crystal systems. In combination with one type of lattice centring (primitive, body-, face-, base-centred) they form the 14 Bravais lattices, listed in Table 2.1 together with the relationships between their unit cell vectors and angles.

Crystal family (symbol)	Crystal system (No. of space groups)	Crystallographic point groups	Restrictions on cell parameters
Triclinic (*a*)	Triclinic (2)	*1*, $\bar{1}$	none
Monoclinic (*m*)	Monoclinic (13)	*2*, *m*, *2/m*	$\alpha = \gamma = 90°$
Orthorhombic (*o*)	Orthorhombic (59)	*222*. *mm2*. *mmm*	$\alpha = \beta = \gamma = 90°$
Tetragonal (*t*)	Tetragonal (68)	*4*, $\bar{4}$, *4/m*, *422*, *4mm*, $\bar{4}2m$, *4/mmm*	$a = b$, $\alpha = \beta = \gamma = 90°$
Hexagonal (*h*)	Trigonal (18)	*3*, $\bar{3}$, *32*, *3m*, $\bar{3}m$	$a = b$, $\alpha = \beta = 90°$, $\gamma = 120°$
	(7)		$a = b = c$, $\alpha = \beta = \gamma$
	Hexagonal (27)	*6*, $\bar{6}$, *6/m*, *622*, *6mm*, $\bar{6}2m$, *6/mmm*	$a = b$, $\alpha = \beta = 90°$, $\gamma = 120°$
Cubic (*c*)	Cubic (36)	*23*, *m3*, *432*, $\bar{4}3m$, $m\bar{3}m$	$a = b = c$, $\alpha = \beta = \gamma = 90°$

Table 2.1: Classification of crystal families and their restriction on the cell parameters in three dimensions [1].

The atoms within a unit cell may or may not be related to each other by symmetry operations (rotation, reflection, improper rotation, screw axis and glide plane). These operations are classified in 32 crystallographic point groups. The combination of different point groups and Bravais lattices results in the 230 standard space groups, which are used to describe the symmetry of a crystal and are listed in the International Tables for Crystallography A [1].

It is often useful to refer to a plane of atoms in a crystal, which is characterized by the intersection points of a given plane with the unit cell edges. The reciprocals of the intercepts give the Miller indices (*hkl*), where *h*, *k* and *l* refer to the intercepts

with a, b and c, respectively. A family of parallel planes, spaced out by d_{hkl}, is identified by the Miller indices of the first plane away from the origin.

The space group description is not only a succinct way of describing the position of the repeating units in a crystal, but is of further importance in solid state chemistry. The intimate link between physical properties and crystal symmetry is summarized by Neumann's principle. It postulates that the symmetry of a physical property must contain the symmetry elements of the point group of the crystal and cannot have lower symmetry [2].

2.1.2 Bragg's Law

The accurate knowledge of the arrangement of atoms in solids is an asset to understand the connections between structure and properties. The interdependence of atoms in a crystalline material can give rise to various forms of long-range order, influencing or even determining the physical properties. This information is generally obtained from diffraction experiments. Although diffraction phenomena arise for every wave that encounters an obstacle in its path, they are most significant when wavelength and diffracting object are of similar dimensions. X-rays ($E \approx 120 - 6$ keV; $\lambda \approx 0.1 - 2$ Å) are well suited to probe interatomic distances in crystalline materials and are probably the most widespread radiation source for diffraction experiments. The principles of diffraction are described in a large number of textbooks, therefore no specific references will be given for the equations in this chapter, but the interested reader is referred to [3], [4], [5] ,[6].

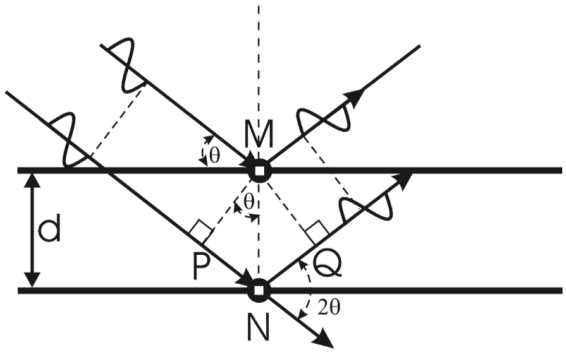

Figure 2.1: Illustration of the reflection of two rays incident at angle θ on two consecutive planes separated by d [4]. Constructive interference according to Bragg's law occurs if the path difference $\overline{PNQ}$ is equal to an integer multiple of the wavelength λ.

If we assume specular reflection of monochromatic X-rays of wavelength λ by planes of atoms (acting as mirrors), a family of planes give rise to Bragg reflection, when the incident angle θ and lattice spacing d is such that the path difference is an integer (n) multiple of λ and gives rise to constructive interference. Bragg's law, illustrated in Figure 2.1, describes this:

$$n \cdot \lambda = 2d \cdot \sin(\theta)$$

Although this relationship gives the correct solution, the model is simplified: firstly, X-rays are scattered by the electrons of an atom (rather than being reflected by the atom). In the classical description of the interaction between X-rays and electrons, an electromagnetic wave hitting elastically an electron at rest makes it vibrate, and a moving charged particle leads to the emission of electromagnetic radiation at an angle 2θ with respect to the incident wave. The quantum mechanical description leads to the same picture, reflecting the wave-particle dualism of X-rays. Another drawback of Bragg's law is that it assumes perfect alignment of the atoms within a crystal. But the atoms in a crystal are subject to displacements, e.g. from thermal vibration or microstrain effects. However, Bloss showed that Bragg's law is also valid for atoms displaced in consecutive layers [4], [7].

2.1.3 Reciprocal Space

Some diffraction phenomena are more conveniently described in reciprocal space. The reciprocal lattice points are described by a set of reciprocal lattice vectors $\boldsymbol{a}^*$, $\boldsymbol{b}^*$, $\boldsymbol{c}^*$, which are normal to the planes of the real lattice vectors $\boldsymbol{b}$-$\boldsymbol{c}$, $\boldsymbol{a}$-$\boldsymbol{c}$ and $\boldsymbol{b}$-$\boldsymbol{a}$, respectively and can be obtained from:

$$\boldsymbol{a}^* = \frac{(\boldsymbol{b}\times\boldsymbol{c})}{V};\ \boldsymbol{b}^* = \frac{(\boldsymbol{a}\times\boldsymbol{c})}{V};\ \boldsymbol{c}^* = \frac{(\boldsymbol{a}\times\boldsymbol{b})}{V}$$

where (x) denotes the cross product. The relationship between real and reciprocal lattice vectors is such that,

$$\boldsymbol{a}^* \cdot \boldsymbol{b} = \boldsymbol{a}^* \cdot \boldsymbol{c} = \boldsymbol{b}^* \cdot \boldsymbol{a} = \boldsymbol{b}^* \cdot \boldsymbol{c} = \boldsymbol{c}^* \cdot \boldsymbol{a} = \boldsymbol{c}^* \cdot \boldsymbol{b} = 0 \text{ and } \boldsymbol{a}^* \cdot \boldsymbol{a} = \boldsymbol{b}^* \cdot \boldsymbol{b} = \boldsymbol{c}^* \cdot \boldsymbol{c} = 1$$

where (·) is the dot product. A reciprocal lattice vector $\boldsymbol{d}^*$

$$\boldsymbol{d}^* = h\boldsymbol{a}^* + k\boldsymbol{b}^* + l\boldsymbol{c}^*$$

is pointing from the origin of the reciprocal lattice to a point *hkl*, and is perpendicular to the family of planes (*hkl*) in real space.

Its magnitude is

$$|\boldsymbol{d}^*| = |h\boldsymbol{a}^* + k\boldsymbol{b}^* + l\boldsymbol{c}^*| = 1/d$$

where d is the spacing between planes (*hkl*) in real space.

2.1.4 Diffraction from Crystalline Materials

From the positions of the reflections, the unit cell size and symmetry can be determined, whereas the intensity can be analysed to determine the contents of a unit cell, i.e. fractional atomic coordinates, thermal displacement factors, occupancies, etc. The intensity I_{hkl} of a Bragg reflection (or line in powder diffraction) is proportional to $|F_{hkl}|^2$, where F_{hkl} is the structure factor, defined as

$$F_{hkl} = \sum_{i=1}^{N} f_i \exp[2\pi i(hx_i + ky_i + lz_i)]$$

where the sum is over all atoms i in the unit cell, f_i is the scattering form factor of the i^{th} atom for X-rays or scattering length b_i for neutrons, *hkl* are the Miller indices of a particular plane and x_i, y_i, z_i are the fractional coordinates of the i^{th} atom. Thermal motion can be described with the temperature factor $B_{iso} = 8\pi^2 U$, where $U = \langle r'^2 \rangle$, and r' is the square mean shift of an atom from its equilibrium position.

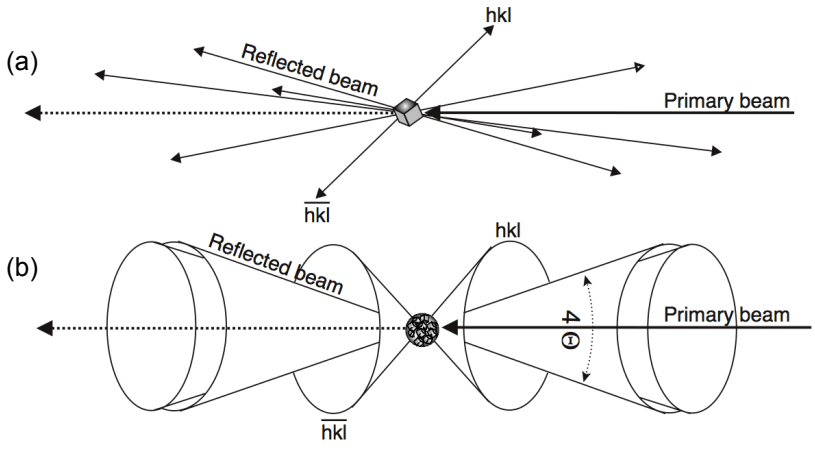

Figure 2.2: (a) Sketch of beams scattered from a single crystal and (b) from a randomly oriented polycrystalline powder [4]. For a polycrystalline sample, the individual reflections (*hkl*) of a single crystal smear out to give the Debye-Sherrer cones.

In single crystal diffraction, the scattering vector for a plane (*hkl*) of atoms, d^*_{hkl} is a spatial vector, pointing into a specific direction. This spatial information is however lost in a polycrystalline powder. The random orientation of crystallites gives rise to coaxial diffraction cones, the Debye-Sherrer cones. The difference between diffraction from a single crystal and a powder is illustrated in Figure 2.2. The analysis of single crystal diffraction uses the integrated intensities of individual reflections (*hkl*) to derive the structure factor and obtain a crystallographic model. However, this approach is limited in the analysis of a powder pattern, as the unambiguous determination of individual peak intensities is limited due to peak overlap. With this approach, used in the early days of powder diffraction, only simple crystal structures, in which Bragg reflections are well spaced, could be analysed.

2.2 Rietveld Method

2.2.1 Fundamentals of Rietveld Refinements

Rather than attempting a decomposition of the observed peaks to the individual contribution from Bragg reflections, H.M. Rietveld developed a different approach, now widely used in powder diffraction analysis [8], [9]: the intensity y_i at each step i of a diffraction pattern arises from the sum of contribution from several Bragg peaks y_h, and the background intensity y_b:

$$y_i = y_b + \sum_i y_h$$

where the individual intensities are represented by mathematical models, each incorporating features related to both sample (e.g. strain, disorder, extinction, absorption, preferred orientation) and instrument (e.g. misalignment, beam divergence, diffractometer geometry). These expressions use adjustable parameters, and can be refined in a least-squares minimization to give the best estimate. The function S_y to be minimized is the weighted difference between observed and calculated intensities:

$$S_y = \sum_i w_i \, (y_{io} - y_{ic})^2$$

where $w_i = 1/\sigma^2(y_{io})$; y_{io} and y_{ic} are observed and calculated intensities at step i, and $\sigma(y_{io})$is the uncertainty estimate for y_{io}. The calculated intensities y_c are given by:

$$y_{ic} = s \sum_k m_k L_k \, |F_k|^2 G \Delta\theta_k + y_{ib}$$

with the scalar s, the Bragg reflection k, the background intensity y_{ib}, the multiplicity factor m_k, the Lorentz-polarization factor L_k, the structure factor F_k, the calculated position of the Bragg peak θ_k, $\Delta\theta_k = 2\theta_i - 2\theta_k$, and $G(\Delta\theta_{ik})$ the reflection profile function.

2.2.2 Background and Peak-Shape Functions

A number of factors contribute to the background of a diffraction profile, including diffuse scattering (from disordered or amorphous material and sample environment), sample fluorescence and detector noise. For diffraction patterns with well-spaced Bragg reflections, the background can be determined by a linear interpolation of (manually selected) background points. In more complex cases, the background must be included as a variable in the refinement. It can be approximated with a polynomial function, given by:

$$y_{ib} = \sum_{n} b_n [2\theta_i]^n$$

where b_n are refinable background parameters and $2\theta_i$ is in radians. For poorly defined peak-shapes, the background tends to correlate with other parameters, in particular temperature factors. The peak-shape is primarily determined by sample and diffractometer characteristics, but is also influenced by absorption and preferred orientation, as well as misalignment and beam divergence. Whereas simple Gaussian functions are often sufficient to describe profiles from neutron diffraction, more complex peak-shapes are required for higher-resolution instruments, where sample effects overcome instrument contributions. A widespread function for constant-wave X-ray patterns is the Pseudo-Voigt, which results from combining a Lorentzian (L) and a Gaussian (G) contribution:

$$\eta L + (1-\eta)G = \eta\left(\frac{\sqrt{4}}{\pi \cdot H_k}\right) \cdot \left(\frac{1}{1+4\mathrm{X}_{ik}^2}\right) + (1-\eta) \cdot \left(\frac{\sqrt{4\ ln2}}{\sqrt{\pi H_k}}\right) \cdot (\exp\left(-4\ ln2\ \mathrm{X}_{ik}^2\right))$$

with the mixing coefficient η, the full-width at half maximum (FWHM) of the k^{th} reflection H_k, and $X_{i,j} = \Delta\theta_{i,j} \,/\, H_k$. Usually the FWHM H_k is considered to vary with θ according to:

$$H_k^{Gauss} = \sqrt{U\ \tan^2\theta_k + V\ \tan\theta_k + W}$$

and

$$H_k^{Lorenztian} = X\ \tan\theta + Y/cos\theta$$

where U, V and W and / or X and Y are variable profile parameters. The variables of background and peak-shape functions are refined in a Rietveld refinement procedure. The Rietveld method allows the simultaneous analysis of multiple

phases and, whilst several parameters are refined for each phase individually, (e.g. lattice parameters, scale factor, fractional coordinates, thermal parameters, preferred orientation) others are determined globally (e.g. zero point, instrumental profile, asymmetry, background, absorption).

2.2.3 Judging the Quality of Fits

In principle, the quality of the obtained (refined) structural model can be judged by the values of residual functions, the R-factors

- the profile R_p $$R_p = \frac{\sum_i y_{io} - y_{ic}}{\sum_i y_{io}}$$

- the weighted profile R_{wp} $$R_{wp} = \frac{\sum_i w_i (y_{io} - y_{ic})^2}{\sum_i w_i y_{io}^2}$$

- the Bragg R_B $$R_B = \frac{\sum_i |I_{ko} - I_{kc}|}{\sum_i I_{ko}}$$

- the expected R-factor R_{exp} $$R_{exp} = \sqrt{\frac{(N-P)}{\sum_i w_i y_{io}^2}}$$

- the goodness of fit or χ^2 $$G^2 = \chi^2 = \frac{R_{wp}}{R_{exp}} = \frac{\sum_i w_i (y_{io} - y_{ic})^2}{(N-P)}$$

where N and P are the number of profile points and refined parameters, respectively. In theory, if the value of the square of the goodness of fit parameter, G, is equal to one ($G^2 = \chi^2 = 1$), then the model is an ideal description of the experiment. Generally, a poor fit is indicated by $\chi^2 >> 1$, whereas $\chi^2 < 1$ indicates over parameterisation.

The indicators of fit are not only subject to the quality of the refinement, but also dependent on the estimation of experimental uncertainties sigma y_{io} that feed directly into the minimization function S_y, through the weight $w_i = 1/\sigma^2(y_{io})$, and are employed in the residual functions above. In practice however, it can be difficult to obtain the estimation of $\sigma(y_{io})$ for detectors that do not directly count quanta, such as image plates (IP) and charge coupled device detectors (CCD) [10]. Over- and underestimation of sigma y_{io} can lead to $\chi^2 < 1$ and $\chi^2 >> 1$, respectively. Similarly, good counting statistics from high-precision data decrease R_{exp} but increase the difference of R_{wp} and R_{exp}, and hence χ^2.

In summary, the R-factors can provide a good indication for the quality of a fit, and should be monitored in the course of a refinement, but graphical inspection of the diffraction profile and chemical sense are as important in judging the quality of a Rietveld fit.

The Rietveld refinements of the collected diffraction profiles were performed using the General Structure Analysis System (GSAS) programs [11]. The GSAS package can be used to process X-ray and neutron data of single crystal or powder samples. The EXPGUI program is a graphical user interface for GSAS and was used to prepare input data and to execute programs inside GSAS [12].

2.3 Total Scattering

2.3.1 Introduction to Local Structure Determination

In conventional crystallography, whose principles are outlined above, one assumes a perfectly ordered periodic array of atoms in a sample and considers only Bragg reflections. However, a large number of solid materials lack the long-range order required for Bragg diffraction, being glassy, amorphous, liquid or nano-sized. Diffraction still occurs, but due to the lack of long-rang order it is only diffuse and generally discarded as background. Yet the background contains contributions from structural short-range order and proper treatment allows the extraction of valuable structural information. The techniques described in this section were originally developed to study materials lacking long-range order, but more recently they are also applied to study short-range correlations and disorder in crystalline solids.

The typical information obtained from conventional crystallography is the average positions of a pair of atoms (i.e. the superposition of atoms in a unit cell) from which the interatomic distances are derived. This averaged-out structure does not always provide a correct picture of the local atomic arrangement and may give e.g. false (or misleading) bond-distances and angles. A more detailed picture can be obtained from the analysis of the total scattering, i.e. Bragg and diffuse, the latter giving information about the atomic arrangement on a local scale (i.e. r = 2 – 50 Å), and the average distance between a pair of atoms.

2.3.2 Obtaining the Atomic Pair Distribution Function

A method commonly used to analyse total scattering data from powders is the pair distribution function (PDF) analysis. The atomic PDF is a radial distribution function, $G(r)$, which gives the probability density of finding two atoms separated by a distance r. It is defined as

$$G(r) = 4\pi r\,(\rho_r - \rho_0)$$

Where ρ_0 is the average atomic number density, ρ_r is the atomic pair density at a radial distance r, given by

$$\rho(r) = \frac{1}{4\pi r^2 N} \sum_i \sum_{j \neq i} \frac{b_i b_j}{\langle b \rangle^2} \delta(r - r_{ij})$$

where the indices i and j go over all N atoms in the sample, b_i is the scattering factor of atom i, $\langle b \rangle$ is the average scattering factor and r_{ij} is the distance between atoms i and j. The construction of $G(r)$ from an array of atoms (that can be ordered or disordered) is shown in Figure 2.3.

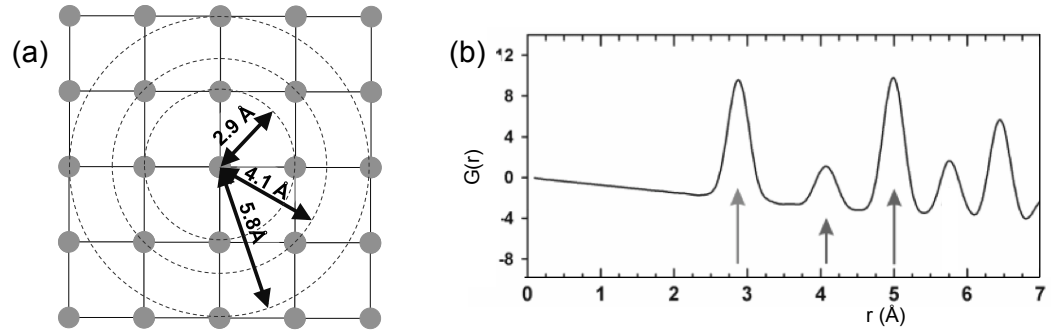

Figure 2.3: $G(r)$ construction from array of atoms: (a) The number of atoms located at a distance r is directly related to (b) the intensity $G(r)$. The arrows mark the peaks for shells at r = 2.9 Å, 4.1 Å and 5.8 Å. Adapted from reference [13].

Experimentally, $G(r)$ can be obtained by a Fourier transform of the total scattering structure function $S(Q)$, which is in principle a normalized and background corrected diffraction profile. The dimensionless structure function $S(Q)$ is obtained from the coherent scattering intensity $I(Q)$

$$S(Q) = \frac{I_{coh}(Q)}{N\langle f(Q) \rangle^2}$$

where N is the number of scatterers and $\langle f(Q) \rangle$ is the average scattering power per atom, i.e. the square of the atomic form factor $f(Q)$ for X-rays or the coherent scattering cross section for neutrons. The magnitude of the scattering vector $\boldsymbol{Q}$ is defined as

$$Q = |\boldsymbol{Q}| = \frac{4\pi \sin\theta}{\lambda}$$

where θ and λ are the incident angle and the wavelength of incident radiation, respectively. In principle, one can fit $S(Q)$ in reciprocal space (Rietveld refinement),

but for a more intuitive approach $S(Q)$ is transformed to real-space data via a Fourier transform to give $G(r)$:

$$G(r) = \frac{2}{\pi}\int_0^\infty Q[S(Q) - 1]\sin(Qr)\, dQ$$

The experimentally obtainable Q limits the integration, which is theoretically up to infinite Q. The oscillations ('termination ripples') arising from the termination of the integral can be minimized by collecting data up to high Q [14], when the Debye-Waller factor becomes insignificant (Q ~ 30 Å^{-1}). $G(r)$ functions using a standard Cu-K_α cathode are subject to termination effects (Q ~ 8 Å^{-1}) and the use of synchrotron or fast neutron sources is desirable. It is further important to obtain good statistics at high Q, which can be obtained considerably faster by using 2D detectors (~ 1 minute collection time) instead of 1D detectors (~ 10 hours collection time).

2.3.3 Modelling of the Local Structure

As the $G(r)$ is a real-space description of the (local) crystal structure, some information is readily available: bond distances can be interfered from peak positions, the integrated peak intensity is correlated to the coordination number, and the peak width is dependent on thermal or static disorder.

The $G(r)$ can also be fitted to a structural model using a least squares algorithm, similar to the Rietveld method. For a given model, the $G(r)$ can be calculated [15]:

$$G_{calc}(r) = \frac{1}{Nr}\sum_i\sum_{j\neq i}\left[\frac{b_i b_j}{\langle b\rangle^2}\delta(r - r_{ij})\right] - 4\pi r\rho_0$$

where the sum goes over all pairs of atoms i and j within the model crystal separated by r_{ij}. The scattering power of arom is b_i and $<b>$ is the average scattering power of the sample. Structural models include refinable parameters, such as lattice constants, scale factors, atomic site occupation and (an)isotropic thermal displacement factors. The correlated movement of atoms that leads to peak sharpening at low r is described by a factor delta d2. The parameters Q_{damp} and Q_{broad} describe the Gaussian dampening due to the limited Q-space and the peak broadening from increased noise at high Q. Q_{damp} and Q_{broad} are obtained by fitting the $G(r)$ of an calibrant (e.g. Ni) and not refined for individual samples. This approach is limited to cases where a comparably small model cell is sufficient to

describe the short- and intermediate range order. It is also possible to define the fitting range in *r*, and compare the length-scale at which the local structure becomes equivalent to the average structure obtained from analysis of the Bragg reflections.

Larger model systems, involving several hundred or thousands of atoms, can be modelled using Monte Carlo simulated annealing. Here, an algorithm tries to find the global minimum in a complex potential energy surface, or the best fit to an experimental pattern in the reverse Monte Carlo (RMC) technique. The energy of the model is repeatedly calculated whilst varying the parameters in a random way. If these changes give a lower potential energy, the changes are accepted, for a higher energy the changes are accepted or rejected in a random fashion. The result of the RMC is one structure consistent with the observed distribution function.

In this work, the diffraction patterns were background corrected and transformed to real space scattering data using the program PDFgetX2 [16]. Real space refinements were carried out in the program PDFgui [15].

2.4 Generation and Characteristics of Radiation

Different types of radiations can be used for the diffraction experiment, for instance X-rays and neutrons. An overview of different sources and main characteristics is given below.

2.4.1 Laboratory X-ray Sources

In the laboratory, X-rays for diffraction experiments are produced inside a vacuum tube, where electrons accelerated by a potential difference ($E < 60$ kV) hit a metal anode target (typically copper). The incident electrons induce electronic transitions in the metal atoms, which leads to the emission of X-rays as relaxation to the ground state occurs. The resulting X-ray spectrum consists of continuous 'white' radiation or 'Bremsstrahlung' and the more intense 'characteristic lines'. The accelerator voltage defines the minimum wavelength of the X-ray radiation ($E_{max} = \text{eV} = hc/\lambda$ or $\lambda_{\min} = 12398/\text{V}$). At certain, material-specific energies, low-lying electrons are ejected from inner shells and electromagnetic radiation is emitted as electrons from higher shells fill the gap. The discrete peaks K_β, $K_{\alpha1}$ and $K_{\alpha2}$ correspond to the relaxation of an electron from $3p \rightarrow 1s$ (K_β) and $2p \rightarrow 1s$ ($K_{\alpha1}$ and $K_{\alpha2}$). The corresponding wavelengths for Cu are $\lambda(K_\beta) = 1.392$ Å, $\lambda(K_{\alpha1}) = 1.54056$ Å and $\lambda(K_{\alpha2}) = 1.54439$ Å. Typical X-ray spectrum for different cathode materials and the voltage dependence of the continuous radiation are shown in Figure 2.4.

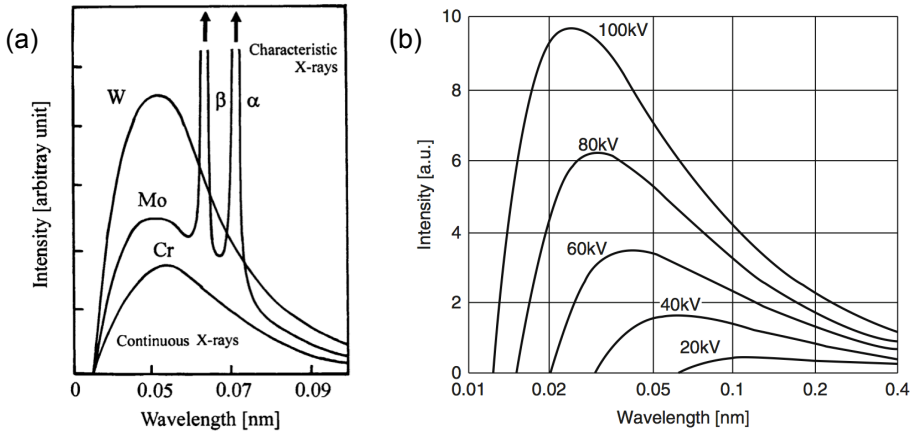

Figure 2.4: (a) Typical X-ray spectrum for different cathode materials, consisting of the continuous Bremsstrahlung and the sharp characteristic lines. (b) The minimum wavelength is dependent on the voltage of the anode [17].

Typically, monochromators (e.g. crystals of Si, Ge, quartz) and filters are used to select a wavelength before a diffraction experiment. The most common anode material is copper, as it provides the shortest wavelength above $\lambda = 1$ Å from its characteristic spectrum. Silver or tungsten anodes provide shorter wavelength (e.g. for total scattering), whereas lower energies X-rays (e.g. from Cr or Co anodes) are used to avoid fluorescence from elements excitable by Cu-radiation; but have the disadvantage of increased absorption and reduced number of accessible reflections.

2.4.2 Synchrotron Sources

Uniformly moving charged particles do not emit electromagnetic radiation unless they are accelerated. This can be observed when charged particles pass through an electrical field: their direction (and speed) is altered from their original path, and electromagnetic radiation is emitted. This effect is used in light sources, such as the synchrotrons, to generate X-rays of high intensity and brilliance over a continuous spectral range. The power that is emitted by a charged particle moving along a circular orbit is given by

$$P = \frac{2e^2cE^4}{3R^2(m_0c^2)^4} = \frac{2e^2c\gamma^4}{3R^2}$$

where P is the energy emitted per unit time, e is the particle charge, c is the speed of light, E is the energy of the particle, m_0 is the mass at rest and R is the radius of the orbit. It is clear from this equation that high-energy particles of small mass are required, usually electrons or positrons.

In synchrotron radiation sources, electrons produced from an electron gun are accelerated in a linear accelerator (linac). The linac consists of a series of chambers with an electrical field that alternates in such a way that the electrons passing through it always experience a positive field ahead and are accelerated. The particles are then transmitted into a circular accelerator, the booster synchrotron. The energy reached by the particles in the booster e.g. at the ESRF in France is $E =$ 6 GeV. The high-energy particles are then injected into the third and largest part of the accelerator system, the storage ring, which can reach several hundred meters in circumference. Here the electrons are kept at a constant energy close to the speed of light, and accelerated on a toroidal trajectory, so that electromagnetic radiation is generated in tangential direction to the ring. The electron beam circulates in vacuum for several hours (lifetime of the beam). High vacuum inside the beam cavity is a

necessary condition, as collisions with (air) particles would slow down the electron beam. Further, a set of bending magnets (the 'lattice') is needed to keep the electrons on their circular path, and a series of radio-frequency cavities restores the electrons energy that is lost as X-rays are emitted.

The storage ring consists of a set of bending magnets (BM) and straight sections, the insertion devices (ID). Bending magnets are dipole magnets that curve the path of the electrons, and produce a stable beam over a wide spectral range. Insertion devices consist of a series of magnets of opposing polarity, and cause the electrons to wiggle as they pass through. Insertion devices can be divided into wigglers and undulators, where the former produce a wide cone of X-rays of a broad spectrum and high energy, and the latter give a bright and narrow beam whose energy can be tuned. In addition to the bending magnets and insertion devices, a further set of focusing devices concentrates the beam to minimize loss.

2.4.3 Neutron Sources

Spallation sources and nuclear reactors are the two methods employed to produce neutrons for diffraction experiments. The Institute Laue Langevin (ILL) in Grenoble, France uses a reactor source to produce the world's highest continuous neutron flux in the moderator regime for research use. An intense neutron flux is generated from the fission reaction of highly enriched ^{235}U. The source is surrounded by a coolant (e.g. deuterated water, D_2O), which reflects the neutrons, concentrating them in space, and equilibrates their energy, to give 'thermal' neutrons with a Maxwell distribution of wavelengths ($\lambda = 1 - 2$ Å). The use of 'cold' and 'hot' moderators makes shorter and longer wavelengths accessible. The Spallation Neutron Source (SNS) in Oak Ridge, Tennessee, USA is an accelerator-based neutron source providing the world's most intense pulsed neutron beam for scientific purposes. High energetic neutrons are released from a heavy-metal target (e.g. Hg or W) by bombarding the target with energetic particles such as protons ($E \sim 1$ GeV). The 'epithermal' neutrons pass through a moderator (water or methane) to reduce their energy corresponding to wavelengths used for diffraction experiments. Regardless of the source, the neutrons are guided to the experimental stations through evacuated tubes (e.g. Ni-coated glass), which convey the neutrons via total reflection from the walls.

2.4.4 Selecting a Suitable Type of Radiation

Synchrotron radiation has a number of advantages compared to conventional X-ray radiation produced by laboratory sources, such as Cu or Mo cathodes (Figure 2.5). Firstly, the wavelength is not limited to discrete values, but can be selected to match the requirements of the experiments and thus minimize radiation damage and absorption effects. Secondly, synchrotron radiation is well known for its high brightness, intensity and collimation (i.e. brilliance), making data collection faster, resulting in higher-resolution data and allowing studying of smaller specimens. In addition, synchrotron light is fully polarized, a property that can be used to study magnetism, and has a defined time-structure/ pulsed light emission that may be used in time-resolved studies.

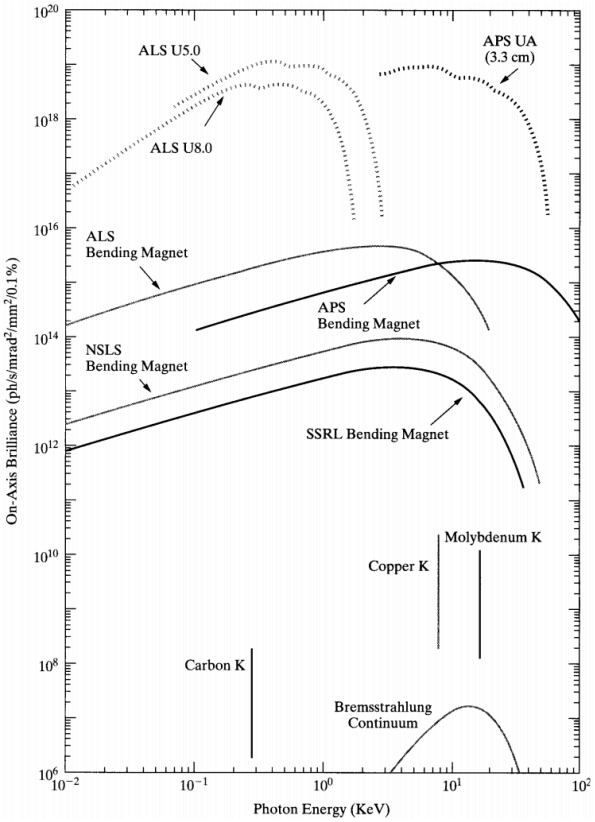

Figure 2.5: Comparison of on-axis brilliance and spectral range from insertion devices (here labelled U) and bending magnet (BM) sources and conventional laboratory sources [18].

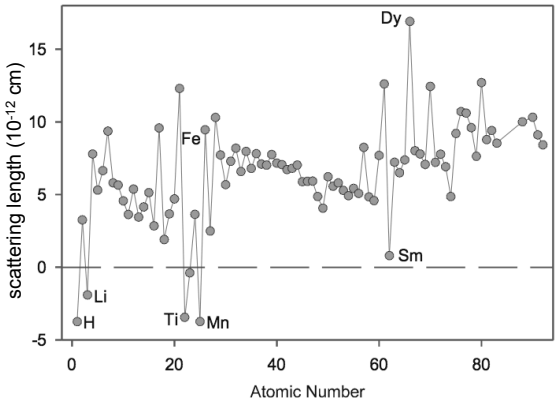

Figure 2.6: Variation of the neutron scattering length with atomic number [19].

There are several drawbacks of X-ray radiation: the scattering power of the elements varies with the number of their electrons, making it difficult to detect the light atoms, and to differentiate between species that are close in the periodic table, e.g. Mn and Cr. The scattering power of the atoms also decreases with increasing scattering angle, a fact, which is in part outweighed by the shorter wavelengths available in synchrotron sources.

For neutrons on the other hand the scattering form factor varies randomly with Z throughout the periodic table, see Figure 2.6. Hence, neutron diffraction is ideal to study light elements, or to distinguish between closely related atom species and even isotopes. Neutrons interact with the nucleus rather then the electron cloud as in X-ray diffraction; and because the scattering power (~ 1 fm) is considerably shorter than the neutron's wavelength, the coherent scattering length b is angle independent. Therefore, accuracy of the atomic positions and thermal parameters determined by neutron and X-ray diffraction is comparable. In addition to constant wavelength diffraction, time dependent (time-of-flight) experiments are possible at pulsed neutron sources, which use the whole spectral range available.

One of the biggest advantages of neutron radiation is that it allows the determination of magnetic structures: neutrons are spin S = ½ particles, and posses a magnetic moment μ = 1.9132 (nuclear magnetons) (μ = -1.04187563(25) x 10^{-3} μ_B) that can interact with the magnetic moments present in a sample. However, the scattering from the magnetic density is of the same order of magnitude as the neutron's wavelength, and therefore angle-dependent. Another advantage of neutron radiation is the weaker interaction of the uncharged particles with matter: although higher flux and significantly larger sample volumes are required as

compared to X-ray diffraction, the uncharged neutrons can penetrate deeply into matter and hence allow the use of more complex sample environments.

2.4.5 High-Pressure Diffraction

Pressure, as a fundamental state variable, is a powerful tool to modify material properties. The combination of diffraction techniques and (high) pressure gives insight into relationships between fundamental state variables, such as volume, pressure and temperature and shed light onto a material's fundamental properties. Equations of state (EoS) relate each variable to a function of the other variables, and can also be formulated as derivatives of thermodynamic functions such as the internal energy U or Helmholtz free energy F. In practice, semi-empirical equations as the Murnaghan or Birch EoS are used to describe properties of solids. Application of pressure leads to a continuous shortening of bond lengths within, and to structural phase transitions outside the stability range of a structural phase. Modifications of the structure are often connected to changes in electronic (and physical) properties, such as the insulator to metal transition occurring in transition-metal oxides at high pressures.

In general, diamond anvil cells (DACs) are used to create high pressures (several GPa up to hundreds of GPa) for structure and/or property measurements. Diamond, the hardest known material, is well suited for high-pressure diffraction studies, due to its transparency to a large portion of the electromagnetic spectrum.

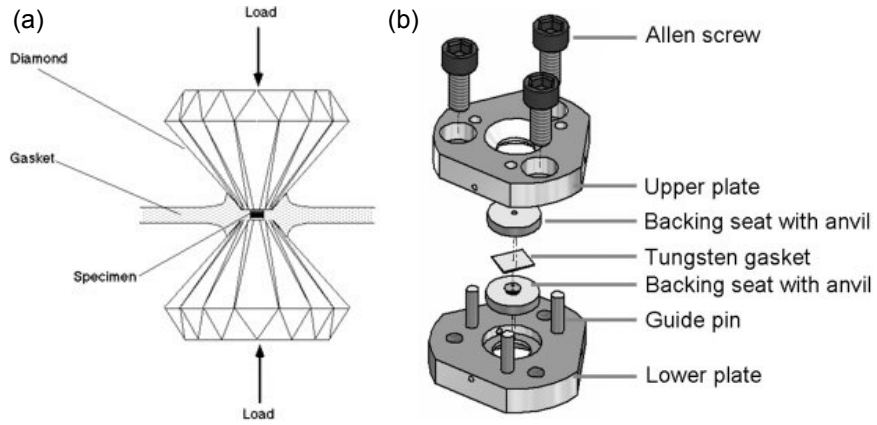

Figure 2.7: (a) Sketch of the working principle of a diamond anvil cell. (b) Assembly of a pressure cell typically used for diffraction experiments [20].

A schematic DAC is shown in Figure 2.7. Two fully parallel opposing diamonds are seated in a cell (commonly manufactured from steel and tungsten carbide). Pressure is generated by tightening screws holding the cell or via gas membranes, and is transferred from the anvils to the sample space. A metallic seal (typically steel) is squeezed between the anvils and has a hole that contains sample, pressure sensor and medium. To assess the pressure in situ, a pressure sensor is contained in the sample space. The pressure dependence of the luminescence of ruby or of the fluorescence of samarium-doped borate can be easily measured with a laser and optical spectrometer. Alternatively, the lattice constants of a salt or metal can be followed with pressure, but overlapping Bragg reflections may limit the usefulness of this approach. The pressure transmitting medium should be inert to sample and cell under experimental conditions. Frequently used pressure mediums are liquids (silicon-oil or a 1:4 mixture of methanol and ethanol), molten salts (e.g. CsCl), or gases such as helium, which shows very good quasi-hydrostatic behaviour even at high pressures and low temperatures.

As the cell is commonly made from a highly absorbent material, it limits the Ewalds sphere available for data collection. Further, the small sample space reduces the number of crystallites available for diffraction. However, the use of hard X-rays and small beamsizes at 3rd generation synchrotron sources counterbalances the constrained geometry and allows focusing on the cell centre where pressure gradients are small. Oscillation of the DAC (± 3°) in combination with 2D detectors can compensate for the missing powder average.

2.5 Magnetism

2.5.1 Origin of Magnetism in Solids

Magnetic phenomena in solids are linked to the magnetic moments of its components. From classical electrodynamics, moving charged particles generate magnetic dipole moment. Magnetism is also a quantum mechanical phenomenon. Many elementary particles, such as electron, protons, neutrons and muons, have a characteristic magnetic moment, connected to their intrinsic spin and orbital angular momentum S and L, via the gyromagnetic ratio (g- or Lande-factor). For a free electron,

$$\mu_J = \frac{-g_J \mu_B J}{\hbar}$$

where J is the total angular momentum $J = S + L$, μ_B is the Bohr magneton $\mu_B = e\hbar/2m$, and g_J is the Lande g-factor given by

$$g_J = \frac{3}{2} + \frac{S(S+1) - L(L+1)}{2J(J+1)} \approx 2$$

2.5.2 Collective Interactions

The macroscopic magnetization observed for a material is the sum of the magnetic moments of all its components. However, the majority of contributions cancel each other out (i.e. paired spins in closed shells), and magnetic ordering phenomena are mainly limited to the collective interaction of unpaired *d* and *f* electrons of transition metals and lanthanides, respectively. Depending on the spin order, different typed of magnetism can be distinguished: materials, in which all electrons are paired and aligned antiparallel, are diamagnetic. The random, parallel and antiparallel orientation of unpaired spins is referred to as para-, ferro- and antiferromagnetism. Para- and antiferromagnetic (PM, AFM) materials do not show net magnetism, whereas ferromagnets (FM) possess a spontaneous magnetic moment. Also the antiparallel order of moments of different magnitude (i.e. arising from different ionic species) gives rise to a net magnetization, and is called ferrimagnetism.

2.5.3 Response to External Magnetic Field

Magnetic interactions can be probed from a material's response in an external magnetic field. The applied magnetic field H induces a magnetization M, which is a function of the magnetic susceptibility χ according to

$$M = \chi H$$

Diamagnetic materials are repelled by a magnetic field; they have small and negative χ. Superconducting materials are perfect diamagnets (χ = -1) and expel magnetic flux from their interior (Meissner-Ochsenfeld effect). The unpaired spins of PM tend to align with an external field, and hence PMs have small positive χ. However, thermal activation counteracts the spin-alignment, and gives rise to a temperature dependence of χ, formulated in the Curie law:

$$\chi = C / \mathrm{T}$$

with the Curie constant C, defined as

$$C = \frac{N_A \mu_{eff}^2 \mu_B}{3k_B}$$

where N_A is Avogadro's number, k_B is Boltzmann constant and μ_{eff} is the effective magnetic moment

$$\mu_{eff} = g_J \sqrt{J(J+1)} \approx g_J \sqrt{S(S+1)}$$

and can be approximated as its spin-only value in transition metals as the orbital moment is quenched by crystal field effects. Also AFM and FM materials have positive χ, where $\chi_{\mathrm{AFM}} \lesssim \chi_{\mathrm{PM}}$ and $\chi_{\mathrm{FM}} >> 1$. Ordering phenomena occur below a critical temperature, which can be determined from the temperature dependence of the magnetization χ: for AFM, it decreases below their Néel temperature T_{N}, whilst it increases in a FM below the Curie temperature T_{C}. Above their ordering temperatures, AFM and FM follow the Curie-Weiss law:

$$\chi = \mathrm{C} / (T - \theta)$$

where the Weiss constant θ is negative for AFM and positive for FM. Typical magnetization curves as a function of temperature are shown in Figure 2.8.

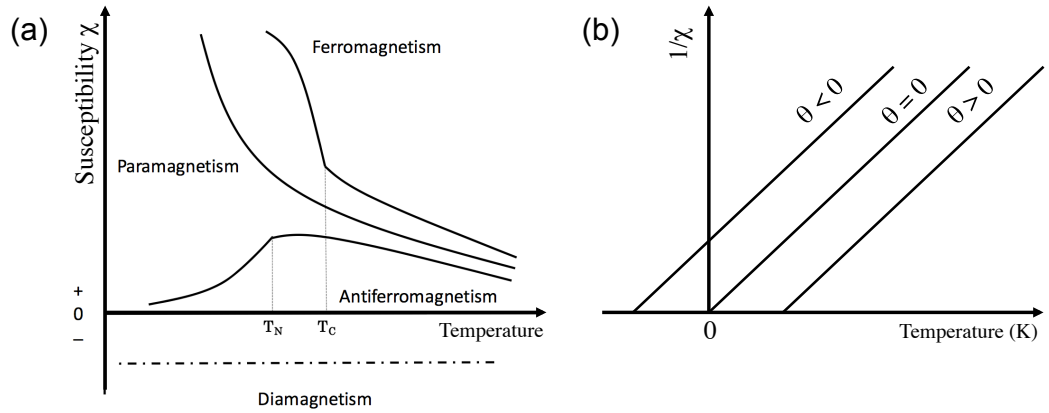

Figure 2.8: (a) Typical curves of the temperature dependent magnetisation for paramagnetic (PM), ferromagnetic (FM), antiferromagnetic (AFM) and diamagnetic (DM) materials. The magnetisation of a FM compound increases below its Curie temperature T_C, whilst the magnetisation of an AFM material decreases below it Néel temperature T_N. (b) Illustration of the Curie-Weiss law; the inverse susceptibility is a linear function of temperature and the intercept with the x-axis gives the Weiss temperature θ.

2.6 Electrical Conduction

2.6.1 The Electronic Band Structure

The electric conduction properties of a solid can be understood from its (electronic) band structure. The energy bands of a material consist of an infinite number of overlapping atomic orbitals, where the filled orbitals form the valence band, and the empty orbitals form the conduction band, separated by a band gap. The different types of electrical behaviour, sketched in Figure 2.9, can be classified depending on the size of the band gap ΔE: materials with $\Delta E > 2.5$ eV are insulators, $\Delta E \approx 0.5 - 2.5$ eV are semiconductors and $\Delta E < 0.5$ eV are metals.

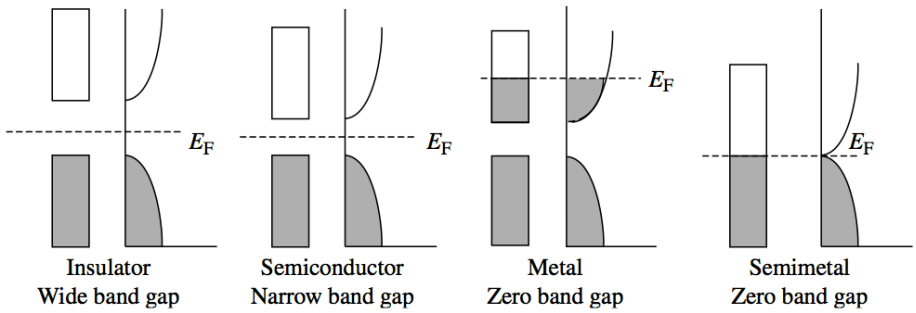

Figure 2.9: Schematic illustrations of the band structure in different types of materials. The classification is made based on the band gap between valence band (grey) and conduction band (white) [21].

The band gap in metals is either very small, or valence and conduction bands overlap, or the bands are not completely filled. Semiconductors and insulators are distinguished by the width of the band gap. In semiconducting materials, electrons can be (thermally) excited into the conduction band, and charge carriers in both bands (i.e. holes in the valence and electrons in the conduction band) give electrical conduction.

In practice, a solid can contain a large number of bands, and the band structure is dependent on the crystal structure. Different empirical methods and *ab initio* approaches have been developed to calculate the band structure. They make use of the periodicity of the structure and employ Bloch functions to describe the wavefunction of electrons in a crystal. A detailed treatment of conduction in the solid state can be found in reference [22].

2.6.2 Superconductivity

Whereas band theory is successful in explaining metallic conduction, it fails to describe the phenomena of superconductivity. The superconducting phase is characterised by zero electrical resistance and the exclusion of a magnetic field below a critical temperature T_c (Meissner-Ochsenfeld effect), shown in Figure 2.10. Bardeen, Cooper and Schrieffer explained the physical properties of conventional (low-temperature, $T_c < 30$ K) superconductors in their BCS theory in 1957 [23]. The BCS theory assumes that the conducting electrons in a superconductor are coupled to Cooper-pairs via electron-phonon interactions. Importantly, the electron pairs are bosons (total spin of zero) and therefore they obey the Bose-Einstein-statistics. This means that all Cooper-pairs can occupy the same low-lying energy-state and electrical current is transported without resistance as no energy exchange occurs. However, BCS theory is not sufficient to explain the high-temperature superconductivity observed in cuprates and in iron-pnictides. Several theoretical approaches have tried to explain the superconducting properties of these materials, but to date a comprehensive description has not yet emerged.

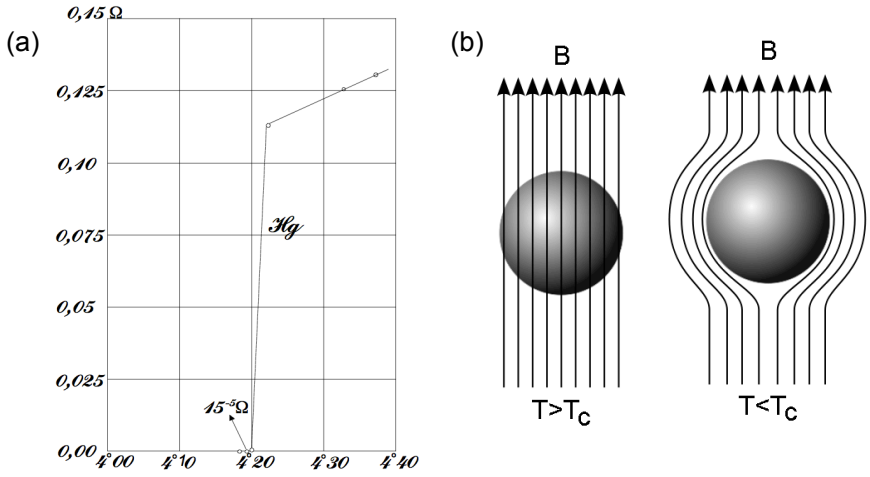

Figure 2.10: (a) The electrical resistance of mercury drops at its superconducting transition temperature $T_c = 4.2$ K. Measured by H.K. Onnes at Leiden University (Netherlands) in 1911. (b) Illustration of the Meissner-Ochsenfeld effect: a magnetic field B penetrates a superconducting material in its normal state ($T > T_c$), but is expelled from its interior below the critical temperature, $T < T_c$.

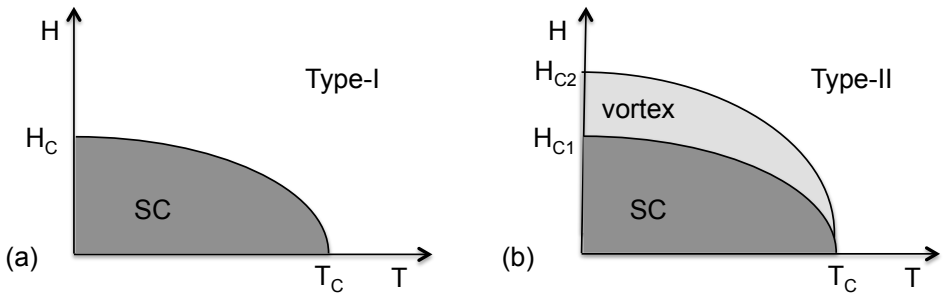

Figure 2.11: The H vs. T curves for a superconductor of (a) type-I and (b) type-II. (a) Type-I superconductors enter the normal state above their critical field H_c and critical temperature T_c. (b) Superconductors of type-II have two critical fields H_{c1} and H_{c2}. In the region between them (vortex state), magnetic field lines can penetrate parts of the material.

The superconducting state is not only associated with a critical temperature T_c, but also a critical magnetic field H_c, see Figure 2.11. Whilst superconductors of type-I enter the normal state above a critical field H_c, type-II materials show a coexistence of superconducting and normal phases (vortex state) for magnetic fields between H_{c1} and H_{c2}. The iron-pnictides are type-II superconductors. They are multiband metals, in which all five 3*d* orbitals of Fe contribute to the Fermi surface, which contains both electron and hole pockets [24]. The formation of Cooper pairs appears to occur through the exchange of antiferromagnetic spin fluctuations between electron and hole pockets [25], rather than through electron-phonon coupling, which was found to be small in LaFeAsO [26]. Depending on the interactions of electron and hole pockets, the pairing symmetry can be an $s^{\pm}$- or *d*–wave [27], but remains controversial in *Re*FeAsO materials [28]. Experimentally one finds a dependency of T_c on the Fe-As-Fe tetrahedral bond angle and the height of As, h_{As}, above the square Fe net [29], [30], [31]. The highest T_c's were observed for the most regular tetrahedrons. It was also found that h_{As} might act as a switch between an *s*-wave and nodal gap structure [30]. Differently to the cuprates, superconductivity can be induced not only by charge-carrier doping, but also by external pressure and isovalent doping. This suggests that structural parameters have an influence on the properties [28]. More experimental and theoretical work will be required to clarify the mechanism of these unconventional superconductors.

2.7 Dielectric Properties

2.7.1 Ferroic Properties

In analogy to ferromagnets, (which show a spontaneous magnetization that can be switched by an external magnetic field), *ferroelectrics* are defined as insulating materials in which the direction of a spontaneous electric dipole moment P_S can be switched by an applied external *electric* field E.

Above a certain temperature, a transition to a paraelectric phase occurs, for example as the consequence of a structural change, that makes the centrosymmetric configuration the most energetically favourable, or because the exchange between the different polar configurations is too fast to result in a net polarization. Above T_C, the polarization of the material is a linear function of the applied electrical field (in analogy to paramagnetic materials in a magnetic field). The polarization in the paraelectric state follows the Curie-Weiss law

$$\varepsilon = \varepsilon_0 + C_P/(T - T_C)$$

where C_P is the paraelectric Curie constant, T_C is the Curie temperature and ε is the electrical polarizability.

Generally one distinguishes between 'displacive' and 'order-disorder' ferroelectrics. Displacive ferroelectrics show a correlated shift of ions away from the centrosymmetric positions (e.g. through orientation of a lone-pair along a polar axis as in $BaTiO_3$ or $Ba_2KNb_5O_{15}$) whereas randomly oriented dipoles become ordered in 'order-disorder' material (e.g. protonic order in KH_2PO_4 or $K_3Fe_5F_{15}$). However, the phase transitions often have a mixed character, and the division into 'order-disorder' and 'displacive' ferroelectricity might be oversimplified [32].

Ferroelastic materials possess two or more stable orientational states connected to the presence of spontaneous strain e_s that can be switched by external stress (along a defined direction). In materials in which ferroelectric and ferroelastic properties are coupled, the spontaneous polarization P_s (spontaneous strain e_s) can be modified by applied mechanical stress (electrical field) (e.g. $Na_5W_3O_9F_5$) [33]. In piezoelectric materials, mechanical stress can give rise to a spontaneous polarization, or vice versa: an electrical field leads to a geometric deformation.

Ferroic materials are of great technological importance and find application as 'smart materials', for example as infrared detectors (pyroelectrics), actuators, positions and micromotors (piezoelectrics), modulators (electro-optic), non-volatile direct random access memory and ferroelectric field-effect transistors (ferroelectrics) [33].

2.7.2 Multiferroicity

Multiferroic compounds show a combination of at least two of ferroic properties, such as ferroelectricity, ferromagnetism and ferroelasticity [34]. Multiferroic materials can be classified into 'structural magnetic ferroelectrics' (structural instability is order parameter; covalency or hybridization), and 'electronic magnetic ferroelectrics' (electronic degrees of freedom are order parameter; correlation effects, spin, charge or orbital order) [35]. Further one distinguishes between 'proper' and 'improper': materials in which the electric polarization is the primary order parameter, are 'proper' ferroelctrics; but if electric polarization appears as a by-product of other order parameters breaking inversion-symmetry, they are called 'improper' ferroelectrics [36].

The 'electronic magnetic ferroelectrics' are always 'improper', because the polarization arises solely from electronic effects without ionic displacements (e.g. $K_3Fe_5F_{15}$ [37]). However, structural relaxations are likely to occur, for instance as a response to the magnetostrictive effect, and the resulting atomic displacements contribute to the purely electronic polarization [35]. In the case of 'structural magnetic ferroelectrics' the analysis of phonon modes is required to decide if are 'proper' (e.g. $BaMF_4$ [38]) or 'improper' (e.g. $YMnO_3$ [39]).

2.7.3 Structural Requirements

The field E and polarisation P are related through the dielectric susceptibility χ_e, which is a second-rank tensor and hence must conform to the crystal symmetry according to Neumann's principle. The presence of structural features, that are mandatory for the emergence of ferroelectric properties, can be determined from the crystal structure. Hence, crystallography may be of great help in search of new materials, in particular because structure determination is done more routinely than polarization measurements.

The existence of a polar axis is a prerequisite for ferroelectricity, and thus it is only allowed in the ten pyroelectric crystal classes that have a unique polar direction (6*mm*, *6*, 4*mm*, 4, 3*m*, 3, *mm*2, 2, *m*, 1) [1], [40]. As a result, all ferroelectric materials are also pyroelectrics (P_s changes with temperature) and piezoelectric (P_s changes through mechanical deformation) but the reverse is not necessarily true. The coexistence of FM and ferroelectric properties is limited to thirteen of the Shubnikov point groups (*1, 2, 2′, m, m′, 3, 3m′, 4, 4m′m′, m′m2′, m′m′2′, 6 and 6m′m′*), which form a subset of the 31 point groups that allow spontaneous magnetic or electric polarization. These 'multiferroic' point groups contain neither spatial-inversion (present in FM, absent in ferroelectrics) nor time-reversal symmetry (absent in FM, present in ferroelectrics).

In practice, one solves the crystal structure in the polar configuration and determines the amplitude of atomic displacements away from the apolar higher symmetry structure. Typical polar displacements are generally larger than $d = 0.1$ Å and smaller than $d = 1$ Å [41], [42]. The lower limit is associated with (inversion) barrier-heights that are comparable to the thermal energy k_BT [43]. Smaller displacements may arise from wrong space-group symmetry assignment and may not be a sign of ferroelectricity [43]. The upper limit is related to the largest potential barrier that may be crossed when the direction of polarisation is reversed [43]. It is comparable to typical atomic displacements in known ferroelectrics [43].

Although ferroelectric materials exhibit certain structural features, the opposite is not always true (i.e. polar materials are not necessarily ferroelectric) and the physical properties still need to be verified experimentally. In addition to crystallographic methods, the absence of centrosymmetry can be confirmed by piezoelectric or non-linear optical measurements. Polar properties may be confirmed by thermocurrent determinations (pyroelectricity) or $P(E)$ hysteresis loops (ferroelectricity). The Curie temperature may be established from temperature dependent XRD, microcalorimetry, dielectric or birefringence measurements [33].

2.8 Synthesis

2.8.1 Solid-State Synthesis: The Ceramic Route

All the materials discussed in this thesis are polycrystalline powders that have been synthesised via solid-state routes. In order to form new compounds from a given set of precursor materials, the different chemical species have to get in close contact in order to react. A simple but effective approach is the grinding of the starting materials to a fine powder, maximizing the surface available for reaction and the mixing between different grains. The contact between grains in improved by pressing the powder into a pellet using a pellet die. High reaction temperatures (several hundred degrees) promote ion-mobility, but nevertheless solid-state reactions are relatively slow and often require long annealing times (days to weeks) to obtain pure products. The products are often polycrystalline so that powder X-ray diffraction is a useful tool to monitor the progress and success of a reaction. The separation of product and by-products is often not feasible and therefore the synthetic conditions have to be adjusted to obtain the desired material in the purest obtainable form.

The synthesis of materials containing transition metal fluorides is known to be challenging: the starting materials are air- and moisture sensitive and tend to be hydroscopic and undergo hydrolysis at elevated temperatures. The use of vacuum techniques and synthesis under inert atmosphere is therefore essential for the development of reliable and reproducible synthetic protocols. The binary metal fluorides used as starting materials, were purchased in the highest purity available (> 99 %) and pre-dried prior to use: small amounts of powder (~ 0.5 g) were filled in small glass vials, placed in glass tubes, which could be evacuated and heated on a vacuum-line to remove residual moisture. Prepared reaction mixtures were contained in suitable vessels (e.g. corundum crucibles, tantalum- and gold tubes) and sealed under high vacuum or protective argon atmosphere in quartz tubes.

The prepared materials were reacted at variable temperatures and times in box or tube furnaces. Unless the synthesised materials were air-stable, caution was taken not to expose the resultant compounds to air and moisture, by opening the sealed quartz tube inside an argon-filled glove-box to recover the samples. When required by sample sensitivity, the capillaries used in diffraction experiments were also filled and sealed inside an argon glove-box.

2.9 Diffraction Instrumentation

Different diffractometers were used in the course of this work, depending on the information sought. Laboratory X-ray diffraction was mainly used for phase identification in the course of optimising the synthetic protocols. Central facilities (i.e. synchrotron and neutron sources) were used to make use of specific properties of the radiation and/ or to collect data over a wide angular range, at low (T = 2 K) and high (T = 1000 K) temperatures and at high-pressures (p = 20 GPa).

2.9.1 Laboratory X-ray Diffractometer D8-Advance (Bruker)

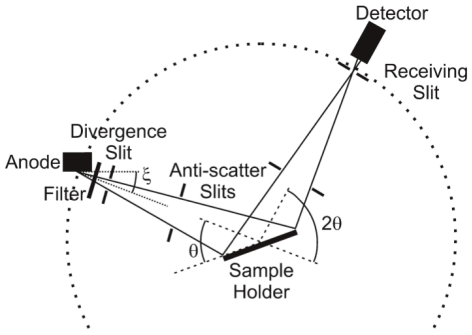

Figure 2.12: Basic Bragg-Brentano geometry [4]. The X-ray source and detector are located at a fixed radius r on the goniometer circle. The divergent beam is focussed by diffraction on the detector. During collection, the sample and detector rotate by θ and 2θ, respectively.

Routine room-temperature X-ray diffraction measurements for phase identification and purity checks were performed on a D8-Advance (Bruker), using Cu-$K_{\alpha 1}$ radiation. The diffractometer is set-up in parafocussing Bragg-Brentano geometry shown in Figure 2.12: the divergent incident beam is reflected from the sample and at a fixed radius r away from the sample position. Slits and Soller collimators control the beams divergence, minimize stray radiation and make the beam more parallel. A linear position sensitive detector (PSD) located at distance r measures the diffracted intensity I as a function of 2θ. The sample is usually spun at an axis perpendicular to the sample plane to improve the powder average, and its tilt angle is coupled to the position of the detector: for an angle θ of the sample, the detector will be located at an angle 2θ from the incident beam. Variable temperature measurements (T = 80 K – 500 K) were possible using a nitrogen-stream 'cold-finger'

(Oxford Cryosystems) on a D8-Advance machine equipped with a capillary sample holder in transmission geometry.

2.9.2 High-Resolution Powder Diffraction Beamline ID31 (ESRF)

The high-resolution powder diffraction beamline ID31 (European Synchrotron Radiation Facility, ESRF, Grenoble, France) is located at a standard ESRF undulator source, which provides a well-collimated high flux synchrotron beam in the energy range of 5 – 60 keV (λ = 2.48 – 0.21 Å). Slits before and after a cryogenically cooled double crystal Si(111) monochromator are used to adjust the beam size between typically 0.5 – 2.5 mm (horizontal) and 0.1 – 1.5 mm (vertical). The illumination of a sufficiently large sample volume is required in powder diffraction to obtain a good powder average; hence the beam passes unfocussed onto the sample. The flux density at the sample is typically 1.5×10^{12} photons mm^{-2} s^{-1} at a wavelength of λ = 0.42 Å, and the possibility of radiation damage must be considered when planning experiments on beamline ID31.

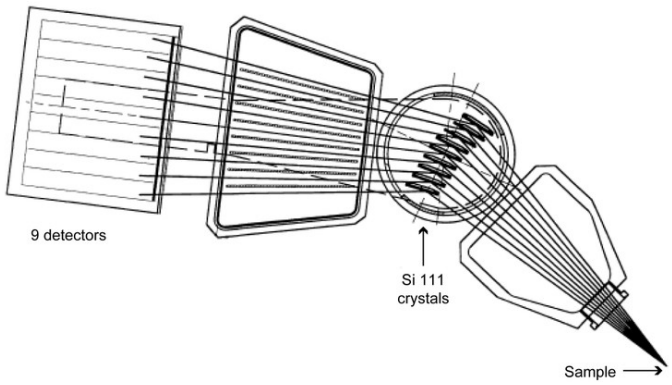

Figure 2.13: Detector array at ID31, consisting of nine individual detectors preceded by Si(111) analyser crystals [44]. The recorded peak position immune to deviations (e.g. misalignment) because only diffracted beams arriving at the correct angle are diffracted into the detector.

A bank of detectors (Figure 2.12) set apart by ca. 2° scans in continuous mode to record simultaneously nine diffraction patterns, eliminating the dead time of the normal step scans. A Si(111) analyser crystal precedes each detector; its small angular acceptance (few arcsec) results in narrow peaks (instrumental contribution to FWHM is 0.003° 2θ) and accurate peak positions (few tenth of millidegree). The

data of different channels is then normalized and combined to give the conventional step scan. Typically the sample is contained in a capillary, which is mounted on the diffractometer axis (transmission geometry) and spinning during data collection to reduce preferred orientation and texture effects. Variable temperature measurements make use of e.g. a liquid-He cryostat (T_{min} = 3 K) or hot air blower (T_{max} = 1473 K), but other sample environments such as gas cells are available.

2.9.3 Diffraction and Total Scattering Beamline 11-ID-C (APS)

The beamline 11-ID-C (Advanced Photon Lightsource, APS; Chicago, USA) operates at a constant energy, E = 115 keV (λ = 0.10793 Å) and is located at a undulator source [45]. The beam is monochromated using a fixed Si(311) crystal, which gives a high intensity beam with a flux of typically 10^{11} photons sec^{-1} with good energy resolution $\Delta E/E$ = 5x10^{-3}. The unfocussed beam has a size of 0.2 x 0.2 mm^2 (horizontal x vertical) but can be adjusted using slits. The diffracted beam is recorded on a two-dimensional Perkin Elmer amorphous silicon detector, which can be positioned as close as d = 0.3 m from the sample for total scattering experiments, and up to d = 3 m for standard diffraction experiments. Typically the samples are contained in capillaries, mounted stationary in the beam path. Variable temperature measurements can be achieved with a cryostat or cryostream (T = 10 K – 700 K), and magnetic fields can be applied using a H_{max} = 7 T cryomagnet.

2.9.4 High-Pressure Diffraction Beamline BL10XU (SPring-8)

The high-pressure beamline BL10XU at SPring-8 (Super Photon Ring – 8 GeV, SPring-8; Hyogo Prefecture, Japan) is designed to perform high-resolution X-ray diffraction experiments under very high pressures (up to p = 300 GPa) and variable temperatures. The schematic layout is shown in Figure 2.14. It is located at a SPring-8 standard type in-vacuum undulator. A Si(111) double crystal gives a quasi-monochromatic, high energy (E = 14 – 58 keV) and high-intensity (> 10^{13} photons s^{-1}) beam with good energy resolution ($\Delta E/E$ = 10^{-4}). The beam is focused using a stacked compound refractive lens. The spot size (FWHM) is 0.08 x 0.12 mm^2 (vertical x horizontal), which can be cut using four-blade slits to give 10 – 200 μm^2 at the sample position.

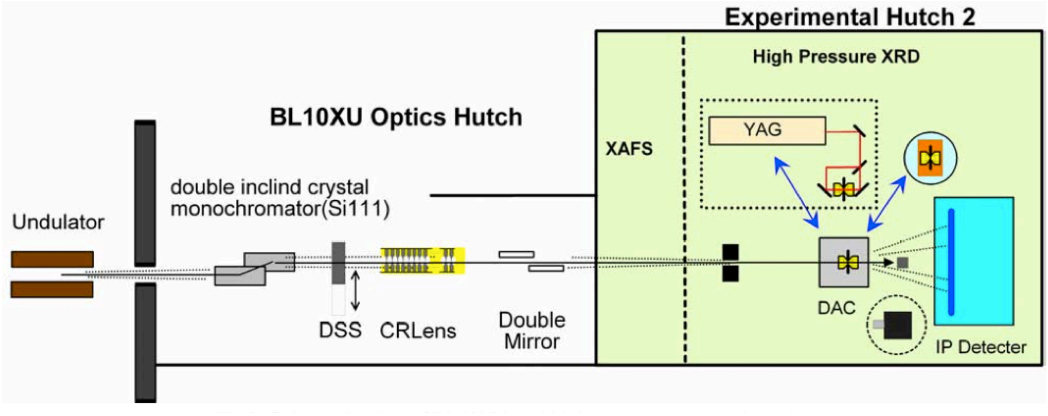

Figure 2.14: Schematic layout of beamline BL10XU [46]. The monochromatic and focussed beam is directed at the sample inside the DAC, and the diffracted intensity recorded on a 2D detector. Various sample environments are available for high (YAG laser heating) or cooling (He cryostat).

The precise alignment (0.001 mm) of the diamond anvil cell (DAC) with respect to the beam position can be monitored through a microscope, which is also used to measure ruby-fluorescence. A ω-stage enables powder sample oscillation and single crystal motion during data collection. Either an image plate (IP; Rigaku R-AXIS IV, 30 x 30 cm^2 and 0.10 mm^2 pixel size) or an X-ray charged coupled device (CCD; Bruker) is positioned at variable distances d to the sample (IP: d = 150 – 450 mm; CCD: d = 80 –230 mm) to record the Debye-Sherrer cones. Typically exposure is in the range of minutes, except for samples with small scattering (amorphous) and containing light elements. Low- and high temperatures are achieved with a He-flow cryostat (T = 10 K – 300 K) and a double-sided laser heating system (T < 3000 K), respectively. An optical spectrometer, CCD detector and He-Cd laser for excitation of ruby fluorescence are located outside the experimental hutch and connected to the microscope through an optical fibre for in-situ pressure determination [47].

2.9.5 High Intensity Neutron Powder Diffraction Beamline D20 (ILL)

D20 is a high intensity two-axis diffractometer; located in the reactor hall of the ILL (Institut Laue-Langevin, ILL, Grenoble, France) at the thermal beam H11 (see Figure 2.15). It can be operated with variable resolution and flux, depending on choice of monochromator (vertical focussing pyrolitic graphite HOPG(002), Cu(200) or Ge(113) monochromator) and take-off angle.

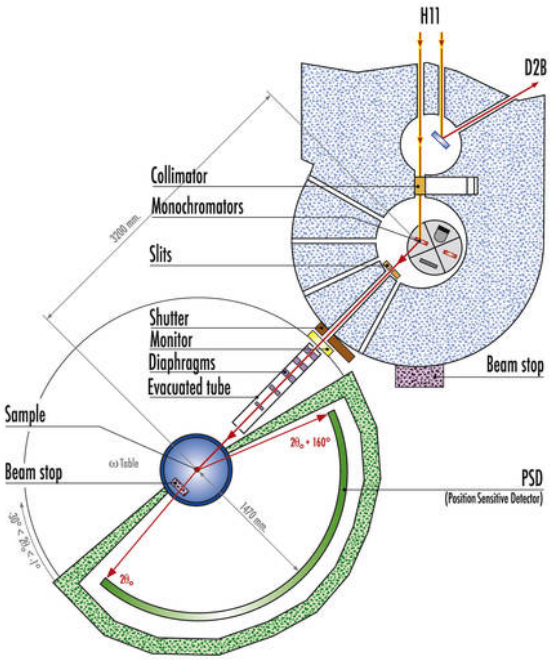

Figure 2.15: Schematic layout of beamline D20 [48]. The collimated and monochromatic beam impedes the sample and the diffracted neutrons are detected by a PSD.

The natural divergence of the monochromatic neutron beam (λ = 0.88 – 2.41 Å) is reduced by Söller collimation; the maximum beam-size at the sample is 30 x 50 mm^2 (H x V). The high-resolution configuration at highest take-off angle gives a neutron flux up to 10^7 n s^{-1} cm^{-2}, whereas fast data collection (several seconds for a pattern of 1536 points) is possible at medium resolution with a high neutron flux of 10^8 n s^{-1} cm^{-2}. The scattered beam is detected by a curved position sensitive detector (PSD) filled with 3.1 bar ^{3}He and 0.8 bar CF_4 that uses a micro-strip gas chamber technology. A detection zone of 4 x 0.15 m^2 (horizontal x vertical) or 153.6° is covered by an array of 48 detection plates consisting of 32 microstrip-cells each (0.1° coverage per cell). Each cell has an independent output, which allows for fast or time-resolved data collection with a dead-time of 160 ms between two successive diagrams in conventional sequential data acquisition mode. An ILL orange cryostat (T = 1.9 K – 300 K) and a furnace (T < 1650 K) are available for variable temperature measurements; other sample environments (e.g. cryomagnet, high-pressure cell) are also obtainable. The samples are contained in cylindrical vanadium cans that can be sealed with indium wire for air-sensitive compounds [48].

2.9.6 High Resolution Neutron Powder Diffraction Beamline D2B (ILL)

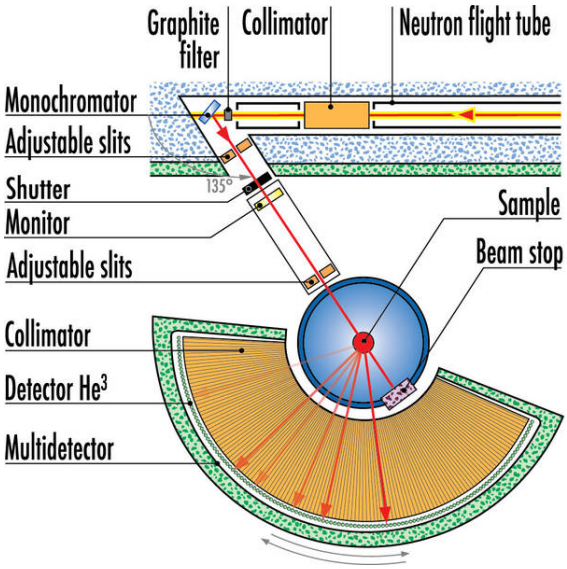

Figure 2.16: Schematic layout of high resolution diffractometer D2B [49]. The collimated and monochromatic beam is diffracted by the sample, and recorded by a detector bank preceded by additional collimation slits.

The powder diffractometer D2B is located in the reactor hall of the ILL (Institut Laue-Langevin, ILL, Grenoble, France) at the thermal beam H11 and designed for high-resolution studies (flux at sample = 10^6 n cm^{-2} s^{-1}); although a lower resolution high-flux / high-intensity configuration (flux at sample = 10^7 n cm^{-2} s^{-1}) is also available. A sketch of the diffractometer layout is shown in Figure 2.16. Varying wavelengths (λ = 1.05 – 6 Å) are selected by a Ge monochromator, which focussed the beam vertically to 50 mm (beam size at sample ~ 20 x 50 mm^2) and provides high-resolution up to very large d-spacings due to the high take-off angle (135°). The height of the collimators and detectors (200 mm) matches the vertical divergence of the beam. The scattered beam is detected by an array of 128 ^{3}He counting tubes, set apart at 1.25° intervals. Complete diffraction profile can be collected after 25 steps of 0.05° 2θ of the detector bank (typically 30 min) and are repeated to improve counting statistics. Besides an ILL orange cryostat (T = 1.5 K – 300 K) and a furnace (T < 1000 K) for variable temperature measurements, other sample environments such as a cryomagnet or high-pressure cell are also available. The samples are contained in cylindrical vanadium cans that can be sealed with indium wire for air-sensitive compounds [49].

2.10 Physical Property Measurements

2.10.1 The MPMS SQUID Magnetometer

Measurements of the magnetization as a function of temperature (T = 2 K – 400 K) and external magnetic field (H = ± 7 T) were carried out using a magnetic properties measurement system (MPMS). At the heart of magnetization detection is a superconducting quantum interference device (SQUID), a closed superconducting loop containing one or two Josephson junctions (thin insulating barriers). To perform a measurement, the sample is moved in discrete steps through the detection coil (Figure 2.17). This causes a change in magnetic flux, and hence influences the current passing through the superconducting solenoid, which is detected and transformed into an output signal. Because of the quantized nature of the current in a superconductor, the SQUID is capable of detecting very small changes in current, and hence very small changes in magnetization. The measurements described in this work were carried out at variable temperatures, between T = 2 K and 400 K ($M_{H=const}$ vs. T) or at constant temperatures and variable field ($M_{T=const}$ vs. H). Samples (~ 20 mg) were contained in gelatine capsules (typical susceptibility of 10^{-7} emu Oe^{-1} g^{-1}) and mounted in plastic drinking straws to minimize magnetic background contributions.

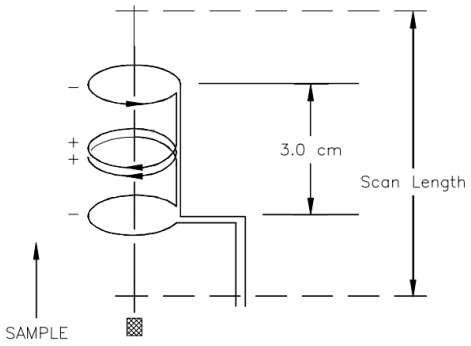

Figure 2.17: Illustration of the pick-up coil [50]. As the sample (grey square) moves through the pickup coil, it induces a variation in magnetic flux and hence changes the current passing though the solenoid. These changes are detected and transformed into an output signal.

2.10.2 The Quantum Design PPMS

The temperature dependent measurements of electrical resistivity were performed in a physical properties measurement system (PPMS) using a four-probe configuration. In this set-up, four copper leads are connected to bar of sintered polycrystalline sample using a conductive adhesive (silver epoxy), see Figure 2.18. A current is passed thorough the two outer wires (I+, I-), whereas the inner leads (V+, V-) measure the potential difference across the sample. The advantage of the four-wire set-up is the reduced contributions of leads and joints to the resistance measurement. The electrical resistivity ρ (Ω cm) can be calculated according to $\rho = (R \cdot A)/L$, with the measured resistance R (Ω), the sample cross-section A (cm^2), and the distance between the voltage leads, L (cm). The sample puck allows simultaneous measurement of three specimens at a time. The electrical resistivity can be measured as a function of temperature, or as isotherms of the resistivity as a function of magnetic field.

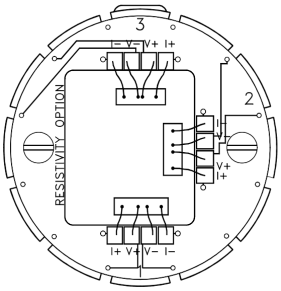

Figure 2.18: Sketch of resistivity sample puck with three samples mounted for four-wire electrical resistance measurement [51].

2.11 References

[1] T. Hahn (2005) *International Tables for Crystallography, Volume A: Space Group Symmetry*. Fifth Edition, 2nd printing. Dordrecht: The International Union Of Crystallography, Springer.

[2] B. McMahon (2012) Online Dictionary of Crystallography [online]. International Union of Crystallography. Available from: http://reference.iucr.org/mediawiki/index.php?title=Neumann%27s_principle&oldid=3228 [Accessed 15.May 2012]

[3] H.L.M. C. Giacovazzo, D. Viterbo, F. Scordari, G. Gilli, G. Zanotti, M.Catti, (1992) *Fundamentals of Crystallography*. Oxford: The International Union of Crystallography.

[4] R.E. Dinnebier and S.L.J. Billinge (2008) *Powder Diffraction: Theory and Practice*. Cambridge: The Royal Society of Chemistry.

[5] C. Hammond (2009) *The Basics of Crystallography and Diffraction*. Oxford: International Union of Crystallography, Oxford University Press.

[6] J. Als-Nielsen, D. Mcmorrow (2011) *Elements of Modern X-Ray Physics*. Chichester: John Wiley & Sons.

[7] F.D. Bloss (1971) *Crystallography and Crystal Chemistry*. New York: Holt, Rinehart, and Winston.

[8] H.M. Rietveld, J. Appl. Crystallogr. 2 (1969) 65.

[9] R.A. Young (1995) *The Rietveld Method*. Oxford: International Union of Crystallography, Oxford University Press.

[10] B. Toby, *Powder Diffraction* 21 (2006) 67.

[11] A.C. Larson, R.B.V. Dreele, Los Alamos National Laboratory Report LAUR 86-748 (2004) 1.

[12] B. Toby, *Journal of Applied Crystallography* 34 (2001) 210.

[13] T. Egami, S.J.L. Billinge (2003) *Underneath the Bragg Peaks. Structural Analysis of Complex Materials.* Oxford: Pergamon Press, Elsevier.

[14] T. Egami, *Zeitschrift für Kristallographie* 219 (2004) 122.

[15] C. Farrow, P. Juhas, J. Liu, D. Bryndin, E. Božin, J. Bloch, T. Proffen, S. Billinge, *Journal of Physics: Condensed Matter* 19 (2007) 335219.

[16] X. Qiu, J.W. Thompson, S.J.L. Billinge, *Journal of Applied Crystallography* 37 (2004) 678.

[17] Y. Waseda, E. Matsubara and K. Shinoda (2011). *X-Ray Diffraction Crystallography: Introduction, Examples and Solved Problems.* Berlin, Heidelberg: Springer.

[18] I. Kempson, K. Kirkbride, W. Skinner, J. Coumbaros, *Talanta* 67 (2005) 286.

[19] A.C. Hannon, R.I. Smith, ISIS Neutron Training Course (2003).

[20] F. White (2011) Chemical Crystallography Research Group, High Pressure Crystallography [online]. Edinburgh, The University of Edinburgh. Available from: http://www.crystal.chem.ed.ac.uk/research/hpcg.php?page=2&image=1 [Accessed 07. July 2012].

[21] J. N. Lalena, D.A. Cleary (2010) *Principles of Inorganic Materials Design*. 2nd edition. Hoboken: John Wiley & sons.

[22] C. Kittel (2004) *Introduction to Solid State Physics*. 8th Edition. Hoboken: John Wiley & sons.

[23] J. Bardeen, L.N. Cooper, J.R. Schrieffer, *Physical Review* 108 (1957) 1175

[24] D.J. Singh, M.H. Du, *Physical Review Letters* 100 (2008) 237003.

[25] I.I. Mazin, D.J. Singh, M.D. Johannes, M.H. Du, *Physical Review Letters* 101 (2008) 057003.

[26] L. Boeri, O.V. Dolgov, A.A. Goblubov, *Physical Review Letters* 101 (2008) 026403.

[27] Platt, *Physical Review B: Condensed Matter and Materials Physics* 85 (2012) 180502(R).

[28] H.-H. Wen, S. Li, *Annual Review of Condensed Matter Physics* 2 (2011) 121.

[29] C.H. Lee, A. Iyo, H. Eisaki, H. Kito, M.T. Fernandez-Diaz, *Journal of the Physical Society of Japan* 77 (2008) 083704.

[30] K. Kuroki, H. Usui, S. Onari, R. Arita, H. Aoki, *Physical Review B: Condensed Matter and Materials Physics* 79 (2009) 224511.

[31] K. Kubo, P. Thalmeier, *Journal of the Physical Society of Japan* 78 (2009) 083704.

[32] R. Blinc, *Ferroelectrics* 301 (2004) 3.

[33] J. Ravez, *Comptes Rendus de l'Académie des Sciences*. 3 (2000) 267.

[34] W. Eerenstein, N.D. Mathur, J.F. Scott, *Nature* 442 (2006) 759.

[35] S. Picozzi, C. Ederer, *Journal of Physics: Condensed Matter* 21 (2009) 303201.

[36] S.-W. Cheong, M. Mostovoy, *Nature Materials* 6 (2007) 13.

[37] K. Yamauchi, S. Picozzi, *Physical Review Letters* 105 (2010) 107202.

[38] C. Ederer, N.A. Spaldin, *Physical Review B: Condensed Matter and Materials Physics* 74 (2006) 024102.

[39] C. Fennie, K. Rabe, *Physical Review B: Condensed Matter and Materials Physics* 72 (2005) 100103.

[40] H. Grimmer, *Acta Crystallographica, Section A: Foundations of Crystallography* 47 (1991) 226.

[41] S.C. Abrahams, *Acta Crystallographica, Section A: Foundations of Crystallography* 50 (1994) 658.

[42] E. Kroumova, M. Aroyo, J. Perez-Mato, A*cta Crystallographica, Section B: Structural Science* 58 (2002) 921.

[43] S.C. Abrahams, *Acta Crystallographica, Section B: Structural Science* 55 (1999) 494.

[44] ID31 Technical Description: Optics and Experimental hutch [online] (2010). Grenoble, ESRF. Available from: http://www.esrf.eu/UsersAndScience/Experiments/StructMaterials/ID31/Technicaldescription [Accessed: 06. March 2012]

[45] Beamline 11-ID-C: Sector 11 - High-energy Diffraction Beamline [online]. X-ray Science Division, APS. Available from: http://www.aps.anl.gov/

Beamlines/Directory/showbeamline.php?beamline_id=15 [Accessed: 03. May 2012].

[46] Y. Ohishi, *High Pressure Research* 28 (2008) 163.

[47] BL10XU Outline [online]. SPring-8. Available from: http://www.spring8.or.jp/wkg/BL10XU/instrument/lang-en/INS-0000000352/instrument_summary_view, [Accessed: 15. August 2012].

[48] High-intensity two-axis diffractometer with variable resolution [online] (2012). Grenoble, ILL. Available from: http://www.ill.eu/instruments-support/instruments-groups/instruments/d20/ [Accessed: 06. March 2012].

[49] High-resolution two-axis diffractometer D2B [online] (2012). Grenoble, ILL. Available from: http://www.ill.eu/instruments-support/instruments-groups/instruments/d2b/ [Accessed: 06. March 2012].

[50] Quantum Design (2004) Magnetic Property Measurement System: MPMS MultiVu Application User's Manual. San Diego: Quantum Design.

[51] Quantum Design (1999) Physical Property Measurement System: Resistivity Option User's Manual. San Diego: Quantum Design.

Chapter 3

The 1111-Type Pnictide Fluorides

3.1 Introduction

The discovery of superconductivity in the fluorine-doped oxypnictide $LaFeAsO_{1-x}F_x$ (T_c = 26 K, 2008) was rather unexpected, as the magnetic properties of iron were believed to oppose the formation of itinerant electronic states [1]. The possible coexistence of magnetism and superconductivity has then triggered a wave of research into this family of materials that adopt the ZrCuSiAs structure (see chapter 1) and are commonly called '1111' type. At room temperature, the parent materials (i.e. *Re*FeAsO, *Re* = rare earth metal) crystallise in a tetragonal layered structure (space group $P4/nmm$) consisting of alternating slabs of conducting $[FeAs]^-$ and insulating $[ReO]^+$, with tetrahedrally coordinated Fe (O) and As (*Re*), respectively. The spin-density wave observed in electrical resistance and magnetic susceptibility manifest into long-range stripped antiferromagnetic order of Fe at T_N. The tetragonal to orthorhombic (herein $T \rightarrow O$) structural phase transition (*Cmma* symmetry) occurs at slightly higher temperatures T_s then the onset temperature of antiferromagnetic order T_N ($T_s > T_N$).

The 1111-type materials can be substituted on all sites, for instance on the *Re* site (with alkaline earth metals, *Ae*) or on the oxygen site (with fluorine or via O vacancies). Doping progressively reduces the spin density wave and leads to the emergence of superconducting phases. For optimal doping levels, the magnetic long-range order and structural transition are suppressed. Superconductivity competes with the structural transition and is observed in both tetragonal and orthorhombic phases. For instance, the structural transition is suppressed by electron doping in $LaFeAsO_{1-x}F_x$, whereas superconductivity in the hole-doped $Sr_xNd_{1-x}FeAsO$ emerges in the orthorhombic phase [2], [3].

The maximum critical temperatures achieved to date reaches $T_c \sim 55$ K (see e.g. $Gd_{0.8}Th_{0.20}FeAsO$, T_c = 56 K) being surpassed only by the high-T_c-cuprate superconductors [4]. One other possible route to achieve superconducting phases is partial replacement of Fe with Ni in the [FeAs] layer, as in $SmFe_{1-x}Ni_xAsO$ (T_c= 10.8 K, x = 0.06) and LaNiAsO (T_c = 2.4 K) [5], [6]. Interestingly also the isovalent substitution of As with P leads to superconducting phases, for instance in $LaFeAs_{1-x}P_xO$ (T_c = 10 K, x = 0.3), LaFePO (T_c = 5 K), LaNiAsO (T_c = 2.4 K) and LaNiPO (T_c = 3 K) [6], [7], [8], [9]. The latter result indicates that not only simple charge-carrier doping but also structural modulations play an important role in determining and optimizing the superconducting properties.

The 1111-type structure forms not only for iron, but supports a wide range of transition metal (T_M) - pnictide (Pn) combinations [10]. The chemical nature of T_M and Pn merely influences the structural properties, but has a strong influence on the electronic and magnetic properties. The effect of different T_M can be understood by considering that while partial substitution of Fe with Co or Ni induces the formation of superconducting phases, replacement with Mn, Cr and Cu results in the suppression of magnetic order but not to superconductivity [11]. Furthermore, upon full substitution of Fe with T_M, a variety of responses are observed, ranging from non-magnetic semiconducting LaMnPnO (Pn = P, As, Sb) through to ferromagnetic LaCoPO and LaCoAsO and antiferromagnetic NdMnAsO and PrMnSbO [11], [12], [13], [14], [15].

Simultaneous to the superconducting oxypnictides, the isostructural fluorine-based parent materials were also prepared by replacing the $[Re\mathrm{O}]^+$ layer with a $[Ae\mathrm{F}]^+$ layer (Ae = Ca, Sr, Eu). In analogy to the oxypnictides, the spin density wave of the parent materials can be suppressed via doping, as in $Sm_xSr_{1-x}FeAsF$ (T_c = 56 K, x = 0.5) and $CaFe_{1-x}Co_xAsF$ (T_c = 22 K, x = 0.1) [16], [17]. In this chapter, the iron-fluoride SrFeAsF and its electron doped derivatives $Sr_{1-x}La_xFeAsF$ (x = 0.1, 0.2) will be discussed as representatives of the iron-pnictide family.

Whilst the iron-based fluorides emerged only during the last years, pnictide fluorides containing other T_M, such as SrZnPF, BaZnPF, BaMnPF, EuMnPF and BaZnSbF have been isolated in the past, but little has been reported on their magnetic and electronic properties [18], [19]. The family of AeMnPnF (Ae = Sr, Ba; Pn = P, As, Sb), hereafter referred to as manganese-pnictides, was prepared to probe the structural and electronic response upon isoelectronic substitution.

3.2 Methods

3.2.1 Synthesis

a) $Sr_{1-x}La_xFeAsF$ (x = 0, 0.1 and 0.2)

The precursor LaAs was synthesised by heating a stoichiometric mixture of La and As at 773 K for 2 hours and 1173 K for 18 hours in evacuated quartz tubes. Powder samples of $Sr_{1-x}La_xFeAsF$ (mass ~1 g) were synthesised by heating a stoichiometric mixture of SrF_2, Sr, LaAs, As and Fe. The powdery starting materials were ground thoroughly in an agate mortar; then small Sr pieces were added to the mixture, which was pressed into pellets and placed in Ta tubes. The tubes were sealed in evacuated quartz tubes and heated to 773 K for 12 hours followed by annealing at 1173 K for 35 to 40 hours. For $x = 0$, the obtained pellets were homogenised; new pellets were pressed and sintered twice at 1273 K for 48 hours.

b) AeMnPnF (Ae = Sr, Ba; Pn = P, As, Sb)

The precursor SrAs was prepared by heating a 1:1 mixture of Sr and As at 973 K for 16 hours in an evacuated quartz tube. Samples of *Ae*Mn*Pn*F (*Ae* = Sr, Ba; *Pn* = P, As, Sb) (mass ~0.3 – 1 g) were synthesised from a 1:1:2:2 mixture of AeF_2, *Ae*, *Pn* and Mn (for *Ae* = Sr and *Pn* = P_{red}, Sb; for *Ae* = Ba and *Pn* = P_{red}, As, Sb) or a 1:1:2:1 mixture of SrF_2, SrAs, As and Mn powders. The starting materials in powder form were ground thoroughly in an agate mortar before adding small pieces of Sr. The reaction mixture was pelletised. Samples of SrMn*Pn*F were placed in tantalum tubes (*Pn* = P, As) or wrapped in tantalum foil (*Pn* = Sb) and sealed in evacuated quartz tubes. Samples of BaMn*Pn*F were placed in corundum crucibles and sealed in quartz tubes under reduced Ar pressure. The annealing procedures are listed below.

SrMnPF was heated at a rate of 200 K h^{-1} to 1423 K for 30 hours, cooled to room temperature (RT) at a rate of 300 K h^{-1}, homogenised, re-pelletised and reheated to 1373 K for 30 hours.

SrMnAsF was heated at a rate of 200 K h^{-1} to 1373 K for 20 hours, cooled to RT at a rate of 200 K h^{-1}, homogenised, re-pelletised and reheated twice: to 1373 K for 30 hours and to 1323 K for 20 hours, with intermediate re-grinding. SrMnAsF was also successfully prepared sealed under reduced Ar pressure in a quartz tube, by heating at a rate of 200 K h^{-1} to 1348 K for 18 hours.

SrMnSbF was heated at a rate of 200 K h^{-1} to 1323 K for 24 hours, cooled to RT at a rate of 300 K h^{-1} and then reheated to 1373 K for 24 hours with intermediate re-grinding and re-pelletising. The sample was quenched in cold water after the first heating stage and cooled slowly after the re-annealing.

BaMnPF was heated at a rate of 100 K h^{-1} to 473 K for 4 hours; then heated further at a rate of 200 K h^{-1} to 1273 K for 24 – 30 hours before cooling at a rate of 300 K h^{-1} to RT. The sample was homogenised and re-pelletised before reheating at a rate of 200 K h^{-1} to 1273 K for 24 to 30 hours and then cooled to RT at a rate of 300 K h^{-1}.

BaMnAsF was annealed following the procedure of BaMnPF.

BaMnSbF was heated twice with intermediate re-grinding and re-pelletising, at a rate of 200 K h^{-1} to 1373 K for 24 hours before cooling to RT at a rate of 300 K h^{-1}. Alternatively, the sample was heated at a rate of 100 K h^{-1} to 473 K for 4 hours; then heated further at a rate of 200 K h^{-1} to 1373 K for 30 hours before cooling at a rate of 300 K h^{-1} to RT.

The starting materials were of at least 99.9 % purity. All samples preparations were carried out in an Ar-atmosphere glovebox, but the resultant black polycrystalline compounds are stable in air.

3.2.2 Laboratory Powder X-ray Diffraction

Laboratory X-ray diffraction data was collected on a Bruker D8-Advance (λ = 1.54056 Å, transmission mode). BaMn*Pn*F samples were contained in 0.5 mm diameter glass-capillaries and diffraction profiles were collected at variable temperatures between T = 80 K and 420 K using a cold nitrogen stream, in the 2θ range 20° – 75° with 0.02° step size.

3.2.3 Synchrotron Powder Diffraction

High-resolution synchrotron X-ray diffraction experiments were performed between T = 80 K and 300 K on beamline ID06, ESRF, France (λ = 0.34798 Å) on the $La_{1-x}Sr_xFeAsF$ materials; between T = 10 K and 473 K on beamline ID31, ESRF, France (λ = 0.4000774 Å) on the SrMn*Pn*F compounds; and at T = 300 K on beamline 11-ID-C, APS, USA (λ = 0.10798 Å) on the BaMn*Pn*F series. The samples were contained in 0.5 mm diameter glass-capillaries; for the low temperature

measurements the sample was contained in an open-ended capillary to avoid freezing of air or argon, and cooled inside a liquid helium cryostat. Temperatures above ambient were achieved using a hot-air-blower. The data were binned in the 2θ range 0.1° – 9° to a step of 0.003° and in the 2θ range 2° – 50° to a step of 0.017° and 0.002°.

X-ray powder diffraction data for pair distribution function analysis were collected at the 11-ID-C beamline at the advanced photon source (APS) at Argonne National Laboratory using synchrotron radiation with a wavelength of λ = 0.107841 Å. Data were collected using a General Electric amorphous Si large panel, a two-dimensional (2D) detector. Finely ground powder samples were loaded into 5 mm diameter glass capillaries. To avoid saturation of the detector, each measurement was carried out in multiple exposures, with an exposure time of 5 seconds and ten exposures per sample to improve counting statistics. Data from an empty container were also collected to correct for container scattering. The 2D data sets were combined and integrated using the program FIT2D prior to further processing [20]. The total scattering function $S(Q)$ was obtained using standard corrections with the program PDFgetX2 [21]. The final PDF was obtained by Fourier transformation of $S(Q)$ according to

$$G(r) = \frac{2}{\pi}\int_0^{Qmax} Q[S(Q) - 1]\ sin\big(Q(r)\big)dQ$$

where Q is the magnitude of the scattering vector [22]. Q_{max} = 27 Å^{-1} was used. The program PDFGUI was employed to model the experimental data [23].

3.2.4 Neutron Powder Diffraction

Complementary neutron powder diffraction (NPD) profiles of SrFeAsF were collected on the high-flux diffractometer D20, ILL, France (λ = 2.398 Å) between T = 2 K and 300 K. The NPD data for SrMnPnF were collected on D20, λ = 2.418 Å (P, As) and λ = 1.88 Å (Sb). The samples (mass ~0.9 g) of the same batch used for the X-ray synchrotron diffraction measurements, were loaded in the cylindrical vanadium cans (diameter = 5 mm) and placed in a standard ILL "orange" liquid helium cryostat for low temperature measurements, and in a standard ILL cryofurnace to access temperatures above ambient. The data were collected between T = 1.5 K and 420 K and binned in the 2θ range 12° – 100° with 0.1° step size.

Analysis of the diffraction data (X-ray and neutron) was performed with the GSAS suite of Rietveld programmes [24], [25].

3.2.5 Physical Properties Measurements

Variable electrical resistivity measurements of sintered pellets were performed in a Quantum Design PPMS instrument using the four-probe method. The magnetic susceptibilities were recorded using a Quantum Design MPMS magnetometer, following zero field cooling (ZFC) and field cooling (FC) procedures in an applied field H = 10 and 10000 Oe.

3.3 Results

3.3.1 Nuclear Structure of $La_xSr_{1-x}FeAsF$

The RT diffraction profile of SrFeAsF collected at beamline ID06 (λ = 0.37571 Å) readily reveals the tetragonal unit cell established previously for the 1111-type iron pnictide materials. All reflections can be indexed in space group $P4/nmm$, and a minority SrF_2 phase (< 2 wt%), see Figure 3.1. The refined lattice constants are a = 4.00522(5) Å and c = 8.9781(2) Å.

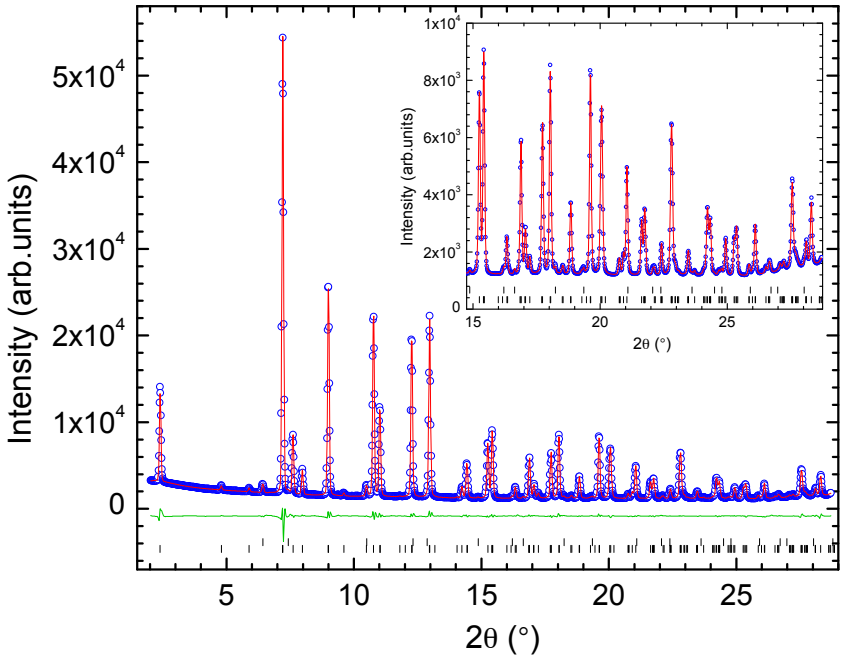

Figure 3.1: Rietveld fit to the RT diffraction profile of SrFeAsF collected on beamline ID06, ESRF, France (λ = 0.3757 Å). Experimental data, Rietveld fit, and difference plot shown as open blue circles, red and green solid line, respectively. The bottom and top tickmarks indicate the reflections positions of SrFeAsF ($P4/nmm$) and SrF_2 phases, respectively. The inset shows a magnification of the high 2θ region.

At low temperatures several peaks split, including the $(220)_T$ reflection[§], and the low temperature phase can be indexed in space group $Cmma$ (Figure 3.2). The orthorhombic a- and b- lattice parameter lie along the base diagonal of the original tetragonal cell, with $a_O = \sqrt{2}\cdot a_T$, $b_O = \sqrt{2}\cdot a_T$, and $c_O = c_T$ and the unit cell volume is

[§] The subscripts T and O indicate Miller indices of the tetragonal and orthorhombic cell, respectively.

doubled. The refined lattice parameters at T = 80 K are a = 5.6316(1) Å, b = 5.6734(1) Å and c = 8.9403(1) Å. The two structural models are shown in Figure 3.3. The isotropic temperature factors, atomic coordinates and selected bond-distances and angles for T = 300 K and 80 K are summarised in Table 3.1.

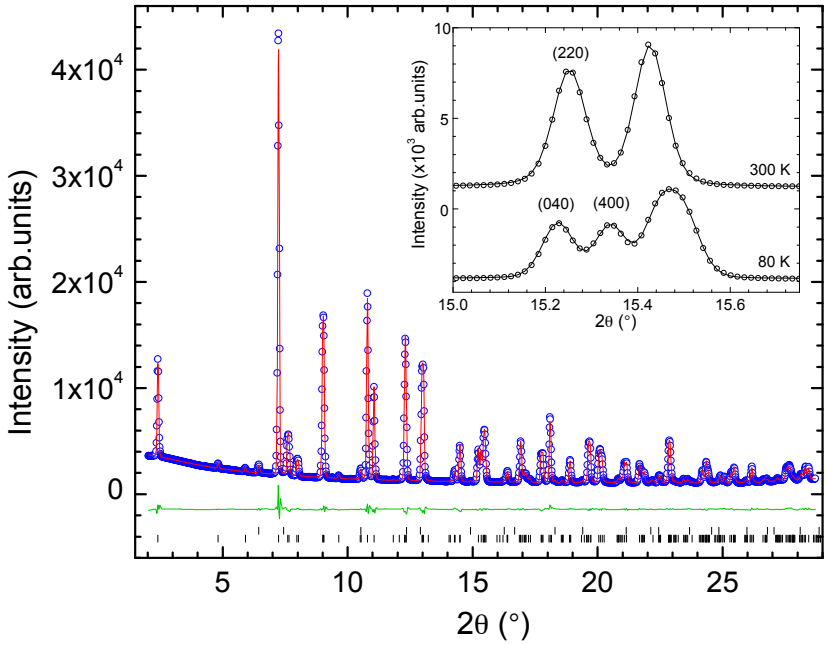

Figure 3.2: Rietveld fit to the diffraction profile of SrFeAsF collected at T = 80 K on beamline ID06, ESRF, France (λ = 0.3757 Å). Experimental data, Rietveld fit, and difference plot shown as open blue circles, red and green solid line, respectively. The bottom and top tickmarks indicate the reflections positions of SrFeAsF (*Cmma*) and SrF_2 phases, respectively. The inset shows the splitting of the $(220)_T$ reflection into the $(040)_O$, $(400)_O$ reflections, indicating the $T \rightarrow O$ structural phase transition.

The number of crystallographic sites remains unchanged in the structural transition and the influence of the orthorhombic distortion $a \neq b$, is subtle: whilst the high temperature phase has only a single Fe-Fe distance ($d_{\text{Fe-Fe}}$ = 2.83212(3) Å), there are two symmetry inequivalent Fe-Fe distances at low temperature ($d_{\text{Fe-Fe}}$ = 2.83668(4) Å and $d'_{\text{Fe-Fe}}$ = 2.81581(4) Å). Similarly, one set of tetrahedral angles, α_2, remains unaltered (α_2 (300 K) = 111.56(7)°; α_2 (80 K) = 111.69(5)°); the second set, α_1, splits into two angles, α_1 and α_1* (α_1 = 108.44(3)° at 300 K; α_1 = 108.68(2)° and α_1* = 108.07(2)° at 80 K), see Figure 3.4 and Table 3.1.

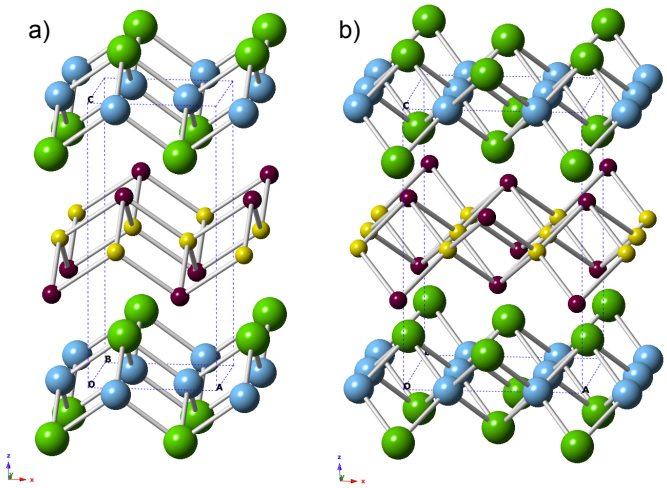

Figure 3.3: The (a) tetragonal $P4/nmm$ and (b) orthorhombic $Cmma$ structures adopted by SrFeAsF at RT and 80 K, respectively. Green, blue, yellow and purple spheres correspond to Sr, F, Fe and As, respectively.

The lattice constants were followed as a function of temperature to determine the $T \rightarrow O$ phase transition temperature. On cooling, several peaks start to broaden at $T = 185$ K, and are clearly split below $T < 170$ K. As an example, the $(332)_T$ reflection is shown in Figure 3.3 in the temperature range between $T = 195$ K and 160 K, together with its full width at half maximum (FWHM).

The onset of the transition can be estimated from the orthorhombic strain parameter $P = (b\text{-}a)/(b+a)$, which generally decreases sharply at the structural transition temperature T_S. The orthorhombic strain was followed as a function of temperature and is shown in the inset of Figure 3.5: P drops sharply from 0.004 ($T = 85$ K) to 0.001 ($T = 175$ K) and is zero at $T = 190$ K. From this, and from the evolution of the FWHM of the $(332)_T$ reflection, the $P4/nmm \rightarrow Cmma$ phase transition temperature can be located at $T = 180$ K. The temperature dependence of the lattice constants is displayed in Figure 3.5; the a- and b- lattice parameters of the orthorhombic phase were divided by √2 for ease of comparison with the tetragonal phase. The structural transition has no influence on either the interlayer c-lattice constant or the unit cell volume V, as both decrease smoothly on cooling across the $T \rightarrow O$ phase boundary.

T/ K	SrFeAsF	
	80	*300*
space group	*Cmma*	*P4/nmm*
a/ Å	5.6316(1)	4.00522(5)
b/ Å	5.6734(1)	
c/ Å	8.9403(1)	8.9781(2)
V/ Å^3	285.645(5)	144.025(3)
z(Sr)	0.1599(1)	0.1603(2)
z(As)	0.6517(1)	0.6517(2)
B_{iso}/ Å^2		
Sr	0.11(3)	0.30(4)
Fe	0.10(3)	0.48(4)
As	0.10(3)	0.30(4)
F	0.11(3)	0.48(4)
distances/ Å:		
Sr-F	2.4569(5)	2.4663(8)
Fe-As	2.4150(7)	2.422(1)
Fe-Fe	2.81581(4), 2.83668(4)	2.83212(3)
angles/ °		
F-Sr-F $(x2)_O$ | $(x4)_T$	69.93(2), 70.52(2)	70.08(3)
(x2)	108.86(4)	108.58(5)
Sr-F-Sr $(x2)_O$ | $(x4)_T$	110.07(2), 109.48(2)	109.92(3)
(x2)	108.86(4)	108.58(5)
As-Fe-As $(x2)_O$ | $(x4)_T$	108.68(2), 108.07(2)	108.44(3)
(x2)	111.69(5)	111.56(7)
Fe-As-Fe $(x2)_O$ | $(x4)_T$	71.32(2), 71.93(2)	71.56(3)
(x2)	111.69(5)	111.56(7)
R_p, wR_p/ %	1.96, 2.82	2.91, 4.54
R_F^2/ %, χ^2	5.31, 1.794	5.65, 5.054

Table 3.1: Lattice parameters, atomic coordinates and selected bond distances and angles of SrFeAsF from Rietveld fit to diffraction profiles collected at T = 80 K and 300 K on beamline ID06. There were 9 and 10 refined structural variables at RT and 80 K, respectively. The fractional atomic coordinates are: Sr (¼, ¼, *z*); Fe (¾, ¼, ½); As (¼, ¼, *z*); F (¾, ¼, 0) in *P*4/*nmm* and Sr (0, ¼, *z*); Fe (¾, 0, ½); As (0, ¼, *z*); F (¼, 0, 0) in *Cmma*. Weight fraction of the SrF_2 impurity is 1.7(1) wt%.

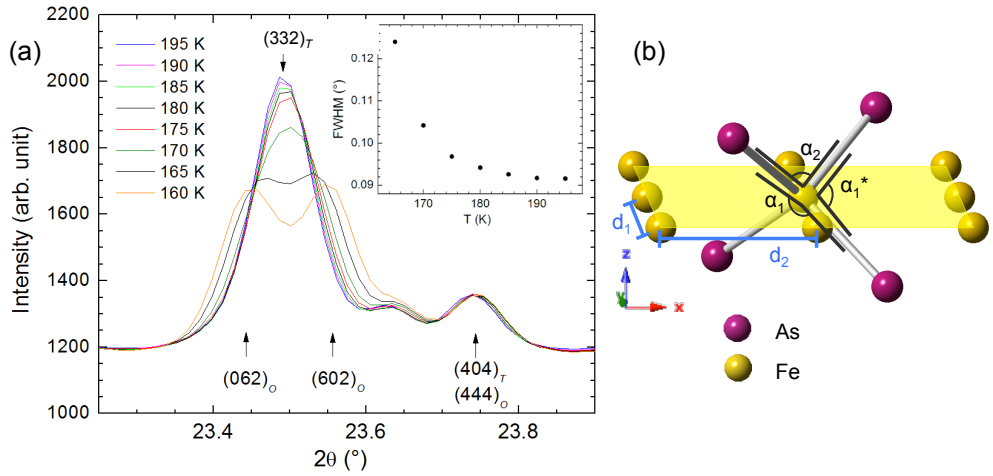

Figure 3.4: (a) The $(332)_T$ reflection broadens on cooling and is clearly split at $T = 165$ K. The doublet can be indexed as $(062)_O$ and $(602)_O$ of the low temperature *Cmma* phase. The inset shows the evolution of the FWHM of the $(332)_T$ reflection between $T = 195$ K and 160 K. The peak broadening commences at $T = 185$ K and becomes more pronounced at $T = 175$ K, indicating the transition to orthorhombic symmetry. (b) Across the $T \rightarrow O$ transition, the tetrahedral angle α_1 splits into twofold sets, α_1 and α_1*. Similarly, the single Fe-Fe distance splits into d_1 and d_2.

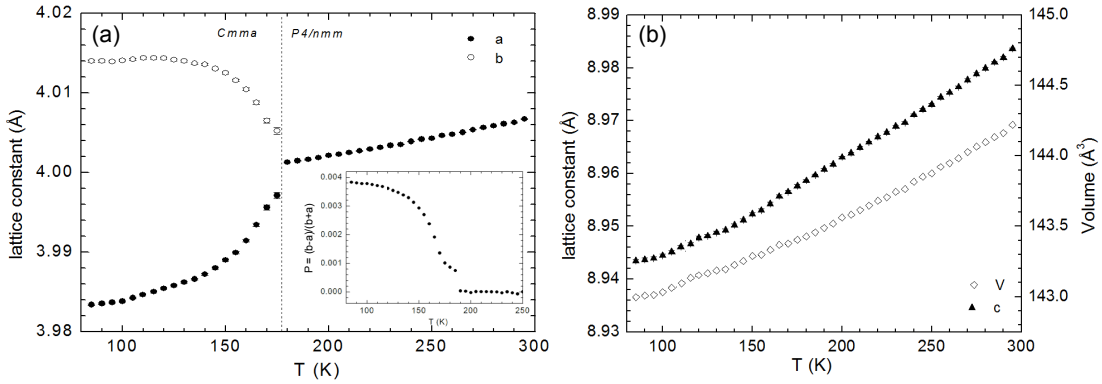

Figure 3.5: The temperature dependence of the lattice parameters of SrFeAsF between $T =$ 85 K and 295 K obtained from Rietveld fits to the *Cmma* ($T = 80 - 180$ K) and the $P4/nmm$ ($T = 180 - 300$ K) model. Both models were tested between $T = 160 - 200$ K. (a) The *a*- and *b*-lattice constants of the orthorhombic phase were divided by √2 for ease of comparison with the tetragonal phase. The inset shows the orthorhombic strain parameter $P = (b\text{-}a)/(b+a)$. (b) The *c*-axis and unit cell volume *V* do not show any discontinuities at the structural phase transition.

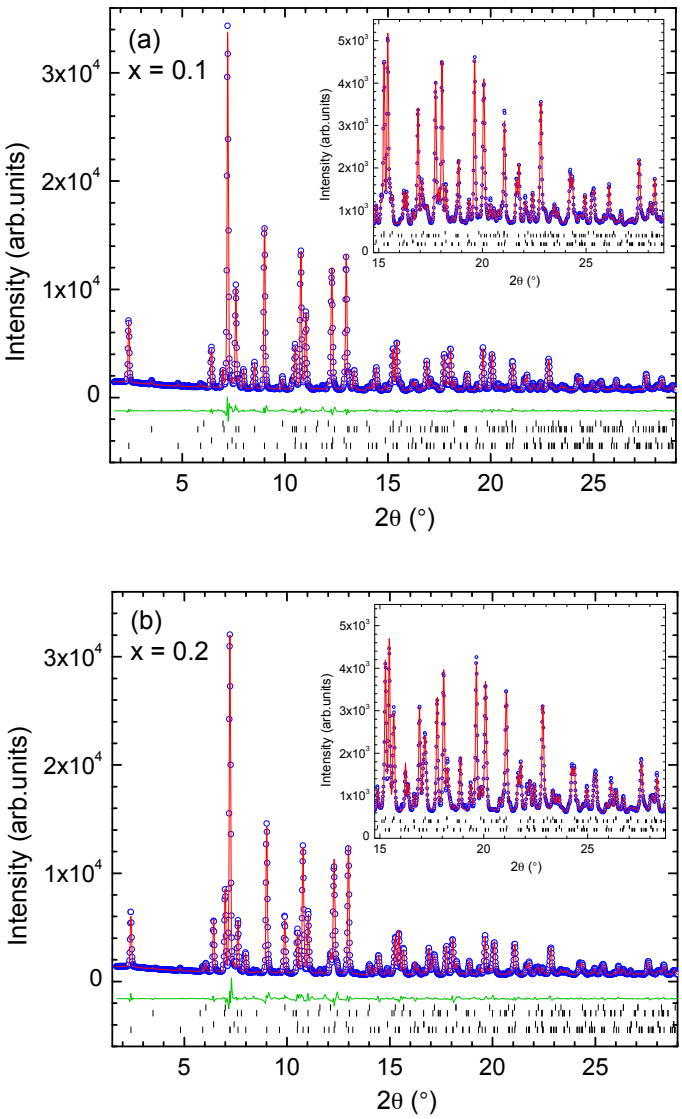

Figure 3.6: Rietveld fit to the RT powder diffraction profile of $La_xSr_{1-x}FeAsF$ for (a) $x = 0.1$ and (b) $x = 0.2$ collected at beamline ID06, ESRF, France ($\lambda = 0.3757$ Å). Experimental data, Rietveld fit, and difference plot shown as open blue circles, red and green solid line, respectively. The tickmarks indicate the reflections positions of $La_xSr_{1-x}FeAsF$ ($P4/nmm$), SrF_2, $SrFe_2As_2$ and LaAs phases (bottom to top). The insets are magnifications of the high 2θ region.

Electron-doping of SrFeAsF can be achieved by partial replacement of Sr^{2+} with La^{3+}. The parent tetragonal structure is robust upon doping and the substitution is only accompanied by a lattice contraction as expected from the reduced ionic radius of La ($r = 1.03$ Å) compared to Sr ($r = 1.18$ Å) [26]. Figure 3.6 shows the final Rietveld refinements of the synchrotron powder diffraction profiles collected on beamline ID06, $\lambda =$ 0.37571 Å. The refined lattice constants are $a =$ 4.00358(6) Å, $c =$

8.9713(2) Å, and a = 4.0010(1) Å, c = 8.9586(4) Å for x = 0.1 and 0.2, respectively. A summary of the refined results at T = 80 K and 300 K is given in Table 3.2.

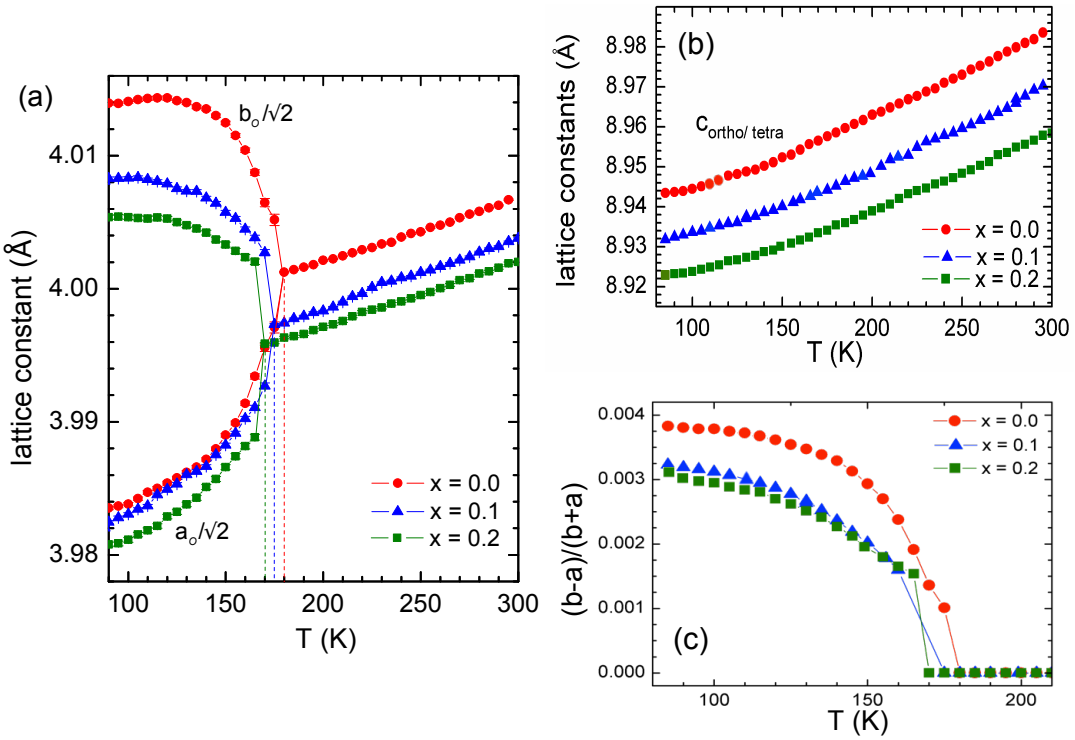

Figure 3.7: Temperature dependence of the lattice parameters of $La_xSr_{1-x}FeAsF$ (x = 0, 0.1 and 0.2) obtained from Rietveld refinements. (a) The lattice parameter of the basal plane, a_T, decreases with increasing La-doping level. The lattice contracts smoothly on cooling, up to the $T \rightarrow O$ phase transition temperature, which is reduced from T = 180 K (x = 0.0) to T = 170 K (x = 0.2). The a- and b- parameters of the orthorhombic phase are divided by √2 for ease of comparison. (b) The c-lattice parameter contracts with increasing La-content and with decreasing temperature. (c) The orthorhombic distortion is diminished along the series.

In addition to the lattice contraction, the temperature of the tetragonal to orthorhombic phase transition drops to T = 175 K and T = 170 K for the nominally 10% and 20% La-doped material, respectively. The presence of impurities (SrF_2, Fe_2As, LaAs) indicates a lower doping level than the nominal composition. The temperature factors of Sr and La were constraint to be the same. Further, the occupanices of Sr and La were constrained to total one and refined for the data collected at T = 80 K. There were no correlations between U_{iso}(La,Sr) and $Occ.$(Sr/La) larger than 0.5 %, when the scale, lattice, coordinates, U_{iso} and occupancies of Sr and La were refined simultaneously. The correlation between U_{iso}(La,Sr) and U_{iso}(As) was < 0.9 % whilst the correlation between U_{iso}(F) and U_{iso}(Fe) was < 0.65 %. The occupancies of La on the Sr site refined to x = 0.04(1) and x = 0.15(1) for samples of

nominally $x = 0.1$ and $x = 0.2$, respectively. The evolution of the lattice constants is shown in Figure 3.7; the *a*- and *b*- lattice parameters of the *Cmma* phase were divided by √2. The orthorhombic strain parameter $P = (b-a)/(b+a)$ (Figure 3.7(c)), shows a gradual suppression of the orthorhombic distortion with increasing doping level.

	$La_{0.1}Sr_{0.9}FeAsF$		$La_{0.2}Sr_{0.8}FeAsF$	
T/ K	80	300	80	300
space group	*Cmma*	*P*4/*nmm*	*Cmma*	*P*4/*nmm*
a/ Å	5.6303(2)	4.00358(6)	5.6312(2)	4.0010(1)
b/ Å	5.6689(2)		5.6672(2)	
c/ Å	8.9320(3)	8.9713(2)	8.9271(4)	8.9586(4)
V/ Å^3	285.09(1)	143.798(4)	284.89(1)	143.409(5)
z(Sr, La)	0.161192)	0.1611(2)	0.1602(2)	0.1599(3)
z(As)	0.6508(3)	0.6511(3)	0.6510(3)	0.6512(3)
B_{iso}/ Å^2				
Sr, La	0.54(7)	1.05(7)	0.58(7)	0.75(7)
Fe	0.69(8)	1.09(8)	0.43(9)	0.42(9)
As	0.43(7)	0.63(7)	0.35(9)	0.38(9)
F	0.5(3)	0.7(2)	0.6(3)	0.63(8)
distances/ Å:				
Sr(La)-F	2.462(1)	2.469(1)	2.456(1)	2.460(1)
Fe-As	2.409(1)	2.417(1)	2.420(2)	2.416(2)
Fe-Fe	2.8152(1), 2.8345(1)	2.83096(4)	2.8156(1), 2.8336(1)	2.82913(6)
angles/ °				
F-Sr(La)-F				
$(x2)_O$ | $(x4)_T$	69.75(4), 70.29(4)	69.96(4)	69.94(4), 70.45(4)	70.19(4)
(x2)	108.46(7)	108.33(7)	108.80(8)	108.8(1)
Sr(La)-F-Sr(La)				
$(x2)_O$ | $(x4)_T$	109.71(4), 110.25(4)	110.04(4)	109.55(4), 110.06(4)	109.81(4)
(x2)	108.46(7)	108.33(7)	108.80(8)	108.8(1)
As-Fe-As				
$(x2)_O$ | $(x4)_T$	107.93(5), 108.50(5)	108.32(5)	107.98(5), 108.51(5)	108.32(6)
(x2)	112.0(1)	111.8(1)	112.0(1)	111.8(1)
Fe-As-Fe				
$(x2)_O$ | $(x4)_T$	71.50(5), 72.07(5)	71.68(5)	71.49(5), 72.02(5)	71.68(6)
(x2)	112.0(1)	111.8(1)	112.0(1)	111.8(1)
R_p, wR_p/ %	4.52, 6.36	4.16, 5.78	3.99, 5.90	4.43, 6.77
R_F^2/ %, χ^2	6.50, 6.392	12.68, 5.04	6.20, 5.736	3.85, 6.746

Table 3.2: Lattice parameters, atomic coordinates and selected bond distances and angles of $La_xSr_{1-x}FeAsF$ obtained from Rietveld fits to data collected at 80 K and 300 K. For the dataset collected at 80 K, the occupancies of La refined to 0.04(1) and 0.15(1) for $x = 0.1$ and 0.2, respectively. There were 18 and 14 refined structural parameters at 80 K and 300 K, respectively. The fractional atomic coordinates are: Sr(La) (¼, ¼, *z*); Fe (¾, ¼, ½); As (¼, ¼, *z*); F (¾, ¼, 0) in *P*4/*nmm* and Sr(La) (0, ¼, *z*); Fe (¾, 0, ½); As (0, ¼, *z*); F (¼, 0, 0) in *Cmma*. Weight fraction of the impurity phases for $x = 0.1$ are: SrF_2 7.2(1) wt%, $SrFe_2As_2$ 13.8(1) wt%, LaAs 1.4(1) wt% and for $x = 0.2$: SrF_2 11.0(1) wt%, $SrFe_2As_2$ 2.7(2) wt%, LaAs 8.3(7) wt%.

3.3.2 Magnetic Structure of SrFeAsF

Neutron powder diffraction profiles collected at $T = 2$ K on beamline D20 showed additional small reflections which could not be indexed on the basis of the orthorhombic nuclear cell. These reflections appear only at low temperature, clearly indicating the presence of magnetic ordering. The magnetic moments of the iron-ions align ferromagnetically (FM) along the *b*-axis and antiferromagnetically (AFM) in direction of the *a*- and *c*-axis (striped antiferromagnetic ordering) as shown in Figure 3.8. This AFM arrangement results in the doubling of the *c*-axis with respect to the nuclear cell, $a_M = 5.5666(2)$ Å, $b_M = 5.6097(2)$ Å and $c_M = 17.684(6)$ Å.

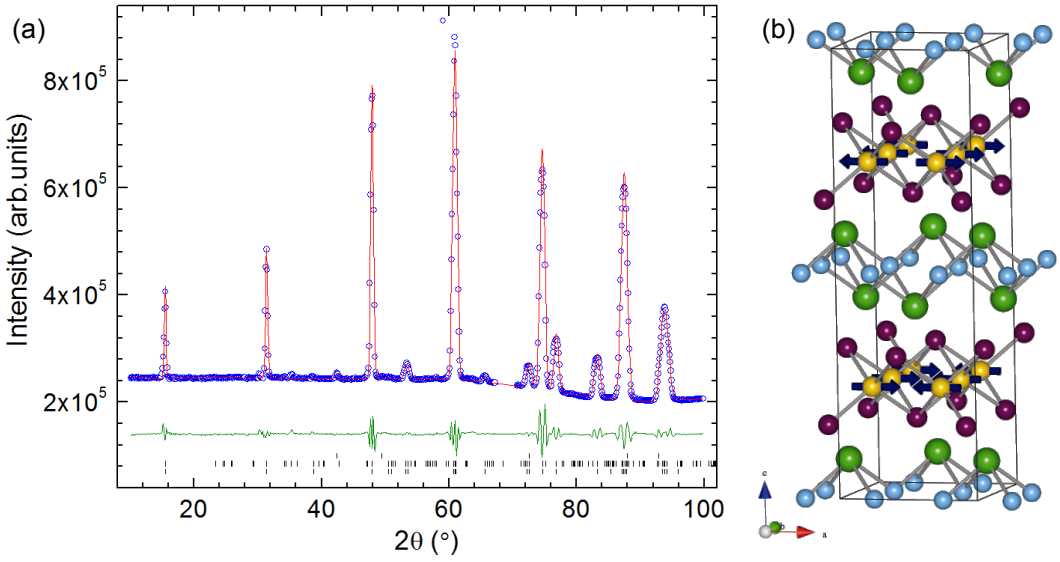

Figure 3.8: (a) Rietveld fit to the neutron powder diffraction profile for SrFeAsF (space-group *Cmma*), collected at T = 2 K on beamline D20 ($\lambda = 2.398$ Å). Experimental data, Rietveld fit, and difference plot shown as open blue circles, red and green solid line, respectively. Tickmarks (bottom to top) indicate the reflection positions of the nuclear *Cmma* cell, the magnetic unit cell and the SrF_2 impurity phase. The excluded region around 70° 2θ corresponds to peaks from the vanadium can. (b) The Magnetic unit cell of SrFeAsF, illustrating the ordering of the Fe moments below the transition temperature (space group *Cmma*). The Fe-spins align ferromagnetically along the *b*-direction and antiferromagnetically along the *a*- and *c*- axis, leading to a striped arrangement, and doubled *c*-axis as compared to the nuclear cell.

The magnetic moment of Fe^{2+} refined to $\mu_{eff} = 0.6(2)\ \mu_B$, which is significantly smaller than the expected moment $\mu_{eff} = 4.90\ \mu_B$ for the free ion ($S = 2$). However, the observed magnetic moment is comparable to related iron-pnictide systems (e.g.

CaFeAsF: μ_{eff} = 0.49 μ_B; LaFeAsO: μ_{eff} = 0.35 μ_B; $SrFe_2As_2$: μ_{eff} = 0.94 μ_B [27]). The recurrent observation of a smaller magnetic moment may be explained with the metallicity of the iron and the strong covalency of the As-Fe bond [18]. The magnetic reflections are observed in neutron powder diffraction profiles below T = 100 K and vanished above T = 150 K. It follows that the onset of magnetic ordering occurs at lower temperatures than the structural transition in analogy with the oxypnictides. This observation was confirmed by a recent neutron diffraction study, that determined precisely the magnetic ordering (Néel) temperature as T_N = 133(3) K [28]. The values of the magnetic moment of Fe (μ_{eff} = 0.58(6) μ_B at T = 2 K) and of the structural transition temperature (T_S = 180(2) K) are in very good agreement with the results discussed here [28].

3.3.3 Physical Properties of $La_xSr_{1-x}FeAsF$

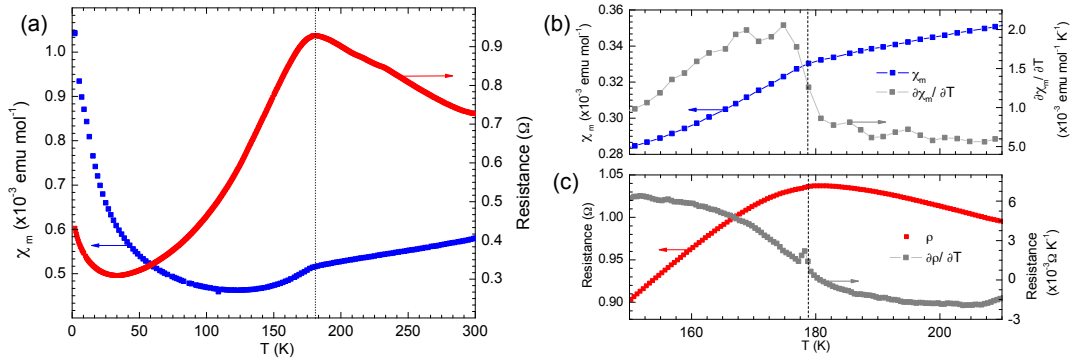

Figure 3.9: (a) The temperature dependence of the electrical resistivity (red curve) and magnetic susceptibility (H = 10000 Oe) (blue curve) of SrFeAsF. The kink in both physical properties measurements is associated to a spin density wave. The inflection points of the derivatives of (b) magnetic susceptibility and (c) electrical resistivity highlight the transition temperature T ~ 177 K.

To assess the physical properties of SrFeAsF, the electrical resistance and magnetic susceptibility were measured as a function of temperature and are shown in Figure 3.9. The electrical resistivity increases with decreasing temperature up to T = 180 K, and then decreases. The upturn below 30 K is probably due to increasing electron scattering coming from small traces of impurities. The magnetic susceptibility measured in H = 10000 Oe shows temperature dependent paramagnetic behaviour above T = 180 K, typical for a paramagnetic metal [9]. The magnetic susceptibility drops at T = 180 K, but increases again below T = 120 K, presumably due to the presence of paramagnetic impurities. The sharp drop in resistance and the anomaly

in the susceptibility at T = 180 K are associated with the occurrence of a spin density wave (SDW) as in the analogous oxypnictides. The onset of the SDW coincides with the structural phase transition in SrFeAsF, but is higher than the onset of the magnetic long-range order, T_N = 133(3) K [28].

The electrical resistance for the series $La_xSr_{1-x}FeAsF$ (x = 0.0, 0.1, 0.2) is shown in Figure 3.10. With increasing doping level, the SDW anomaly is partially supressed and shifts to lower temperatures. In both samples (x = 0.1 and 0.2) the electrical resistance decreases further at T = 26 K and 28 K, respectively. $La_{0.1}Sr_{0.9}FeAsF$ shows a finite conductivity down to the lowest temperature, whereas $La_{0.2}Sr_{0.8}FeAsF$ shows a sharp drop in resistance, typical for a superconducting material. In both cases, the contact between grains and the presence of impurities influences the absolute value of the resistivity measured.

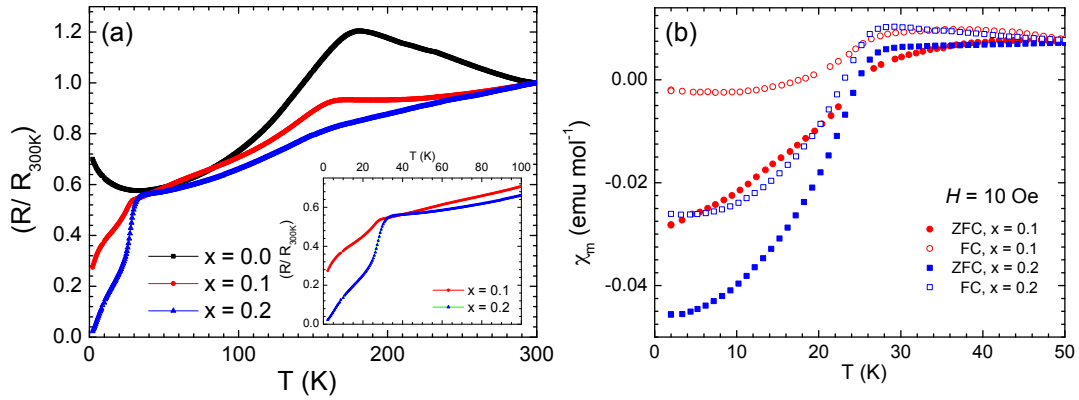

Figure 3.10: (a) The temperature dependence of the electrical resistivity of $La_xSr_{1-x}FeAsF$ shows a successive suppression of the SDW anomaly with increasing La-doping. The inset magnifies the low temperature regime, showing the sharp drop at 26 K and 28 K for x = 0.1 and 0.2, respectively. (b) The temperature dependence of zero field cooled (ZFC) and field cooled (FC) magnetic susceptibility of $La_xSr_{1-x}FeAsF$ (x = 0.1, 0.2), measured in H = 10 Oe, reveals the superconducting transition at T_c = 29 K and 27 K for x = 0.1 and 0.2, respectively.

The zero-field cooled (ZFC) and field cooled (FC) magnetic susceptibilities of $La_xSr_{1-x}FeAsF$ measured in H = 10 Oe (Figure 3.10 (b)) support the onset of a superconducting transition. The shape of ZFC and FC curves for x = 0.1 and 0.2 are similar. In $La_xSr_{1-x}FeAsF$, the onset of the superconducting transition occur at T_c = 29 K and 27 K for x = 0.1 and 0.2, respectively. $Sr_{0.8}La_{0.2}AsF$ has a small superconducting volume fraction** of 2 %. It is clear that the doping is not

** The superconducting fraction (%) was calculated according to: $C\,frac. = [4\pi\rho \cdot (M_{50K} - M_{2K})/H \cdot m] \cdot 100\,\%$, with the magnetisation M (emu) at T = 50 K

homogeneous throughout the sample and hampers the observation of zero resistance in the electrical conductivity measurements.

3.3.4 Nuclear Structure of *Ae*Mn*Pn*F

Inspection of the RT synchrotron X-ray powder diffraction (SRXD) data of the series *Ae*Mn*Pn*F (*Ae* = Sr, Ba; *Pn* = P, As, Sb) readily reveals the tetragonal unit cell (*P*4/*nmm*) established before for the manganese-based 1111-type system [18], [19]. Rietveld refinements were performed to elucidate the structural effects of *Pn* substitution in the [Mn*Pn*] layer and *Ae* substitution in the [*Ae*F] layer. The lattice parameters deduced from synchrotron powder X-ray diffraction (SXRD) patterns at RT are summarised in Table 3.3 and details of the Rietveld refinement can be found in Table 3.4 and Table 3.5. As expected from the differences in atomic radii, both alkaline earth metal *Ae* (Sr → Ba) and pnictide *Pn* replacement (P → As → Sb) lead to an expansion of the unit cell.

T = 300K	SrMnPF	BaMnPF	SrMnAsF	BaMnAsF	SrMnSbF	BaMnSbF
a/ Å	4.07277(2)	4.18086(3)	4.138739(8)	4.27601(3)	4.32597(1)	4.47827(5)
c/ Å	9.03247(7)	9.5070(1)	9.12688(3)	9.5904(1)	9.48548(5)	9.8301(2)
V/ Å^3	149.826(2)	166.179(2)	156.336(1)	175.353(2)	177.511(1)	197.141(4)

Table 3.3: Unit cell parameters of the *Ae*Mn*Pn*F series as obtained from Rietveld fits to RT synchrotron powder diffraction data, collected at beamlines ID31 and 11-ID-C for *Ae* = Sr and Ba, respectively. The cell expands with increasing *Pn* and *Ae* radius.

The volume, *a*- and *c*- lattice parameters as a function of combined *Ae* and *Pn* radius are shown in Figure 3.12. An increase in *Ae* or *Pn* radius elongates the *a*-axis almost by equal value. The *c*-axis on the other hand expands upon *Pn* replacement according to the radii-difference, but jumps when Ba replaces Sr. *Pn* and *Ae* substitutions do not only change the lattice parameters, but also affect the geometry (distortion) of the edge-sharing tetrahedra that form the [Mn*Pn*] and [*Ae*F] slabs. Each layer can be described as a square net of Mn (or of F) that is capped alternating above and below the plane by *Pn* (or of *Ae*) to give a square pyramidal geometry with *Pn* (or *Ae*) at the pyramid tip (Figure 3.11).

---

and 2 K, the density ρ (g cm^{-3}) using ρ = 7 g cm^{-3}, the applied magnetic field *H* (Oe) and the sample mass *m* (g).

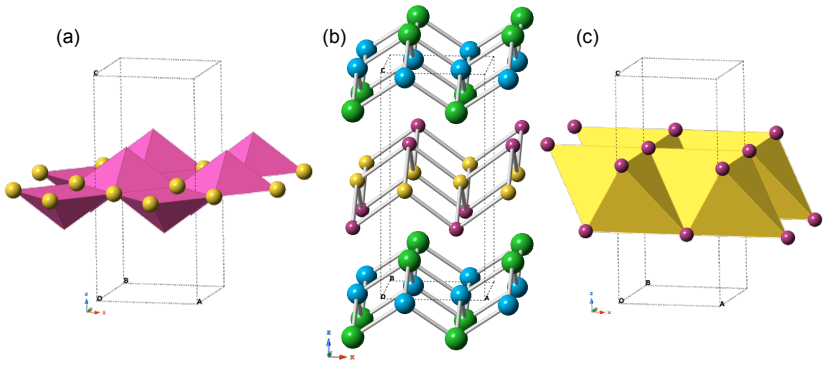

Figure 3.11: (a) Sketch of the [Mn*Pn*] layer emphasising the square-pyramidal coordination of [Mn_4*Pn*]. (b) The unit cell, consisting of stacked [*Ae*F]$^+$ and [Mn*Pn*]$^-$ layers. (c) A layer of edge-sharing [MnPn_4] tetrahedrons.

Let us first consider the changes introduced along the series P → As → Sb. In good agreement with the increasing radius of *Pn* (r(P) = 2.12 Å, r(As) = 2.22 Å, r(Sb) = 2.45 Å), the Mn-*Pn* bond elongates and the square planar Mn-net stretches to accommodate the larger pnictide [29]. The height of *Pn* above the manganese plane (h_{Pn}) increases simultaneously, resulting in a compression of the [MnPn_4] tetrahedra in the *ab*-plane (reduced twofold tetrahedral angle α) and a thicker [Mn*Pn*] layer. As a consequence of the increase of the *a*-axis parameter, the unsubstituted [*Ae*F] layer is stretched in the basal *ab*-plane, which reduces the height of *Ae* above the fluorine plane (h_{Ae}) and flattens the [Ae_4F] tetrahedra.

The substitution of Sr with Ba (r(Sr) = 1.18 Å, r(Ba) = 1.35 Å) elongates the *Ae*-F bond by 0.14 – 0.15 Å, which is in good agreement with the difference in ionic radii and comparable to the case of SrF_2 (Sr-F = 2.5089 Å) and BaF_2 (Ba-F = 2.6831 Å) [26], [30], [31]. The effect is similar to *Pn* replacement: h_{Ae} increases to account for the larger cation; the [Ae_4F] tetrahedra are compressed in the *ab*-plane and the layer becomes thicker. On the other hand, the unsubstituted [Mn*Pn*] layer becomes thinner, as h_{Pn} decreases and the [MnPn_4] tetrahedrA flatten.

Both, alkaline earth metal *Ae* and pnictide *Pn* replacement expand and thicken their comprising layers; the respective other layer has to stretch too and consequently flattens. A summary of bond-distances and angles, obtained from SXRD Rietveld refinements, are present in Table 3.4 and Table 3.5. The lattice mismatch is smallest in SrMnPF and BaMnAsF, for which the [MnPn_4] geometries are close to the ideal tetrahedron (i.e. *Pn*-Mn-*Pn* angle of 109.47°).

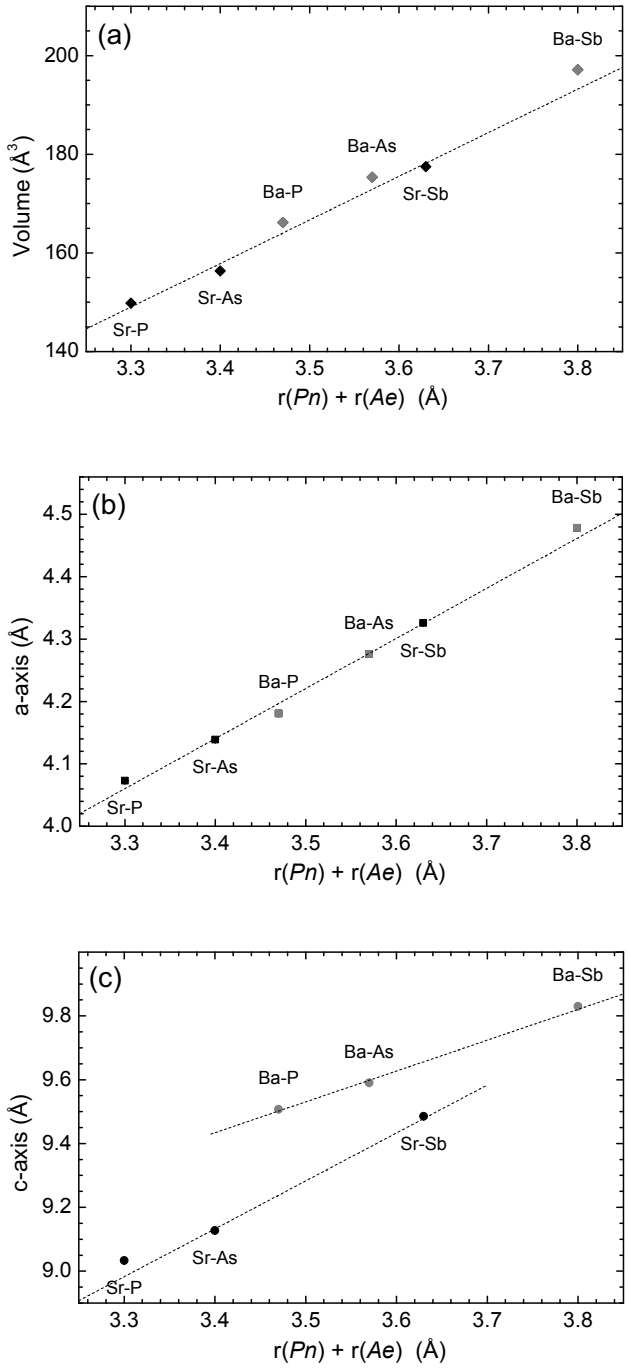

Figure 3.12: (a) The unit cell volume and (b, c) the *a*- and *c*- lattice parameters of the series *Ae*Mn*Pn*F, obtained from Rietveld fits of RT diffraction profiles, and plotted as a function of combined *Pn* and *Ae* radius. Both volume and *a*-axis increase smoothly with increasing radius, whereas the *c*-axis shows a jump for Sr to Ba replacement. The dashed lines are guides to the eye.

	SrMnPF	SrMnAsF	SrMnSbF
T/ K	300	300	300
space group	*P*4/*nmm*	*P*4/*nmm*	*P*4/*nmm*
a/ Å	4.07277(2)	4.138739(8)	4.32597(1)
c/ Å	9.03247(7)	9.12688(3)	9.48548(5)
V/ Å^3	149.826(2)	156.336(1)	177.511(1)
z(Sr)	0.15527(9)	0.15072(5)	0.13593(8)
z(*Pn*)	0.6621(2)	0.66755(5)	0.68014(7)
Occ. (Sr)	0.896(7)	1.002(1)	0.993(1)
Occ. (Mn)	0.896(7)	0.982(1)	0.989(2)
Occ. (*Pn*)	1.15(1)	0.98(1)	0.998(1)
Occ. (F)	0.944(9)	0.988(4)	1.030(5)
B_{11}=B_{22}, B_{33}/ Å^2			
Sr	0.49(2), 0.68(3)	0.71(1), 0.62(2)	0.52(3), 1.04(5)
Mn	1.09(4), 0.34(6)	0.53(2), 0.67(3)	0.60(5), 0.78(7)
Pn	1.38(6), 0.55(7)	0.48(2), 0.57(2)	0.56(2), 0.79(4)
F	0.2(1), 1.6(2)	1.10(8), 0.6(1)	1.2(2), 0.4(2)
distances/ Å:			
Sr-F	2.4726(4)	2.4848(3)	2.5181(4)
Mn-*Pn*	2.508(1)	2.5731(3)	2.7565(4)
Mn-Mn	2.87989(2)	2.92653(1)	3.05892(1)
angles/ °			
F-Sr-F (x4)	71.23(2)	72.153(9)	74.80(1)
(x2)	110.89(3)	112.77(2)	118.40(3)
Sr-F-Sr (x4)	108.77(2)	107.847(9)	105.20(1)
(x2)	110.89(3)	112.77(2)	118.40(3)
Pn-Mn-*Pn* (x4)	109.93(3)	110.684(9)	112.60(1)
(x2)	108.55(7)	107.07(2)	193.38(2)
Mn-*Pn*-Mn (x4)	70.07(3)	69.316(9)	67.40(1)
(x2)	108.55(7)	107.07(2)	103.38(2)
R_p/ %, wR_p/ %	8.00, 11.01	7.81, 9.90	6.43, 8.35
R_F^2/ %, χ^2	5.08, 1.985	3.89, 3.00	4.01, 1.138
wt% SrF_2	1.3(2)	1.5(3)	1.9(3)

Table 3.4: Results of Rietveld refinement of SXRD profiles of SrMn*Pn*F (*Pn* = P, As, Sb) collected at beamline ID31 at *T* = 300 K. There were 16 refined structural parameters. The fractional atomic coordinates are: Sr (¼, ¼, *z*); Mn (¾, ¼, ½); *Pn* (¼, ¼, *z*); F (¾, ¼, 0).

	BaMnPF	BaMnAsF	BaMnSbF
T/ K	300	300	300
space group	*P*4/*nmm*	*P*4/*nmm*	*P*4/*nmm*
a/ Å	4.18086(3)	4.27601(3)	4.47827(5)
c/ Å	9.5070(1)	9.5904(1)	9.8301(2)
V/ Å^3	166.179(2)	175.353(2)	197.141(4)
z(Ba)	0.16595(6)	0.15975(9)	0.1456(1)
z(*Pn*)	0.6452(3)	0.6543(2)	0.6681(1)
B_{iso}/ Å^2			
Ba	0.734(8)	0.73(2)	0.90(2)
Mn	0.71(2)	0.89(5)	1.33(7)
Pn	0.63(4)	0.93(3)	1.06(3)
F	0.71(8)	0.9(2)	1.67(2)
distances/ Å:			
Ba-F	2.6190(4)	2.6302(5)	2.6574(5)
Mn-*Pn*	2.505(1)	2.6001(9)	2.7826(7)
Mn-Mn	2.95632(2)	3.02360(2)	3.16662(4)
angles/ °			
F-Ba-F (x4)	68.72(1)	70.17(2)	73.14(2)
(x2)	105.91(2)	108.75(3)	114.83(4)
Ba-F-Ba (x4)	111.28(1)	109.83(2)	106.86(2)
(x2)	105.91(2)	108.75(3)	114.83(4)
Pn-Mn-*Pn* (x4)	107.68(4)	108.90(3)	110.64(2)
(x2)	113.12(9)	110.63(6)	107.16(4)
Mn-*Pn*-Mn (x4)	72.32(4)	71.11(3)	69.36(2)
(x2)	113.12(9)	110.63(6)	107.16(4)
R_p/ %, wR_p/ %	3.00, 4.26	2.97, 4.16	3.08, 4.06
R_F^2/ %, χ^2	4.27, 1.213	5.51, 1.25	5.09, 1.059
wt% BaF_2	0.5(3)	1.0(3)	0.4(3)

Table 3.5: Results of the Rietveld refinements of SXRD profiles of BaMn*Pn*F (*Pn* = P, As, Sb) at collected at beamline 11-ID-C at T = 300 K. There were 8 refined structural parameters. The fractional atomic coordinates are: Ba (¼, ¼, *z*); Mn (¾, ¼, ½); *Pn* (¼, ¼, *z*); F (¾, ¼, 0).

3.3.5 Temperature Dependence of the Structure of *Ae*Mn*Pn*F

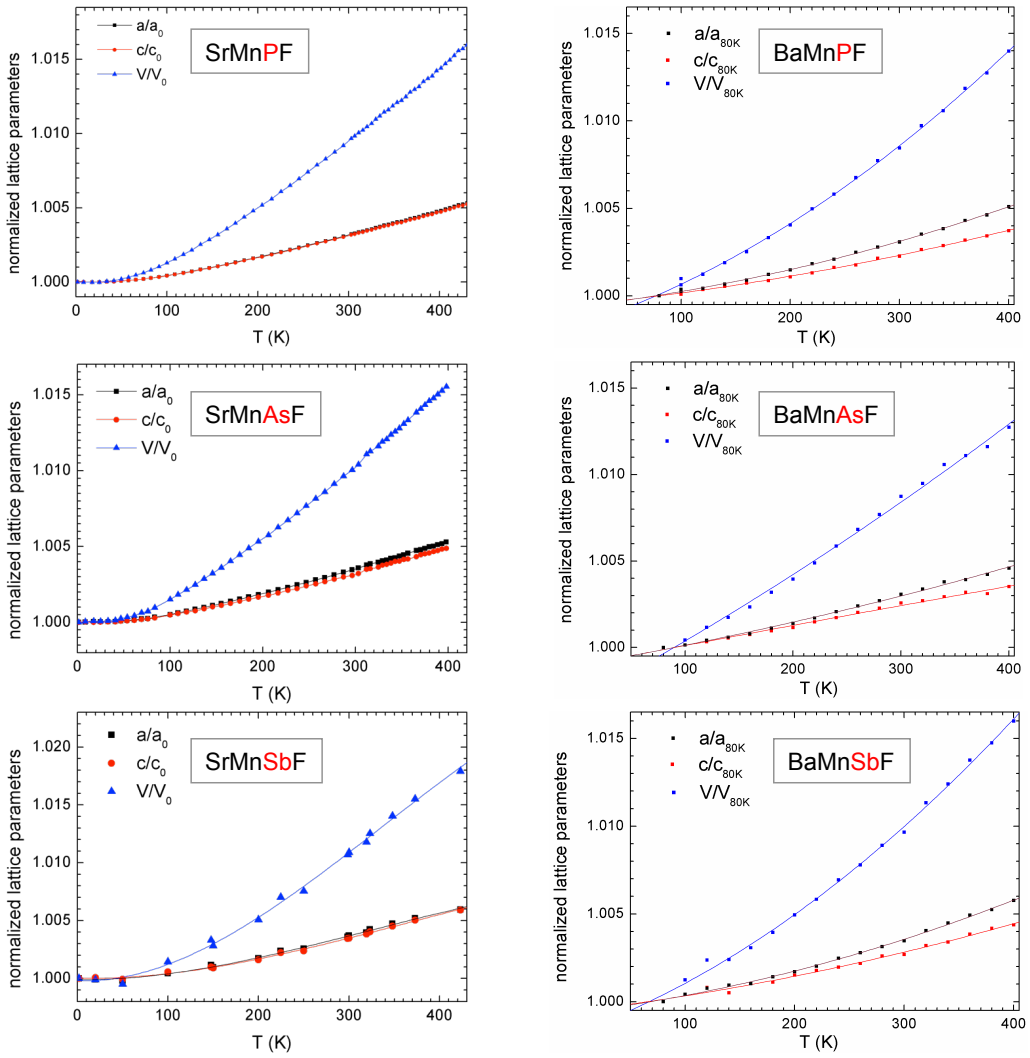

Figure 3.13: The unit cell volume and lattice parameters of the *Ae*Mn*Pn*F family obtained form Rietveld fits to variable temperature diffraction data. The lattice increases smoothly with increasing temperature. The lattice constants were normalized to the low temperature values, T = 20 K and T = 80 K for *Ae* = Sr and Ba, respectively. The line is a guide only.

Variable temperature diffraction profiles were collected down to T = 1.5 K and 80 K for the SrMn*Pn*F and BaMn*Pn*F series, respectively. In contrast to the isostructural iron pnictides *Ae*FeAsF (*Ae* = Ca, Sr, Eu) that show a tetragonal ($P4/nmm$) to orthorhombic ($Cmma$) transition between T = 150 K and 200 K, the manganese-based systems remain strictly tetragonal at all temperatures. The thermal expansion of the SrMn*Pn*F lattice was followed between T = 1.5 K and 420 K by neutron powder

diffraction (NPD) and SXRD. Upon cooling, the unit cell *a*- and *c*- constants decrease smoothly and isotropically for all prepared compositions (Figure 3.13). The contraction in stacking direction (*c*-axis) and basal *ab*-plane is approximately 0.5 %. Temperature dependent diffraction profiles of BaMn*Pn*F were collected by laboratory powder X-ray diffraction (XRD) between T = 80 K and 400 K. The Ba-series shows similar behaviour to the Sr-compounds: the lattice contracts by circa 0.4 % along *a*- and *c*-axis (Figure 3.13).

	SrMnPF	SrMnPF	SrMnAsF	SrMnAsF	SrMnSbF	SrMnSbF
T/ K	1.5	303	1.5	303	1.8	298
space group	*P*4/*nmm*	*P*4/*nmm*	*P*4/*nmm*	*P*4/*nmm*	*P*4/*nmm*	*P*4/*nmm*
a/ Å	4.0591(1)	4.0722(2)	4.1243(1)	4.1390(1)	4.3101(1)	4.3256(2)
c/ Å	9.0032(3)	9.0318(5)	9.0972(6)	9.1264(7)	9.4527(6)	9.4853(6)
V/ Å^3	148.34(2)	149.77(2)	154.74(1)	156.35(1)	175.60(1)	177.48(1)
z(Sr)	0.1585(6)	0.1590(8)	0.1517(3)	0.1513(3)	0.1386(3)	0.1381(4)
z(*Pn*)	0.6575(7)	0.658(1)	0.6680(3)	0.6680(3)	0.6804(5)	0.6789(5)
μ_{eff}/ μ_B	3.29(2)	2.29(4)	3.46(2)	2.27(1)	3.59(4)	1.14(9)
distances/ Å:						
Sr-F	2.481(3)	2.492(4)	2.481(1)	2.488(2)	2.522(2)	2.529(2)
Mn-*Pn*	2.476(4)	2.488(5)	2.567(2)	2.576(2)	2.748(3)	2.749(3)
Mn-Mn	2.8702(1)	2.8795(1)	2.91632(9)	2.9267(1)	3.0477(1)	3.0586(1)
angles/ °						
F-Sr-F (x4)	70.69(9)	70.6(1)	71.98(5)	72.06(5)	74.34(5)	74.44(6)
(x2)	109.8(2)	109.6(3)	112.4(1)	112.6(1)	117.4(1)	117.6(1)
Sr-F-Sr (x4)	109.31(9)	109.4(1)	108.02(5)	107.94(5)	105.66(5)	105.56(6)
(x2)	109.8(2)	109.6(3)	112.4(1)	112.6(1)	117.4(1)	117.6(1)
Pn-Mn-*Pn* (x4)	109.1(1)	109.3(2)	110.76(5)	110.76(5)	112.64(7)	112.40(8)
(x2)	110.1(2)	109.9(3)	106.92(9)	106.9(1)	103.3(1)	103.8(2)
Mn-*Pn*-Mn (x4)	70.9(1)	70.7(2)	69.24(5)	69.24(5)	67.36(7)	67.60(8)
(x2)	110.1(2)	109.9(3)	106.92(9)	106.9(1)	103.3(1)	103.8(2)
R_p, wR_p/ %	4.03, 5.99	7.04, 8.92	2.87, 4.37	3.01, 4.50	2.14, 2.94	2.09, 2.84
R_F^2/ %, χ^2	94.0, 34.76	77.0, 77.8	1.95, 124.4	3.68, 18.8	12.6, 8.375	15.05, 7.729

Table 3.6: The lattice parameters of SrMn*Pn*F (*Pn* = P, As, Sb) obtained from Rietveld fits to neutron powder diffraction profiles at low and ambient temperature. Each refinement used four structural parameters.

3.3.6 Magnetic Structure of *Ae*Mn*Pn*F

The magnetic ordering of the Mn^{2+} (S = 5/2) ions in SrMn*Pn*F was investigated by NPD between T = 1.5 K and 420 K (Table 3.6). Comparison of SXRD and NPD shows the presence of magnetic Bragg peaks at RT. Fitted NPD data of SrMn*Pn*F is presented in Figure 3.14; the asterisk marks the reflection (100), (010) which is of

magnetic origin only. A small reflection at 42.5° 2θ can be attributed to the SrF_2 impurity phase, which was not included in the refinement.

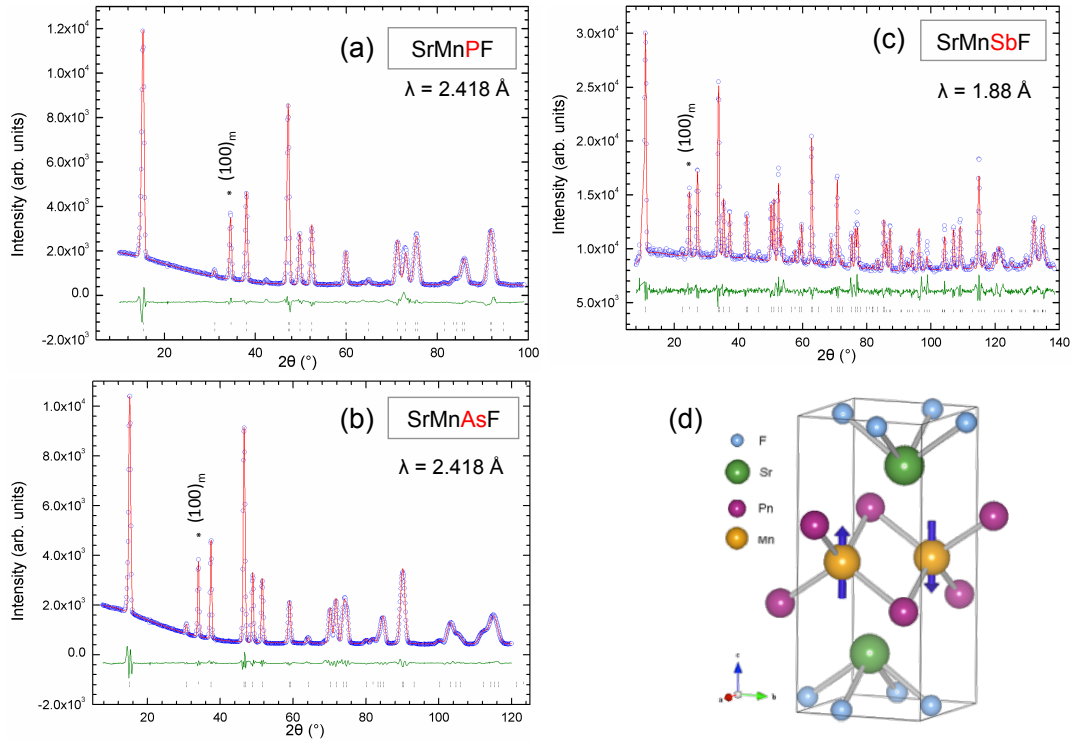

Figure 3.14: (a – c) Rietveld fits to the NPD profiles of the SrMn*Pn*F series (space group *P*4/*nmm*), collected at D20, at T = 1.5 K. Experimental data, Rietveld fit, and difference plot shown as open blue circles, red and green solid line, respectively. The asterix marks the reflection that is of magnetic origin only. (d) The blue arrows in the unit cell model show the so-called G-type AFM Mn-spin arrangement.

For all compositions, the indexing of the magnetic reflections leads to a magnetic model where the Mn moments are aligned parallel to the *c*-axis (Figure 3.14). The antiferromagnetic arrangement is of so-called G-type: the coupling in the basal plane is antiparallel with nearest [110] direction and parallel with second nearest [100] and [010] direction Mn ions. No indication of a unit cell doubling was observed in the NPD data. Therefore the ordering between two adjacent [Mn*Pn*] layers is described as FM in [001] direction. Models of the magnetic cell with a component of the magnetic moment along the basal *ab*-plane did not give a satisfactory fit.

The magnetic moment of SrMn*Pn*F at base temperature increases with the size of *Pn*, from μ_{eff} = 3.29(2) μ_B to μ_{eff} = 3.46(1) μ_B to 3.59(4) μ_B, for *Pn* = P, As and Sb,

respectively. The Néel temperature was determined from the temperature evolution of the effective magnetic moment (Figure 3.15) μ_{eff} to be T_N = 365 K, 360 K and 320 K (for *Pn* = P, As, Sb).

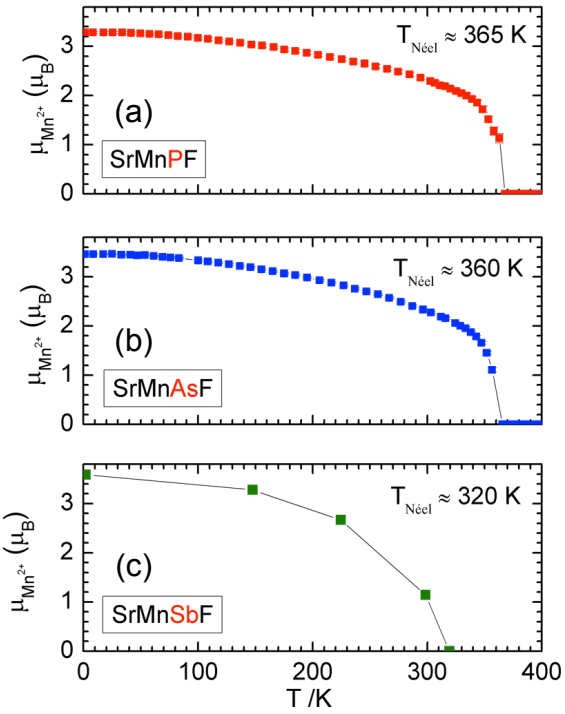

Figure 3.15: (a – c) Temperature dependence of the effective magnetic moment of SrMn*Pn*F obtained from Rietveld fits to variable temperature NPD profiles. The line is a guide to the eye.

3.3.7 Local Structure of *Ae*Mn*Pn*F

The experimental radial distribution function $G(r)$ of *Ae*Mn*Pn*F series were fitted using the parameters obtained from Rietveld refinements as a starting model. Along the series, changes in lattice constants with *Ae* and *Pn* replacement are reflected in a shift of pairs, e.g. the first peak (Mn-*Pn* and F-*Ae* pairs) moves towards higher r as the cell expands. The general features of the $G(r)$ are described reasonably well with the average structure as obtained from Rietveld refinements. However, the long-range structure is insufficient to describe the local environment, where discrepancies are observed especially for the second peak (at r = 2.8 – 3.1 Å, depending on composition) involving the Mn-Mn and F-F pairs. This is especially true for SrMnPF and BaMnSbF, see Figure 3.16. A good agreement between the average structure and the local structure is found for the fitting range of r = 5 – 20 Å, which indicates that the distortion are of very short-range nature.

Initial fitting of the data (r = 1 – 5 Å) used the average XRD model as a starting point. Refined parameters were the scale factor, lattice constants a and c, height of the alkaline earth metal $z(Ae)$ and pnictide $z(Pn)$, isotropic thermal parameters U_{iso} and the dynamic correlation factor delta d2, which accounts for the correlated motion between atom pairs. The fit improves (not shown), but yields unphysical values for U_{iso}(F) (0.03 – 0.12 Å^2, except for SrMnPF) and does not resolve the problem of the position of the second peak, which is predicted at a higher r value than experimentally observed.

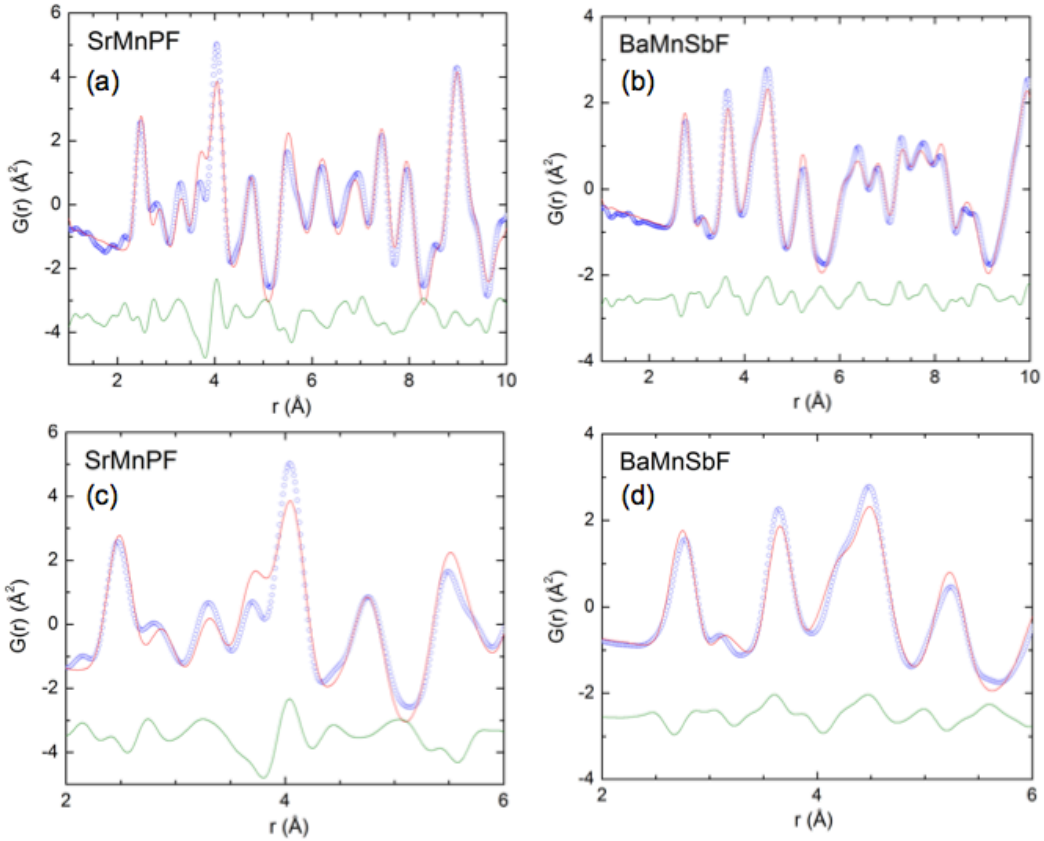

Figure 3.16: The $G(r)$ of (a) SrMnPF and (b) BaMnSbF, fitted using the average structure obtained from Rietveld refinement. Refined parameters were the scale and d2 factors; isotropic thermal parameters were assumed to be U_{iso} = 0.009 Å^2 for all atoms. Blue open circles show experimental data, the red line is a fit based on parameters obtained from the Rietveld refinement, the green line is the difference between experiment and calculation. The average structure models reproduce well the general features of the $G(r)$, but discrepancies on the short range (c, d) indicate that structural modifications of the local environment occur. Indicator of fit is R_w = 24.99 % and 16.61 % for SrMnPF and BaMnSbF, respectively.

Due to their special positions, the Mn-Mn and F-F pairs contribute equally towards the initial peak. But the light fluorine atom is difficult to detect by X-rays, and its

large thermal displacement factor might bias the atomic displacements calculated for Mn and F. Hence we focus on the contribution of Mn-Mn and Mn-*Pn* pairs, especially as the [Mn*Pn*] layer corresponds to the active superconducting layer in the iron-pnictide materials. The isotropic thermal displacement parameter of F was fixed to U_{iso}(F) = 0.025 Å^2 for all following real space refinements.

Model: Uaniso(Mn)					
	U11(Mn)	U33(Mn)	Uavg(Mn)	Uiso(*Pn*)	U33(Mn)/U11(Mn)
SrMnPF	0.0087	0.0367	0.018	0.008	4.2017
SrMnAsF	0.0074	0.0208	0.0118	0.0071	2.8229
SrMnSbF	0.0094	0.0072	0.0087	0.007	0.7613
BaMnPF	0.0061	0.0196	0.0106	0.0141	3.2184
BaMnAsF	0.0068	0.0228	0.0121	0.0089	3.375
BaMnSbF	0.0094	0.0172	0.012	0.0051	1.8308

Model: Uaniso(Pn)					
	Uiso(Mn)	U11(Pn)	U33(Pn)	Uavg(Pn)	U33(Pn)/U11(Pn)
SrMnPF	0.0201	0.0024	0.0356	0.0135	14.6015
SrMnAsF	0.0113	0.0041	0.0169	0.0084	4.0728
SrMnSbF	0.0084	0.0085	0.0044	0.0072	0.5217
BaMnPF	0.0071	0.0052	0.008	0.0062	1.536
BaMnAsF	0.017	0.0042	0.0282	0.0122	6.7245
BaMnSbF	0.0118	0.0047	0.0031	0.0042	0.6452

Table 3.7: Variation of thermal displacement parameters for *Ae*Mn*Pn*F, assuming anisotropic and isotropic for Mn and *Pn* ('Uaniso(Mn)') or isotropic and anisotropic temperature factors for Mn and *Pn* (Uaniso(Pn)'). The U_{33}/U_{11} ratio is an indication for the anisotropy present on a site. The results were obtained by fitting the RT $G(r)$ data.

The next step in the analysis was to model the short range (r = 1 – 5 Å) using the average structure and then introducing anisotropic thermal displacement parameters ($U_{11} = U_{22} \neq U_{33}$) on either Mn or *Pn*. The thermal displacement parameters were not set anisotropic simultaneously, because the number of parameters is limited for such a short fitting range. A list of the refined thermal displacements is provided in Table 3.7. It can be seen that the 'goodness of fit' indicator R_w improves when anisotropic thermal displacement parameters are used (see Table 3.8) and for most members of the series anisotropic thermal displacement parameters of Mn (as opposed to *Pn*) result in a better fit. For both Mn and *Pn* the thermal ellipsoids elongate along the *z*-axis. The exceptions are SrMnSbF, where $U_{11} > U_{33}$ for the models U_{aniso}(Mn) and U_{aniso}(*Pn*), and BaMnSbF where $U_{11} > U_{33}$ for the model U_{aniso}(*Pn*). Also there is a notable spread in U_{33}/U_{11} ratios varying from 0.5 to 14.5 (Table 3.7), which is a clear indication for a distribution of atomic sites. Generally the displacement appears more significant in those members of the series

whose average structure is least distorted. SrMnPF and BaMnAsF show the largest anisotropy of $U_{33}/U_{11}(Pn)$.

model	XRD	XRD	XRD	z(Mn)	z(Pn)
t.d.p. Mn	Uiso	Uaniso	Uiso	Uiso	Uiso
t.d.p. Pn	Uiso	Uiso	Uaniso	Uiso	Uiso
SrMnPF	18.67	14.19	17.11	14.07	15.05
SrMnAsF	11.87	10.18	10.75	10.68	11.75
SrMnSbF	9.1	9.05	8.24	9.1	9.06
BaMnPF	10.66	9.34	10.65	10.15	10.43
BaMnAsF	9.2	7.07	8.09	7.78	7.18
BaMnSbF	8.89	8.74	8.79	8.85	8.71

Table 3.8: $R_w(\%)$ values for various structural models; left to right: average structure using isotropic thermal displacement parameters (t.d.p.); average structure, anisotropic t.d.p. for Mn; average structure, anisotropic t.d.p for *Pn*; atomic displacement of Mn within the 'zMn' model; atomic displacement of *Pn* within the 'zPn' model.

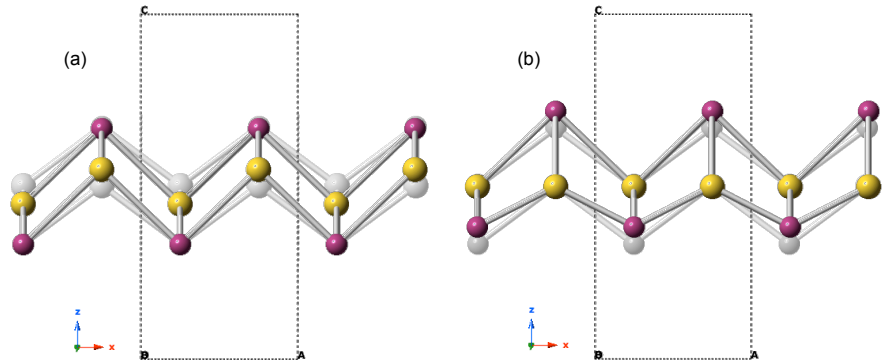

Figure 3.17: Illustration of the proposed models to fit the experimental $G(r)$ data. (a) 'zMn' model: The two Mn ions in the unit cell, Mn1 and Mn2, move by the same amount delta, but in opposite direction along the *c*-axis. (b) 'zPn' model: The two *Pn* ions of the unit cell, Pn1 and Pn2, move by the same amount delta in the same direction along the *c*-axis.

As mentioned previously, the Mn-Mn bond appears to be shortened in the experimental data. However, a structural model featuring shorter Mn-Mn pairs will simultaneously introduce longer Mn-Mn bonds. To fit the experimental data, two models were proposed, involving split positions of Mn and *Pn* along the *c*-axis, respectively (Figure 3.17). Splitting the Mn and *Pn* sites will broaden the peaks of the Mn-Mn and the Mn-*Pn* pair, respectively. There are two manganese and pnictide ions in each unit. In both models, the fractional coordinates *x* and *y* of Mn and *Pn* were kept constant, whilst the *z* coordinate was varied. The first model, hereafter abbreviates 'zMn', splits the Mn site into Mn1 and Mn2. The *z*-coordinate of Mn1 and Mn2 are described by a common variable, z_{Mn}, such that $z(Mn1) = z_{Mn}$ and $z(Mn2) = -z_{Mn} + 1$ are fulfilled. The second proposed model, called 'zPn' splits

the *Pn* site into Pn1 and Pn2. Differently to the special position of Mn, which is located at $z = 0.5$ in the average XRD model, the z-coordinate of the *Pn* site is a variable. To keep the number of refinable parameters of the two local structure models the same, the z-coordinate obtained from the XRD model was used as fixed starting point z_0, from which Pn1 and Pn2 move away by an amount d during the refinement of the local structure. The z-coordinates were described as $z(\text{Pn1}) = z_0 + d$ and $z(\text{Pn2}) = 1 - z_0 + d$. In the 'zMn' model the movements of the Mn atoms within the unit cell are opposite: as Mn1 moves up (along z) the Mn2 moves downwards by the same amount. In the 'zPn' model Pn1 moves up by distance d (i.e. away from the Mn plane) and the Pn2 moves up too (i.e. towards the plane). Opposite movement of Pn1 and Pn2 would simply correspond to a change in z(*Pn*), already allowed in the average crystallographic model.

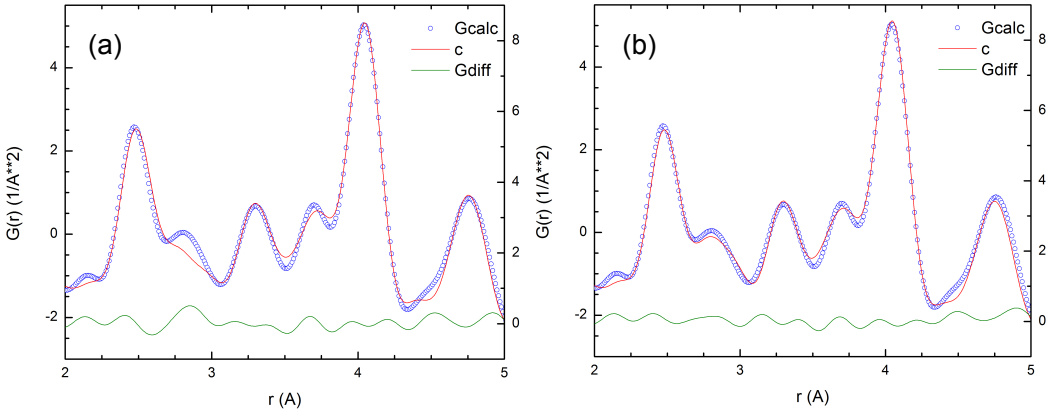

Figure 3.18: The RT $G(r)$ of SrMnPF, fitted in the range of r = 1- 5 Å. Experimental data, fit and difference plot shown as open blue circles, red and green solid line, respectively. (a) The structure was refined within the constraints of the XRD model; $R_w = 13.9$ %. (b) The structure was refined with the zPn model; $R_w = 13.5$ %. Isotropic temperature factors were used in both models. Note especially the improvement on the second peak at r = 2.8 Å.

On the one hand, one would expect 'zMn' to result in a better fit compared to 'zPn' simply by looking at the goodness of fit for the models with anisotropic thermal displacement parameters described earlier (Table 3.8). However, the anisotropy of the thermal ellipsoids is larger on the pnictide site, which would favour the 'zPn' model. The R_w values for 'zMn' and 'zPn' models listed in Table 3.8 do not indicate that one model should be favoured over the other. Based on this analysis it is likely that the true structure is a combination of small displacements on both sites. The distortion is of very local nature, and it is not possible to refine 'zPn' and 'zMn' simultaneously, without risking over-parameterization.

3.3.8 Physical Properties of *Ae*Mn*Pn*F

In agreement with the structural data, no discontinuities were observed for SrMn*Pn*F in the susceptibility and resistivity measurements (T = 2 K – 300 K); consistent with the onset of magnetic order above RT. The ZFC magnetic susceptibilities χ_m of *Ae*Mn*Pn*F were measured in an applied field of H = 10000 Oe (Figure 3.19, Figure 3.20). The values of χ_m increase with decreasing temperature and along P → As → Sb (at 300 K: χ_m(Sr-P) = $0.8 \cdot 10^{-3}$, χ_m(Sr-As) = $1.0 \cdot 10^{-3}$, χ_m(Sr-Sb) = $2.8 \cdot 10^{-3}$, χ_m(Ba-P) = $1 \cdot 10^{-3}$, χ_m(Ba-As) = $1.2 \cdot 10^{-3}$ and χ_m(Ba-Sb) = $2 \cdot 10^{-3}$ emu mol^{-1} Oe^{-1}). The RT susceptibilities of the P and As compounds are comparable, whereas Sb materials have a larger magnetic susceptibility, reflecting that the effective magnetic moment of Mn is enhanced from P to Sb. The antiferromagnetic order of SrMn*Pn*F series that is present at RT is reflected in the deviation from Curie-Weiss behaviour. This can be seen in the temperature dependence of χ_m^{-1} (Figure 3.19). With the exception of BaMnAsF – for which the χ_m^{-1} plot shows flat temperature dependence – the magnetic susceptibilities of the Ba- and Sr-series are alike and indicate that the magnetic order in both groups of compounds is similar.

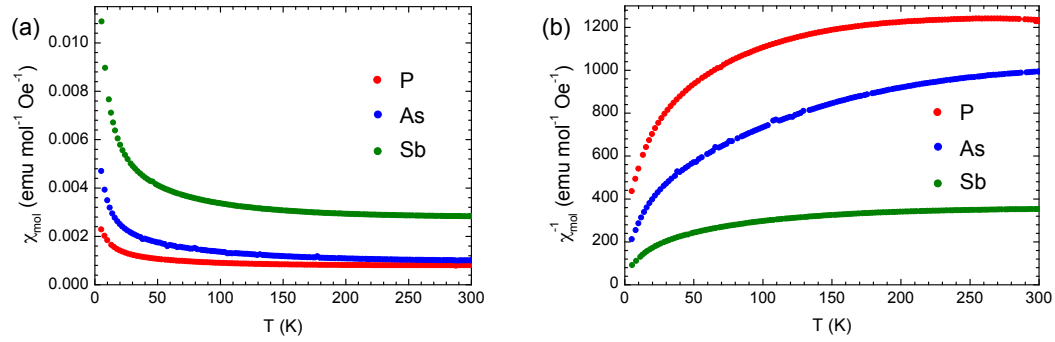

Figure 3.19: Temperature dependence of (a) the magnetic susceptibility χ_m and (b) the inverse χ_m^{-1} of the SrMn*Pn*F series, *Pn* = P (red), As (blue) and Sb (green), collected at H = 10000 Oe. No discontinuities are observed in the measured temperature range (T = 2 K – 300 K). The inverse susceptibility does not follow Curie Weiss behaviour.

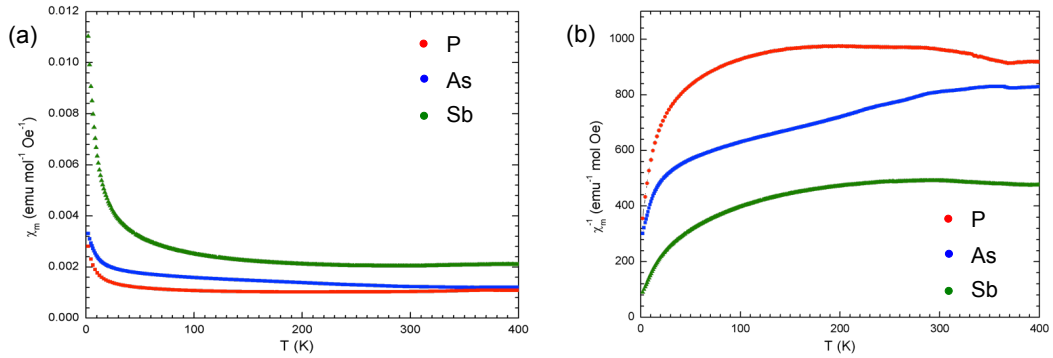

Figure 3.20: Temperature dependence of (a) the magnetic susceptibility χ_m and (b) the inverse χ_m^{-1} of the BaMn*Pn*F series *Pn* = P (red), As (blue) and Sb (green), collected at $H = 10000$ Oe. Small discontinuities between $T = 350$ K and 400 K may indicate the onset of magnetic ordering in this family of materials.

Measurements of the electrical conductivity (Figure 3.21(a)) show insulating to semiconducting behaviour of SrMn*Pn*F, with an increase in conductivity for the heavier pnictides (ρ at 300 K: 1200, 6.4 and 2.6 Ω cm for *Pn* = P, As and Sb, respectively). The electrical resistance in BaMn*Pn*F materials (Figure 3.21(b)) increases with P > Sb >> As (ρ at 300 K: 2.7, 10^5, and 7.8 Ω cm for *Pn* = P, As and Sb, respectively). The conductivity decreases with temperature. Further decrease in temperature results in the loss of the signal, due to the limiting current of the measurement setup.

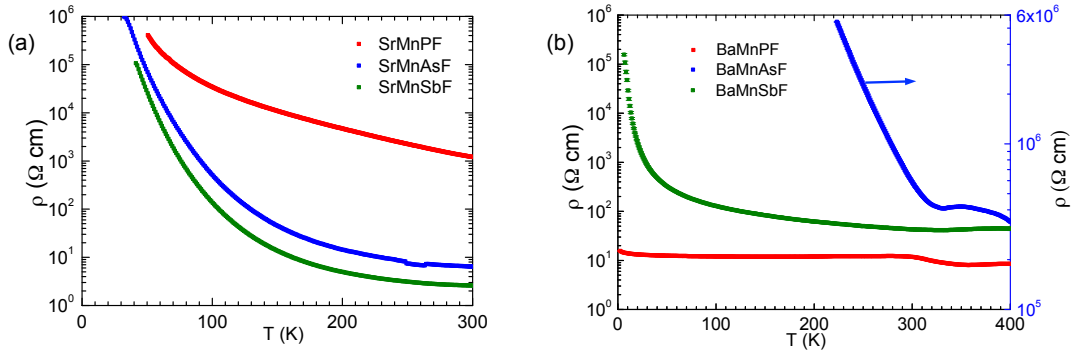

Figure 3.21: Temperature dependence of the electrical resistivity of (a) SrMn*Pn*F and (b) BaMn*Pn*F. At low temperatures, the signal is lost due to the very insulating character of these materials and the limiting current of the measurement setup. Anomalies in the high temperature region (BaMn*Pn*F) are likely to correspond to the onset of magnetic order of the Mn spins.

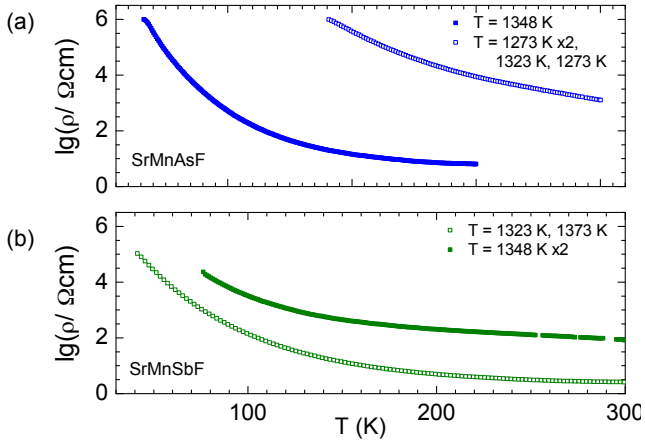

Figure 3.22: The temperature dependence of the electrical resistivity of (a) SrMnAsF and (b) SrMnSbF, synthesised under different conditions indicated in the figure. The resistivity increases with maximum annealing temperature.

The electrical resistivity of *Ae*Mn*Pn*F depends not only on its constituents, but also on the preceding heat treatment during synthesis. For example, the resistivity of SrMnAsF and SrMnSbF increases when the maximum synthesis temperature is higher (Figure 3.22). This is probably related to the loss of fluorine at elevated temperatures, but was not investigated in further detail.

3.4 Discussion

3.4.1 Superconductivity in $La_xSr_{1-x}FeAsF$

Similar to the oxypnictides *Re*FeAsO, the fluoride based analogue SrFeAsF described herein adopts the tetragonal *P*4/*nmmm* structure and undergoes a structural transition to orthorhombic *Cmma* symmetry at T = 180 K (Figure 3.5). The structural transition is connected to the development of a spin density wave that is appreciable from physical properties measurements (Figure 3.9). Long-range magnetic ordering occurs between T = 150 K and 100 K, and the spin structure is of striped antiferromagnetic type. The discrepancy between structural and magnetic transition temperatures was confirmed by Xiao *et al*. and the latter determined as T_N = 133(3) K [28].

Partial replacement of Sr with La (electron-doping) shifts the structural $T \rightarrow O$ transition to lower temperatures and suppresses the spin density wave of the parent material. The extra charge carriers formally reduce Fe^{2+} to Fe^{+}, according to $La^{3+}_{x}Sr^{2+}_{1-x}Fe^{+}_{x}Fe^{2+}_{1-x}As^{3-}F^{-}$. The La-doped SrFeAsF samples show typical superconducting transitions, with T_c = 29 K for x = 0.2. The superconducting volume fraction of $La_{0.2}Sr_{0.8}FeAsF$ is very small (2 %) compared to other iron-pnictides (i.e. $CaFe_{1-x}Co_xAsF$, superconducting fraction ~60 % [17]). This might indicate that the doping is not homogenous throughout the sample and/ or that the optimum doping level is not reached.

The crystal structure gives a further indication that $La_{0.2}Sr_{0.8}FeAsF$ is in the under-doped regime of the phase diagram: the structural transition is supressed in optimally doped $CaFe_{0.88}Co_{0.12}AsF$, but still present in the samples presented herein [17]. It is likely that higher doping levels will lead to bulk superconductivity if La can be successfully incorporated into the structure. Unfortunately, higher doping levels cannot be achieved using the ambient pressure synthetic route, as can be appreciated from the increasing impurity levels (Table 3.2). High-pressure synthesis techniques may be more adequate to obtain higher doping levels, as pressure could help to stabilise the reduced volume of the unit cell.

Despite the small volume fraction, the superconductivity observed is likely arising from the $La_{0.2}Sr_{0.8}FeAsF$ phase rather than secondary phases present in the sample. The contributions from impurities identified by X-ray diffraction towards the

observed transitions can be ruled out easily: SrF_2 and LaAs are non-magnetic. $SrFe_2As_2$ undergoes a structural transition and orders in a spin-striped AFM arrangement at T ≈ 205 K, which is significantly higher than T_S = 170 – 180 K for $La_xSr_{1-x}FeAsF$ [32], [33]. Only samples of $La_xSr_{1-x}Fe_2As_2$ synthesised at high pressure are superconducting with a maximum $T_c \approx 22$ K ($0.2 < x < 0.5$), but the observed T_c (~29 K) does not correspond to such an impurity [34]. The superconducting transition may be related to small amounts of $LaFeAsO_{1-x}F_x$. The T_c observed for La-doped SrFeAsF is similar to the T_c of F-doped LaFeAsO (maximum T_c = 26 K, $x = 0.11$) [1]. But there is no indication[††] for the presence of detectable amounts of $LaFeAsO_{1-x}F_x$ in the diffraction profiles.

3.4.2 Comparison of SrT_MAsF (T_M = Fe, Mn)

The layered metal-arsenides of Fe and Mn adopt the same ZrCuSiAs-type structure. Alternating antifluorite $[FeAs]^-$ or $[MnAs]^-$ and fluorite $[SrF]^+$ type slabs build up the layered structure of tetragonal $P4/nmm$ symmetry. The unit cell volume of SrMnAsF is circa 8 % larger compared to SrFeAsF, which can be mainly explained with the larger cation-radius ($r(Mn^{2+})$ = 0.66 Å, $r(Fe^{2+})$ = 0.63 Å). On cooling below T = 180 K, SrFeAsF undergoes a phase transition to orthorhombic *Cmma* symmetry whereas SrMnAsF remains strictly tetragonal. The structural phase transition in the iron arsenide compounds coincides with anomalies in the electrical resistivity and magnetic susceptibility and is connected to a spin-density wave (SDW).

Both materials contain magnetically active ions in the same formal oxidation state, i.e. Fe^{2+} ($3d^6$, $S = 2$) and Mn^{2+} ($3d^5$, $S = 5/2$), and order below their Néel temperatures, T_N = 180 K and T_N = 365 K for SrFeAsF and SrMnAsF, respectively. Their respective magnetic unit cells are shown in Figure 3.23. The Fe-moments show a striped AFM arrangement: the spins are ordered AFM and FM in the two respective directions of the basal *ab*-plane and AFM between adjacent [FeAs] layers. As a result of the AFM coupling along *c*, the magnetic unit cell is twice as large as the nuclear unit cell. The magnetic moment $\mu_{eff}(Fe^{2+}) = 0.6(2)\ \mu_B$ is considerably smaller than expected for the free ion ($\mu_{eff} = 4.90\ \mu_B$), which can be explained with the itinerancy of the conducting electrons [35]. The value obtained is in agreement with the reported moments of the iron-fluorides *Ae*FeAsF (*Ae* = Ca, Sr) [36], [37]. In SrMnAsF however, the spins order

[††] The strongest reflection of the $LaFeAsO_{1-x}F_x$ and $La_xSr_{1-x}FeAsF$ phases, $(003)_T$, are expected at different *d*-spacing ($d \approx 2.91$ Å, $c \approx 8.73$ Å and $d \approx 2.99$ Å, $c \approx 8.97$ Å for $LaFeAsO_{1-x}F_x$ and $La_xSr_{1-x}FeAsF$, respectively). No peaks are observed at $d \approx 2.91$ Å.

above RT and align parallel to the *c*-axis and order AFM between next-neighbours and FM between adjacent layers. Again, the experimentally determined magnetic moment (μ_{eff} = 3.46(1) μ_B) is smaller than the expected value for the free ion (μ_{eff} = 5.92 μ_B), but is comparable with the value calculated for BaMnPF (μ_{eff} = 3.3 μ_B) [18].

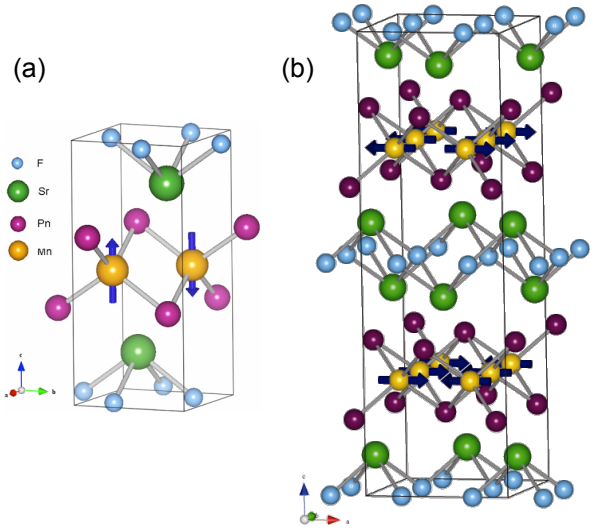

Figure 3.23: The nuclear and magnetic unit cells of (a) SrMnAsF, space group *P*4/*nmm* and (b) SrFeAsF, space group *Cmma*. The size of the magnetic and nuclear cell is identical for the Mn-compounds, whereas the antiferromagnetic coupling in the Fe material leads to a doubling of the unit cell *c*-axis.

Compared to SrMnAsF, the iron compound contains one additional electron per unit cell. This gives rise to different magnetic ordering, and is also responsible for the remarkably different physical properties: The iron-pnictide is a poor metal and shows SDW in specific heat, electrical conductivity and magnetisation [6]. Through charge-carrier-doping the SDW can be suppressed and superconductivity is achieved. This was successfully demonstrated by partial replacement of Sr^{2+} with La^{3+} (electron doping): $La_{0.2}Sr_{0.8}FeAsF$ is superconducting with T_c = 27 K. On the contrary, the AFM order of insulating SrMnAsF persists above RT and no anomalies were observed in electrical conductivity and magnetic susceptibilities.

Density of states (DOS) calculations have shown that the bonding mechanism in SrFeAsF is not of purely ionic character, but includes intraplanar covalent interaction within the $[FeAs]^-$ and $[SrF]^+$ layers [38]. Between adjacent layers the bonding is of ionic nature. The Fermi sub-band is of importance for the conducting properties and formation of the superconducting states; its main contribution comes from the Fe 3*d* states. The structural similarity implies that a similar covalent (ionic)

character is also present within (between) the layers of SrMnAsF. DOS calculations performed for the isostructural BaMnPF predict a band gap at the Fermi level, which is consistent with the observed insulating behaviour of SrMnAsF [18].

The largest difference between the Fe and Mn compounds is certainly the magnetic properties. SrFeAsF is at the verge of a magnetic instability, as indicated by the very small magnetic moment. This instability is considered as an important prerequisite for the development of superconducting properties upon charge-carrier doping. On the contrary, the magnetic order in SrMnAsF is very robust (T_N = 365 K) and the strength of the magnetic moment reflects the localisation of the charge-carriers. This is also demonstrated by its very insulating behaviour.

3.4.3 Comparison of SrMn*Pn*F (*Pn* = P, As, Sb)

The effect of isoelectronic replacement in the $[AeF]^+$ and $[MnPn]^-$ layers on the structure and properties was investigated in the *Ae*Mn*Pn*F series for *Ae* = Sr, Ba and *Pn* = P, As, Sb.

a) Structure

The Mn-based pnictide materials studied in this work are tetragonal (space group $P4/nmm$) in the measured temperature range (T = 1.5 K – 420 K). The unit cell volume expands according to the increasing *Ae* (*Pn*) radius, from SrMnPF, SrMnAsF, BaMnPF, BaMnAsF to SrMnSbF and BaMnSbF. The alkaline earth metal and pnictide sit in similar crystallographic positions, above a square net of F and Mn, respectively. The size of *Pn* (*Ae*) modulates the coordination environment of the [MnPn_4] ([FAe_4]) tetrahedra, and, in addition, changes the geometry of the adjacent layer, which has to stretch in order to compensate the introduced lattice mismatch.

With larger pnictides the *Pn*-Mn-*Pn* angle in the Sr- and Ba-based compounds increases, i.e. the height of *Pn* above the Mn square net increases. The combined influence of *Ae* and *Pn* site gives the most regular tetrahedrons for the compositions SrMnPF and BaMnAsF, as can be appreciated from the angles displayed in Figure 3.24. The thickness of the [Mn*Pn*] and [*Ae*F] slabs increases along P → As → Sb and Sr → Ba, respectively, whereas the unsubstituted layer flattens to compensate the lattice mismatch (see Figure 3.24).

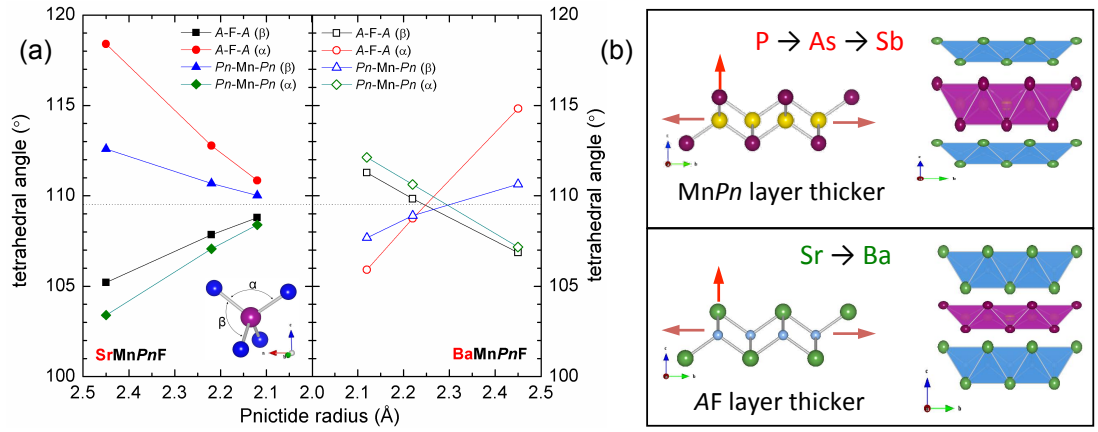

Figure 3.24: (a) The variation of the [MnPn_4] tetrahedral angles with *Pn* radius as obtained form Rietveld fits to RT diffraction data. The dashed line marks the ideal tetrahedral angle of 109.47°. (b) Isoelectronic replacement increases the thickness of the substituted layer, and forces the respective other layer to stretch and flatten.

The temperature dependence of the lattice does not show any discontinuities, and the percentual lattice contractions are very similar for all members of the series. No structural transitions were found in connection with the magnetic ordering, or at higher temperatures up to $T = 420$ K.

b) Magnetism

The magnetic structure or SrMn*Pn*F (*Pn* = P, As, Sb) was determined from variable temperature neutron powder diffraction. The materials show the same magnetic order: the spins align parallel to the *c*-axis and order AFM with the nearest-neighbour, along the [110] direction, and FM with the next-nearest neighbour and between adjacent layers, i.e. along the [100] and [001] directions, see Figure 3.23. The onset of the ordering lies well above RT, and decreases for P → As → Sb, with T_N = 365 K, 360 K and 320 K, respectively. The effective magnetic moment of Mn^{2+} at T = 1.5 K increases to μ_{eff} = 3.29(2) μ_B, 3.46(1) μ_B and 3.59(4) μ_B for P, As and Sb, respectively.

The experimentally determined μ_{eff} ~ 3.5 μ_B is smaller than the expected value for the free ion, $\mu_{eff}(Mn^{2+})$ = 5.9 μ_B (high spin configuration, $S = 5/2$; $g = 2$), but it is in good agreement with electronic band-structure calculations performed for BaMnPF ($\mu_{eff}(Mn^{2+})$ = 3.3 μ_B) [18]. The same work also predicts a splitting of the manganese *3d* bands by magnetic exchange, which results in a reduced spin ($S < 5/2$).

Pn	μ_{eff}/ μ_B	d(Mn-*Pn*)/ Å	d(Mn-Mn)/ Å	Mn-*Pn*-Mn (x4, x2)/ °	*Pn*-Mn-*Pn* (x4, x2)/ °
P	3.29(2)	2.476(4)	2.8702(1)	70.9(1), 110.1(2)	109.1(1), 110.1(2)
As	3.46(2)	2.567(2)	2.9163(1)	69.24(5), 106.9(1)	110.76(5), 106.9(1)
Sb	3.59(4)	2.748(3)	3.0477(1)	67.36(7), 103.3(1)	112.64(7), 103.3(1)

Table 3.9: Effective magnetic moment, interatomic distances and angles of SrMn*Pn*F (*Pn* = P, As, Sb) determined form Rietveld refinements of NPD patterns collected at T = 1.5 K.

Magnetic exchange interactions may occur via direct exchange due to overlap of Mn *3d*-orbitals or through the [MnPn_4] tetrahedron via a superexchange mechanism [38]. The intraplanar Mn-Mn distances, as well as the Mn-*Pn*-Mn angle therefore influence the strength of the magnetic moment and ordering temperature. Moving from P to Sb, the bonds elongate, and the distortion of the [MnPn_4] tetrahedra is greater (Table 3.9). This is reflected in the lower ordering temperature of SrMnSbF. In addition, the effective magnetic moment (at T = 1.5 K) increases, suggesting that the localisation of the Mn *3d* states is strengthened with heavier pnictides [11]. The diminished orbital overlap leads to a more ionic bonding picture in the [Mn*Pn*] layer.

One may expect that the onset of the magnetic ordering is connected with a change in the nuclear structure, similar to the iron pnictides where the magnetic ordering is connected to a phase transition. The alignment of the Mn spins parallel to the *c*-axis does not appear to be the driving force for an orthorhombic distortion, but might give rise to a contraction of the lattice. However, Rietveld analysis of SXRD and NPD data of SrMn*Pn*F (recorded between T = 1.5 K and 473 K) shows no evidence of such magneto-elastic coupling.

The structural information obtained from synchrotron diffraction measurements at temperatures up to T = 420 K did not reveal a sudden structural transition, but the lattice expands rather smoothly. The temperature dependence of the lattice constants show a small change in slope at circa T = 550 K (not shown), which is significantly higher than the expected temperature. Most likely it cannot be attributed to the onset of the magnetic ordering but rather to onset of sample decomposition.

Neutron diffraction experiments were not performed on the BaMn*Pn*F series, however we expect the magnetic order to be very similar to SrMn*Pn*F. This is also supported by reports on the *Re*Mn*Pn*O materials which exhibit the same G-type

antiferromagnetic arrangement above the ordering temperature of the rare earth metal [14], [15], [39].

c) Local Structure

The crystal structure of compounds is routinely determined by powder or single crystal diffraction methods. The obtained structure is a representation of the distance between the average positions of two atoms. Although this average structure provides a wealth of information, it is not always sufficient to describe the observed physical properties. For example in the iron-pnictide superconductors, the magnitude of the magnetic ordering is not well reproduced in calculations based on the average structure [40].

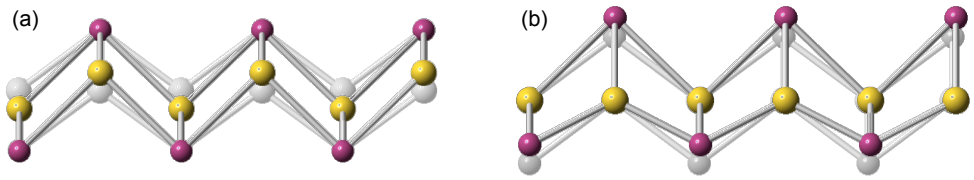

Figure 3.25: The structural models (a) 'zMn' and (b) 'zPn' used to fit the short range $G(r)$ (r = 1 – 5 Å). The displacement of Mn and *Pn* is restricted to the z-direction. Both models give a satisfactory fit to the experimental data, and likely a combined model is closest to describe the real local environment.

Total scattering methods on the other hand, determine the average distance between a pair of atoms. What seems to be a subtle distinction has important implications in systems with local disorder [41]. This sort of intermediate range disorder cannot be accessed by other methods, such as EXAFS, which is often limited to the first coordination shells. Hence, the additional structural information obtained from real-space fitting of the $G(r)$ can give valuable input for theoretical calculations and predictions and make local structure studies highly desirable.

The RT $G(r)$ of the *Ae*Mn*Pn*F series were analysed to evaluate the differences between local and long range structure. The average structure obtained from high-resolution SXRD gave a satisfactory fit to the experimental $G(r)$; however, some discrepancies were observed on the local scale (r = 1 – 5 Å). The analysis of differently disordered models revealed a distribution of *Pn* and Mn sites, which give a slight buckling of the [Mn*Pn*] layers. The local structure description involves a splitting of either Mn or *Pn* site into two sites with different z coordinate, which

give rise to two distinct sets of Mn-*Pn* bond distances. A sketch of the two structural models is shown in Figure 3.25. Following the indication given by the anisotropic thermal displacement parameters, the displacements were constrained to the z-direction. It is stressed that the models had to be simplified due to the limited fitting range, but it is likely that a combination of Mn and *Pn* displacement is present.

The observed distortion of the [Mn*Pn*] layer is also reported for related systems, such as the 1111-type SmFeAsO [42]. Its local structure could not be described with the average XRD structure (*P*4/*nmm* and *Cmma* at room and low temperature, respectively) but by displacement of both Fe and As along *x*, *y*, and *z*-direction, which gives a set of eight distinct Fe-As distances. Further displacement of the O site with respect to the XRD structure was observed for the doped $SmFeAsO_{1-x}F_x$.

Although total scattering investigations are still relatively scarce, careful analysis of conventional XRD can also hint towards local disorder. The joint Se/Te site as well as the Fe site in $FeSe_{1-x}Te_x$ was reported to be anisotropic (U_{33}/U_{11} ~3 and ~2, respectively) [43]. A splitting of the joint site was expected due to the different ionic radii of Se and Te, and resulted in an improved U_{33}/U_{11} ratio. The anisotropy on the Fe atom is explained as a response to the different coordination environment, however a model featuring a split Fe site was not reported.

These examples demonstrate that local disorder might be a general feature, not only of the iron-pnictide materials, but also of the isostructual *Ae*Mn*Pn*F family. The density of states at the Fermi level is strongly influenced by the tetrahedral angle in the iron-based materials. For given lattice constants, this angle is dependent on the position of the pnictide, which was refined in the local structure model presented herein. Isoelectronic substitution modulates the tetrahedrons local geometry may serve as a useful tool to tune this important structural parameter [44], [45].

d) Physical Properties

Examination of the electronic properties revealed insulating to semiconducting behaviour of the manganese pnictides. In general electrical conductivity increases with atomic number of the pnictide, although conversely, the phosphorus-containing compound shows the lowest resistivity in the BaMn*Pn*F series. The general trend can be explained with the increasing nearest-neighbour *d*(Mn-Mn) and *d*(Mn-*Pn*) distances, which reduce the covalent character. The ionic character enhances the localisation of electron, resulting in decreased charge carrier mobility.

In the related LaCu*Ch*O, an increase of conductivity (hole-mobility) from P to As to Sb is explained by a reduced hole effective mass for the heavier chalcogenide *Ch* and the formation of more disperse valence bands from the *Ch* orbitals [46]. The isostructural LaMn*Pn*O (*Pn* = P, As, Sb) are described as an indirect-transition type semiconductors and their electrical properties show a similar trend to *Ae*Mn*Pn*F [11].

The magnetic susceptibility increases along the series P → As → Sb, which is consistent with an increasing magnetic moment. The absence of a maximum in the measured temperature range suggests that the Néel temperature lies well above RT, which is in agreement with the neutron diffraction data collected for SrMn*Pn*F. The similarities in magnetic susceptibility between the Sr and Ba compounds suggest similar magnetic order in both compounds. Neutron diffraction experiments are required to confirm the spin arrangement and would also help to determine the overall dependence of magnetic moment and ordering temperature on the bond-distances and angles.

Between T = 1.5 K and 300 K, no anomalies were observed either in electrical resistivity or magnetic susceptibility measurements, reflecting that the materials are magnetically ordered well above RT and do not undergo further transitions on cooling. The susceptibility measurements are comparable to the 1111-type manganese oxide based materials, such as LaMnPO and PrMnSbO. The later undergoes a further magnetic transition at low temperatures, involving spin-reorientation on Mn induced by the ordering of the Pr moments [15], [46], [47].

The *Ae*Mn*Pn*F materials are insulators, and electrical conductivity is independent of an applied magnetic field (*Ae* = Sr; Ba not measured). On the other hand, the *Re*MnAsO (*Re* = Nd, Sm, Gd, La) compounds are semiconductors and PrMnSbO is a metal [14], [15], [39], [47]. The *Re*MnAsO (*Re* = La, Nd) materials were reported by Emery *et al.* to show magnetoresistance (MR) with MR_{max} of -24 % and -11 %, respectively [39]. But the MR properties were in disagreement with results of NdMnAsO by Marcinkova *et al.* [14]. In a follow-up investigation, Emery *et al.* established that the MR properties were linked to non-stoichiometry of Nd_xMnAsO: MR is < 2 % for $x \sim 1$ and increases as x decreases [48].

3.5 Summary

The SrFeAsF parent compound shows a $T \rightarrow O$ phase transition from $P4/nmm$ to $Cmma$ symmetry (T = 300 K: a_T = 4.00522(5) Å, c_T = 8.97781(2) Å; T = 20 K: a_O = 5.6316(1) Å, b_O = 5.6734(1) Å, c_O = 8.9403(1) Å). The structural transition coincides with the observation of a spin density wave at T = 180 K. Electrical resistivity and magnetic susceptibility measurements showed that the parent compound behaves as a poor metal. Low temperature neutron powder diffraction were employed to determine its magnetic structure. This can be described as stripped antiferromagnetic order of the Fe-spins with an effective magnetic moment μ_{eff} = 0.6(2) μ_B.

Upon electron doping, i.e. replacement of Sr^{2+} with the smaller La^{3+}, the lattice contracts as expected, and the temperature of the tetragonal to orthorhombic transition is lowered to T = 175 K and 170 K for 10 % and 20 % doping, respectively. At the same time, the spin density wave is suppressed and superconductivity emerges for 20% La-doped SrFeAsF, with T_c = 27 K.

The nuclear structure of the series *Ae*Mn*Pn*F (*Ae* = Sr, Ba; *Pn* = P, As, Sb) was confirmed to be tetragonal, in analogy with LaFeAsO (space group $P4/nmm$). With increasing radius of *Ae* and *Pn*, the unit cell expands and the tetrahedral coordination environment is progressively distorted. Further short-range distortions of the tetrahedral geometry are most pronounced in SrMnPF and BaMnAsF that have the most regular average structure. The spin-configuration in the Mn-compounds (half-filled pseudo closed shell, $3d^5$) is expected to be different from the Fe- and Ni- materials, which have even numbers of *3d*-electrons. Indeed, neutron powder diffraction measurements revealed antiferromagnetic arrangement of the Mn spins. The effective magnetic moment at T = 1.5 K increases with *Pn* radius (μ_{eff} = 3.29(2) μ_B, 3.46(1) μ_B and 3.59(4) μ_B, for *Pn* = P, As and Sb, respectively), whereas T_N decreases from T_N = 365 K, 360 K to 320 K.

3.6 References

[1] Y. Kamihara, T. Watanabe, M. Hirano, H. Hosono, *Journal of the American Chemical Society* 130 (2008) 3296.

[2] H. Luetkens, H.-H. Klauss, M. Kraken, F.J. Litterst, T. Dellmann, R. Klingeler, C. Hess, R. Khasanov, A. Amato, C. Baines, M. Kosmala, O.J. Schumann, M. Braden, J. Hamann-Borrero, N. Leps, A. Kondrat, G. Behr, J. Werner, B. Buechner, *Nature Materials* 8 (2009) 305.

[3] K. Kasperkiewicz, J.-W.G. Bos, A.N. Fitch, K. Prassides, S. Margadonna, *Chemical Communications* (2009) 707.

[4] C. Wang, L. Li, S. Chi, Z. Zhu, Z. Ren, Y. Li, Y. Wang, X. Lin, Y. Luo, S. Jiang, X. Xu, G. Cao, Z.A. Xu, *EPL (Europhysics Letters)* 83 (2008) 67006.

[5] Y.K. Li, X. Lin, T. Zhou, J.Q. Shen, Q. Tao, G.H. Cao, Z.A. Xu, *Journal of Physics: Condensed Matter* 21 (2009) 355702.

[6] T. Watanabe, H. Yanagi, Y. Kamihara, T. Kamiya, M. Hirano, H. Hosono, *Journal of Solid State Chemistry* 181 (2008) 2117.

[7] C. Wang, S. Jiang, Q. Tao, Z. Ren, Y. Li, L. Li, C. Feng, J. Dai, G. Cao, Z.-A. Xu, *EPL (Europhysics Letters)* 86 (2009) 47002.

[8] Y. Kamihara, H. Hiramatsu, M. Hirano, R. Kawamura, H. Yanagi, T. Kamiya, H. Hosono, *Journal of the American Chemical Society* 128 (2006) 10012.

[9] T. Watanabe, H. Yanagi, T. Kamiya, Y. Kamihara, H. Hiramatsu, M. Hirano, H. Hosono, *Inorganic Chemistry* 46 (2007) 7719.

[10] R. Pöttgen, D. Johrendt, *Zeitschrift für Naturforschung, B: A Journal of Chemical Sciences* 63 (2008) 1135.

[11] K. Kayanuma, H. Hiramatsu, T. Kamiya, M. Hirano, H. Hosono, *Journal of Applied Physics* 105 (2009) 073903.

[12] H. Yanagi, T. Watanabe, K. Kodama, S. Iikubo, S. Shamoto, T. Kamiya, M. Hirano, H. Hosono, *Journal of Applied Physics* 105 (2009) 093916.

[13] H. Yanagi, R. Kawamura, T. Kamiya, Y. Kamihara, M. Hirano, T. Nakamura, H. Osawa, H. Hosono, *Physical Review B: Condensed Matter and Materials* 77 (2008) 224431.

[14] A. Marcinkova, T. Hansen, C. Curfs, S. Margadonna, J. Bos, *Physical Review B: Condensed Matter and Materials Physics* 82 (2010) 174438.

[15] S. Kimber, A. Hill, Y.-Z. Zhang, H. Jeschke, R. Valentí, C. Ritter, I. Schellenberg, W. Hermes, R. Pöttgen, D. Argyriou, *Physical Review B: Condensed Matter and Materials Physics* 82 (2010) 100412.

[16] G. Wu, Y.L. Xie, H. Chen, M. Zhong, R.H. Liu, B.C. Shi, Q.J. Li, X.F. Wang, T. Wu, Y.J. Yan, J.J. Ying, X.H. Chen, J*ournal of Physics: Condensed Matter* 21 (2009) 142203.

[17] S. Matsuishi, Y. Inoue, T. Nomura, H. Yanagi, M. Hirano, H. Hosono, *Journal of the American Chemical Society* 130 (2008) 14428.

[18] H. Kabbour, L. Cario, F. Boucher, *Journal of Materials Chemistry* 15 (2005) 3525.

[19] M. Tegel, S. Welzmiller, D. Johrendt, *Zeitschrift für Anorganische und Allgemeine Chemie* 634 (2008) 2085.

[20] A.P. Hammersley, S. Svensson, M. Handland, A.N. Fitch, D. Haeusermann, *High Pressure Research* 14 (1996) 235.

[21] X. Qiu, J.W. Thompson, S.J.L. Billinge, *Journal of Applied Crystallography* 37 (2004) 678.

[22] C.L. Farrow, S.J.L. Billinge, *Acta Crystallographica, Section A: Foundations of Crystallography* 65 (2009) 232.

[23] C. Farrow, P. Juhas, J. Liu, D. Bryndin, E. Božin, J. Bloch, T. Proffen, S. Billinge, *Journal of Physics: Condensed Matter* 19 (2007) 335219.

[24] B. Toby, *Journal of Applied Crystallography* 34 (2001) 210.

[25] A.C. Larson, R.B.V. Dreele, Los Alamos National Laboratory Report LAUR 86-748 (2004) 1.

[26] R.D. Shannon, *Acta Crystallographica Section A: Foundations of Crystallography* 32 (1976) 751.

[27] S. Brock, N. Raju, J. Greedan, S. Kauzlarich, *Journal of Alloys and Compounds* 237 (1996) 9.

[28] Y. Xiao, Y. Su, R. Mittal, T. Chatterji, T. Hansen, S. Price, C.M.N. Kumar, J. Persson, S. Matsuishi, Y. Inoue, H. Hosono, T. Brueckel, *Physical Review B: Condensed Matter and Materials Physics* 81 (2010) 094523.

[29] U. Wahl, J.G. Correia, T. Mendonca, S. Decoster, *Applied Physics Letters* 94 (2009) 261901.

[30] O. Greis, T. Petzel, *Zeitschrift für Anorganische und Allgemeine Chemie* 403 (1974) 1.

[31] W.P. Davey, *Physical Review* 19 (1922) 248.

[32] C. Krellner, N. Caroca-Canales, A. Jesche, H. Rosner, A. Ormeci, C. Geibel, *Physical Review B: Condensed Matter and Materials Physics* 78 (2008) 100504.

[33] M. Tegel, M. Rotter, V. Weiss, F.M. Schappacher, R. Poettgen, D. Johrendt, *Journal of Physics: Condensed Matter* 20 (2008) 452201.

[34] Y. Muraba, S. Matsuishi, S.-W. Kim, T. Atou, O. Fukunaga, H. Hosono, *Physical Review B: Condensed Matter and Materials Physics* 82 (2010) 180512.

[35] I.I. Mazin, D.J. Singh, M.D. Johannes, M.H. Du, *Physical Review Letters* 101 (2008) 057003.

[36] X. Zhu, F. Han, P. Cheng, G. Mu, B. Shen, L. Fang, H.-H. Wen, *EPL (Europhysics Letters)* 85 (2009) 17011.

[37] Y. Xiao, Y. Su, R. Mittal, T. Chatterji, T. Hansen, *Physical Review B: Condensed Matter and Materials Physics* 79 (2009) 060504(R).

[38] I.R. Shein, A.L. Ivanovskii, *JETP Letters* 88 (2008) 683.

[39] N. Emery, E.J. Wildman, J.M.S. Skakle, G. Giriat, R.I. Smith, A.C. Mclaughlin, *Chemical Communications* 46 (2010) 6777.

[40] T.-M. Chuang, M.P. Allan, J. Lee, Y. Xie, N. Ni, S.L. Bud'ko, G.S. Boebinger, P.C. Canfield, J.C. Davis, *Science* 327 (2010) 181.

[41] C.A. Young, A.L. Goodwin, *Journal of Materials Chemistry* 21 (2011) 6464.

[42] L. Malavasi, G.A. Artioli, H. Kim, B. Maroni, B. Jospeh, Y. Ren, T. Proffen, S.J.L. Billinge, Journal of Physics: Condensed Matter 23 (2011) 272201.

[43] M. Tegel, C. Löhnert, D. Johrendt, Solid State Communications 150 (2010) 383.

[44] M.J. Calderón, B. Valenzuela, E. Bascones, New Journal of Physics 11 (2009) 013051.

[45] M.J. Calderón, B. Valenzuela, E. Bascones, Physical Review B: Condensed Matter and Materials Physics 80 (2009) 094531.

[46] S.-I. Inoue, K. Ueda, H. Hosono, N. Hamada, Physical Review B: Condensed Matter and Materials Physics 64 (2001) 245211.

[47] H. Yanagi, K. Fukuma, T. Kamiya, M. Hirano, H. Hosono, Materials Science & Engineering, B: Advanced Functional Solid-State Materials 173 (2010) 47.

[48] N. Emery, E.J. Wildman, J.M.S. Skakle, A.C. Mclaughlin, R.I. Smith, A.N. Fitch, Physical Review B: Condensed Matter and Materials Physics 83 (2011) 144429.

Chapter 4

The Structural and Magnetic Phase Diagram of $KMnCrF_6$

4.1 Introduction

Transition metal fluorides adopting the tetragonal tungsten bronze (TTB) structure with general formula $K_{1-x}M^{2+}_{1-x}M^{3+}_{x}F_6$ (M = transition metal) have been studied in the past as potential multiferroic materials. For instance, it has been demonstrated experimentally that members of the series $K_{1.2-x}Fe^{2+}_{1.2-x}Fe^{3+}_{0.8+x}F_6$ are multiferroic at low temperatures and that the exact interplay between the different ordering parameters (ferroelectric, ferroelastic and magnetic) is finely tuned by subtle changes in compositions [1], [2], [3]. Also the related TTB fluoride $KMnFeF_6$ has been suggested as a potential multiferroic material, but experimental confirmation of its ferroelectric properties is still pending [4]. The analogous compound $KMnCrF_6$ was initially synthesized in 1971, and reported to crystallize in the conventional TTB structure (space group $P4/mbm$, $c = c_{TTB}$) [5]. A decade later, Banks *et al.* investigated the structural and magnetic properties of the series $K_{1-x}Mn_{1-x}Cr_{1+x}F_6$ (x = 0.43 – 0.58). They suggested that the correct space group symmetry for all the members of the series should be $P4_2bc$ ($c = 2c_{TTB}$) [6]. The c-axis doubling of $KMnCrF_6$ arises from partial Mn^{2+}/ Cr^{3+} order: there are two distinct 8c (perovskite-type) sites that are occupied by either Mn^{2+} or Cr^{3+}, such that the divalent and trivalent cation alternate around the perovskite cage (square channel) and along the c-axis. On the other hand, the single 4b (extra-perovskite-type) site is occupied statistically by both ions.

However, Banks *et al.* did not observe superlattice peaks corresponding to the c-axis doubling in the powder XRD data [6]. They based their space group assignment on the measured magnetic properties that showed similar behaviour to $KMnFeF_6$, which was known to adopt the $P4_2bc$ symmetry with $c = 2c_{TTB}$ [6], [7]. In addition to the space group suggestion, Banks *et al.* proposed an overall ferromagnetic structure for $K_{1-x}Mn_{1-x}Cr_{1+x}F_6$ with $x = 0$ (i.e. $KMnCrF_6$), which was obtained by satisfying the maximum number of M-F-M' magnetic interactions present in the unit cell [6]. Their model implied that $KMnCrF_6$ is fully ordered, that means that Mn^{2+} and Cr^{3+} order not only on the perovskite site, but also on the extra-perovskite site [6] and it was thus chosen as a representative of the series.

To evaluate the potential of $KMnCrF_6$ as a ferroelectric and/or multiferroic compound, knowledge of its crystal structure (including e.g. atomic coordinates) is mandatory in order to test if the structural criteria for the occurrence of ferroelectricity are satisfied and to elucidate the nature of the possible ordering mechanism. Such detailed studies require the use of variable temperature high-

resolution diffraction data with excellent counting statistics, especially because superlattice peaks that could arise by the doubling of the tetragonal *c*-axis are expected to be very weak and to have only a fraction of the intensity of the main Bragg reflections. In addition, the criteria that are used to predict potential ferroelectrics are based on the atomic coordinates. Uncertainties in these structural parameters could, for example, lead to a wrong estimation of the ferroelectric – paraelectric transition temperature. The availability of variable temperature measurements is also of fundamental importance to identify possible structural phase transitions linked to the onset of the different ordering phenomena (ferroelectric and magnetic). The structural analysis needs to be complemented by detailed magnetic measurements for a full description of $KMnCrF_6$ as a multiferroic material.

The detailed structural analysis of $KMnCrF_6$ discussed in this chapter addresses a number of open questions. Firstly, whether superlattice reflections present in the diffraction data confirm the doubling of the unit cell *c*-axis and hence an ordering of the Mn^{2+} and Cr^{3+} ions around the perovskite cage. Secondly, whether the magnitude of the atomic displacements in the proposed acentric structure (space group $P4_2bc$) are sufficiently different from the centric higher-symmetry structure (space group $P4_2/mbc$), to justify the assignment of a polar space group. Lastly, whether there is also a centrosymmetric (higher temperature) structural variant and at what temperature the polar-apolar structural phase transition occurs.

4.2 Methods

4.2.1 Synthesis

Polycrystalline samples of $KMnCrF_6$ of light green colour were obtained via solid-state synthesis from a stoichiometric mixture of KF, MnF_2 and CrF_3. The starting materials were pre-dried at 393 K for 12 hours under vacuum. The dry powders were ground and mixed repetitively in an agate mortar to maximize homogenization of the educts. The reactants were pelletized using a 7 mm die set and a manually operated KBr-pellet press. The pelletised reactants were contained in well-clamped gold tubes. The gold tubes were either sealed in a quartz tube under reduced argon pressure (sample I) or kept under nitrogen flow (sample II) for the duration of the heat treatment. All sample manipulations were performed inside a glove box under inert argon atmosphere to prevent the starting materials from degrading. Sample I (mass = 0.145 g) was heated at a rate of 100 K h^{-1} to 1023 K and kept at this temperature for 72 hours, before cooling at a rate of 100 K h^{-1} to room temperature. Sample II (mass = 2.0 g) was heated to 1023 K at a rate of 120 K h^{-1}, annealed for 72 hours, and then allowed to cool naturally.

4.2.2 Synchrotron Powder Diffraction

High-resolution synchrotron X-ray diffraction experiments were performed on beamlines ID31 and ID11 at the ESRF, France. The samples were sealed in 0.5 mm diameter thin-wall glass capillaries, which were spinning on the diffractometer axis during data collection to minimize preferred orientation effects. Diffraction profiles of sample I were recorded at various temperatures between T = 5 K – 823 K on beamline ID31 (λ = 0.39992 Å). The data were binned in the 2θ range 0.1° – 48° to a step of 0.002°. Diffraction profiles of sample II were collected on ID11 (λ = 0.42 Å) between T = 300 K – 1150 K. The data were collected on a Frelon2k camera and integrated with Fit2D in the 2θ range 1.8° – 26.2° with an increment of 0.014°.

X-ray powder diffraction data for pair distribution function analysis were collected at beamline 11-ID-C, at APS, USA (λ = 0.107841 Å). Data were collected using an amorphous Si large panel detector. The finely ground powder sample was loaded into a 5 mm diameter glass capillary. To avoid saturation of the detector and to improve counting statistics, the measurement was carried out in ten exposures with

an exposure time of 5 seconds each. Data were collected also from an empty container and used to correct for scattering arising from the container. The 2D data sets were combined and integrated using the program FIT2D [8]. Form these, the total scattering function $S(Q)$ was obtained using standard corrections with the program PDFgetX2 [9]. The final $G(r)$ was obtained by Fourier transformation of $S(Q)$, with $Q_{max} = 27$ Å^{-1}.

High-pressure synchrotron X-ray diffraction experiments were performed on beamline BL10XU, at SPring-8, Japan ($\lambda = 0.41429$ Å). The powder (sample I) together with a small ruby chip was loaded in a diamond anvil cell (DAC). Helium was used as a hydrostatic pressure transmitting medium. The applied pressure was measured immediately before and after exposure by the ruby fluorescence method without dismounting the cell. The calibration method suggested by Mao was used to determine the pressure from the shift of the maxima in fluorescence [10]. Diffraction patterns were collected at room temperature between 0.2 and 17.75 GPa. Data was recorded using a flat image plate detector and integrated with an increment of 0.005° using the program WinPIP [11].

Analysis of powder diffraction data was carried out with the GSAS suite of Rietveld programs [12], [13]. The program PDFgui was employed to model the total scattering data [14].

4.2.3 Physical Properties Measurements

DC magnetization measurements of sample I were measured on a Quantum Design MPMS magnetometer. The temperature dependence of magnetization was determined following zero-field cooled and field-cooled (ZFC, FC) protocols in magnetic fields $H = 100$, 1000, 10000 Oe. Magnetic hysteresis loops up to $H = 10000$ Oe were collected at $T = 5$ K.

4.2.4 Elemental Analysis

The weight fractions of K, Mn and Cr of sample I as determined by inductive coupled plasma (ICP) elemental analysis from a solution of $KMnCrF_6$ in diluted $HCl_{(aq)}$. The F content was determined from the difference between the sample mass used to make up the solution, and the mass fractions determined experimentally. The theoretical weight fractions are K: 15.0 %, Mn: 21.1 %, Cr: 20.0 %, F: 43.8 %. The determined weight fractions are as follows, K: 13.7(2) %, Mn: 19.5(2) %,

Cr: 20.7(2) %, F: 46(1) %. From this, the experimental formula was calculated by setting Mn + Cr = 2, and found to be $K_{0.93}Mn_{0.94}Cr_{1.06}F_{6.4}$. Incorporation of nitrogen in sample II was ruled out by CHNS elemental analysis.

4.3 Results

4.3.1 The High-Temperature Structure

As mentioned before, Banks *et al*. proposed that $KMnCrF_6$ crystallises in the tetragonal space group $P4_2bc$ with the *c*-axis doubled as compared to the conventional TTB cell [3]. This structural model implies an ionic order pattern where Mn^{2+} and Cr^{3+} are alternating around the perovskite cage while the extra-perovskite site is statistically occupied by the two species. The doubling of the *c*-axis should be readily observable in a high-resolution powder diffraction pattern by the presence of super-lattice reflections *(hkl)* ($l = 1$, $c = 2c_{TTB}$) in the low 2θ region. Indeed, the (201) and (211) reflections are present in the temperature range $T = 5$ K to 823 K (for sample I), see for example the diffraction pattern collected at $T = 373$ K see inset of Figure 4.1. The diffraction profiles collected at high temperatures ($T \geq 373$ K) can be indexed in the tetragonal space groups $P4_2bc$ or $P4_2/mbc$. Rietveld refinements were carried out in both settings, which differ only in the presence of an inversion centre. In both cases, the lattice constants at $T = 373$ K were found to be $a_{TTB} \approx a = 12.67146(1)$ Å and $2 \cdot c_{TTB} \approx c = 7.96514(1)$ Å.

After the size of the unit cell was established, Rietveld refinements were initiated to fully describe the structure. Soft constraints were applied to the transition metal fluorine bonds (Mn-F and Cr-F; $d = 2.0 \pm 0.3$ Å) and removed at later stages of the refinement process. Occupancies of Mn and Cr on the perovskite-type sites (8*c* and 8*h*, for $P4_2bc$ and $P4_2/mbc$, respectively) refined to *Occ.* = 1 within error, and were fixed to unity in the final refinement cycles. The occupancy of the mixed extra-perovskite type site (4*b* and 4*c*, respectively) was constraint to total one (*Occ.*(Mn) + *Occ.*(Cr) = 1). In agreement with the elemental analysis, the occupancies refined to *Occ.*(Mn) = 0.44(3) and *Occ.*(Cr) = 0.56(3) in both space group settings. However, the improvement in reliability factor was marginal (decrease in χ^2 by 0.01, F^2 unchanged) and the Mn/ Cr ratio was kept at 1:1 in subsequent refinement cycles. The pentagonal site hosting K (8*c* and 8*g* for $P4_2bc$ and $P4_2/mbc$, respectively) is fully occupied, whereas the square channels (4*a* and 4*b*, respectively) are only partially filled by K, *Occ.*(K2) = 0.587(3). The correlation between U_{iso}(K2) and *Occ.*(K2) is 0.62 %.The refined occupancies give an overall stoichiometry of $K_{1.035(1)}MnCrF_6$ that is in good agreement with the elemental analysis.

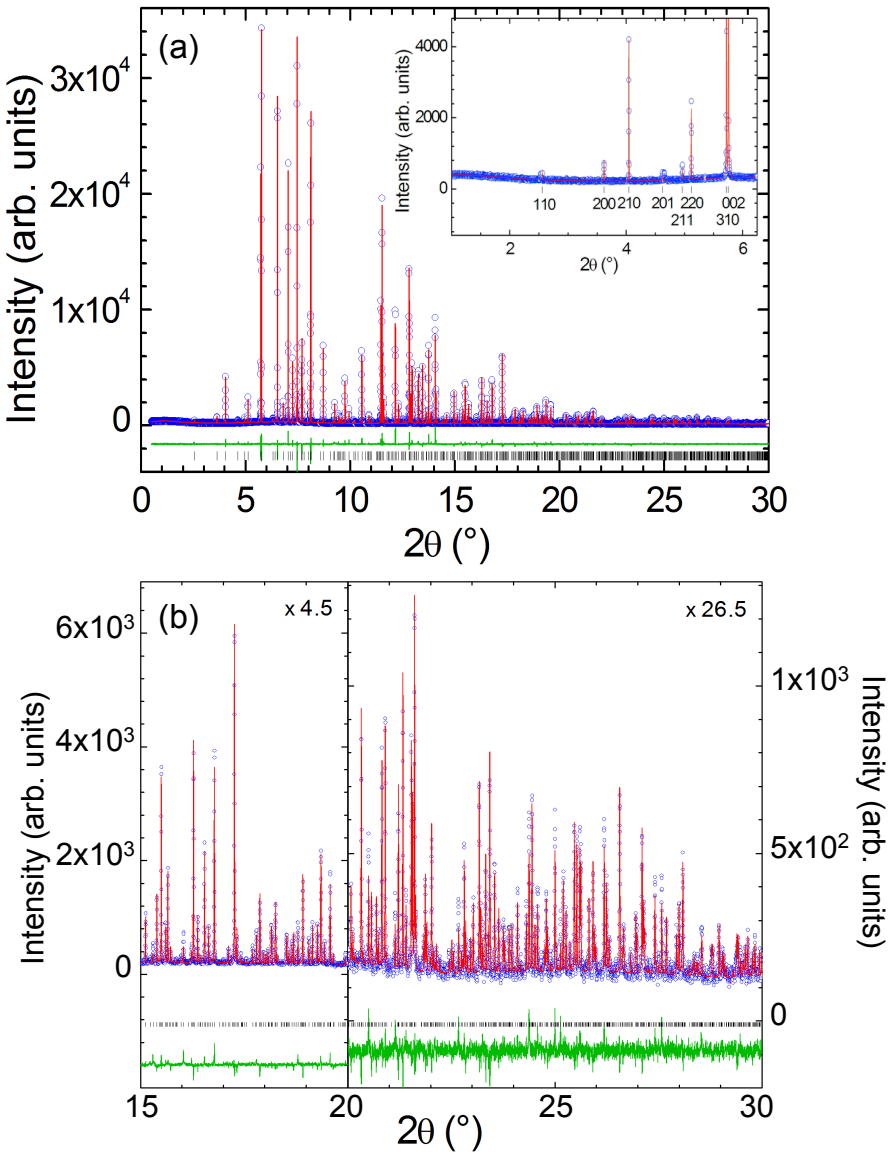

Figure 4.1: (a) Observed (open blue circles), calculated (red line) and difference (green line) synchrotron powder diffraction Rietveld profile of $KMnCrF_6$ at $T = 373$ K (space group $P4_2/mbc$), collected at ID31, $\lambda = 0.39992$ Å. Black tickmarks are reflection markers. (inset) The low 2θ region of the powder pattern highlights the superlattice reflections (201) and (211) that indicate a doubling of the c-axis with respect to the conventional TTB cell (b) Magnification of the high 2θ region.

It is expected that the difference in the refinements using the two different space groups $P4_2bc$ or $P4_2/mbc$ would be rather small. Space group $P4_2bc$ is the subgroup of $P4_2/mbc$ that is obtained when an inversion centre is added to the symmetry elements of $P4_2/mbc$. However, it is not trivial to differentiate between two closely related space groups from powder diffraction data. A possible way to distinguish between centric and acentric variant, could be to calculate the atomic displacements

in the lower symmetry space group (here $P4_2bc$) with respect to its supergroup (here $P4_2/mbc$). It was already outlined in chapter 2, that small atomic displacements away from the higher symmetry positions, i.e. $d(z) < 0.1$ Å, indicates doubtful space group assignment and that the higher symmetry structure should be considered to be more likely [15], [16].

In the case of the high temperature phase of $KMnCrF_6$, the fitting statistics improve only marginally by changing from the apolar $P4_2/mbc$ structure ($\chi^2 = 2.194$; $F^2 = 8.37\,\%$; $wR_p = 8.31\,\%$; $R_p = 6.36\,\%$) to the polar $P4_2bc$ symmetry ($\chi^2 = 2.008$; $F^2 = 7.39\,\%$; $wR_p = 7.94\,\%$; $R_p = 6.02\,\%$), whilst increasing the number of refinable positional parameters from 19 to 33. The atomic displacements $d(z)$ along the polar c-axis are obtained by comparing the atomic positions in space groups $P4_2bc$ and $P4_2/mbc$. The atomic displacements of K, Mn and Cr they are found to be smaller than $d(z) < 0.1$ Å (see Table 4.1). Slightly larger displacements were calculated for F8 and F15, $d(z) < 0.19$ Å, but given the large thermal displacement factors and the small scattering cross section of fluorine (form factors are f′ = 0.003 and f′′ = 0.003 for $\lambda = 0.4$ Å), the structure is most likely acentric $P4_2/mbc$.

	Wyckoff site					
	$P4_2bc$	$P4_2/mbc$	$z(P4_2bc)$	$z(P4_2/mbc)$	$d(z)$	$d(z)\cdot c$/ Å
Mn1	4*b*	4*c*	0.0122	0	0.0122	0.0972
Cr1	4*b*	4*c*	0.0121	0	0.0121	0.0964
Mn2	8*c*	8*h*	0.5092	0.5	0.0092	0.0733
Cr2	8*c*	8*h*	0.0085	0	0.0085	0.0677
K1	8*c*	8*g*	0.759	0.75	0.0090	0.0717
K2	4*a*	4*b*	0.747	0.75	-0.0030	-0.0239
F1	8*c*	8*h*	-0.015	0	-0.0150	-0.1195
F2	8*c*	8*h*	0.496	0.5	-0.0040	-0.0319
F3	8*c*	8*h*	-0.001	0	-0.0010	-0.0080
F4	8*c*	8*h*	-0.012	0	-0.0120	-0.0956
F5	8*c*	8*h*	0.503	0.5	0.0030	0.0239
F6	4*b*	4*d*	0.741	0.75	-0.0090	-0.0717
F7	8*c*	16*i*	0.747	0.7451	0.0019	0.0151
F8	8*c*		0.263	0.2451	0.0179	0.1426

Table 4.1: The atomic positions as determined from Rietveld refinements in space groups $P4_2bc$ and $P4_2/mbc$ at $T = 373$ K. The displacements along the polar c-axis, $d(z)$, are calculated by comparing the atomic positions of $P4_2bc$ and $P4_2/mbc$. The absolute displacements in Å are smaller than $d(z) < 0.1$ Å, suggesting the centrosymmetric space group choice $P4_2/mbc$.

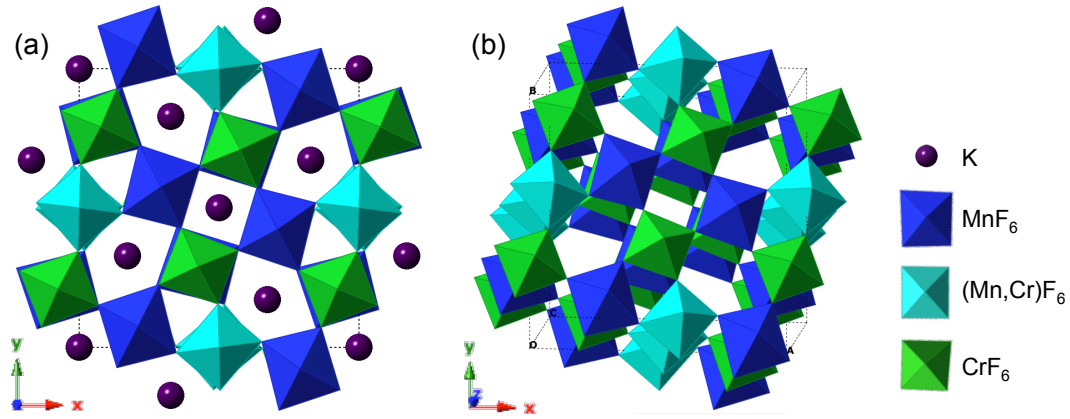

Figure 4.2: The $P4_2/mbc$ cell adopted by $KMnCrF_6$ at high temperatures ($T > 373$ K). (a) View down the *c*-axis. (b) Tilted view, highlighting the alternating order of MnF_6 (blue) and CrF_6 (green) octahedra on the perovskite site. Mn and Cr occupy the extra-perovskite site (turquoise) statistically. The K^+ ions (purple) were omitted for clarity in (b).

space group: $P4_2/mbc$		No. 135		$T = 373$ K		
$a = 12.67146(1)$ Å		$c = 7.96514(1)$ Å		$V = 1278.929(2)$ Å^3		
		x	*y*	*z*	B_{iso}/ Å^2	*Occ.*
Mn1	4*c*	0	0.5	0	0.69(2)	0.5
Cr1	4*c*	0	0.5	0	0.69(2)	0.5
Mn2	8*h*	0.0738(2)	0.7866(2)	0	0.58(4)	1
Cr2	8*h*	0.4251(2)	0.2894(2)	0.5	0.63(4)	1
K1	8*g*	0.8281(1)	0.6720(1)	0.75	2.99(3)	1
K2	4*b*	0	0	0.75	0.93(7)	0.587(3)
F1	8*h*	0.5668(5)	0.3482(4)	0	2.52(3)	1
F2	8*h*	0.9273(5)	0.8648(4)	0.5	2.52(3)	1
F3	8*h*	0.7853(4)	0.2742(4)	0	2.52(3)	1
F4	8*h*	0.4953(4)	0.1556(5)	0	2.52(3)	1
F5	8*h*	0.9804(4)	0.6535(6)	0.5	2.52(3)	1
F6	4*d*	0	0.5	0.75	2.52(3)	1
F7	16*i*	0.2095(2)	0.0764(2)	0.7451(6)	2.52(3)	1
$\chi^2 = 2.194$		$F^2 = 8.37$ %		$wR_p = 8.31$%		$R_p = 6.36$ %

Table 4.2: Results of Rietveld refinement of high-temperature SXRD diffraction profile of $KMnCrF_6$, collected at ID31, $T = 373$ K. There were 28 refined structural parameters. (Data collection time ~23 minutes.)

Results of the final refinement in the centric space group $P4_2/mbc$ are summarised in Table 4.2 and the fit is plotted in Figure 4.1. The structure is shown in Figure 4.2. The transition-metal – fluorine bond distances *M*-F obtained from the structural solution are listed in Table 4.3. The average *M*-F distances are found to be in good agreement with the proposed Mn^{2+}/ Cr^{3+} order on the two perovskite-type (8*h*) sites: $d_{Mn\text{-}F} = 2.090(6)$ Å and $d_{Cr\text{-}F} = 1.924(6)$ Å. The intermediate *M*-F distance on the extra-

perovskite type (4*c*) site, $d_{M\text{-}F}$ = 1.975(7) Å, confirms mixed site occupancy by Mn^{2+} and Cr^{3+}.

Mn1/Cr1-F	*d*/ Å	Mn2-F	*d*/ Å	Cr2-F	*d*/ Å
Mn1/Cr1-F4	1.972(7)	Mn2-F1	2.105(6)	Cr2-F1	1.944(7)
Mn1/Cr1-F4	1.972(7)	Mn2-F2	2.104(7)	Cr2-F2	1.907(6)
Mn1/Cr1-F5	1.961(7)	Mn2-F3	2.132(7)	Cr2-F3	1.946(6)
Mn1/Cr1-F5	1.961(7)	Mn2-F5	2.059(6)	Cr2-F4	1.915(7)
Mn1/Cr1-F6	1.991(1)	Mn2-F7	2.069(4)	Cr2-F7	1.915(4)
Mn1/Cr1-F6	1.991(1)	Mn2-F7	2.069(4)	Cr2-F7	1.915(4)
average	1.975(7)	average	2.090(6)	average	1.924(6)

Table 4.3: Bond-distances of Mn-F and Cr-F obtained from Rietveld refinement in space group $P4_2/mbc$, at T = 373 K. The average bond lengths are in good agreement with Mn^{2+} and Cr^{3+} occuping one of the two 8*h* sites each (Mn2, Cr2) and suggest that both cations occupy the 4*c* site (Mn1/ Cr1) statistically.

4.3.2 The Ambient and Low Temperature Structure

The diffraction profile obtained at room temperature shows several reflections that, compared to the data collected at T = 373 K, broaden or split at higher 2θ, including the (*hh0*) reflection (see Figure 4.4.a). This type of splitting is related to a monoclinic distortion of the unit cell, and cannot be described simply by a divergence of the *a*- and *b*- unit cell parameter (i.e. primitive orthorhombic cell). Instead of using the monoclinic setting, such a distortion can be conventionally described with an orthorhombic supercell. The conversion is illustrated in Figure 4.3.b. This conversion automatically leads to a change in centering from $P \rightarrow C$ and a doubling of the unit cell volume. The unit cell parameters of the orthorhombic supercell, a_0 and b_0, lie along the *ab* face diagonal of the original tetragonal TTB cell and are connected to them through the relationship: $a_0 \approx a_{TTB} \cdot \sqrt{2}$, $b_0 \approx a_{TTB} \cdot \sqrt{2}$.

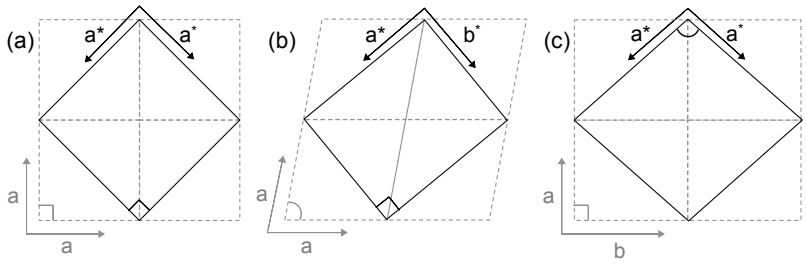

Figure 4.3: Relationships between different cells (grey) and supercells (black). (a) Tetragonal cell with tetragonal supercell. (b) Monoclinic cell with orthorhombic supercell, illustrating the conversion from $P4_2/mbc$ to *Cccm*. (c) Orthorhombic cell with monoclinic supercell.

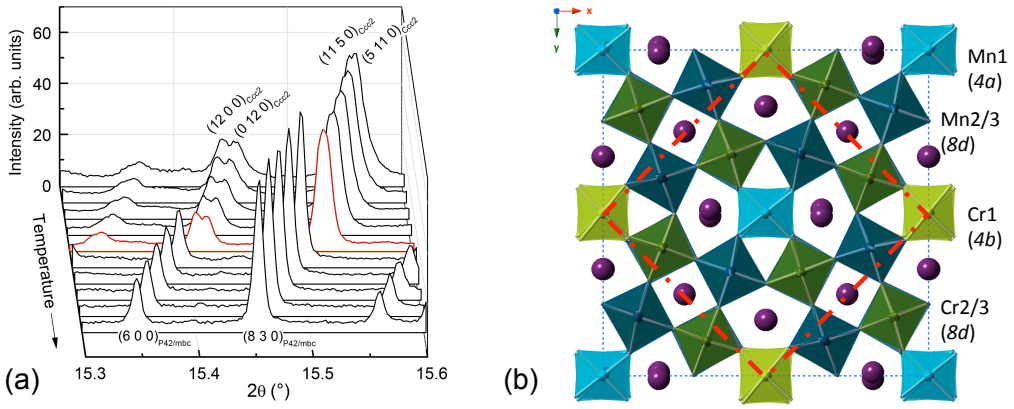

Figure 4.4: (left) Diffraction profiles at variable temperature shows the splitting of the (660) reflection (indexed in $P4_2/mbc$) at $T \leq 300$ K (red line). The splitting can be indexed as (12 0 0) and (0 12 0) in the orthorhombic space group *Ccc*2. (right) The *Ccc*2 unit cell seen along the *c*-axis. The $P4_2/mbc$ cell is outlined with by the dashed red line.

The only suitable subgroup of $P4_2/mbc$ to describe this distortion is *Cccm*, illustrated in Figure 4.4. In addition to the *Cccm* symmetry, also subgroups of $P4_2bc$ (see also Figure 4.15) were considered in the space group assignment of the room temperature phase, because the structure of $KMnCrF_6$ was previously reported to be acentric. Of the subgroups of $P4_2bc$, only space group *Ccc*2 is suitable to describe the observed peaksplitting. *Ccc*2 is a common subgroup of $P4_2bc$ and *Cccm*. Therefore, Rietveld refinements were initiated using structural models with *Cccm* and *Ccc*2 symmetry. The lattice constants refined to $a_{Cccm} = 17.90000(3)$ Å, $b_{Cccm} = 17.88807(3)$ Å, $c_{Cccm} = 7.93838(1)$ Å and $a_{Ccc2} = 17.90002(3)$ Å, $b_{Ccc2} = 17.88804(3)$ Å, $c_{Ccc2} = 7.93839(1)$ Å. The Refinement in space group *Ccc*2 is shown in Figure 4.5.

In the course of the refinements, soft constraints were initially applied to the transition metal fluoride bonds (Mn-F and Cr-F; $d = 2.0 \pm 0.3$ Å) but removed at later stages in both models. In analogy with the results obtained at high temperature, occupancies were fixed to unity except for the potassium residing in the pentagonal channels, which refined to *Occ.*(K3, 8*k*) = 58.3(4) % in *Cccm*, and to *Occ.*(K3, 4*c*) = 52.3(7) % and *Occ.*(K4, 4*c*) = 64.4(7) % in *Ccc*2. The correlation between *Occ.*(K3) and *Occ.*(K4) is 0.5 % for the *Ccc*2 refinement. The refined compositions are $K_{1.033(2)}MnCrF_6$ and $K_{1.033(3)}MnCrF_6$ for *Cccm* and *Ccc*2, respectively, which is in agreement with the results of the high temperature refinement and of the elemental analysis. The number of positional parameters approximately increases from 37 in *Cccm* to 66 in *Ccc*2 symmetry. The fitting statistics improved from the

centrosymmetric *Cccm* structure (χ^2 = 10.27; F^2 = 9.28 %; wR_p = 9.43 %; R_p = 6.65 %) to the polar *Ccc*2 symmetry (χ^2 = 8.679; F^2 = 7.2 %; wR_p = 8.67 %; R_p = 5.98 %) [‡‡].

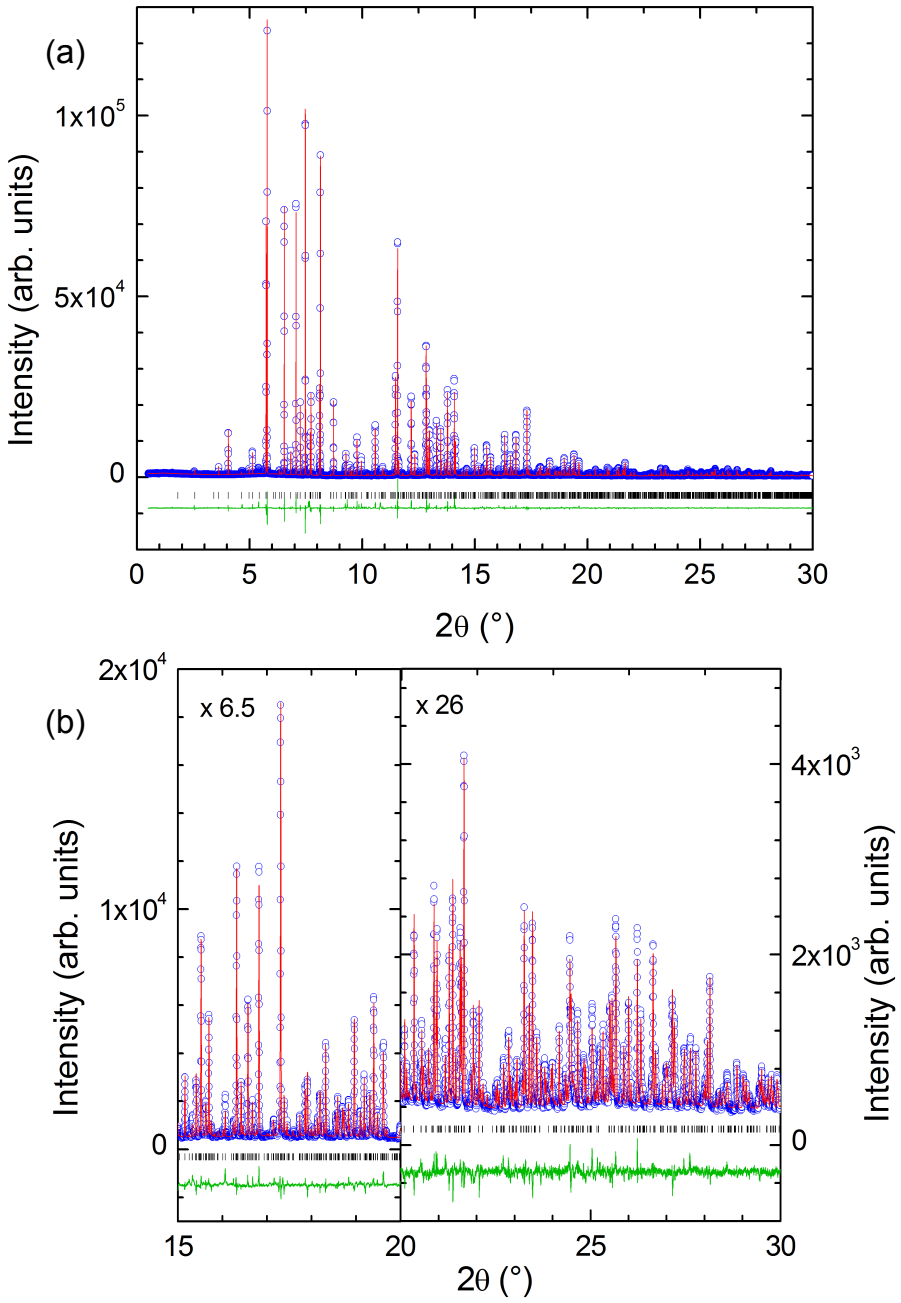

Figure 4.5: (a) Observed (open blue circles), calculated (red line) and difference (green line) synchrotron powder diffraction Rietveld profile of $KMnCrF_6$ (space group *Ccc*2), collected at ID31, λ = 0.39992 Å, *T* = 300 K. (b) Magnification of the high 2*θ* region.

[‡‡] Data were collected over ~110 min at *T* = 300 K compared to ~23 min at *T* = 373 K.

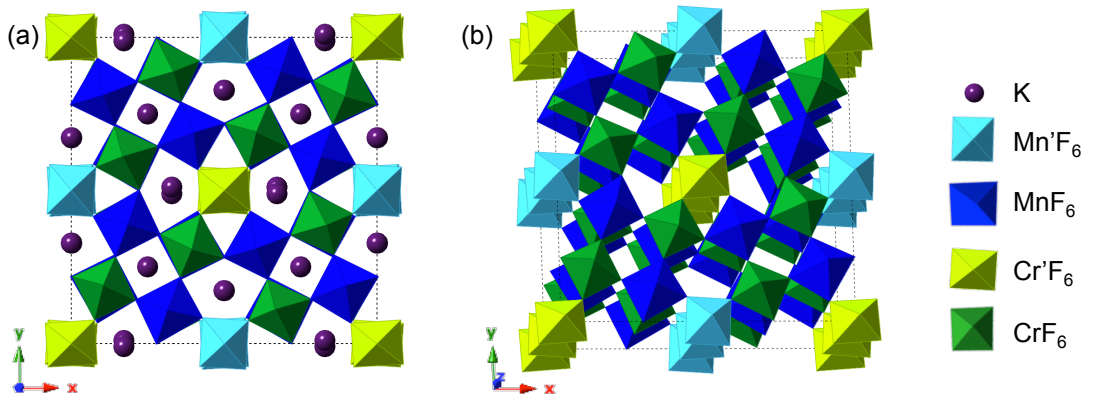

Figure 4.6: The *Ccc*2 cell adopted by $KMnCrF_6$ at room temperature. Mn' and Mn correspond to Mn1 on the extra-perovskite site (*4b*) and to Mn2, Mn3 on the perovskite site (*8d*), respectively. Cr' and Cr correspond to Cr1 on the extra-perovskite site (*4a*) and to Cr2, Cr3 on the perovskite site (*8d*), respectively. (a) View down the *c*-axis. (b) Tilted view, highlighting the alternating order of MnF_6 and CrF_6 octahedra on the perovskite site, and the columns of MnF_6 and CrF_6 octahedra on the extra-perovskite site. K^+ was omitted for clarity.

The orthorhombic distortion of the TTB cell is very subtle; therefore also the differences in atomic positions of related atoms are very small. We find that it was not possible to refine the atomic positions of all potassium atoms simultaneously due to the high number (e.g. 66 positional variables) and correlation of parameters. Thus, the coordinates of Mn, Cr, F and K(1, 2) were refined together, but separately from K(3, 4) and the temperature factors of all atoms were refined simultaneously. In analogy to the structure determination at high-temperature, the displacements along the polar *c*-axis with respect to the higher symmetry phase (*Cccm*) were calculated and are summarized in Table 4.7. The displacements of all cations (Mn, Cr and K) and those of several F are $d(z) > 0.1$ Å. Compared to the displacements at $T = 373$ K, the distortions of Mn and Cr away from the high-symmetry structure at $T = 300$ K are significantly larger. This and the improved refinement statistics provide a good indication that the structure is likely acentric in *Ccc*2 symmetry.

The tetragonal to orthorhombic structural phase transition described above doubles the number of crystallographic sites and could have strong implications on the ionic ordering pattern. Very importantly, it generates two distinct extra-perovskite sites (4*a* and 4*b*), implying additional Mn^{2+}/ Cr^{3+} order. This is in contrast to the $P4_2bc$ structure, in which the extra-perovskite site is described by one crystallographic site, and is occupied statistically by both Mn^{2+} and Cr^{3+}. In *Ccc*2, the multiplicities of the 4*a* and 4*b* sites are such that sites of the same type are stacked on top of each other. Assuming that the 4*a* and 4*b* site are solely occupied by one type of cation

(Mn or Cr), the *Ccc*2 structure forms columns of MnF_6 and CrF_6 octahedra. On the other hand, the alternating order of Mn^{2+} and Cr^{3+} around the perovskite unit is the same as in the high temperature $P4_2/mbc$ structure. The *Ccc*2 cell adopted by $KMnCrF_6$ is illustrated in Figure 4.6, illustrating a possible fully ordered structure.

To evaluate possible Mn^{2+}/ Cr^{3+} order on the extra-perovskite sites, Rietveld refinements were initiated for differently ordered models of $KMnCrF_6$. In these models, the extra-perovskite sites were occupied (I) by Mn (4*a*) and Cr (4*b*), (II) Cr (4*a*) and Mn (4*b*), and (III) by a 1:1 mixture of Mn and Cr on both sites. If the 4-fold sites are disordered, one expects similar refinement statistics for models (I) and (II). Conversely, the fit statistics are best for models (II) and (III), which is considered significant because of the extremely high-resolution of the diffraction data. This result is a first indication that there may be additional Mn/Cr order in $KMnCrF_6$.

model	χ^2	F^2/ %	wR_p/ %	R_p/ %
I: Mn (4*a*), Cr (4*b*)	8.747	7.24	8.71	6.01
II: Mn (4*b*), Cr (4*a*)	8.696	7.20	8.67	5.98
III: mixed sites	8.679	7.18	8.67	5.99

Table 4.4: Rietveld refinement statistics for different ordered orthorhombic models of $KMnCrF_6$ at RT. The extra-perovskite sites (4*a*) and (4*b*) were assumed to be occupied by either Mn or Cr; or by a 1:1 mixture. Refinement statistics are best for models II and III.

Mn1-F	*d*/ Å	Mn2-F	*d*/ Å	Mn3-F	*d*/ Å
Mn1_F4	1.98(2)	Mn2-F1	2.10(2)	Mn3-F2	2.09(3)
Mn1_F4	1.98(2)	Mn2-F5	2.07(2)	Mn3-F6	2.02(2)
Mn1_F6	1.81(2)	Mn2-F8	2.07(2)	Mn3-F7	2.06(2)
Mn1_F6	1.81(2)	Mn2-F10	2.07(2)	Mn3-F9	2.09(2)
Mn1_F16	1.78(3)	Mn2-F11	2.10(3)	Mn3-F12	2.12(3)
Mn1_F16	2.19(3)	Mn2-F13	1.97(4)	Mn3-F14	1.97(4)
average	1.98(2)	average	2.07(2)	average	2.06(2)
Cr1-F	*d*/ Å	Cr2-F	*d*/ Å	Cr3-F	*d*/ Å
Cr1-F3	1.97(2)	Cr2-F1	1.98(2)	Cr3-F2	1.99(3)
Cr1-F3	1.97(2)	Cr2-F3	1.95(2)	Cr3-F4	1.92(2)
Cr1-F5	1.95(2)	Cr2-F7	1.96(2)	Cr3-F8	2.00(2)
Cr1-F5	1.95(2)	Cr2-F9	1.96(2)	Cr3-F10	1.92(2)
Cr1-F15	1.84(4)	Cr2-F11	1.90(2)	Cr3-F12	1.91(3)
Cr1-F15	2.12(4)	Cr2-F13	2.01(4)	Cr3-F14	1.98(4)
average	1.97(2)	average	1.96(2)	average	1.95(2)

Table 4.5: Bond-distances of Mn-F and Cr-F obtained from Rietveld refinement of the room temperature diffraction profile in space group *Ccc*2. The average bond lengths are in good agreement with Mn^{2+} and Cr^{3+} on the four 8*d* sites (Mn2, Mn3, Cr2, Cr3), whereas the 4*a* and 4*b* site (Cr1, Mn1) appear to be occupied by both Mn^{2+} and Cr^{3+}.

space group: *Ccc2*		No. 37		*T* = 300 K		
a = 17.90002(3) Å		*b* = 17.88804(3) Å		*c* = 7.93839(1) Å	*V* = 2541.842(5) Å^3	
		x	*y*	*z*	B_{iso}/ Å^2	*Occ.*
Mn1	4*b*	0	0.5	0.520(2)	0.44(4)	1
Cr1	4*a*	0	0	0.024(2)	0.65(5)	1
Mn2	8*d*	0.8925(5)	0.8196(4)	0.519(2)	0.44(4)	1
Mn3	8*d*	0.1813(4)	0.3936(5)	0.020(2)	0.44(4)	1
Cr2	8*d*	0.8927(5)	0.8195(5)	0.019(2)	0.65(5)	1
Cr3	8*d*	0.1821(5)	0.3936(5)	0.518(2)	0.65(5)	1
K1	8*d*	1.0008(3)	0.6724(2)	0.268(2)	2.21(3)	1
K2	8*d*	0.3284(2)	0.4896(2)	0.769(2)	2.21(3)	1
K3	4*c*	0.25	0.25	0.765(2)	0.94(5)	0.523(7)
K4	4*c*	0.25	0.25	0.266(2)	0.94(5)	0.644(7)
F1	8*d*	0.997(1)	0.7811(4)	0.014(4)	2.17(3)	1
F2	8*d*	0.2217(4)	0.497(2)	0.502(3)	2.17(3)	1
F3	8*d*	0.924(1)	0.923(1)	0.985(3)	2.17(3)	1
F4	8*d*	0.079(1)	0.424(1)	0.497(3)	2.17(3)	1
F5	8*d*	0.086(1)	0.933(1)	0.003(3)	2.17(3)	1
F6	8*d*	0.071(1)	0.585(1)	0.505(3)	2.17(3)	1
F7	8*d*	0.290(1)	0.358(1)	0.007(3)	2.17(3)	1
F8	8*d*	0.642(1)	0.790(1)	0.487(2)	2.17(3)	1
F9	8*d*	0.855(1)	0.717(1)	0.996(2)	2.17(3)	1
F10	8*d*	0.282(1)	0.355(1)	0.512(3)	2.17(3)	1
F11	8*d*	0.8946(5)	0.8081(5)	0.256(4)	2.17(3)	1
F12	8*d*	0.1665(4)	0.3883(4)	0.755(4)	2.17(3)	1
F13	8*d*	0.8979(6)	0.8105(5)	0.767(5)	2.17(3)	1
F14	8*d*	0.1849(5)	0.3900(5)	0.268(5)	2.17(3)	1
F15	4*a*	0	0	0.256(5)	2.17(3)	1
F16	4*b*	0	0.5	0.745(3)	2.17(3)	1
χ^2 = 8.679		F^2 = 7.2 %		wR_p = 8.67 %	R_p = 5.98 %	

Table 4.6: Results of Rietveld refinement of the room temperature SXRD diffraction profile of $KMnCrF_6$, collected at ID31, λ = 0.39992 Å. There were 77 refined structural parameters. (Data collection time was ~110 minutes.)

In further refinements, starting from model (III), the fractional occupancies of the 4-fold sites were constrained such that the site occupancies are equal to one. It is known from the elemental analysis that the Mn:Cr ratio of this sample is close to 1:1. Therefore, the occupancies of Mn and Cr were constrained to *Occ.*(Mn, 4*a*) = *Occ.*(Cr, 4*b*) = -*Occ.*(Mn, 4*b*) = -*Occ.*(Cr, 4*a*). The refined occupancies on the 4*b* site are 74(6) % of Mn and 26(6) % of Cr; whereas the occupancies on the 4*a* site refined to 74(6) % of Cr and 26(6) % of Mn. These results suggest that the order imposed by the *Ccc*2 symmetry is likely realized in $KMnCrF_6$ and that the 4*a* and 4*b* sites are preferentially occupied by Cr and Mn, respectively.

	Wyckoff site						
	*Ccc*2	*Cccm*	*z*(*Ccc*2)	*z*(*Cccm*)	*d*(*z*)	*d*(*z*)·*c*/ Å	T_C/ K
Mn1	4*b*	4*c*	0.520(2)	0.5	0.020	0.159	356(10)
Cr1	4*a*	4*d*	0.024(2)	0	0.024	0.191	380(15)
Mn2	8*d*	8*l*	0.519(2)	0.5	0.019	0.151	350(9)
Mn3	8*d*	8*l*	0.020(2)	0	0.020	0.159	356(10)
Cr2	8*d*	8*l*	0.019(2)	0	0.019	0.151	350(9)
Cr3	8*d*	8*l*	0.518(2)	0.5	0.018	0.143	345(8)
K1	8*d*	8*h*	0.268(2)	0.25	0.018	0.143	345(8)
K2	8*d*	8*g*	0.769(2)	0.75	0.019	0.151	350(9)
K3	4*c*	8*k*	0.765(2)	0.750(3)	0.015	0.119	331(6)
K4	4*c*		0.266(2)	0.250(3)	0.016	0.127	336(7)
F1	8*d*	8*l*	0.014(4)	0	0.014	0.111	327(5)
F2	8*d*	8*l*	0.502(3)	0.5	0.002	0.016	300.6(1)
F3	8*d*	8*l*	0.985(3)	0	-0.015	-0.119	331(6)
F4	8*d*	8*l*	0.497(3)	0.5	-0.003	-0.024	301.2(2)
F5	8*d*	8*l*	0.003(3)	0	0.003	0.024	301.2(2)
F6	8*d*	8*l*	0.505(3)	0.5	0.005	0.040	303.5(6)
F7	8*d*	8*l*	0.007(3)	0	0.007	0.056	307(1)
F8	8*d*	8*l*	0.487(2)	0.5	-0.013	-0.103	323(4)
F9	8*d*	8*l*	0.996(2)	1	-0.004	-0.032	302.2(4)
F10	8*d*	8*l*	0.512(3)	0.5	0.012	0.095	320(4)
F11	8*d*	16*m*	0.256(4)	0.240(2)	0.006	0.127	336(7)
F12	8*d*		0.755(4)	0.760(2)	-0.005	-0.040	303.5(6)
F13	8*d*	16*m*	0.767(5)	0.741(2)	0.026	0.206	394(17)
F14	8*d*		0.268(5)	0.259(2)	0.009	0.071	311(2)
F15	4*a*	4*a*	0.256(5)	0.25	0.006	0.048	305(1)
F16	4*a*	4*b*	0.745(3)	0.75	-0.005	-0.040	303.5(6)

Table 4.7: The atomic positions as determined from Rietveld refinements in space groups *Ccc*2 and *Cccm* at T = 300 K. The displacement *d*(*z*) is calculated by comparing the atomic positions of group (*Ccc*2) and subgroup (*Cccm*). The absolute displacements in Å are used to estimate the ferroelectric-paraelectric T_C according to Kroumova [16].

As mentioned before, the space group *Ccc*2 is assigned to the room temperature phase. This is based on the substantial difference in atomic positions between *Cccm* and *Ccc*2 and the improvement in fit statistics. Results of the final refinement in space group *Ccc*2 are summarized in Table 4.6 and the structure illustrated in Figure 4.6. The *M*-F distances of Mn2, Mn3, Cr2 and Cr3 (8*d* sites) are in good agreement with an ordered perovskite subunit. The additional order implied by the *Ccc*2 structure (Mn^{2+} and Cr^{3+} on the 4*b* and 4*a* sites, respectively) is not strongly reflected in the bond distances (Table 4.5), which instead indicate at least partial disorder of Mn^{2+} and Cr^{3+} over the fourfold sites. This is in agreement with the refined fractional occupancies.

Polar materials with a centric pseudosymmetry are good candidates for ferroelectrics, and empirical relationships between the atomic displacement *d*(*z*) and

the ferroelectric-paraelectric transition temperature T_C have been proposed. Abrahams *et al.* estimates the T_C (in K) according to $T_C = C \cdot d(z)^2$, with $C \approx 2.0 \cdot 10^4$ K Å^{-2} (AKJ relationship) [17]. Kroumova *et al.* proposed an alternative empirical formula: $T_C = \alpha \cdot d(z)^2 + \beta$, with $\alpha = 0.22(4) \cdot 10^4$ K Å^{-2} and $\beta = T$(experiment) [16]. In this thesis, the relationship suggested by Kroumova was used to estimate the ferroelectric-paraelectric transition temperature, as it takes into account that the atomic coordinates correspond to a non-zero temperature.

The displacements are calculated from the atomic positions in their lower symmetry phase compared to their higher symmetry phase. In the TTB materials, the *c*-axis is the polar axis, and only displacements in this direction are considered in the following analysis. The calculated displacements $d(z)$ directly influence the estimation of T_C, but can be dependent on the origin choice [18]. The origin should be chosen such as to minimize the maximum distortion and to keep the mass centre at rest [16]. This can be conveniently checked with the aid of programs as PSEUDO [19]. In this case, no origin shift was necessary. The displacements $d(z)$ calculated from comparison of *Cccm* and *Ccc*2 structures, along with their corresponding Curie temperatures T_C, are listed in Table 4.7.

The estimation of T_C has been based only on the displacements of Mn and Cr. The $d(z)$ calculated for K and F are subject to larger uncertainties than those of Mn and Cr. Firstly, the thermal displacement parameter of K1, K2 is considerably larger ($B_{iso} \approx 2.21(3)$ Å^2), indicative of static or dynamic disorder (see for instance references Fujihisa [20], [21]). Secondly, X-rays are not particularly sensitive to light atoms such as fluorine due to their small scattering cross-sections. For the maximum (Mn1) and average displacement (Mn and Cr), the estimated ferroelectric-paraelectric transition temperature is T_C(max) ≈ 380 K and T_C(avg.) ≈ 354 K, respectively. As known from the structural determination, $KMnCrF_6$ is likely centric and apolar at $T \geq 373$ K. Hence the average estimated transition temperature of $T_C \approx 354$ K is in clear agreement with the XRD data.

4.3.3 Temperature Dependence of the Structure

The temperature dependence of the lattice constants and the volume of sample I are shown in Figure 4.7. At $T \leq 300$K, a distortion to orthorhombic *Ccc*2 symmetry is observed through a small peak splitting in the high-resolution diffraction data. At $T = 373$ K, the orthorhombic splitting disappears and the diffraction profile is indexed with the tetragonal space group $P4_2/mbc$.

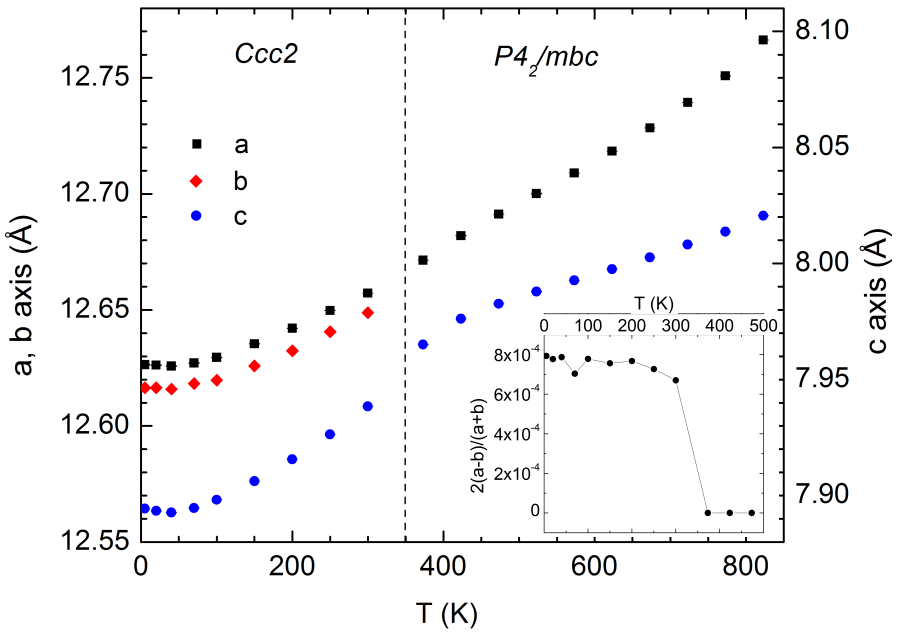

Figure 4.7: Temperature evolution of the lattice of sample I obtained from Rietveld refinements of synchrotron powder diffraction profiles collected on beamline ID31. At 300 K and below, the *Ccc*2 model was used, whilst the $P4_2/mbc$ model was used for the high temperature region (T > 350 K). Both structural models were tested between 300 K and 500 K. The *a*- and *b*- lattice parameters of the orthorhombic cell have been converted to the tetragonal setting, $a^* = a_O/\sqrt{2}$. The dashed line marks the estimated phase transition temperature. (inset) The orthorhombic strain, $P = 2(a-b)/(a+b)$, that was obtained from fits in the *Ccc*2 model drops to zero at the transition temperature.

A distinctive change in expansivity of the *c*-axis is observed at the point of phase transition. This can be understood from the cooperative tilting of MnF_6 and CrF_6 octahedra: the Mn-F-Cr angles (along *c*) straighten as the temperature increases and contribute to the expansion of the *c*-parameter. The octahedral tilt angle approaches 180° at T_C and the slope of thermal expansion of the *c*-axis flattens at higher temperatures. This change is connected to a decrease of the octahedral angle, which changes from α(Mn2-F11-Cr2) = 168.0(6)°, α(Mn2-F13-Cr2) = 169.2(6)°, α(Mn3-F12-Cr3) = 163.5(4)° and α(Mn3-F14-Cr3) = 174.9(5)° in Ccc2 (T = 300 K) to α(Mn15-F14-Cr16) = 174.8(3)° and α(Mn15-F15-Cr16) = 171.1(3)° in $P4_2bc$ (T = 373 K) [§§].

[§§] α(Mn14-F14-Cr15) = 177.7(1)° in $P4_2/mbc$

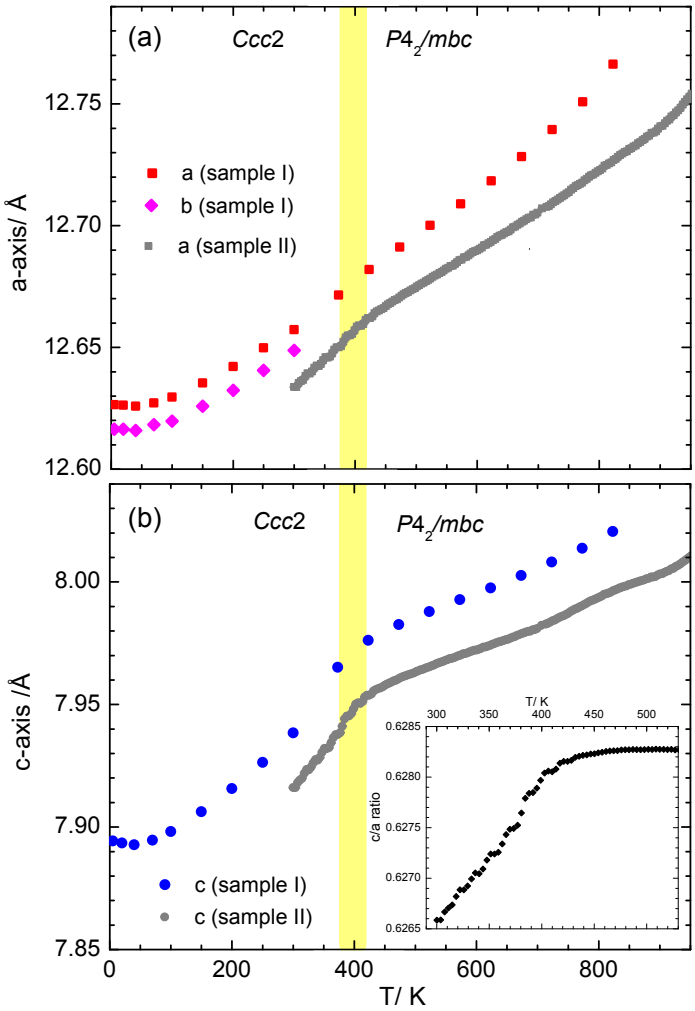

Figure 4.8: The lattice parameters of sample I and II of $KMnCrF_6$ were obtained from Rietveld refinements of powder synchrotron diffraction data. The temperature behaviour of (a) the *a*-, *b*- and (b) *c*-axis of sample I and II shows good agreement, although absolute values vary due to slight changes in composition. The lattice parameters of sample I in the *Ccc*2 phase were converted to the tetragonal setting, $a^* = a_O/\sqrt{2}$. Rietveld refinements of sample I were carried out in space groups *Ccc*2 and $P4_2/mbc$ as described in the caption of Figure 4.7. Refinements of sample II were carried out in space group $P4_2bc$. The change in slope of the *c*-axis and c/a ratio (inset panel b) at $T \approx 400$ K is likely connected to the orthorhombic → tetragonal phase transition, as for sample I.

For a more precise determination of the *O*–*T* transition temperature, the lattice constants of sample II were followed on beamline ID11. The area detector allows for much faster data collection but does not resolve the subtle orthorhombic splitting[***].

[***] Diffraction profiles collected subsequently on beamline ID31, $\lambda = 0.3541907$ Å, $T = 300$ K confirmed the orthorhombic *Ccc*2 symmetry of sample II, with

Hence, Rietveld refinements were carried out in space group $P4_2bc$. At T = 300 K, the lattice constants are a = 12.6334(2) Å and c = 7.9161(2) Å. Compared to sample I, the unit cell is smaller. This is probably related to a reduced K content, which decreases the filling of the channels, increases the Cr^{3+} content in order to preserve charge neutrality. Although the absolute values of the lattice constants (at RT) vary between the samples, their temperature evolution is comparable (see Figure 4.8). In sample II, the c-axis and the c/a ratio change slope at $T \approx 400$ K. This is likely connected to the orthorhombic – tetragonal phase transition. The difference in the transition temperature between the two samples could be explained in terms of small changes in composition.nIt has been observed that very slight variations in potassium content result in drastic changes of the transition temperatures in the series K_xFeF_3 [22]. Variations in composition could also explain the different slopes of expansions of samples I and II. It should also be noted that data on beamline ID31 was collected at discrete temperature steps, whilst data on ID11 were collected on a rapid temperature ramp. Variations in heat treatment might have an effect on the sample and hence on the temperature behaviour.

4.3.4 Local Structure

The local structure of $KMnCrF_6$ was investigated using total scattering methods, and initial fitting of the experimental $G(r)$ was carried out based on the orthorhombic structural model (space group $Ccc2$) obtained from RT SXRD data described above. The general features of the $G(r)$ are well reproduced by the average structure. However, the low r-range (r = 1.5 - 3.5 Å) corresponding to first neighbour the M-F, K-F and F-F distances shows distinct shoulders in the experimental PDF but are smeared out in the average model. In addition, isotropic thermal displacement parameters were relatively large for K (U_{iso} = 1.0(5) Å ^{2}) and F (U_{iso} = 2.3(5) Å^2); fit statistics are χ^2 = 0.0351; R_w = 23.56 %. The use of anisotropic temperature factors (for each atom type) improved fit statistics (χ^2 = 0.0319; R_w = 22.42 %) but did not capture the features at r < 5 Å.

---

a = 17.87752(5) Å, b = 17.85775(5) Å and c = 7.91733(2) Å. The refined K-occupancies gave a stoichiometry of $K_{1.008(3)}MnCrF_6$.

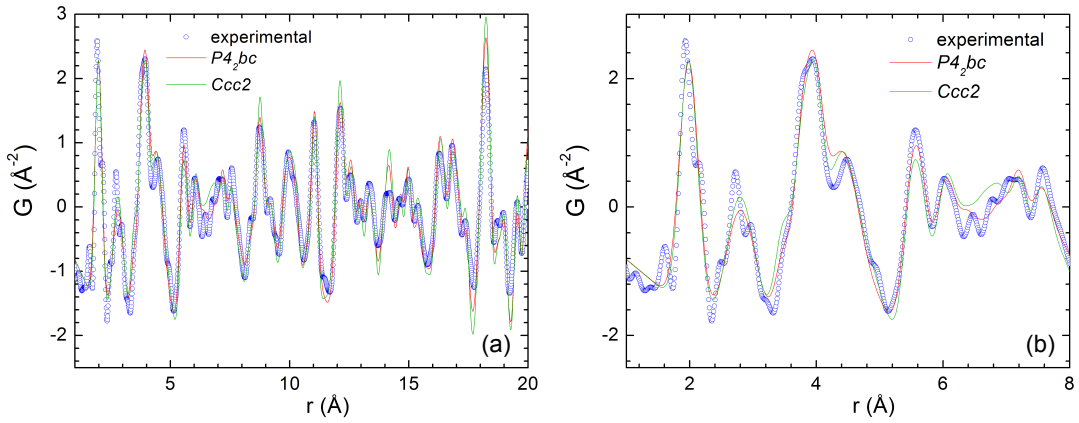

Figure 4.9: (a) The experimental (open blue circles) and simulated $G(r)$ for the *Ccc*2 (green line) and $P4_2bc$ (red line) models obtained from SXRD, T = 300 K. (b) Both models reproduce the general features of the $G(r)$ equally well, but do not capture the shoulders on the peaks corresponding to nearest- and next-nearest neighbour.

Trial refinements of the PDF were also carried out using a tetragonal model (space group $P4_2bc$). Similarly to the orthorhombic model, the general features are well reproduced, but the short-range features (r = 1.5 ~ 3.5 Å) are not properly described. The fits obtained from both *Ccc*2 and $P4_2bc$ models are very similar; this reflects the fact that the orthorhombic distortion observed in the average structure is very small, and has no appreciable effect on the local structure. $G(r)$'s were simulated for the average tetragonal and orthorhombic models and are shown together with the experimental $G(r)$ in Figure 4.9. It is clear that the local environment is unaffected by the orthorhombic distortion, and further refinements were carried out in the tetragonal setting to limit the number of refinable parameters.

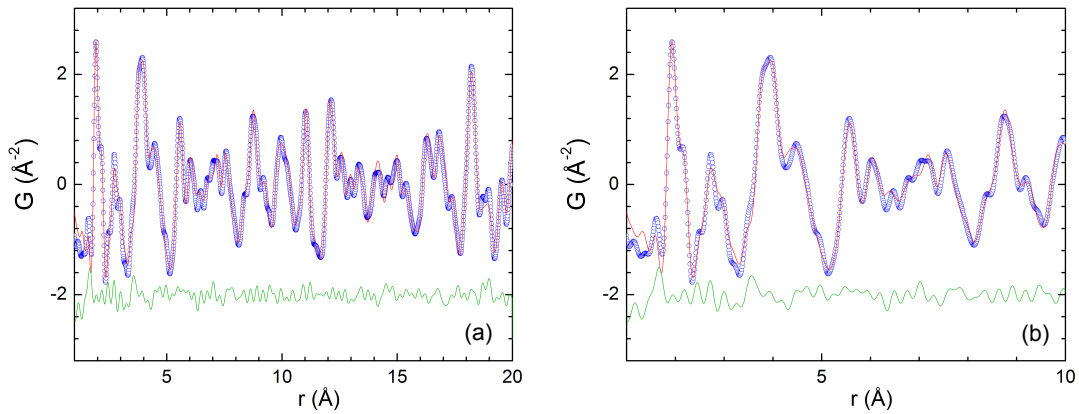

Figure 4.10: (a) Observed (open blue circles), calculated (red line) and difference (green line) $G(r)$ of $KMnCrF_6$ (space group $P4_2bc$), T = 300 K. (b) Magnification of the low r region.

space group: $P4_2bc$		No. 106		T = 300 K	
a = 12.64(1) Å		c = 7.94(1) Å		V = 1268.6(4) Å^3	
		x	y	z	B_{iso}/ Å^2
Mn1	4*b*	0.5	0	0.209(4)	0.4(2)
CR2	4*b*	0.5	0	0.209(4)	0.3(2)
Mn2	8*c*	0.215(2)	0.925(3)	0.718(3)	0.4(2)
Cr1	8*c*	0.210(2)	0.925(3)	0.217(3)	0.3(2)
K1	8*c*	0.166(4)	0.683(3)	0.469(7)	0.9(5)
K2	4*a*	0	0	0.97(2)	0.8(5)
F1	8*c*	0.27(1)	0.79(1)	0.21(2)	1.2(5)
F2	8*c*	0.34(1)	0.00(1)	0.17(1)	1.2(5)
F3	8*c*	0.52(1)	0.85(1)	0.19(1)	1.2(5)
F4	8*c*	0.15(1)	0.06(1)	0.20(1)	1.2(5)
F5	8*c*	0.08(1)	0.86(1)	0.16(1)	1.2(5)
F6	8*c*	0.20(1)	0.91(1)	0.459(7)	1.2(5)
F7	8*c*	0.21(1)	0.95(1)	0.947(5)	1.2(5)
F8	4*b*	0.5	0	0.43(1)	1.2(5)
fit statistics		red. χ^2 = 0.0155		R_w =15.51%	

Table 4.8 Results of the $G(r)$ analysis of the total scattering data of $KMnCrF_6$ collected at T = 300 K, using the symmetry constraints of space group $P4_2bc$. There were 41 refined structural parameters.

In the next step, lattice parameters, scale factors and isotropic temperature factors were refined within the constraints of $P4_2bc$ symmetry and provided a good fit to the $G(r)$, capturing the shoulders on the first and second peak well (Figure 4.10). The results are summarized in Table 4.8. Fit statistics improved to reduced χ^2 = 0.0155 and R_w = 15.51 %. Further, the thermal displacement parameters decreased significantly to B_{iso} = 1.2(5) Å^2 for F and to B_{iso} = 0.9(5) Å^2 and 0.8(5) Å^2 for K in the pentagonal and square channels, respectively.

4.3.5 Pressure Dependence of Structure

From the high-resolution powder diffraction data the orthorhombic cell of $KMnCrF_6$ was established at $T \leq$ 300 K, which is a more conventional description of the monoclinic distortion of the tetragonal high-temperature cell. The distortion away from tetragonal symmetry is very subtle, and therefore the broadening and splitting of peaks is only resolved in extremely high-resolution powder diffraction profiles at higher angles (e.g. in ID31 data collected for angles > 15° 2θ). For example, the difference in position between the (12 0 0) and the (0 12 0) reflections is only 0.01° (2θ) at 300 K. Powder diffraction profiles of sample I were collected on the high-pressure beamline BL10XU (SPring-8, Japan), but the resolution of the 2D detector is not sufficiently high to observe the splitting at low pressures. Trial Rietveld refinements at p = 0.19 GPa returned lattice constants that refined to $a = b$ (within less than one standard deviation).

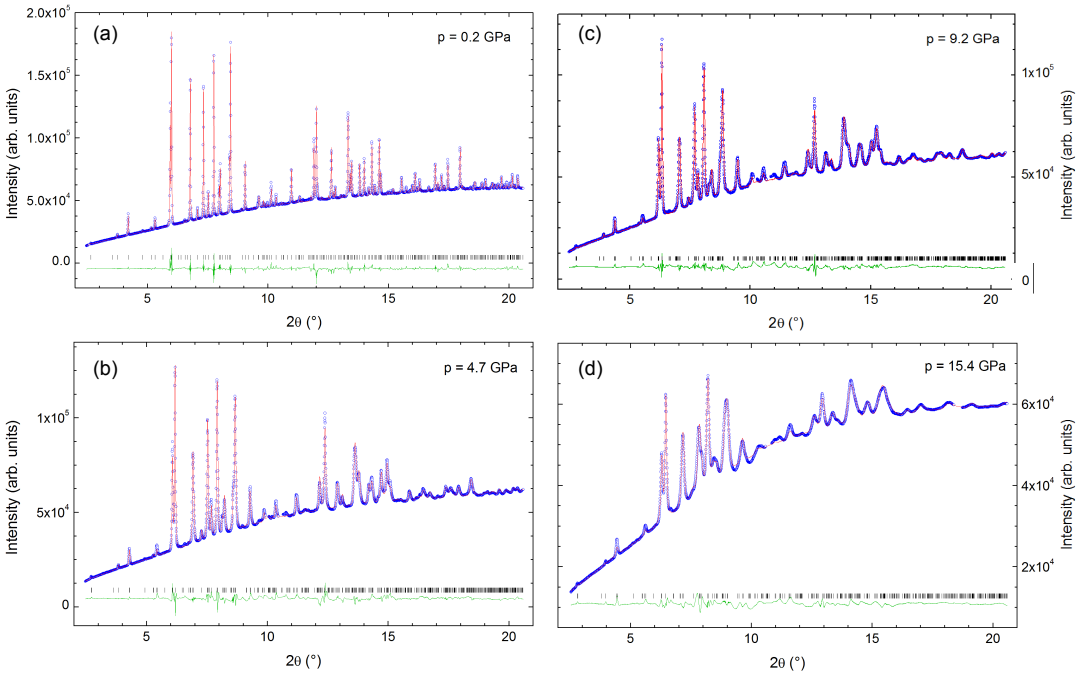

Figure 4.11: Observed (open blue circles), calculated (red line) and difference (green line) high-pressure synchrotron diffraction Rietveld profile of $KMnCrF_6$ in space group *Ccc*2, collected at beamline BL10XU, $\lambda = 0.41429$ Å at $T = 300$ K. (a) $p = 0.2$ GPa, (b) $p = 4.7$ GPa. (c) $p = 9.2$ GPa, (d) $p = 15.4$ GPa.

On increasing pressure however, several reflections (i.e. (220), (530), (630)) broaden and split, as the compressibility along the *a*- and *b*- axis is anisotropic. Throughout the measured pressure range, the lattice parameters contract smoothly on increasing pressures, and discontinuities indicating a structural transition are not observed. Rietveld refinements at selected pressures are shown in Figure 4.11. The pressure evolution of the lattice metrics is shown in Figure 4.12, together with a least squares fit to the semiempirical 3rd order Birch-Murnaghan (BM) equation of state. The data was fitted using the program Eosfit [23].

The isothermal bulk modulus K_0 and its pressure derivative K' are $K_0 = 48.8(8)$ GPa and $\partial K_0/\partial p = K' = 5.1(2)$. The pressure dependence of the lattice parameters was fitted using the same equation of state (3rd order BM) by substituting the cubed lattice parameter for the volume. The linear bulk moduli for the different cell directions are $K_0(a) = 65(2)$ GPa, $K_0(b) = 48(1)$ GPa, $K_0(c) = 38.8(7)$ GPa. The compressibilities of the axes are $K''(a) = -0.0993$ GPa^{-1}, $K''(b) = -0.1820$ GPa^{-1} and $K''(c) = -0.1323$ GPa^{-1}. The equation of state function of the unit cell volume was extrapolated to higher pressures ($p = 30$ GPa) and compared to the volume obtained

from the extrapolated lattice constants, which give the same values, supporting the robustness of the calculation for both linear and cubic data.

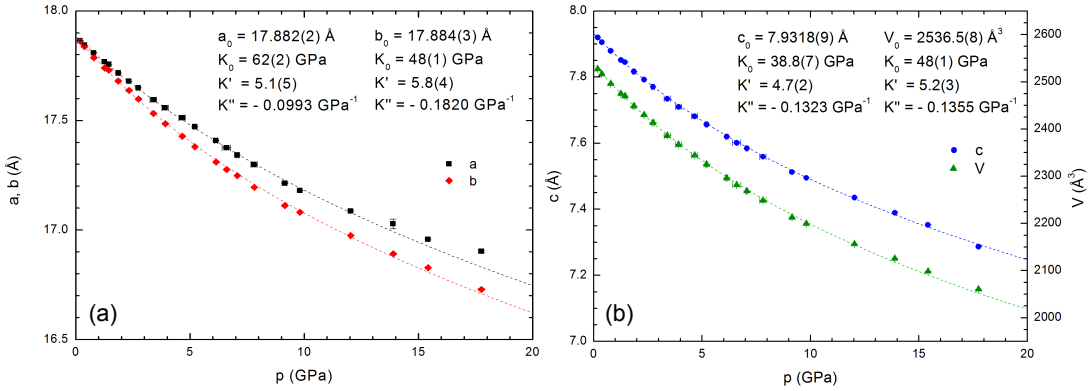

Figure 4.12: Pressure evolution of the basal lattice constants (a), the *c*-axis and unit cell volume (b) as deduced from Rietveld refinements of room temperature diffraction profiles collected at BL10XU, $T = 300$ K. The solid line is a least-squares fit to a 3rd order Birch-Murnaghan equation of state, extended to $p = 20$ GPa.

4.3.6 Magnetic Properties

The magnetic susceptibility measurements in different applied fields (see Figure 4.13.a) agree with the weak ferromagnetic behaviour reported earlier [6]. The magnetic ordering temperature can be estimated from the increase in magnetisation and also from the kink in the $1/\chi_m$ *vs.* T plot (Figure 4.13) to be $T_N = 23$ K. The applied field H only marginally affects the transition temperature T_N. The bifurcation of zero-field-cooled (ZFC) and field cooled (FC) branches vanishes in fields $H \geq 1000$ Oe. A Curie-Weiss fit to the high temperature regime of the inverse susceptibility yields $C = 6.42$ emu K mol^{-1}, $\theta = -5.9(1)$ K and $\mu_{eff} = 2.828 \cdot \sqrt{C} = 7.2\ \mu_B$. The small opening of the S-shaped magnetic hysteresis loop collected at $T = 5$ K shows that $KMnCrF_6$ behaves as a soft ferromagnet (see Figure 4.14).

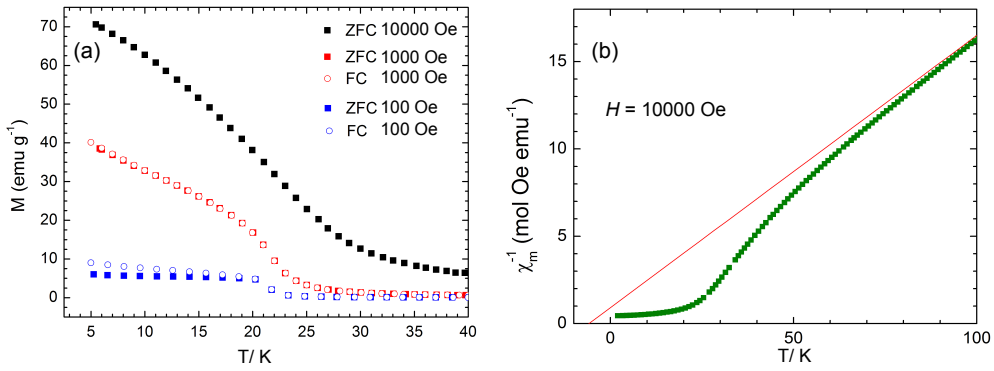

Figure 4.13: (a) Temperature dependence of magnetic susceptibility in applied fields H = 100, 1000 and 10000 Oe after zero-field-cooling (ZFC) and field cooling (FC). (b) Temperature dependence of the inverse magnetic susceptibility χ_m^{-1}, measured in H = 10000 Oe. At high temperatures the Curie – Weiss law is obeyed; the extrapolated fit is shown as a red line. The ferromagnetic transition temperature is determined from the $1/\chi_m$ *vs.* T plot as T_C = 23 K.

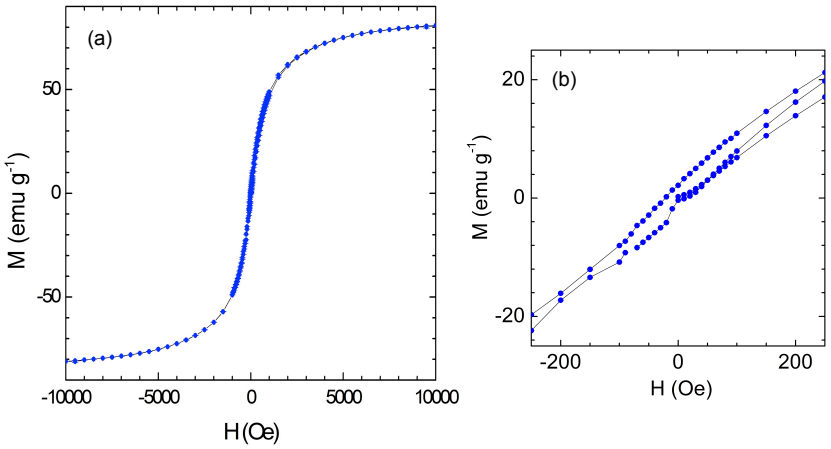

Figure 4.14: (a) Magnetic hysteresis loop collected at T = 5 K, H_{max} = 10000 Oe. The curved saturation curve is typical for a soft ferromagnetic material. (b) Magnification of the low field part of the magnetic hysteresis loop. The small opening of the loop indicates weak ferromagnetic behaviour.

4.4 Discussion

The aim of this investigation was to establish a detailed structural description of the tetragonal tungsten bronze $KMnCrF_6$ at variable temperatures and pressures, to define the magnetic properties and analyse the results with respect to potential multiferroic behaviour.

4.4.1 The Structure at Variable Temperatures

The TTB fluoride $KMnCrF_6$ was initially synthesised some 40 years ago and in 1982 its crystal structure was determined by Banks as tetragonal $P4_2bc$, with $a \approx 12.651$ Å and $c \approx 7.936$ Å [5], [6]. The doubling of the c–axis compared to the conventional TTB cell arises from the alternating arrangement of Mn^{2+} and Cr^{3+} around the perovskite cage. Banks interfered this from magnetic susceptibility measurements, but not confirmed by the presence of the corresponding (hkl, $l = 1$) reflections in the diffraction pattern [6].

The powder diffraction data presented in this work clearly show the reflections corresponding to the c-axis doubling. Furthermore, the very high resolution of the data reveals a hitherto unknown subtle distortion of the $P4_2bc$ cell to orthorhombic symmetry at room temperature that vanishes at higher temperatures.

In the course of the crystal structure determination of the orthorhombic room temperature phase, space group candidates were considered in their centric and acentric variants, because the TTB fluorides are potential ferroelectrics and ferroelectricity can emerge only in polar (acentric) materials. Group – subgroup relationships are a useful tool to describe second-order phase transitions that involve displacement of atoms (i.e. distortion of the structure) rather than reconstruction of the atomic arrangement. Subgroups of both $P4_2/mbc$ and $P4_2bc$ were considered in the search. Two of the seven non-isomorphic subgroups of $P4_2/mbc$ (i.e. *Pbam* and *Cccm*) are also centrosymmetric variants of subgroups of $P4_2bc$ (i.e. *Pba*2 and *Ccc*2); in the latter the mirror plane perpendicular to the 4-fold axis is lost. The group-subgroup relationships are displayed in Figure 4.15.

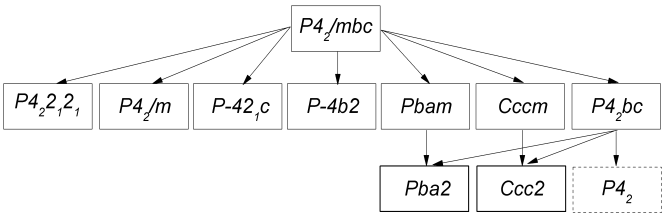

Figure 4.15: Group – Subgroup relationships for $P4_2/mbc$ and $P4_2bc$. The relation of $P4_2/mbc$ to $P4_2bc$ is the same as between *Pbam* and *Pba*2; and *Cccm* and *Ccc*2: in all cases a mirror plane perpendicular to the prinicpal rotation axis is lost.

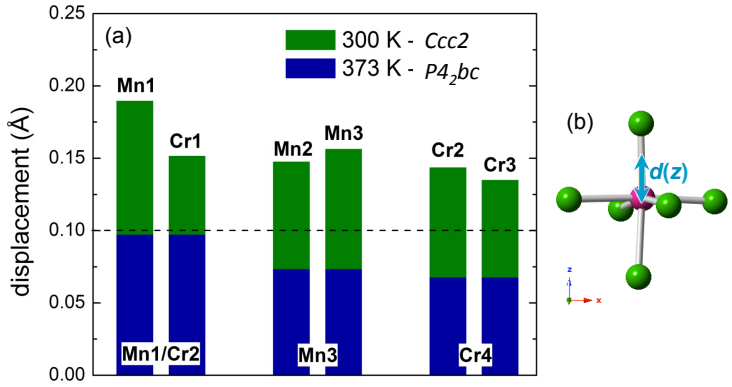

Figure 4.16: (a) Atomic displacements of Mn^{2+} and Cr^{3+} at T = 300 K and 373 K compared to the acentric structure variants *Cccm* and $P4_2/mbc$, respectively. (b) The displacement $d(z)$ is related to the displacement of the transiton metal ion (pink) from the mean plane of the coordinating fluorine (green) octahedron.

Trial refinements were carried out in *Pba*2 and *Ccc*2, but only the latter is suited to produce the splitting of the (*hh0*) reflections (see results section for details). The transformation between the tetragonal and the orthorhombic cell involves a 45° rotation parallel to the *c*-axis. The resulting orthorhombic lattice vectors a_O and b_O lie along the face diagonal of the original cell and the cell volume is doubled. Comparison of the atomic positions in *Cccm* and *Ccc*2 settings shows that the apical displacements of Mn and Cr (away from the higher symmetry positions) at T = 300 K are significantly larger than the $d(z)$ = 0.1 Å threshold (Figure 4.16), making the polar space group choice more likely [15]. The acentric symmetry also strengthens the possibility for ferroelectricity in $KMnCrF_6$.

In the originally suggested tetragonal $P4_2bc$ setting the extra-perovskite sites and the perovskite sites are described by one fourfold and two eightfold sites, respectively [6]. It was found that Mn^{2+} and Cr^{3+} order around the perovskite cage, and along the c-axis, whilst the extra-perovskite site is statistically occupied. The high-resolution

data presented in this thesis enabled us to detect a subtle orthorhombic distortion to *Ccc*2 symmetry. The extra-perovskite site splits in two distinct positions, 4*a* and 4*b*, which implies additional cationic order. Rietveld refinements starting from different occupancy configurations were initiated. Their fit statistics indicated a preferential occupation of Cr and Mn on the 4*a* and 4*b* site respectively, and not vice versa (see Table 4.4 for details). The alternating order of Mn and Cr around the perovskite cage is maintained in *Ccc*2 symmetry and is confirmed by the distribution of *M*-F bond distances (Table 4.5).

Supercells larger than the fundamental TTB cell are not unknown in the TTB fluorides, but their observation has so far been limited to electron diffraction (ED) experiments. Satellite reflections observed in ED patterns of $K_xM^{2+}M^{3+}F_6$ compounds (M^{2+} = Fe, Mn, Co; M^{3+} = Fe, Mn, Cr, In) were described as 'ferroelastic superstructure (FES)' (space group *Bbm*2, $a_{Bbm2} = 2 \cdot a_{TTB} \cdot \sqrt{2}$, $b_{Bbm2} = a_{TTB} \cdot \sqrt{2}$, $c_{Bbm2} = 2 \cdot c_{TTB}$), analogous to modulation reflections of $Ba_2NaNb_5O_{15}$ (BNN) [24]. In BNN, the *Bbm*2 supercell arises from NbO_6 tilting and is also connected to the presence of ferroelastic domains. Compared to the *Ccc*2 cell adopted by $KMnCrF_6$, the BNN type superstructure is doubled along the *a*-axis. However the diffraction data of $KMnCrF_6$ does not indicate a further doubling of the cell.

It was reported that octahedral tilt modulations in $K_xM^{2+}{}_xM^{3+}{}_{1-x}F_3$ compounds can arise independently of charge or chemical, but they are triggered by ordered arrangements [2], [25]. In ordered compounds, the size difference of the $M^{2+}F_6$ and $M^{3+}F_6$ octahedra inevitably triggers deformations and/or tilting of the octahedra, which are reflected in the crystal symmetry [2]. Fabbrici *et al.* addressed the origin of charge/ chemical order in TTB fluorides [24]. They find that charge order exists for M^{2+}/M^{3+} combinations with sufficiently different cationic radii, regardless of the atomic species. For example, replacing Fe^{3+} with In^{3+} in $K_{0.8}Fe^{2+}{}_{0.8}Fe^{3+}{}_{1.2-x}In^{3+}{}_xF_6$ gives a disordered compound, because the radii of In^{3+} (r = 0.8 Å) and Fe^{2+} (r = 0.78 Å) are very similar [24]. Other mixed TTB fluoride compounds appear to be disordered, for instance $K_{1.2}Cr_{0.8}Fe_{1.2}F_6$ and $K_{1.2}Cu_{1.2}Fe_{0.8}F_6$ that adopt a tetragonal cell, space group $P4/mbm$, $c = c_{TTB}$ [26], [27].

The description of independent charge order and tilt modulation in $K_xM^{2+}M^{3+}F_6$ compounds (M^{2+} = Fe, Mn, Co; M^{3+} = Fe, Mn, Cr, In) is in contrast to $K_{1.2}Fe_2F_6$, for which a strong coupling of charge order (CO), octahedral tilting, ferroelectricity and ferroelasticity was found in a theoretical study: full CO is a prerequisite for electrical polarization and is also responsible for its ferroelastic properties [28]. In case of

$KMnCrF_6$, the tilt modulations and the off centring of cations could, in principle, be described in space group $P4_2bc$, and there is no necessity for a larger supercell. It seems that an additional parameter drives the observed orthorhombic distortion: charge/ chemical ordering of Mn^{2+} and Cr^{3+}.

The tilt modulation in $KMnCrF_6$ is temperature dependent. On cooling, the tilting of the octahedra becomes more pronounced, which is also reflected in the steeper slope of thermal expansion of the *c*-axis below $T = 300$ K. The need for an increase in octahedral tilting can be deduced from simple bond distance considerations: for a regular shaped octahedron, the height h_{Oct} can be estimated as twice the average *M*-F bond length. Octahedral tilting (or distortion) becomes necessary when $h_{Oct} > c/2$. From $T = 373$ K to 300 K, the average height of an octahedron is approximately constant ($h_{Oct.} = 4.001(1)$ Å and 4.004(2) Å, respectively) whilst the *c*-axis changes from $c/2 = 3.983$ Å to 3.969 Å.

Concomitant with the change in slope of *c*-axis and decreased octahedral tilt, a structural transition to tetragonal symmetry occurs at $T = 373$ K. The structural transition is also associated with the reduction of the off centring of the Mn and Cr ions in their octahedral fluorine cages. The analysis of atomic positions shows that the space group of the high temperature phase is likely centrosymmetric $P4_2/mbc$. It should be stressed that $K_{1.2}Fe_2F_6$ also shows a distinct change in the *c*-axis expansivity at the ferroelectric-paraelectric $T_C = 490$ K. Hence, the *O*-*T* transition of $KMnCrF_6$ is not only a mere structural change, but most probably coincides with the ferroelectric-paraelectric transition. The structural transition occurs around $T \sim 350$ K in sample I and around $T \sim 400$ K in sample II. This is in good agreement with the ferroelectric-paraelectric $T_C = 354(10)$ K, which was estimated for sample I from the displacements $d(z)$ of Mn and Cr at $T = 300$ K. These findings highlight the intimate coupling of structural features and physical properties in the TTB fluorides, and the strength of crystallographic methods in the search for new functional materials.

4.4.2 The Local Structure

Analysis of the $G(r)$, which is a real-space distribution of the density of pairs of atoms, showed that the average structure obtained from Rietveld refinement is not a good description of the local geometry: The peaks corresponding to first neighbour pairs of *M*-F, K-F and F-F show distinct shoulders in the experimental data ($r = 1.5$ – 3.5 Å). The simulated $G(r)$ for the average $Ccc2$ structure and $P4_2bc$ model (obtained

from Rietveld fits of RT SXRD data) are very similar, indicating that the local structure is not influenced by the orthorhombic distortion. The fit of $G(r)$ can be considerably improved if the atomic coordinates are released within the constraints of $P4_2bc$ symmetry. The resulting fit is shown in Figure 4.17, together with a sketch of the perovskite-type subunit. Locally, the distortion and tilting of the octahedra is more pronounced as compared to the average structure. For example, the octahedral tilt angles along the c-axis are α(Mn2-F6-Cr1) = 163.7(4)° and α(Mn2-F7-Cr1) = 163.9(4)°.

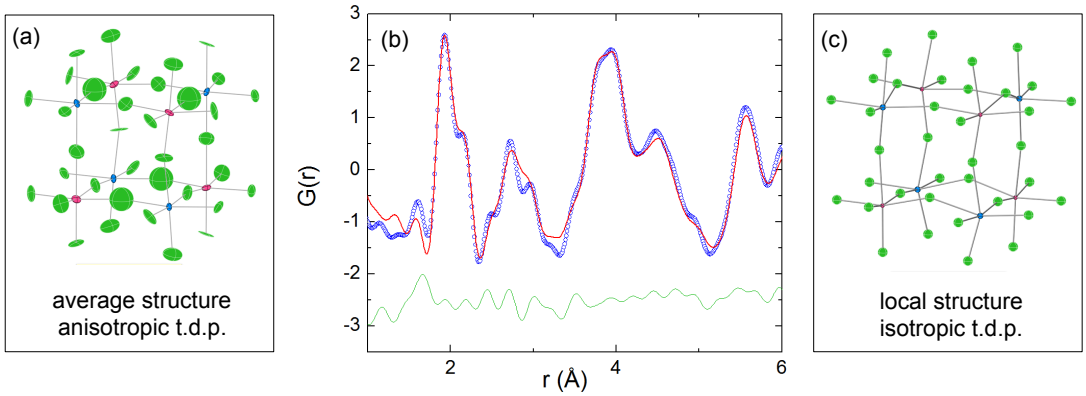

Figure 4.17: (a) The perovskite-type building block of the average crystal structure refined in space group $P4_2bc$, with anisotropic thermal displacement parameters (t.d.p.). (b) Observed $G(r)$ (open blue circles), calculated (red line) $G(r)$ and difference (green line) of $KMnCrF_6$ at RT, refined within the constraints of $P4_2bc$ symmetry and isotropic t.d.p. (c) Perovskite building block as obtained from the local structure refinement.

The structural model obtained from a Rietveld refinement using anisotropic thermal displacement factors (space group $P4_2bc$) features large thermal ellipsoids on the fluorine ions (Figure 4.17.a). It can be thought of as a superposition of a number of more tilted local units, reconciling the local and average structure model.

4.4.3 The Structure at Variable Pressures

To the best of our knowledge, no prior high-pressure structural studies of TTB materials were performed; hence the determined bulk modulus will be compared to related fluoride-perovskite structures. The isothermal bulk modulus of $KMnCrF_6$ (K_0 = 48.8(8) GPa), is smaller compared to perovskite type $KMnF_3$ (K_0 = 64(1) GPa) [29]. The orthorhombic distortion at ambient pressure is very small, and not resolved in the low-pressure data collected on the 2D detector at beamline BL10XU. However, the compressibilities of the a- and b- axis differ, and peak splitting

consistent with *Ccc*2 symmetry is observed at higher pressures. As a result of the geometry in TTB compounds, the unit cell *c*-axis is softest ($K_0(c) = 38.8(7)$ GPa) compared to the in plane *a*- and *b*- directions, as the cooperative tilting of MF_6 units along the *c*-axis compensate for the volume reduction more readily. The in-plane directions are more constrained geometrically and the *a*-axis is most rigid: $K_0(a) = 65(2)$ GPa, whereas $K_0(b) = 48(1)$ GPa. This is also reflected in the ratio of the lattice constants at highest ($p = 17.8$ GPa) and lowest pressures ($p = 0.19$ GPa) that are $a/a_{0.19} = 0.946$, $b/b_{0.19} = 0.937$ and $c/c_{0.19} = 0.920$.

4.4.4 Magnetic Properties

Correlation effects of the magnetically active ions govern the magnetic properties in TTB materials, but are complicated by geometric constraints. The magnetic structure is known for only two TTB fluoride materials, $KMnFeF_6$ and $K_{1.2}Fe_2F_6$ and were both described in space group *Pb'a*2'; the spins are constraint to the *ab*- plane and arrange antiparallel and star-like on the square and on the triangular units, respectively [30], [31]. The coupling of Mn^{2+}-Fe^{3+} and Fe^{2+}-Fe^{3+} is antiferromagnetic (d^5-d^5 and d^6-d^5 interactions) on the square perovskite units, but the triangular units evoke some degree of frustration. The resulting spin canting might give rise to a small magnetic moment responsible for the ferrimagnetic properties observed in magnetic susceptibility measurements ($T_N = 148$ K and 122 K for $KMnFeF_6$ and $K_{1.2}Fe_2F_6$ [32], [33]).

In the case of $KMnCrF_6$ three different types of exchange paths are present: Mn^{2+}-F-Cr^{3+}, Mn^{2+}-F-Mn^{2+}, Cr^{3+}-F-Cr^{3+}. The *d*-orbitals in Mn^{2+} are half filled (d^5, $e_g^2\, t_{2g}^3$), whereas the e_g orbital of Cr^{3+} remain empty (d^3, $t_{2g}^3\, e_g^0$). Each *M*-F-*M'* combination has three contributions, one σ (d_{x2-y2}) and two π (d_{xy}, d_{xz}; for bonding along the *x*-axis). The σ and π interactions between the e_g and t_{2g} orbitals of the transition metal are mediated via correlation superexchange mechanisms through the fluorine ligand. The different orbital contributions can be estimated according to the Goodenough-Kanamori rules, and the overall magnetic interactions for a given pair is the combined effect of all individual contributions [24]. The possible interactions are illustrated in Figure 4.18. The resulting interactions for the Mn^{2+} – Mn^{2+} (d^5 – d^5), Cr^{3+} – Cr^{3+} (d^3 – d^3) and Mn^{2+} – Cr^{3+} (d^5 – d^3) pairs are expected to be strongly AFM, moderately AFM and (very) weakly FM, respectively.

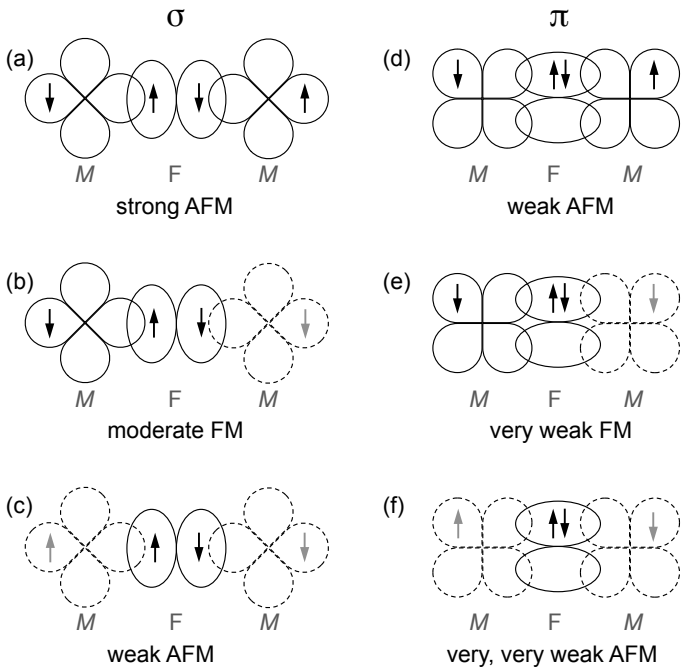

Figure 4.18: (a-f) The magnetic interactions according to the GKA rules (filled orbital: solid line, empty orbital: dashed line). (a – c) The three possible σ interactions strongly antiferromagnetic (AFM) [$d(e_g^2) - p - d(e_g^2)$], moderate ferromagnetic (FM) [$d(e_g^2) - p - d(e_g^0)$] and weak AFM [$d(e_g^0) - p - d(e_g^0)$]. (d – f) The exchange expected for the π interactions are weak AFM [$d(t_{2g}^2) - p - d(t_{2g}^2)$], very weak FM [$d(t_{2g}^2) - p - d(t_{2g}^0)$] and very, very weak AFM [$d(t_{2g}^0) - p - d(t_{2g}^0)$].

Let us consider the atomic arrangement proposed by Banks (Figure 4.19) [6]. In their model, Mn and Cr alternate along the *c*-axis on all crystallographic positions. They obtain their magnetic model (Figure 4.19) with four Mn-Mn pairs, four Cr-Cr pairs and 54 Mn-Cr pairs. All bond conditions except eight Mn-Cr pairs are satisfied. In this work, the room temperature structure of $KMnCrF_6$ was found to crystallise in the orthorhombic space group *Ccc*2, which implied that Mn and Cr on the extra-perovskite sites do not alternate along the *c*-axis. One possible spin arrangement for this structure is shown in Figure 4.19, with the maximum number of bond conditions satisfied. For ease of comparison only a section corresponding to the tetragonal cell is shown. The differences in atomic and possible spin arrangement are highlighted. The ratio of *M*-*M*′ pairs in this model is the same as in the one proposed by Banks (4x Mn-Mn, 4x Cr-Cr, 54x Mn-Cr). Likewise it is possible to satisfy all but eight pairs (4x Mn-Cr, 2x Cr-Cr, 2x Mn-Mn). For these hypothetical models, it is clear that the magnetism of $KMnCrF_6$ is dominated by the Mn-Cr interaction, which is in agreement with the experimental observations.

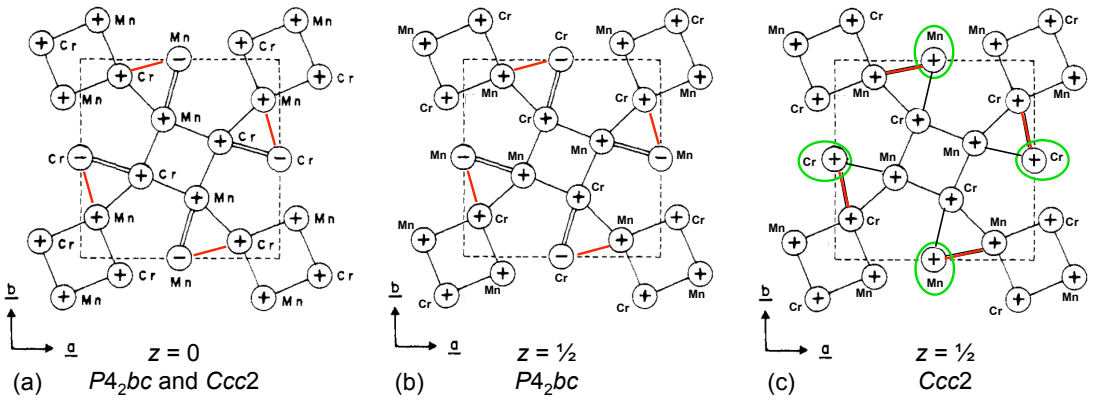

Figure 4.19: Possible spin arrangement at $z = 0$ and $z = ½$ in $KMnCrF_6$. Different spin directions are indicated by (+) and (–). The double line highlights cations pairs of the same species. The red lines indicate pairs for which the magnetic exchange interactions are not fulfilled. (a, b) Magnetic structure proposed by Banks in space group $P4_2bc$ [6]. (a, c) A possible magnetic order based on the ideal atomic arrangement in space group $Ccc2$. The green circles highlight the differences between (b) and (c).

Banks argued that from the relative strength of the interactions one can expect that short range order of Mn-Mn and Cr-Cr pairs occur at higher temperatures than the coupling of Mn-Cr pairs and that leads to long-range magnetic order [6]. Our magnetic susceptibility measurements confirm the overall ferromagnetic properties reported for the series $K_xMn_xCr_{1-x}F_6$ (negative divergence from Curie-Weiss behaviour in the χ_m^{-1} *vs.* temperature plot) [6]. The transition temperature $T_N =$ 23 K is lower compared to $KMnF_3$ ($T_N = 88$ K) and $KCrF_3$ ($T_N = 40$ K), which might be a result of the partially frustrated geometry [34], [35]. $KMnCrF_6$ can be described as a soft ferromagnet.

The majority of exchange interactions present are FM, and offer the comparison of $KMnCrF_6$ and the related $K_{1.2}Cr_{0.8}Fe_{1.2}F_6$ ($Cr^{3+}(d^3)$ – $Fe^{2+}(d^6)$, FM) [26]. The composition does not allow for the same order pattern of M^{2+} and M^{3+} cations as $KMnCrF_6$, but could resemble the order in $K_{1.2}Fe_2F_6$, i.e. one 8-fold site is occupied by Fe^{2+}, the other 8-fold and the 4-fold site are occupied by Cr^{3+} and Fe^{2+} in the ratio 3:1 and 1:1, respectively. However, an ordered pattern was not observed in XRD data and the perovskite sites in $K_{1.2}Cr_{0.8}Fe_{1.2}F_6$ were described as disordered (space group $P4/mbm$). Two AFM transitions are observed at $T = 37$ K and 17 K, and the M-H curves show a FM contribution below $T = 30$ K. The observed behaviour might be connected to AFM interactions of Fe-Fe and further ordering arising from Cr-Fe exchange coupling at lower temperatures. Clearly, more detailed structural and

magnetic characterizations are required to determine the nature of the ionic ordering (if present) and magnetic exchange in this mixed TTB fluoride.

4.4.5 Multiferroic Potential

To evaluate the potential multiferroic properties of $KMnCrF_6$, its structure is compared to other TTB fluorides that have been suggested to be multiferroic in the past, namely $K_{1.2-x}Fe_2F_6$ and $KMnFeF_6$. The TTB fluoride $K_{1.2}Fe_2F_6$ was characterized as an improper multiferroic material, in which the electrical polarization occurs as a result of the full CO and is of purely electronic origin where atomic displacements play a minor role [28]. In this system, ferroelasticity is strongly correlated to ferroelectricity. It was suggested that full charge order triggers ionic displacements, which may contribute to the electronic polarization [28]. However, $K_{0.6}FeF_3$ is a purely charge ordered material, different from the herein studied $KMnCrF_6$, which is chemically ordered. Furthermore, the different compositions allow for different type of ordering patterns.

A better comparison can be made with another member of the $K_{1.2-x}Fe_2F_6$ family, for instance with $K_{1.04}FeF_6$; its room temperature structure of was reported in the acentric space groups *P*4*bm* and $P4_2bc$ [24]. To increase our understanding of the relationship between structure and the emergence of ferroelectricity, the structures published for $K_{1.04}FeF_6$ were compared to the centric higher symmetry structures ($P4/mbm$ and $P4_2/mbc$) using the program PSEUDO [36]. This analysis revealed that the maximum apical displacements are $d(z, \text{Fe}) = 0.005$ Å, $d(z, \text{K}) = 0.01$ Å and $d(z, \text{F}) = -0.07$ Å (for $P4bm \rightarrow P4/mbm$), and $d(z, \text{Fe}) = -0.007$ Å, $d(z, \text{K}) = -0.007$ Å and $d(z, \text{F}) = -0.05$ Å (for $P4_2bc \rightarrow P4_2/mbc$). These small displacements point towards centrosymmetric structures, rather than the suggested acentric structures. This is consistent with an earlier report on the series $K_{1.2-x}Fe^{2+}_{1.2-x}Fe^{3+}_{0.8+x}F_6$ by Ravez *et al.* [37]. They linked the ferroelectric → paraelectric transition to the orthorhombic → tetragonal transition, which disappears for $x > 0.08$, i.e. $K_{1.12}FeF_6$ [37].

In addition to the iron compounds, the closely related $KMnFeF_6$ material was suggested to be potentially ferroelectric and multiferroic below its magnetic ordering temperature $T_C = 148$ K [4]. The prediction of $KMnFeF_6$ as potential multiferroic was based on the symmetry of the magnetic phase ($Pb'a2'$), instead of the pure nuclear phase ($P4_2bc$), because the point group of the later space group (4*mm*) does not allow the coexistence of ferroelectricity and ferromagnetism.

However, the maximum apical displacements of the published (RT) structure away from its centrosymmetric structure variant are small, i.e. $d(z, \mathrm{Mn}) =$ -0.003 Å, $d(z, \mathrm{Fe})$ = -0.003 Å, $d(z, \mathrm{K})$ = 0.002 Å and $d(z, \mathrm{F})$ = -0.06 Å (for $P4_2bc \rightarrow P4_2/mbc$).

In the light of these findings, it is very likely that $KMnCrF_6$ is ferroelectric and multiferroic. It possesses a non-centrosymmetric structure (space group *Ccc*2, polar point group *mm*2), with apical displacements exceeding $d(z) > 0.1$ Å (see Figure 4.16). It is potentially fully ionically (i.e. charge) ordered and magnetic long-range order is present at low temperatures. The magnetic properties reveal that $KMnCrF_6$ is a weak ferromagnet below T_N = 23 K, but some magnetic frustration is likely to occur due to the presence of triangular structural units.

The magnetoelectric effect describes the coupling of magnetic and electric orders, i.e. the influence of a magnetic field on the electrical polarisation, and that of an electrical field on the magnetisation. Nenert and Palstra noted that ferroelectric and ferromagnetic materials are more likely to show a sizeable magnetoelectric effect, which suggests to look for these properties in the search for new multiferroic materials [4]. The ferromagnetic and insulating character of $KMnCrF_6$ makes it a promising multiferroic candidate. In addition, the transition metal sublattice (which potentially gives rise to a ferroelectric polarization) is simultaneously carrying the magnetic properties, and a coupling of magnetic and ferroelectric ordering parameters is likely in the TTB fluorides. This is in contrast to most complex multiferroic materials, in which the magnetic and ferroelectric properties are connected to different ionic species, and are often only weakly coupled.

$KMnCrF_6$ is an interesting candidate, in which chemical order and octahedral tilting appear to be linked. The electrical polarization in $KMnCrF_6$ could arise from the combination of cationic displacements and tilting of the MF_6 octahedra. It is feasible to think that ferroelectricity and ferromagnetism couple at low temperatures. If this is the case, $KMnCrF_6$ could be described as a 'structural magnetic ferroelectric' material, similarly to $BaMF_4$ and $YMnO_3$ [38], [39].

4.5 Summary

The TTB fluoride $KMnCrF_6$ was reported to crystallise in a tetragonal space group, $P4_2bc$ [6]. Indeed, the high temperature structure ($T \geq 373$ K) was found to be $P4_2/mbc$, which is the centrosymmetric variant of the $P4_2bc$ structure. Bond-distance calculation show, that Mn and Cr occupy the perovskite sites occupied alternatingly, whilst the extra-perovskite site is occupied statistically. The tetragonal phase is stable at least up to $T = 950$ K.

On cooling to $T \approx 350$ K, a structural transition to orthorhombic symmetry (space group $Ccc2$) takes place, linked to the cooperative tilting of the MF_6 octahedra and the displacement of the transition metal cations away from the centre of fluorine octahedra. The distortion away from tetragonal symmetry is very subtle. However, it splits the extra-perovskite site, which is occupied by both Mn^{2+} and Cr^{3+} in the tetragonal phase. Thus the orthorhombic symmetry it may be an indication for full chemical order on all crystallographic sites. The structural transition from tetragonal to orthorhombic symmetry is also connected to an increase in the atomic positions away from their high-symmetry locations. Such displacements might give rise to a spontaneous electrical polarisation and suggest $KMnCrF_6$ is a potential ferroelectric material.

In addition to the ambient pressure variable temperature measurements, diffraction experiments were also carried out at high-pressure. Our results show that the orthorhombic distortion increases upon pressurisation, but that the $Ccc2$ structure remains robust up to $p = 18$ GPa.

Magnetic susceptibility measurements were employed to study the nature of the magnetic ordering. These revealed that $KMnCrF_6$ behaves as a weak ferromagnet with a transition temperature $T_N = 23$ K, in agreement with the earlier report by Banks *et al.* [6]. Although the ferroelectric polarisation was not measured, we suggest that $KMnCrF_6$ might be ferroelectric in the orthorhombic phase, which would make $KMnCrF_6$ a magnetic ferroelectric material.

4.6 References

[1] J.A. Ravez, S.C.; De Pape, R., *Journal of Applied Physics* 65 (1989) 4.

[2] S. Fabbrici, E. Montanari, L. Righi, G. Calestani, A. Migliori, *Chemistry of Materials* 16 (2004) 3007.

[3] F. Mezzadri, S. Fabbrici, E. Montanari, L. Righi, G. Calestani, E. Gilioli, F. Bolzoni, A. Migliori, *Physical Review B: Condensed Matter and Materials Physics* 78 (2008) 064111.

[4] G. Nénert, T. Palstra, *Journal of Physics: Condensed Matter* 19 (2007) 406213.

[5] E. Banks, O. Berkooz, J. De Luca, *Materials Research Bulletin* 6 (1971) 659.

[6] E. Banks, M. Shone, Y. Hong, R. Williamson, W. Boo, *Inorganic Chemistry* 21 (1982) 3894.

[7] E. Banks, S. Nakajima, G.J.B. Williams, *Acta Crystallographica, Section B: Structural Science* 35 (1979) 46.

[8] A.P. Hammersley, S. Svensson, M. Handland, A.N. Fitch, D. Haeusermann, *High Pressure Research* 14 (1996) 235.

[9] X. Qiu, J.W. Thompson, S.J.L. Billinge, *Journal of Applied Crystallography* 37 (2004) 678.

[10] H.K. Mao, J. Xu, P.M. Bell, *Journal of Geophysical Research* 91 (1986) 4673.

[11] H. Fujihisa, *Review of High Pressure Science and Technology* 1 (2005) 29.

[12] A.C. Larson, R.B.V. Dreele, Los Alamos National Laboratory Report LAUR 86-748 (2004) 1.

[13] B. Toby, *Journal of Applied Crystallography* 34 (2001) 210.

[14] C. Farrow, P. Juhas, J. Liu, D. Bryndin, E. Božin, J. Bloch, T. Proffen, S. Billinge, *Journal of Physics: Condensed Matter* 19 (2007) 335219.

[15] S.C. Abrahams, *Acta Crystallographica, Section A: Foundations of Crystallography* 50 (1994) 658.

[16] E. Kroumova, M. Aroyo, J. Perez-Mato, *Acta Crystallographica, Section B: Structural Science* 58 (2002) 921.

[17] S.C. Abrahams, *Acta Crystallographica* A50 (1994) 658.

[18] E. Kroumova, M. Aroyo, J. Perez-Mato, R. Hundt, *Acta Crystallographica, Section B: Structural Science* 57 (2001) 599.

[19] C. Capillas, E.S. Tasci, G. De La Flor, D. Orobengoa, J.M. Perez-Mato, M.I. Aroyo, *Zeitschrift für Kristallographie* 226 (2011) 186.

[20] S.W. Kim, S.-H. Kim, P.S. Halasyamani, M.A. Green, K.P. Bhatti, C. Leighton, H. Das, C.J. Fennie, *Chemical Science* 3 (2012) 741.

[21] P.J. Lin, L.A. Bursill, *Acta Crystallographica Section B: Structural Crystallography and Crystal Chemistry* 43 (1987) 504.

[22] J.A. Ravez, S.C.; Mercier, A.M.; Rabardel, L.; De Pape, R., *Journal of Applied Physics* 67 (1990) 3.

[23] R. Angel, *Reviews in Mineralogy and Geochemistry* 41 (2000) 35.

[24] S. Fabbrici, E. Montanari, L. Righi, G. Calestani, A. Migliori, *Chemistry of Materials* 16 (2004) 3007.

[25] A. Caramanian, N. Dupont, P. Gredin, A. De Kozak, *Zeitschrift für Anorganische und Allgemeine Chemie* 625 (1999) 933.

[26] R. Blinc, P. Cevc, A. Potocnik, B. Zemva, E. Goreshnik, D. Hanzel, A. Gregorovic, Z. Trontelj, Z. Jaglicic, V. Laguta, M. Perovic, N.S. Dalal, J.F. Scott, *Journal of Applied Physics* 107 (2010) 043511.

[27] R. Blinc, G. Tavcar, B. Zemva, E. Goreshnik, D. Hanzel, P. Cevc, A. Potocnik, V. Laguta, Z. Trontelj, Z. Jaglicic, *Journal of Applied Physics* 106 (2009) 023924.

[28] K. Yamauchi, S. Picozzi, *Physical Review Letters* 105 (2010) 107202.

[29] M. Guennou, P. Bouvier, G. Garbarino, J. Kreisel, E.K.H. Salje, *Journal of Physics: Condensed Matter* 23 (2011) 485901.

[30] P. Lacorre, J. Pannetier, G. Ferey, *Journal of Magnetism and Magnetic Materials* 94 (1991) 331.

[31] F. Mezzadri, G. Calestani, C. Pernechele, M. Solzi, G. Spina, L. Cianchi, F. Del Giallo, M. Lantieri, M. Buzzi, E. Gilioli, *Physical Review B: Condensed Matter and Materials Physic* 84 (2011) 104418.

[32] E. Banks, M. Shone, R. Williamson, W. Boo, *Inorganic Chemistry* 22 (1983) 3339.

[33] R. Blinc, G. Tavcar, B. Zemva, D. Hanzel, P. Cevc, C. Filipic, A. Levstik, Z. Jaglicic, Z. Trontelj, N. Dalal, *Journal of Applied Physics* 103 (2008) 074114.

[34] K.H. K. Hirakawa, T. Hashimoto, *Journal of the Physical Society of Japan*. 15 (1960) 2063.

[35] K.H. S. Yoneyama, *Journal of the Physical Society of Japan*. 21 (1966) 183.

[36] C. Capillas, E. Sururi Tasci, G. De La Flor, D. Orobengoa, J. Manuel Perez-Mato, M. Ilia Aroyo, Zeitschrift für Kristallographie 226 (2011) 186.

[37] J. Ravez, S. Abrahams, A. Mercier, L. Rabardel, R. De Pape, Journal of Applied Physics 67 (1990) 2681.

[38] C. Ederer, N.A. Spaldin, *Physical Review B: Condensed Matter and Materials Physics* 74 (2006) 024102.

[39] C. Fennie, K. Rabe, P*hysical Review B: Condensed Matter and Materials Physics* 72 (2005) 100103.

Chapter 5

The Charge Ordered Multiferroic $K_{0.6}CrF_3$

5.1 Introduction

Materials of the general formula K_xCrF_3 form three-dimensional networks of corner-sharing CrF_6 octahedra. The connectivity of the octahedra is dependent on the potassium content. The K^+ ions are located in the cavities, stabilize the framework and balance its negative charge. In general, the perovskite structure is stable up to 40 % potassium deficiency ($1 < x < 0.6$). Reduction of the potassium level leads to the formation of tetragonal tungsten bronze (TTB) type structures ($0.6 < x < 0.4$) and further hole doping results in materials adopting hexagonal tungsten bronze (HTB) type structures ($x < 0.4$).

The perovskite type materials $KCrF_3$ and $K_{0.9}CrF_3$ have been well characterized [1], [2], [3]. Increasing doping levels ($x = 0.80 – 0.65$) leads to the formation of mixtures of perovskite- and TTB-type phases (see Figure 5.1). The less well characterised TTB structure forms for $0.6 < x < 0.4$, which corresponds to completely filled and fully emptied pentagonal channels, respectively. Single-phase TTB products are obtained for $x < 0.6$, whereas lower potassium contents ($0.54 < x < 0.46$) results in a mixture of TTB and HTB phases, seemingly making $K_{0.6}CrF_3$ a line phase [4]. However, the synthetic conditions were not explored exhaustively and the possibility for existence of cation-deficient perovskite or TTB materials with lower potassium content than $x = 0.6$ cannot be ruled out.

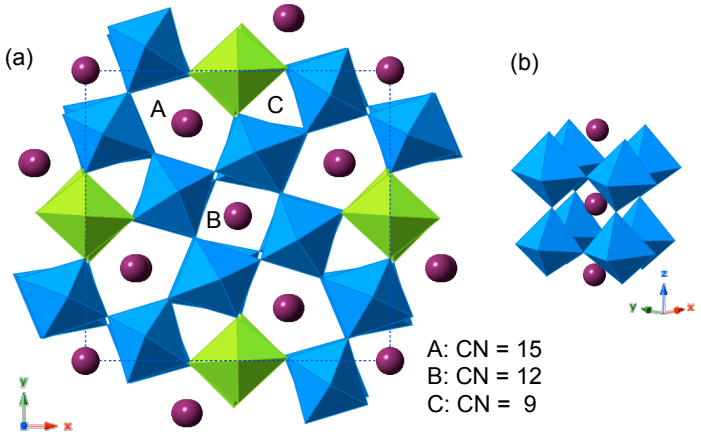

Figure 5.1: (a) The tetragonal tungsten bronze cell, adapted by the TTB fluorides. The blue and green octahedra correspond to the perovskite and extra-perovskite site. The pentagonal, square and triangular channel hosting the potassium are labelled A, B and C, respectively. (b) The perovskite-type subunit, in which potassium is coordinated 12-fold.

In this chapter, the structure and properties of $K_{0.6}CrF_3$ adopting the TTB structure are discussed as a function of variable temperature and pressure. The intriguing properties of $K_{0.6}FeF_3$, which is known for its frustrated magnetism and ferroelectric properties, have triggered this investigation. Single crystal diffraction measurements on $K_{0.6}FeF_3$ have revealed that it adopts an orthorhombic structure (space group *Pba*2) with partial Fe^{2+}/ Fe^{3+} order [5]. However, subsequent theoretical work showed that a fully charge ordered structure is needed to obtain an insulating state [6]. The optimized structure obtained from this calculation is a monoclinic distortion of the orthorhombic cell [6]. The symmetry lowering is induced by complete Fe^{2+}/ Fe^{3+} order, which determines the direction of the polarisation and is therefore responsible for the ferroelectric properties [6]. Similar to the Fe-based material, $K_{0.6}CrF_3$ adopts an orthorhombic distorted TTB structure (space group *Pba*2) at room temperature [4]. The ionic radii vary with the oxidation state of the metal ($r(Cr^{2+}$ HS) = 0.94 Å, $r(Cr^{3+})$ = 0.755 Å), and – for an ordered compound – this is expected to be reflected in the size of the [CrF_6] octahedra and the Cr-F bond distances [7]. Therefore, charge-order (CO) patterns can be deduced from the crystal structure determination. Further, it may be possible to establish the orbital ordering pattern of the Jahn-Teller (JT) active Cr^{2+} ion from the orientation of the elongated coordination octahedra.

5.2 Methods

5.2.1 Synthesis

Polycrystalline samples of $K_{0.6}CrF_3$ were prepared by Dr. Takeshi Nakagawa, (University of Edinburgh) via solid-state reaction from a stoichiometric mixture of KF, CrF_2 and CrF_3. The starting materials were pre-dried at 393 K for 12 hours under vacuum before carefully mixing and grinding them in an agate mortar inside an argon-filled glove box. The reactants were pelletised in a 7 mm die set with a hand-operated KBr pellet press. The pellets were contained in well-clamped gold tubes and sealed in a quartz tube under reduced Ar-atmosphere. Sample (A) was heated to 1023 K for 72 hours before being cooled to room temperature. Sample (B) was heated twice to 943 K for 120 hours, with intermediate re-grinding and re-pelletizing. Heating and cooling ramps were 100 K h^{-1} in both cases.

5.2.2 Synchrotron Powder Diffraction

High-resolution synchrotron X-ray diffraction experiments were performed on beamline ID31 ESRF, France (λ = 0.39992 Å and 0.35419 Å). To minimize the preferred orientation effects the samples were sealed in 0.5 mm thin-wall glass or quartz capillaries, which spun on the diffractometer axis during data collection. Diffraction profiles were recorded at various temperatures between T = 5 K and 873 K. The data were binned in the 2θ range 0.1° – 48° to a step of 0.002°.

High-pressure synchrotron X-ray diffraction experiments were performed on beamline BL10XU, SPring-8, Japan (λ = 0.41429 Å). The powder sample together with a small ruby chip was loaded in a diamond anvil cell (DAC); Helium was used as a hydrostatic pressure-transmitting medium. The applied pressure was measured immediately before and after exposure by the ruby fluorescence method without dismounting the cell. The calibration method suggested by Mao was used to determine the pressure from the shift of the maxima in fluorescence. Diffraction patterns were collected at room temperature between p = 0.2 GPa and 18.5 GPa. Data was recorded using a flat image plate detector and integrated with a step of 0.005° using WinPIP [8].

Analysis of all diffraction data was carried out with the GSAS suite of Rietveld programs [9], [10].

5.2.3 Physical Properties Measurement

The temperature dependence of magnetization was determined following zero-field cooled and field-cooled (ZFC, FC) protocols in magnetic fields H = 10, 20, 100, 1000 and 10000 Oe. Magnetic hysteresis loops up to H = 50000 Oe were collected at 15 K. The characteristics and transition temperatures of both samples (A) and (B) are in good agreement.

5.2.4 Elemental Analysis

The weight fractions of K and Cr of sample A were determined by ICP elemental analysis from a solution of $K_{0.6}CrF_3$ in diluted $HCl_{(aq)}$. The experimental and theoretical weight fractions are K: 30.5 wt%, Cr: 69.5 % and K: 31.1 wt% Cr: 68.9 wt%. Assuming full fluorine occupancy, the experimental stoichiometry is $K_{0.584}CrF_3$.

5.3 Results

5.3.1 The Room Temperature Structure

The structure of $K_{0.6}CrF_3$ was previously described as an orthorhombic distorted TTB type, space group *Pba*2 [4]. Compared to the conventional tetragonal cell (space group *P*4/*mbm*), the *c*-axis is doubled ($c = 2c_{TTB}$) due to the Cr^{2+}/Cr^{3+} charge ordering (CO) around the perovskite cage. The orthorhombic distortion of the unit cell was linked to the cooperative orbital ordering (OO) of the Cr^{2+} ions [4].

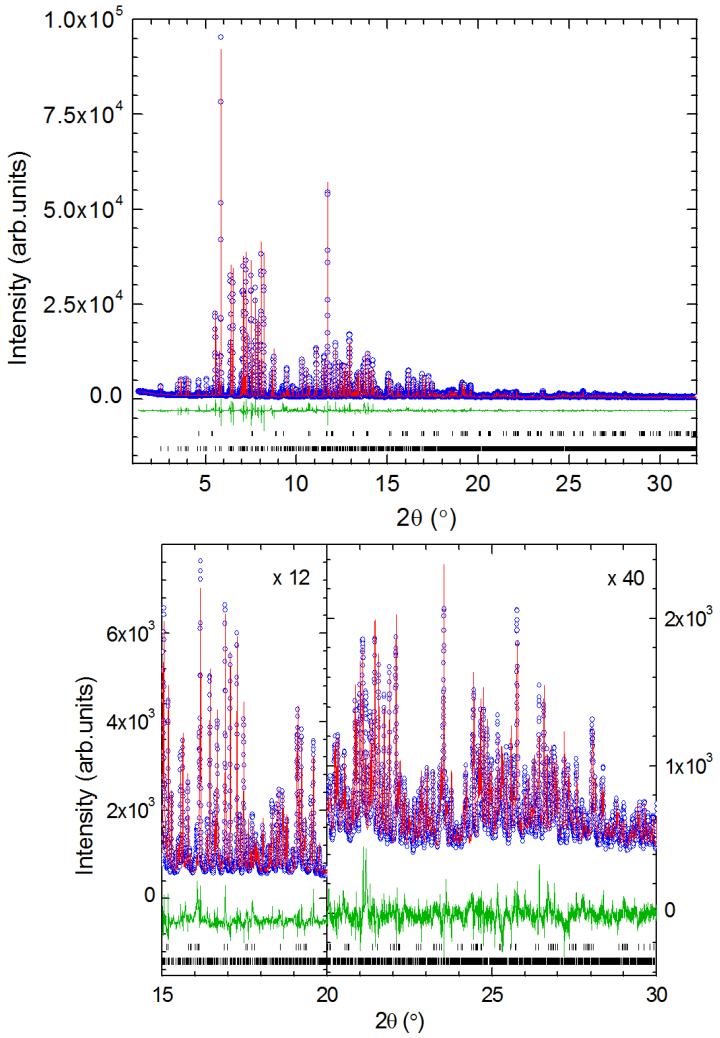

Figure 5.2: (top): Observed (open blue circles), calculated (red line) and difference (green line) synchrotron powder diffraction Rietveld profile of $K_{0.6}CrF_3$ at $T = 300$ K (space group *Pba*2), collected at ID31, $\lambda = 0.39992$ Å. (bottom): Magnification of the high 2θ region of the synchrotron powder diffraction Rietveld profile. Bottom and top tick marks indicate the reflection positions of the $K_{0.6}CrF_3$ and $KCrF_4$ phase, respectively.

Indeed, all major peaks of the room temperature diffraction profile collected at the high-resolution powder-diffraction beamline ID31 (ESRF, France; λ = 0.39992 Å) could be indexed assuming orthorhombic *Pba*2 symmetry. The presence of a minority K_2CrF_4 phase (~ 4 wt %), was also observed, see Figure 5.2. The doubling of the *c*-axis is confirmed by the presence of e.g. the (201), (021), (211) and (121) reflections. The refined lattice constants are *a* = 13.14861(5) Å, *b* = 12.55886(4) Å and *c* = 7.84013(2) Å.

space group: *Pba2*		No. 32		*T* = 300 K	
a = 13.14861(5) Å		*b* = 12.55886(4) Å		*c* = 7.84013(2) Å	*V* = 1294.652(5) Å^3
		x	*y*	*z*	B_{iso}/ Å^2
Cr1	*2b*	0.5	0	0.241(1)	0.46(2)
Cr2	*2b*	0.5	0	0.757(1)	0.46(2)
Cr3	*4c*	0.4210(6)	0.2808(5)	0.250(1)	0.46(2)
Cr4	*4c*	0.4208(6)	0.2848(5)	0.749(1)	0.46(2)
Cr5	*4c*	0.2142(5)	0.0639(5)	0.2513(9)	0.46(2)
Cr6	*4c*	0.2121(5)	0.0688(5)	0.7518(9)	0.46(2)
K1	*2a*	0.5	0.5	-0.004(2)	1.87(6)
K2	*2a*	0	0	0.486(2)	1.87(6)
K3	*4c*	0.6605(5)	0.1808(6)	1.003(2)	1.87(6)
K4	*4c*	0.1724(5)	0.3185(6)	0.493(2)	1.87(6)
F1	*2b*	0.5	0	0.528(3)	1.37(6)
F2	*2b*	0.5	0	-0.015(4)	1.37(6)
F3	*4c*	0.4430(7)	0.281(1)	0.002(3)	1.37(6)
F4	*4c*	0.4108(8)	0.294(1)	0.502(4)	1.37(6)
F5	*4c*	0.1962(8)	0.0839(8)	0.010(3)	1.37(6)
F6	*4c*	0.2134(8)	0.0435(7)	0.499(4)	1.37(6)
F7	*4c*	0.265(1)	0.201(1)	0.221(2)	1.37(6)
F8	*4c*	0.278(1)	0.217(1)	0.727(2)	1.37(6)
F9	*4c*	0.351(1)	-0.016(2)	0.248(3)	1.37(6)
F10	*4c*	0.337(1)	-0.011(2)	0.725(2)	1.37(6)
F11	*4c*	0.513(1)	0.162(1)	0.221(2)	1.37(6)
F12	*4c*	0.499(1)	0.148(1)	0.711(2)	1.37(6)
F13	*4c*	0.353(1)	0.423(2)	0.204(2)	1.37(6)
F14	*4c*	0.138(1)	-0.077(1)	0.726(2)	1.37(6)
F15	*4c*	0.571(1)	0.377(1)	0.245(3)	1.37(6)
F16	*4c*	0.075(1)	0.152(1)	0.701(2)	1.37(6)
χ^2 = 20.53		F^2 = 9.33 %		wR_p = 12.99 %	R_p = 8.69 %

Table 5.1: Results of Rietveld refinement of room temperature SXRD diffraction profile of $K_{0.6}CrF_3$, (space group *Pba*2) collected at ID31. There were 72 refined structural parameters.

After confirming the size and symmetry of the unit cell, the atomic positions and contents of the unit cell were determined. The *Pba*2 model published for $K_{0.6}FeF_3$ was used to obtain starting coordinates for the refinement [5]. Soft constraints

initially applied to the transition metal fluoride bonds (Cr-F; d = 2.0 ± 0.3 Å) were removed at later stages of the refinement process. Occupancies of chromium and potassium refined to *Occ.* = 1 within error and were fixed to unity in the final refinement cycles. The pentagonal and square sites (*4c* and *2a*, respectively) hosting the potassium are fully occupied giving a stoichiometry of $K_{0.6}CrF_3$, which corresponds to the results of the elemental analysis. The results of the refinement are summarized in Table 5.1.

It was proposed that the *c*-axis of K_xCrF_3 is doubled as a result of CO [4]. A CO pattern should be reflected in a distinct distribution of Cr-F bond distances, due to the differences in ionic radii of Cr^{2+} and Cr^{3+} ($r(Cr^{2+}$, HS) = 0.94 Å and $r(Cr^{3+})$ = 0.755 Å) [7]. Furthermore, possible OO patterns of JT active Cr^{2+} may present in the orientation of JT-elongated [CrF_6] octahedra. The possible ordering patterns in space group *Pbam* are limited (20 Cr atoms per unit cell distributed over three crystallographic sites). Therefore, the structural analysis on $K_{0.6}CrF_3$ was continued in space group *Pba*2, which allows for more and different CO patterns. The Cr-F bond distances obtained from the *Pba*2 structure (Table 5.1) are listed in Table 5.2.

Cr1_F	d/ Å	Cr2_F	d/ Å	Cr3_F	d/ Å
Cr1_F1	2.25(2)	Cr2_F1	1.79(2)	Cr3_F3	1.96(3)
Cr1_F2	2.01(4)	Cr2_F2	1.79(4)	Cr3_F4	1.99(3)
Cr1_F9	1.98(2)	Cr2_F10	2.16(2)	Cr3_F7	2.30(1)
Cr1_F9	1.98(2)	Cr2_F10	2.16(2)	Cr3_F11	1.93(2)
Cr1_F11	2.05(1)	Cr2_F12	1.90(1)	Cr3_F13	2.03(2)
Cr1_F11	2.05(1)	Cr2_F12	1.90(1)	Cr3_F15	2.32(2)
average	2.05(2)	average	1.950(2)	average	2.09(2)

Cr4_F	d/ Å	Cr5_F	d/ Å	Cr6_F	d/ Å
Cr4_F3	2.01(3)	Cr5_F5	1.92(2)	Cr6_F5	2.05(2)
Cr4_F4	1.94(3)	Cr5_F6	1.96(3)	Cr6_F6	2.01(3)
Cr4_F8	2.07(1)	Cr5_F7	1.86(2)	Cr6_F8	2.06(2)
Cr4_F12	2.02(2)	Cr5_F9	2.05(2)	Cr6_F10	1.94(2)
Cr4_F14	1.92(2)	Cr5_F13	2.01(2)	Cr6_F14	2.08(2)
Cr4_F16	2.21(2)	Cr5_F15	2.02(2)	Cr6_F16	2.12(2)
average	2.03(2)	average	1.97(2)	average	2.04(2)

Table 5.2: Bond-distances obtained from Rietveld refinement (space group *Pba*2) of room temperature diffraction profile of $K_{0.6}CrF_3$. Cr1 and Cr2 are located on the extra-perovskite (2*b*) sites, whereas Cr3, Cr4, Cr5 and Cr6 occupy the perovskite (4*c*) sites

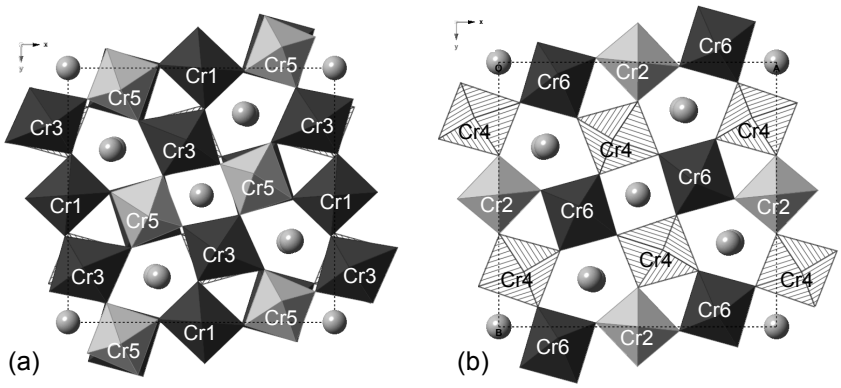

Figure 5.3: The room temperature phase of $K_{0.6}CrF_3$, space group *Pba*2, at $z = 0.25$ (a) and $z = 0.75$ obtained from Rietveld refinement. Bond valence calculations were used to assist the assignment of Cr oxidation states. (b) Cr1 and Cr2 occupy the extra-perovskite (2*b*) sites, whereas Cr3 to Cr6 are located on the perovskite (4*c*) sites. Dark and light octahedra can be assigned to Cr^{2+} and Cr^{3+}, respectively, whereas striped octahedra correspond to an intermediate oxidation state.

The ordering pattern of Cr^{2+}/ Cr^{3+} was established by analysing the bond-distances via bond-valence calculations using the program VaList [11]. Indeed, the Cr-F bond distances indicate that Cr^{2+} occupies the positions of Cr1 (2*b*, $z = 0.25$), Cr3 (4*c*, $z = 0.25$) and Cr6 (4*c*, $z = 0.75$), whereas Cr^{3+} can be located on the Cr2 (2*b*, $z = 0.75$) and Cr5 (4*c*, $z = 0.25$). For these sites, the deviation from the assumed valence state are smaller than 15%, whereas the deviation from the respective other valence state are significantly higher, i.e. ~ 30 %. On the other hand, the Cr4 position appears to be of mixed valence: the deviation from the calculated oxidation state is comparable for the 2+ and 3+ state (18 % and 24 %, respectively). The bond distances and results of the bond-valence calculation are summarised in Table 5.2 and Table 5.3, respectively; the resulting charge order pattern is shown in Figure 5.3.

The TTB fluorides are known for their ferroelectric properties, which require the abscence of an inversion centre. This can be tested through comparison of the atomic positions in the polar and apolar space group settings. In this case space group *Pbam* is the centrosymmetric supergroup of *Pba*2. However, the alternating order of Cr^{2+} and Cr^{3+} along the *c*-axis cannot be obtained in the *Pbam* setting. Therefore, the CO pattern of $K_{0.6}CrF_3$ justifies the description in the polar setting.

Atom no./ Wyckoff site	assumed valence state	Bond Valence sum	% Deviation from assumed valence state	Reference
Cr1 (*2b*)	2+	2.193*	10	b
Cr1 (*2b*)	2+	2.651	33	e
Cr1 (*2b*)	3+	2.118	29	a
Cr1 (*2b*)	3+	2.022	33	b
average		2.2		
Cr2 (*2b*)	2+	3.052	53	b
Cr2 (*2b*)	2+	3.688	84	e
Cr2 (*2b*)	3+	2.947*	2	a
Cr2 (*2b*)	3+	2.815	6	b
average		3.1		
Cr3 (*4c*)	2+	2.110*	5	b
Cr3 (*4c*)	2+	2.550	27	e
Cr3 (*4c*)	3+	2.038	32	a
Cr3 (*4c*)	3+	1.945	35	b
average		2.2		
Cr4 (*4c*)	2+	2.357*	18	b
Cr4 (*4c*)	2+	2.847	42	e
Cr4 (*4c*)	3+	2.276	24	a
Cr4 (*4c*)	3+	2.174	28	b
average		2.4		
Cr5 (*4c*)	2+	2.7	35	b
Cr5 (*4c*)	2+	3.262	63	e
Cr5 (*4c*)	3+	2.608*	13	a
Cr5 (*4c*)	3+	2.491	17	b
average		2.8		
Cr6 (*4c*)	2+	2.229*	11	b
Cr6 (*4c*)	2+	2.693	35	e
Cr6 (*4c*)	3+	2.15	28	a
Cr6 (*4c*)	3+	2.056	31	b
average		2.3		

* marks most consistent valence state

[a] Brown and Altermatt, (1985), Acta Cryst. B41, 244-247 (empirical)
[b] Brese and O'Keeffe, (1991), Acta Cryst. B47, 192-197 (extrapolated)
[e] I.D.Brown Private communication

Table 5.3: Results of bond-valence calculations carried out with the VaList program [11]. Cr1, Cr3 and Cr6 can clearly be assigned to a 2+ oxidation state, whereas Cr2 and Cr5 correspond to Cr in 3+ oxidation state. Cr4 appears to have mixed valence.

5.3.2 The Room Temperature Superstructure

As mentioned in the previous section, the *Pba*2 model used implies only partial charge order $K_{0.6}CrF_3$. A fully CO model is possible if the symmetry is lowered to monoclinic and could be identified experimentally by the presence of additional reflections. Here, the possible superstructures were limited to the three monoclinic subgroups of *Pba*2, in analogy to the theoretical analysis reported for $K_{0.6}FeF_3$ [6]. Indeed, a more detailed inspection of the room temperature diffraction profile revealed the presence of small peaks at low angles (d_1 = 1.75°, d_2 = 1.83° in 2θ; λ = 0.3999 Å). These peaks are not indexed in *Pba*2, but can be indexed with a monoclinic distorted cell that was suggested for $K_{0.6}FeF_3$ as shown in Figure 5.4 [6]. A further peak is observed at d_1 = 1.55° and is not indexed by the monoclinic space groups. Whilst it is clear that this peak is not related to a multiple of the *Pba*2 unit cell (e.g. doubled or tripled lattice constants), it may be related to a triclinic cell or an arise from an unknown impurity phase.

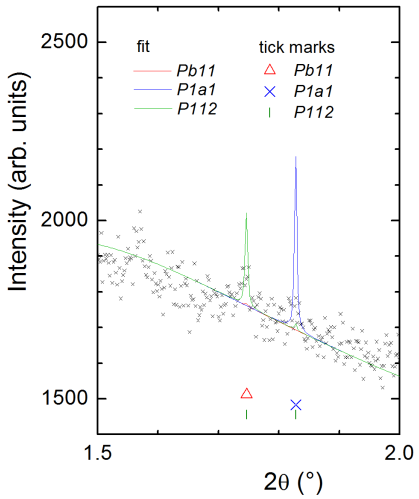

Figure 5.4: Superlattice peaks observed in the room temperature diffraction profile of $K_{0.6}CrF_3$, collected at beamline ID31 (λ = 0.3999 Å). The monoclinic space groups *Pb*11, *P*1*a*1 and *P*112 index the first, second and both reflections, respectively.

The observed superlattice peaks of $K_{0.6}CrF_3$ do not indicate an increase in unit cell size typically observed as a result of [MX_6] tilt modulation as for example in the TTB niobates [12]. The driving force of the observed symmetry lowering must therefore be connected to full CO, which does not require a larger unit cell. Hence, only the three monoclinic subgroups of *Pba*2, i.e. *P*1*a*1, *Pb*11 and *P*112, were considered candidate structures, each breaking two of the four symmetry operations of *Pba2* and leading to a different CO pattern, displayed in Figure 5.5 [6].

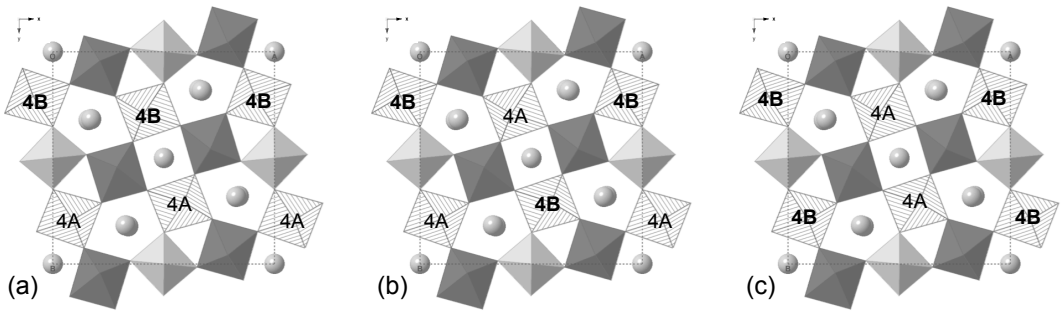

Figure 5.5: The unit cells of the monoclinic models showing the different type of splitting of the Cr4 site (mixed occupied *4c* site in *Pba*2) at $z = 0.75$. (a) – (c): *P*1*a*1, *Pb*11 and *P*112.

The space-groups *Pb11* and *P1a1* index the first and second superlattice peak as $(100)_{Pb11}$ and $(100)_{P1a1}$, respectively; but only space group *P112* indexes both reflections as $(100)_{P112}$ and $(010)_{P112}$. Nevertheless, starting models for all three space groups were calculated from the refined *Pba*2 structure. To limit the number of structural parameters, only the positions of the mixed Cr site (Cr4) and bonded F were refined in addition to the lattice constants and scale factors.

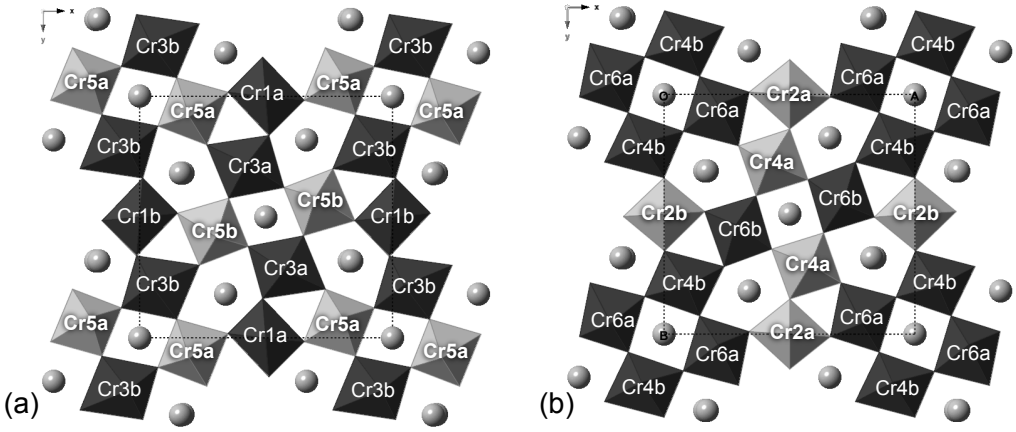

Figure 5.6: The fully CO room temperature phase of $K_{0.6}CrF_3$, space group *P*112, at $z = 0.25$ (a) and $z = 0.75$ (b). Dark and light octahedra can be assigned to Cr^{2+} and Cr^{3+}, respectively.

Parallel Rietveld refinements statistics revealed that the most suited space-group is *P*112. This agrees with the fact that only space group *P*112 indexed both superlattice peaks. The atomic positions of Cr4 (mixed valence in *Pba*2 model) and of F3, F4, F8, F12, F14 and F16 (first neighbours) were refined and the results are summarized in Table 5.4. The final structure was used for bond-valence calculations, which were carried out using the program VaList (see Table 5.5) [11]. The mixed valence site Cr4 (*4c*) split into Cr4a and Cr4b positions (*2e*) and changed from mixed valence $Cr^{2.5+}$ to charge ordered Cr^{3+} (Cr4a) and Cr^{2+} (Cr4b) (see Table 5.3 and Table 5.5). It is noted

that the valence state of Cr4b can be assigned more clearly than Cr4a (9 % and 18 % deviation from assumed oxidation state, respectively). The resulting CO pattern is shown in Figure 5.6.

space group: *P112*		No. 3		T = 300 K
a = 13.14851(5) Å		b = 12.55884(4) Å		c = 7.84013(2) Å
		γ = 89.980(2)°		V = 1294.641(5) Å^3
		x	*y*	*z*
Cr4a	*2e*	0.425(1)	0.284(1)	0.752(3)
Cr4b	*2e*	0.916(1)	0.215(1)	0.747(3)
F3a	*2e*	0.426(2)	0.279(3)	0.000(8)
F3b	*2e*	0.956(2)	0.219(2)	0.002(8)
F4a	*2e*	0.416(3)	0.289(4)	0.500(8)
F4b	*2e*	0.909(3)	0.201(3)	0.502(8)
F8a	*2e*	0.295(2)	0.214(2)	0.715(4)
F8b	*2e*	0.762(2)	0.282(2)	0.744(5)
F12a	*2e*	0.500(3)	0.145(4)	0.709(7)
F12b	*2e*	0.999(3)	0.348(4)	0.711(7)
F14a	*2e*	0.143(3)	0.924(4)	0.715(4)
F14b	*2e*	0.634(3)	0.577(4)	0.737(6)
F16a	*2e*	0.077(3)	0.155(3)	0.701(6)
F16b	*2e*	0.572(3)	0.355(3)	0.701(6)
χ^2 = 20.21		F^2 = 9.66 %	wR_p = 12.91 %	R_p = 8.58 %

Table 5.4: Results of Rietveld refinement of room temperature (T = 300 K) SXRD diffraction profile of $K_{0.6}CrF_3$, (space group $P112$) collected at ID31. Only the lattice constants, scale factors and atomic positions of Cr4 and attached fluorine (F3, F4, F8, F12, F14, F16) were refined; there were 48 refined structural parameters. Isotropic temperature factors were fixed to values obtained from *Pba*2 refinement: B_{iso}(Cr) = 0.46(2) Å^2; B_{iso}(K): 1.87(6) Å^2; B_{iso}(F): 1.37(6) Å^2. The full details are printed on the following page.

Table 5.4 (continued).

space group *P112*		No. 3	*T* = 300 K	*a* = 13.14851(5) Å	*b* = 12.55884(4) Å		*c* = 7.84013(2) Å		*V* = 1294.641(5) Å^3
		x	*y*	*z*			*x*	*y*	*z*
Cr1a	*2e*	0.5	0	0.2407	F4a	*2e*	0.416(3)	0.289(4)	0.500(8)
Cr1b	*2e*	0	0.5	0.2407	F4b	*2e*	0.909(3)	0.201(3)	0.502(8)
Cr2a	*2e*	0.5	0	0.7569	F5a	*2e*	0.1962	0.0839	0.0101
Cr2b	*2e*	0	0.5	0.7569	F5b	*2e*	0.6962	0.4161	0.0101
Cr3a	*2e*	0.421	0.2808	0.2499	F6a	*2e*	0.2134	0.0435	0.499
Cr3b	*2e*	0.921	0.2192	0.2499	F6b	*2e*	0.7134	0.4565	0.499
Cr4a	*2e*	0.425(1)	0.284(1)	0.752(3)	F7a	*2e*	0.2651	0.2007	0.2208
Cr4b	*2e*	0.916(1)	0.215(1)	0.747(3)	F7b	*2e*	0.7651	0.2993	0.2208
Cr5a	*2e*	0.2142	0.0639	0.2513	F8a	*2e*	0.295(2)	0.214(2)	0.715(4)
Cr5b	*2e*	0.7142	0.4361	0.2513	F8b	*2e*	0.762(2)	0.282(2)	0.744(5)
Cr6a	*2e*	0.2121	0.0688	0.7518	F9a	*2e*	0.3505	0.984	0.2483
Cr6b	*2e*	0.7121	0.4312	0.7518	F9b	*2e*	0.8505	0.516	0.2483
K1a	*2e*	0	0	0.9962	F10a	*2e*	0.3374	0.9891	0.725
K1b	*2e*	0.5	0.5	0.9962	F10b	*2e*	0.8374	0.5109	0.725
K2a	*2e*	0	0	0.4856	F11a	*2e*	0.5126	0.1622	0.221
K2b	*2e*	0.5	0.5	0.4856	F11b	*2e*	0.0126	0.3378	0.221
K3a	*2e*	0.6605	0.1808	0.003	F12a	*2e*	0.500(3)	0.145(4)	0.709(7)
K3b	*2e*	0.1605	0.3192	0.003	F12b	*2e*	0.999(3)	0.348(4)	0.711(7)
K4a	*2e*	0.1724	0.3185	0.4927	F13a	*2e*	0.3527	0.4228	0.2042
K4b	*2e*	0.6724	0.1815	0.4927	F13b	*2e*	0.8527	0.0772	0.2042
F1a	*2e*	0.5	0	0.5281	F14a	*2e*	0.143(3)	0.924(4)	0.715(4)
F1b	*2e*	0	0.5	0.5281	F14b	*2e*	0.634(3)	0.577(4)	0.737(6)
F2a	*2e*	0.5	0	0.985	F15a	*2e*	0.5713	0.3771	0.2452
F2b	*2e*	0	0.5	0.985	F15b	*2e*	0.0713	0.1229	0.2452
F3a	*2e*	0.426(2)	0.279(3)	0.000(8)	F16a	*2e*	0.077(3)	0.155(3)	0.701(6)
F3b	*2e*	0.956(2)	0.219(2)	0.002(8)	F16b	*2e*	0.572(3)	0.355(3)	0.701(6)
B_{iso}/ Å^2: Cr: 0.46(2); K: 1.87(6); F: 1.37(6)				χ^2 = 20.21	F^2 = 9.66 %		wR_p = 12.91 %		R_p = 8.58 %

Atom no.	assumed Valence state	Bond valence sum	% Deviation from assumed valence state	Ref.	Atom no.	assumed Valence state	Bond valence sum	% Deviation from assumed valence state	Ref.
Cr1a	2+	2.199*	10	b	Cr4a	2+	2.544	27	b
Cr1a	2+	2.659	33	e	Cr4a	2+	3.075	54	e
Cr1a	3+	2.124	29	a	Cr4a	3+	2.457*	18	a
Cr1a	3+	2.028	32	b	Cr4a	3+	2.347	22	b
Cr1b	2+	2.199*	10	b	Cr4b	2+	2.175*	9	b
Cr1b	2+	2.659	33	e	Cr4b	2+	2.629	31	e
Cr1b	3+	2.124	29	a	Cr4b	3+	2.101	30	a
Cr1b	3+	2.028	32	b	Cr4b	3+	2.007	33	b
Cr2a	2+	3.174	59	b	Cr5a	2+	2.702	35	b
Cr2a	2+	3.836	92	e	Cr5a	2+	3.264	63	e
Cr2a	3+	3.067*	2	a	Cr5a	3+	2.609*	13	a
Cr2a	3+	2.928*	2	b	Cr5a	3+	2.492	17	b
Cr2b	2+	2.942	47	b	Cr5b	2+	2.702	35	b
Cr2b	2+	3.554	78	e	Cr5b	2+	3.264	63	e
Cr2b	3+	2.841*	5	a	Cr5b	3+	2.609*	13	a
Cr2b	3+	2.712	10	b	Cr5b	3+	2.492	17	b
Cr3a	2+	2.137*	7	b	Cr6a	2+	2.177*	9	b
Cr3a	2+	2.581	29	e	Cr6a	2+	2.632	32	e
Cr3a	3+	2.062	31	a	Cr6a	3+	2.102	30	a
Cr3a	3+	1.969	34	b	Cr6a	3+	2.008	33	b
Cr3b	2+	2.066*	3	b	Cr6b	2+	2.277*	14	b
Cr3b	2+	2.496	25	e	Cr6b	2+	2.752	38	e
Cr3b	3+	1.995	33	a	Cr6b	3+	2.198	27	a
Cr3b	3+	1.904	37	b	Cr6b	3+	2.1	30	b

* marks most consistent valence state
[a] Brown and Altermatt, (1985), Acta Cryst. B41, 244-247 (empirical)
[b] Brese and O'Keeffe, (1991), Acta Cryst. B47, 192-197 (extrapolated)
[e] I.D.Brown Private communication

Table 5.5: Results of bond-valence calculations carried out with the VaList program [11] based on the refinement in space group *P*112 (cf. table 5.4). All Cr atoms occupy 2*e* sites. The fourfold mixed valence Cr4 site of *Pba*2 split into Cr4a and Cr4b site in *P*112, which can be assigned to Cr^{3+} and Cr^{2+}, respectively.

5.3.3 The Structure at High Temperatures

On heating, structural phase transitions are observed from monoclinic to orthorhombic at $T = 423$ K and then to tetragonal at $T = 823$ K, respectively. The superlattice peaks of the *P*112 phase vanish at the monoclinic → orthorhombic transition temperature. But their small intensities make it difficult to judge their disappearance visually. Nevertheless, the superlattice peaks of the structure disappear for $T \geq 473$ K. The transition is also accompanied by a change in slope of the *c*-axis and an increase in the monoclinic angle from $\gamma = 89.980(2)°$ ($T = 300$ K) to $\gamma = 89.997(2)°$ ($T \approx 423$ K), see Figure 5.7 and Figure 5.8.

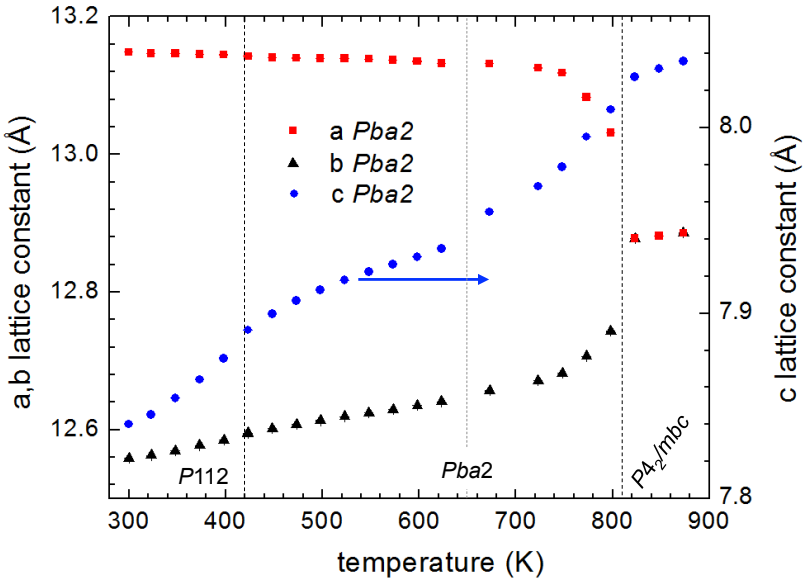

Figure 5.7: Temperature dependence of the lattice constants of $K_{0.6}CrF_3$, as obtained from Rietveld refinements of the high-resolution powder diffraction data collected at ID31. The structural models used are *P*112 (T = 300 K – 423 K), *Pba*2 (T = 473 K – 800 K) and $P4_2/mbc$ (T = 823 K – 873 K). Further test structures include a *Pba*2 model (T = 300 K – 423 K), a *Pbam* model (T = 400 – 800 K) and a *P*4*bm*, a $P\bar{4}b2$, and a $P4_2bc$ model (T = 823 – 873 K). The structural phase transitions from monoclinic to orthorhombic at $T \approx 425$ K and then to tetragonal at $T \approx 823$ K are marked. A further change of slope is observed for the *c*-axis at $T \approx$ 650 K and is connected to a change in octahedral tilting.

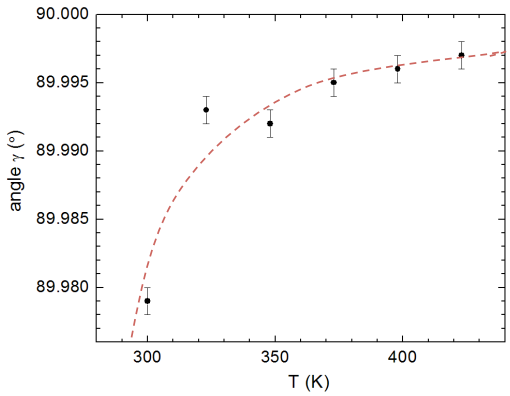

Figure 5.8: Temperature dependence of the monoclinic angle γ of the monoclinic *P*112 cell. The angle approaches $\gamma = 90°$ at T = 423 K. The dashed line is a guide to the eye only.

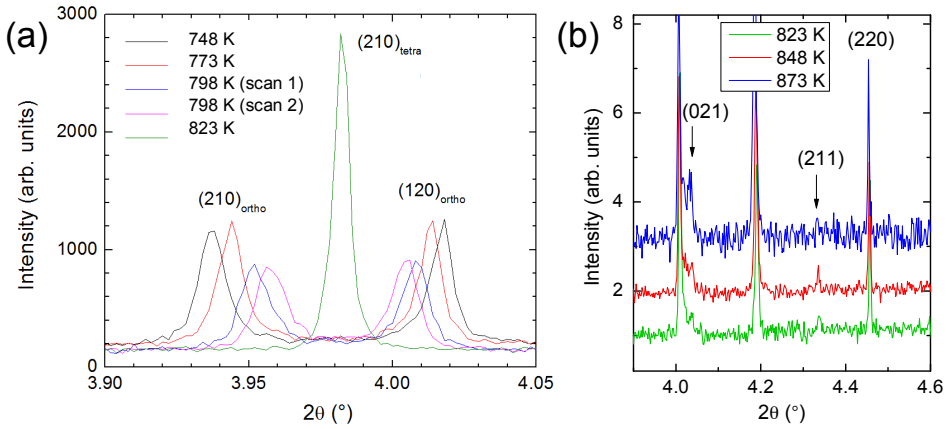

Figure 5.9: (a) Temperature dependence of the $(210)_O$ and $(120)_O$ reflection, which merge into the $(210)_T$ at T = 823 K. (b) The (021) and (211) reflection are still present in the diffraction profile collected at T = 873 K, showing that the c-axis doubling is preserved.

Between T = 423 K and 623 K the lattice adopts the *Pba*2 symmetry and expands smoothly. Further increases in temperature gradually reduce the orthorhombic splitting and several reflections, such as (210) and (120), start to merge at T = 773 K (Figure 5.9(a)). The phase transition to tetragonal symmetry is completed at T = 823 K. The doubling of the unit cell c-axis is preserved up to the highest temperature measured (T = 873 K), as (021) and (211) reflections are still present, see Figure 5.9.

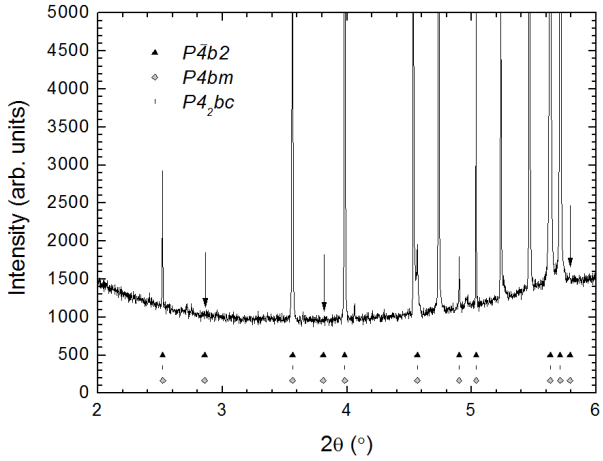

Figure 5.10:. Diffraction profile of $K_{0.6}CrF_3$, collected at T = 823 K. The reflection markers are for *P*4*bm*, $P4_2bc$ and $P\bar{4}b2$ from bottom to top. The arrows indicate the positions indexed by *P*4*bm* and $P\bar{4}b2$ only.

		z($P4_2bc$)	z($P4_2/mbc$)	d(z)	d(z)*c (Å)
Cr1	*4b*	0.24042	0.25	-0.0096	-0.0769
Cr2	*8c*	0.24595	0.249625	-0.0037	-0.0295
Cr3	*8c*	0.7467	0.750375	-0.0037	-0.0295
K1	*4a*	0.49696	0.5	-0.0030	-0.0244
K2	*8c*	0.49993	0.5	-0.0001	-0.0006
F1	*4b*	0.00881	0	0.0088	0.0708
F2	*8c*	-0.00161	0	-0.0016	-0.0129
F3	*8c*	0.49819	0.5	-0.0018	-0.0145
F4	*8c*	0.26176	0.25	0.0118	0.0944
F5	*8c*	0.25961	0.2505	0.0091	0.0732
F6	*8c*	0.25861	0.2495	0.0091	0.0732
F7	*8c*	0.26258	0.249635	0.0129	0.1040
F8	*8c*	0.26331	0.250365	0.0129	0.1040

Table 5.6: The atomic positions as determined from Rietveld fits of diffraction profiles at T = 823 K. The displacement $d(z)$ is calculated by comparing the lower- and higher symmetry positions ($P4_2bc$ and $P4_2/mbc$, respectively); $d(z)$ multiplied by the lattice vector c = 8.031241(9) Å yields the displacement in Å.

It is often possible to assign a higher order symmetry phase by considering the supergroups of a given space group. Hence, the three isomorphic tetragonal supergroups of *Pba*2, i.e. $P4_2bc$, $P4bm$ and $P\bar{4}b2$, were considered as candidate structures of the high-temperature phase. All observed reflections could be indexed in space group $P4_2bc$; whereas the space groups $P4bm$ and $P\bar{4}b2$ index addition reflections (e.g. (001), (111), (211), (003)), which are not observed experimentally (cf. Figure 5.10). In addition, the fit statistics of trial refinements carried out in each space group clearly pointed towards $P4_2bc$ as the correct symmetry (χ^2 ($P4bm$) = 47.90; χ^2 ($P4_2bc$) = 39.11; χ^2 ($P\bar{4}b2$) = 209.5).

The refined atomic coordinates of the tetragonal phase (space group $P4_2bc$) were analysed for existence of pseudosymmetry: The atomic displacements away from the higher symmetry positions of a hypothetical centric $P4_2/mbc$ structure were calculated using the program PSEUDO [13]. Table 5.6 summarizes the results of the analysis; the atomic displacements were found not to exceed the $d(z)$ = 0.1 Å (except for F7 and F8) and therefore the structure at T = 823 K is likely of centric $P4_2/mbc$ symmetry.

space group: $P4_2bc$		No. 135		T = 823 K	
a = 12.87981(1) A		c = 8.03132(1)		V = 1332.311(3)	
		x	y	z	B_{iso}/ Å^2
Cr1	*4d*	0	0.5	0.25	2.19(2)
Cr2	*16i*	0.2155(1)	0.0750 (1)	0.2494(3)	2.19(2)
K1	*4a*	0	0	0.5	4.81(6)
K2	*8h*	0.1626(2)	0.3177(2)	0.5	4.81(6)
F1	*4c*	0	0.5	0	4.99(5)
F2	*8h*	0.2126(6)	0.0739(5)	0	4.99(5)
F3	*8h*	0.2058(6)	0.0712(5)	0.5	4.99(5)
F4	*8g*	0.2806(3)	0.2194(3)	0.25	4.99(5)
F5	*16i*	0.5061(2)	0.1524(3)	0.250(1)	4.99(5)
F6	*16i*	0.3580(2)	0.4277(3)	0.249 (1)	4.99(5)
χ^2 = 14.35		F^2 = 9.23%		wR_p = 9.95 %	R_p = 6.08 %

Table 5.7: Results of Rietveld refinement of the high temperature (T = 823 K) SXRD diffraction profile of $K_{0.6}CrF_3$, (space group $P4_2/mbc$) collected at ID31. There were 22 refined structural parameters.

Cr1-F	d/ Å	Cr2-F	d/ Å
Cr1_F1	2.00783(0)	Cr2_F2	2.004(2)
Cr1_F1	2.00783(0)	Cr2_F3	2.017(2)
Cr1_F5	1.9465(3)	Cr2_F4	2.039(2)
Cr1_F5	1.9465(3)	Cr2_F5	1.996(3)
Cr1_F5	1.9465(3)	Cr2_F6	2.120(4)
Cr1_F5	1.9465(3)	Cr2_F6	2.036(4)
average	1.979(2)	average	2.035(3)

Table 5.8: Bond-distances obtained from Rietveld refinement (space group $P4_2/mbc$) of high temperature (T = 823 K) diffraction profile of $K_{0.6}CrF_3$. Cr1 and Cr2 are located on 4*d* and 16*i* sites and an oxidation state cannot be assigned from the bond-distance distribution.

The results of the final Rietveld refinement in space group $P4_2/mbc$ are summarized in Table 5.7 and the Cr-F bond distances listed in Table 5.8. No constraints on atomic coordinates were used during the refinement. Isotropic displacement factors were constraint to be the same for atoms of same species. There are two distinct Cr site in the $P4_2/mbc$ setting: the perovskite (16*i*) and the extra-perovskite (4*d*) site. An ordered arrangement of the 12 Cr^{2+} and 8 Cr^{3+} ions cannot be proposed. This is also reflected in the bond-distances, which suggest that Cr^{3+} preferentially occupies the extra-perovskite Cr1 (4*d*) site (d_{avg} = 1.979(2) Å), whereas the perovskite Cr2 (16*i*) site (d_{avg} = 2.035(3) Å) is of mixed valence (cf. Table 5.9).

Atom no./ Wycoff site	assumed valence state	Bond Valence sum	% Deviation fom assumed valence state	Reference
Cr1 (*4d*)	2+	2.618	31	b
Cr1 (*4d*)	2+	3.166	58	e
Cr1 (*4d*)	3+	2.530*	16	a
Cr1 (*4d*)	3+	2.416	19	b
Cr2 (*16i*)	2+	2.244*	12	b
Cr2 (*16i*)	2+	2.711	36	e
Cr2 (*16i*)	3+	2.167	28	a
Cr2 (*16i*)	3+	2.069	31	b

*marks most consistent valence state
[a] Brown and Alternatt, (1985), Acta Cryst. B41, 244-247 (empirical)
[b] Brese and O'Keeffe, (1991), Acta Cryst. B47, 192-197 (extrapolated)
[c] I.D. Brown, Private communication

Table 5.9: Results of bond-valence calculations carried out with the VaList program based on the refinement in space group $P4_2/mbc$ at T = 873 K (cf. table 5.8) [11].

At T = 650 K the c-axis expansivity changes – as compared to the intermediate temperature range (T = 423 K – 623 K) – but is not connected to a change in space-group symmetry. However, it can be related to a successive reduction of the octahedral tilt between adjacent [CrF_6] octahedra along the c-axis (see Table 5.10). At the same time, the average apical displacement of the Cr atoms from the mean plane of the basal fluorine ligands is reduced from d(Cr) = 0.217 Å at T = 300 K, to d(Cr) = 0.169 Å at T = 523 K, to d(Cr) = 0.130 Å at T = 773 K, and becomes negligibly small in the tetragonal phase: d(Cr) = 0.001 Å at T = 823 K.

angle (°) *Pba2*	300 K	523 K	773 K	798 K	angle (°) $P4_2/mbc$	823 K
Cr3-F4-Cr4	168.9(7)	168.5(9)	170.1(9)	173(1)	Cr2-F2-Cr2	177.7(4)
Cr4-F3-Cr3	163.1(6)	166.4(8)	165.1(8)	167(1)	Cr2-F3-Cr2	172.4(4)
Cr5-F6-Cr6	163.4(6)	167.7(8)	169(1)	164(1)		
Cr6-F5-Cr5	161.7(6)	164.4(8)	168(1)	170(1)		

Table 5.10: The temperature dependence of the tilting angle between two adjacent CrF_6 octahedra along the c-axis, obtained from Rietveld refinements in space groups *Pba*2 (T = 300 K – 798 K) and $P4_2/mbc$ (at T = 823 K). With increasing temperature, the octahedra straighten along c, and contribute the c-axis expansion in addition to the thermal expansion

5.3.4 The Low Temperature X-ray Induced Phase

The monoclinic *P*112 structure established at room temperature is robust upon cooling down to $T = 5$ K. Below $T < 150$ K however, a remarkable effect is observed: with continuous X-ray exposure the diffraction peaks shift and a new phase (hereafter called 'induced phase') is stabilised after one hour ($T = 5$ K). Once the structural transition was completed (i.e. no further peak shift or intensity change between subsequent scans), multiple scans of the induced phase were collected over 140 minutes and processed to a single diffraction profile to obtain better counting statistics.

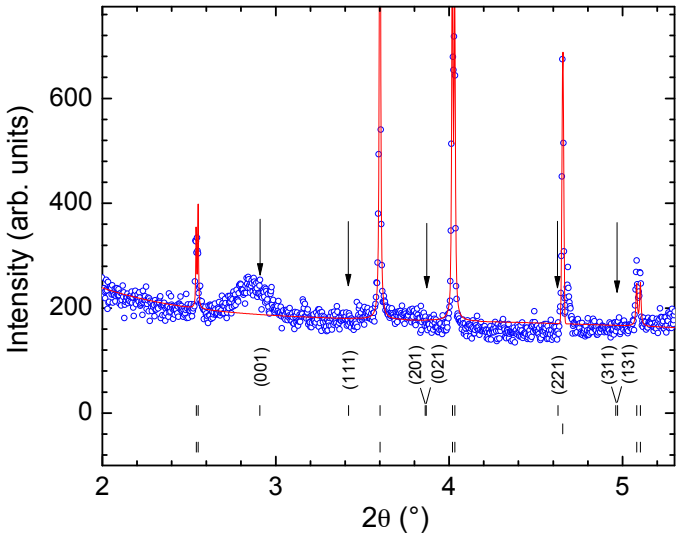

Figure 5.11: Observed (open blue circles), calculated (red line) and difference (green line) synchrotron powder diffraction Rietveld profile of the X-ray induced phase of $K_{0.6}CrF_3$ in space group *Cmm*2 at $T = 5$ K, collected at ID31, $\lambda = 0.39992$ Å. Tick marks indicate the reflection positions for *Cmm*2 phase, K_2CrF_4 impurity phase and a hypothetical *Cmm*2 phase with $c = 2\ c_{TTB}$ (bottom to top). Clearly, the doubling of the *c*-axis is lost in the X-ray induced *Cmm*2 phase. The bump at 3° (2θ) can be attributed to the cryostat.

The small superlattice peaks indicating the monoclinic *P*112 symmetry established at room temperature are not observed in the low-temperature diffraction profiles, due to the shadowing from the cryostat. Hence, refinements were carried out using the *Pba*2 structure model. The doubling of the *c*-axis is lost in the induced phase: e.g. the $(211)_{Pba2}$, $(111)_{Pba2}$ and $(201)_{Pba2}$ reflections vanish, see Figure 5.11. The $(220)_{Pba2}$ reflection splits into a doublet, indicating a change in centring. Further pairs of reflections (*hkl*), (*khl*) of *Pba*2, such as (200), (020); (202), (022); (402), (042) and (602), (062) merge into singlets. The new phase can be indexed in space group *Cmm*2, with

$c_{Cmm2} \approx c_{Pba2}/2 \approx c_{TTB}$. The *a*- and *b*- lattice parameter of the *Cmm*2 unit cell lie along the *ab*-base diagonal of the *Pba*2 cell, and are related through $a_{Cmm2} \approx a_{Pba2} \cdot \sqrt{2}$ and $b_{Cmm2} \approx b_{Pba2} \cdot \sqrt{2}$, see also Figure 5.12. Superlattice reflections that may indicate a doubling or tripling of the *a*- or *b*- axis are not observed.

After the unit cell size and symmetry were established, isotropic thermal displacement factors (constrained to be the same for atoms of same species) and atomic coordinates were refined. The results of the final Rietveld refinement cycle are summarized in Table 5.11; the lattice constants refine to a = 18.0590(1) Å, b = 17.9768(1) Å and c = 3.94524(2) Å. The change in centering from $P \rightarrow C$ doubles the area of the basal (*ab*) plane of the unit cell; but as the *c*-axis is halved at the same time, the cell volume of *Pba*2 and *Cmm*2 phase is comparable. The unit cell of the induced phase is shown in Figure 5.12.

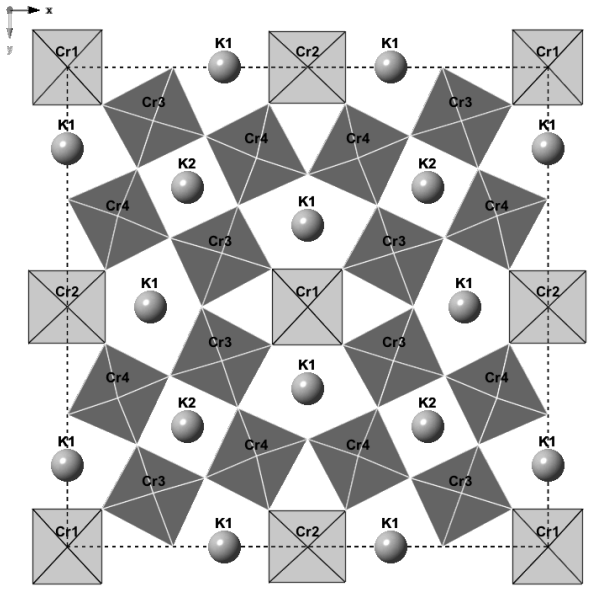

Figure 5.12: The low temperature X-ray induced phase of $K_{0.6}CrF_3$, space group *Cmm*2. Cr1 and Cr2 (light grey) occupy the 2*a* and 2*b* site, respectively whereas Cr3 and Cr4 (dark grey) are located on the 8*f* sites. The lattice vectors of the *Cmm*2 phase go along the face diagonal of the room temperature *Pba*2 cell; the *c*-axis is halved ($c = c_{Pba2}/2 \approx c_{TTB}$).

space group *Cmm2*		No. 35		*T* = 5 K	
a = 18.0590(1) Å		*b* = 17.9768(1) Å		*c* = 3.94524(2) Å	*V* = 1280.79(1) Å^3
		x	*y*	*z*	B_{iso} (Å^2)
Cr1	*2a*	0	0	0.515(6)	0.67(2)
Cr2	*2b*	0	0.5	0.514(6)	0.67(2)
Cr3	*8f*	0.3194(2)	0.3944(2)	0.505(4)	0.67(2)
Cr4	*8f*	0.6052(2)	0.8197(2)	0.505(4)	0.67(2)
K1	*4d*	0.3273(3)	0	1.004(7)	1.39(5)
K1	*4e*	0	0.8305(3)	1.004(7)	1.39(5)
K2	*4c*	0.25	0.25	-0.005(5)	1.39(5)
F1	*8f*	0.8550(6)	0.7882(6)	0.456(7)	2.64(6)
F1	*8f*	0.2144(6)	0.3564(6)	0.442(5)	2.64(6)
F2	*4d*	0.2212(8)	0	0.48(1)	2.64(6)
F2	*4e*	0	0.7262(8)	0.49(1)	2.64(6)
F3	*8f*	0.9270(5)	0.9212(5)	0.460(7)	2.64(6)
F3	*8f*	0.0787(5)	0.4268(5)	0.461(8)	2.64(6)
F4	*2a*	0	0	0.99(2)	2.64(6)
F4	*2a*	0	0.5	0.97(2)	2.64(6)
F5	*8f*	0.3185(6)	0.3911(6)	0.99(1)	2.64(6)
F5	*8f*	0.6072(6)	0.8127(6)	0.99(2)	2.64(6)
χ^2: 5.485		F^2: 9.93 %		wR_p: 12.09 %	R_p: 8.72 %	R_{exp}: 4.95 %

Table 5.11: Results of Rietveld refinement of the low temperature SXRD diffraction profile of $K_{0.6}CrF_3$, collected at *T* = 5 K on beamline ID31 after the X-ray induced phase (space group *Cmm*2) had been stabilised. There were 43 refined structural parameters.

Cr1_F	*d* (Å)	Cr2_F	*d* (Å)
Cr1_F3	1.95(1)	Cr2_F3	1.945(1)
Cr1_F3	1.95(1)	Cr2_F3	1.945(1)
Cr1_F3	1.95(1)	Cr2_F3	1.945(1)
Cr1_F3	1.95(1)	Cr2_F3	1.945(1)
Cr1_F4	2.06(9)	Cr2_F4	2.14(6)
Cr1_F4	1.89(9)	Cr2_F4	1.80(6)
average	1.96(4)	average	1.96(3)
Cr3_F	*d* (Å)	Cr4_F	*d* (Å)
Cr3_F1	2.02(1)	Cr4_F1	2.08(1)
Cr3_F1	2.03(1)	Cr4_F1	2.09(1)
Cr3_F2	2.039(7)	Cr4_F2	2.073(7)
Cr3_F3	2.009(9)	Cr4_F3	1.993(9)
Cr3_F5	2.02(5)	Cr4_F5	2.02(5)
Cr3_F5	1.93(5)	Cr4_F5	1.93(5)
average	2.01(2)	average	2.03(2)

Table 5.12: Bond-distances obtained from Rietveld refinement (space group *Cmm*2) of low temperature (*T* = 5 K) diffraction profile of the induced phase of $K_{0.6}CrF_3$. Cr1 and Cr2 are located on the perovskite (2*a* and 2*b*) sites, respectively whereas Cr3 and Cr4 occupy the extra-perovskite (8*f*) sites.

The charge order pattern established at room temperature cannot be maintained in the induced phase, as there is no direct correspondence between the different crystallographic sites. In analogy to the room temperature analysis, the bond-distances were examined to establish the ordering pattern of the induced phase.

The average Cr-F bond-length of the 2*a* and 2*b* site are slightly shorter as compared to the average Cr-F distances of the 8*f* sites, $d_{\text{Cr-F}}(2a, 2b) \approx 1.96(4)$ Å and $d_{\text{Cr-F}}(8f) \approx 2.02(2)$ Å, respectively (see Table 5.12). Bond valence calculations using the program VaList indicate Cr^{3+} occupies both extra-perovskite sites (2*a*), whilst $Cr^{2.5+}$ and Cr^{2+} occupy the Cr3 and Cr3 perovskite sites, respectively (see Table 5.13) [11]. However, taking the estimated standard deviation into account the variation in bond-length is negligible, and it is clear that the induced phase is charge disordered. The average Cr-F bond length in *Cmm2* (d_{avg} = 2.01(2) Å) is similar to the mean Cr4-F distance at room temperature (d_{avg} = 2.03(2) Å), where it was attributed to a mixed valence state.

Atom no./ Wycoff site	assumed valence state	Bond Valence sum	% Deviation fom assumed valence state	Reference
Cr1 (2*a*)	2+	2.789	39	b
Cr1 (2*a*)	2+	3.368	68	e
Cr1 (2*a*)	3+	2.689*	10	a
Cr1 (2*a*)	3+	2.570	14	b
Cr2 (2*b*)	2+	2.873	44	b
Cr2 (2*b*)	2+	3.469	73	e
Cr2 (2*b*)	3+	2.770*	8	a
Cr2 (2*b*)	3+	2.648	12	b
Cr3 (*8f*)	2+	2.414*	21	b
Cr3 (*8f*)	2+	2.916	46	e
Cr3 (*8f*)	3+	2.331	22	a
Cr3 (*8f*)	3+	2.227	26	b
Cr4 (*8f*)	2+	2.289*	14	b
Cr4 (*8f*)	2+	2.766	38	e
Cr4 (*8f*)	3+	2.210	26	a
Cr4 (*8f*)	3+	2.111	30	b

*marks most consistent valence state
[a] Brown and Alternatt, (1985), Acta Cryst. B41, 244-247 (empirical)
[b] Brese and O'Keeffe, (1991), Acta Cryst. B47, 192-197 (extrapolated)
[c] I.D. Brown, Private communication

Table 5.13: Results of bond-valence calculations carried out with the VaList program [11] based on the Rietveld refinement of the T = 5 K diffraction profile in space group *Cmm*2. The intermediate oxidation state values indicate the loss of CO in the induced phase.

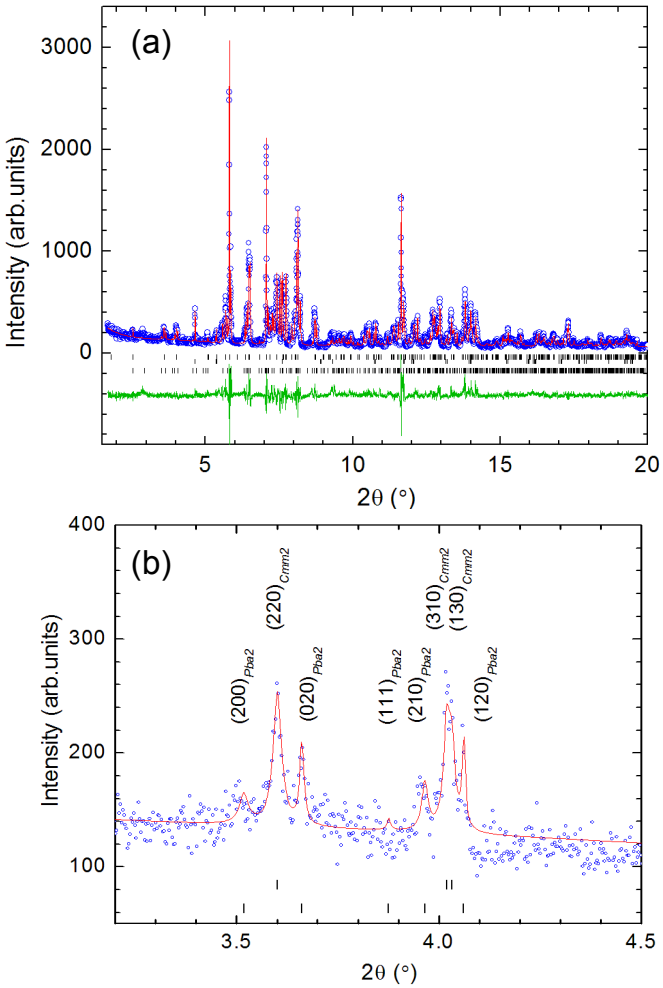

Figure 5.13: (a) Observed (open blue circles), calculated (red line) and difference (green line) synchrotron powder diffraction Rietveld profile of $K_{0.6}CrF_3$ at T = 5 K, collected at ID31, λ = 0.39992 Å. After the induced phase had been stabilised, X-ray exposure was interrupted for one hour, before this diffraction profile was collected. The room temperature phase is partially recovered, showing that the transition between X-ray induced and ambient temperature phase is reversible. Tick marks (bottom to top) indicate the reflection positions for *Pba*2 (representative of full CO *P*112) K_2CrF_4 impurity phase and *Cmm*2 phase. (b) Magnification of the low 2θ region with reflection markers for *Pba*2 and *Cmm*2 phase.

The X-ray induced structural transition is reversible: after the induced phase was stabilized at T = 5 K, the X-ray exposure was interrupted for one hour. Then a new diffraction profile was collected, showing partial recovery of the room temperature phase, see Figure 5.13.

5.3.5 The X-ray Induced Transition

The transition between ambient temperature and induced phase is very fast at T = 5 K. Additional reflections of the *Cmm*2 phase are already present in the dataset collected during the first 90 seconds of X-ray exposure. To study the kinetics of the phase transition, the diffraction data was processed as a function of time: diffraction profile were created by summing the data from different detectors over a specified time range instead of summing the data from all detectors per scan.

The lattice constants of *Pba*2 and *Cmm*2 (converted to *Pba*2 setting) phase are plotted as a function of time in Figure 5.14. Initially (t ~ 0 – 1500 sec) the orthorhombic splitting of the *Pba*2 phase is reduced whilst the *c*-axis expands, leading to a small overall volume expansion (V_{90sec} = 1279.722 Å^3 and $V_{1234\ sec}$ = 1280.768 Å^3). The phase fraction of the *Pba*2 phase is constant throughout this period (~ 75 wt %). At around $t \approx$ 1500 sec the expansion of the *c*-axis comes to a halt and $c_{Pba2} \approx 2 \cdot c_{Cmm2}$. The *a*- and *b*- parameters continue to converge. Between t ~ 1500 sec and 3500 sec, the weight fraction of *Pba*2 starts to decrease, whilst the *Cmm*2 phase grows at the same rate ($k \approx$ 1.5 wt% min^{-1}). After t = 3500 sec, changes in the lattice metrics are minor, and the *a*- and *b*- parameter of the *Pba*2 phase approach the values of the induced phase. The phase fractions stabilise (75 % *Cmm*2, 20 % *Pba*2, 5 % K_2CrF_4) as the transfer from *Pba*2 to *Cmm*2 reaches a constant level.

Throughout the measurement, the lattice parameters of the induced *Cmm*2 phase remain approximately constant. After the induced phase was stabilized at T = 5 K, the sample was warmed up to T = 150 K with open X-ray shutter. The unit cell volume expands on heating (Figure 5.15).

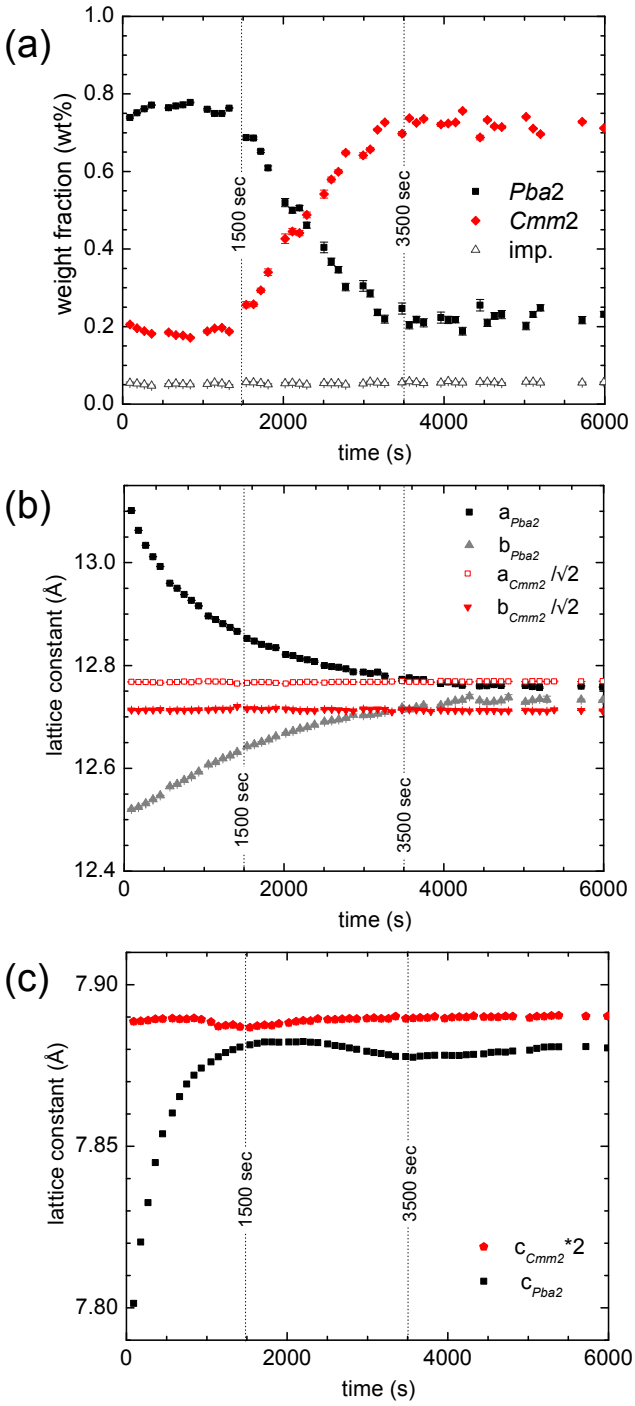

Figure 5.14: Results obtained from Rietveld refinements to SXRD data collected during the X-ray induced transition at $T = 5$ K on beamline ID31. (a) The time dependence of the weight fractions of *Pba*2 and *Cmm*2 phase. The fractions of the room temperature and induce phases stabilise after ca. 3000 seconds at a ratio of 20:75% ratio (4 % K_2CrF_4 impurity phase). (b, c) Time dependence of the lattice constants of $K_{0.6}CrF_3$. The lattice parameters of the *Cmm*2 phase were converted to the setting of the *Pba*2 phase. With increased irradiation time, (a) the lattice *a*- and *b*- constants of the *Pba*2 phase become more similar to the induced phase (reduced orthorhombic distortion), whereas (c) the *c*-axis (*Pba*2) expands.

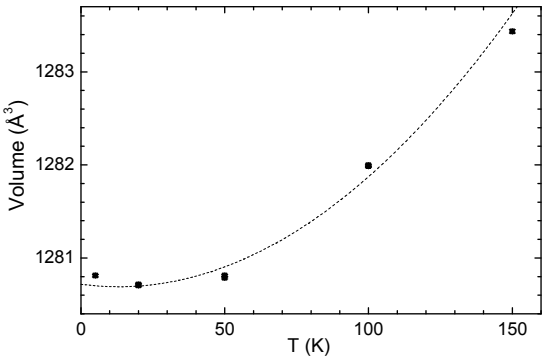

Figure 5.15: Temperature dependence of the unit cell volume of the *Cmm*2 phase of $K_{0.6}CrF_3$. obtain from Rietveld refinements of SXRD data collected on beamline ID31. The dashed line is a guide to the eye. Above T = 150 K, the induced phase is not observed.

At T = 150 K, the induced and room temperature phase start to compete and new peaks corresponding to the room-temperature *Pba*2 structure start to appear in the diffraction profile. Figure 5.16 shows selected regions of the diffraction profile after t = 15 min and 236 min, collected at T = 150 K. The $(220)_{Cmm2}$ reflection disappears and vanishes after t = 236 min, indicating that the phase transition to *Pba*2 is completed.

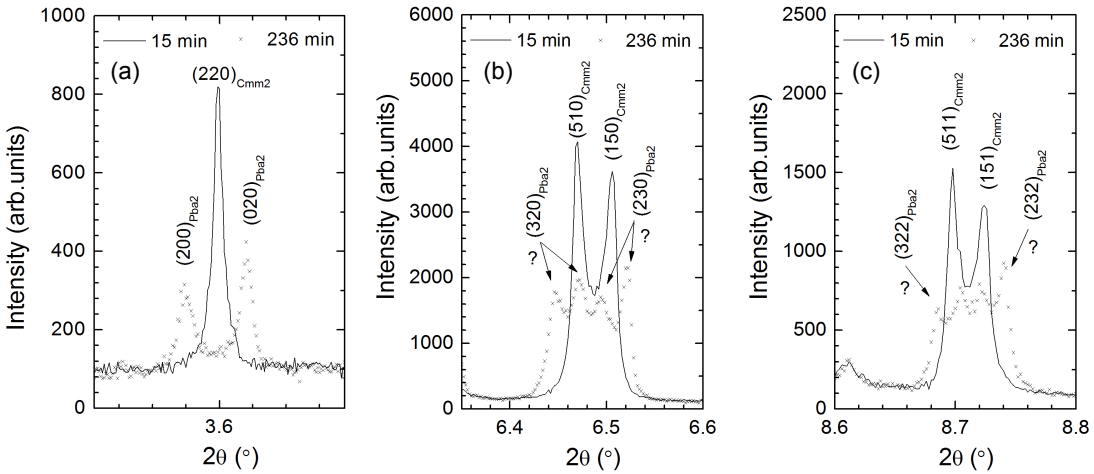

Figure 5.16: Selected regions of the diffraction profiles collected at T = 150 K, after t = 15 min and 236 min. (a) The transition from *Cmm*2 to *Pba*2 symmetry is indicated by the splitting of e.g. the $(220)_{Cmm2}$ into $(200)_{Pba2}$ and $(020)_{Pba2}$ reflection; the $(220)_{Cmm2}$ reflection disappears with time and has vanished after t = 236 min. (b, c) The peak splitting observed after t = 236 min could only be indexed using two *Pba*2 phases of slightly different lattice parameters.

However, the diffraction profiles (after t ~ 236 min) could not be indexed assuming only a single *Pba*2 phase nor with a combination of *Pba*2 and residual *Cmm*2 phase.

For instance, some reflections[†††] split into four peaks whereas only a doublet is expected for a pure *Pba*2 (or pure *Cmm*2) phase.

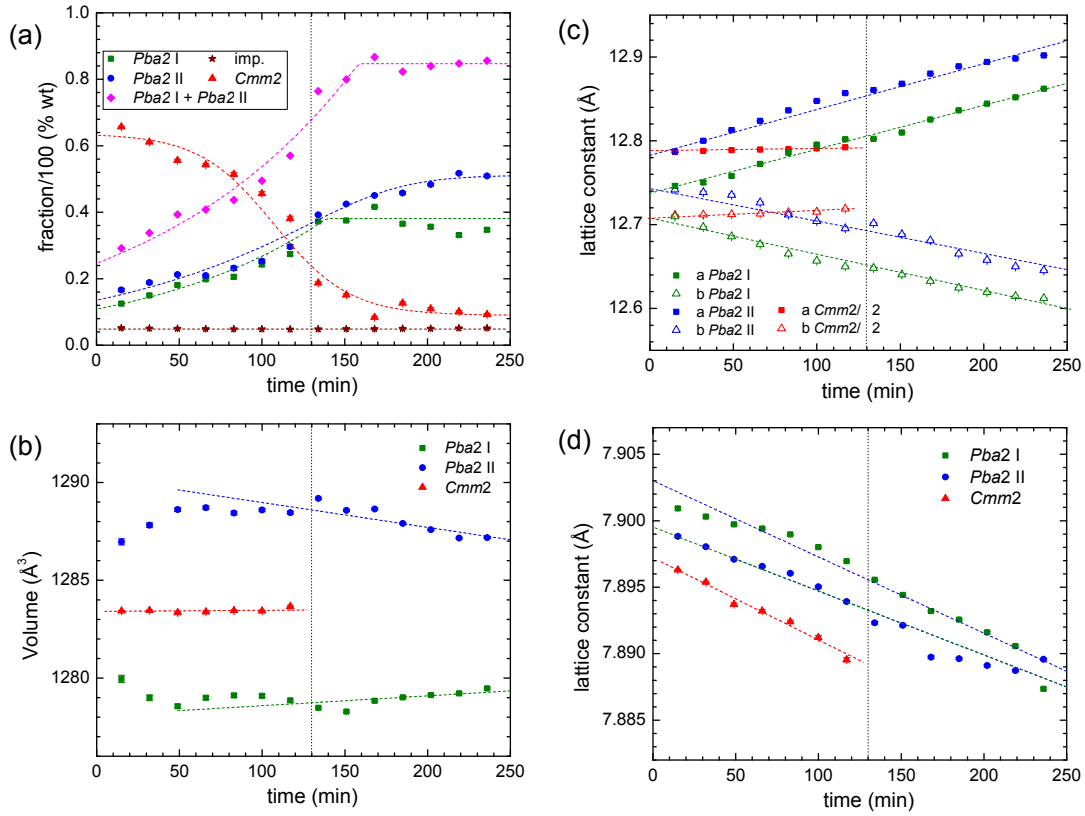

Figure 5.17: (a) – (c) Time dependence of the lattice parameters and unit cell volume of the *Pba*2-I, *Pba*2-II and *Cmm*2 phase at T = 150 K, obtained from Rietveld refinements of SXRD data collected on beamline ID31. The dashed lines are guides to the eye. Visual inspection of the diffraction profiles does not indicate the presence of *Cmm*2 phase after t ~ 130 min. (d) However, as all phases are closely related, the majority of reflections overlaps and phase fractions cannot be reliably refined, therefore the weight fraction of the X-ray induced *Cmm*2 phase drops significantly, but does not reach zero.

The observed peak splitting could only be indexed with two *Pba*2 phases of slightly different cell size. The initial lattice constants were calculated from the peak splitting shown in Figure 5.16(b). Trial refinements were carried out for all possible combinations of peaks, i.e. for model (i): (peak 1 + 2), (peak 2 + 3); for (ii): (peak 1 +3), (peak 2 + 4) and for (iii): (peak 1 + 4), (peak 2 + 3) corresponding to *Pba*2-I and *Pba*2-II phase, respectively. The refinements of starting model (iii) did not converge. On the other hand, the starting models (i) and (ii) converged to give the same lattice parameters and where used in subsequent refinements.

[†††] For example the (310), (130); (510), (150) and (511), (151) reflections of *Cmm*2.

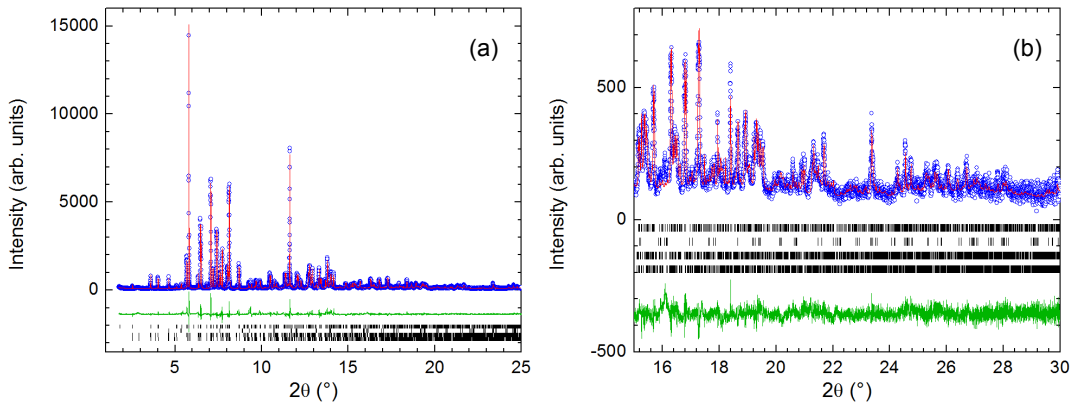

Figure 5.18: (a) Observed (open blue circles), calculated (red line) and difference (green line) synchrotron powder diffraction Rietveld profile of $K_{0.6}CrF_3$ after t = 15 min at T = 150 K, collected at ID31, λ = 0.39992 Å. Tick marks indicate reflection positions of *Pba*2 phase (I and II), K_2CrF_4 impurity phase and *Cmm*2 phase (from bottom to top). (b) Magnification of the high 2θ region.

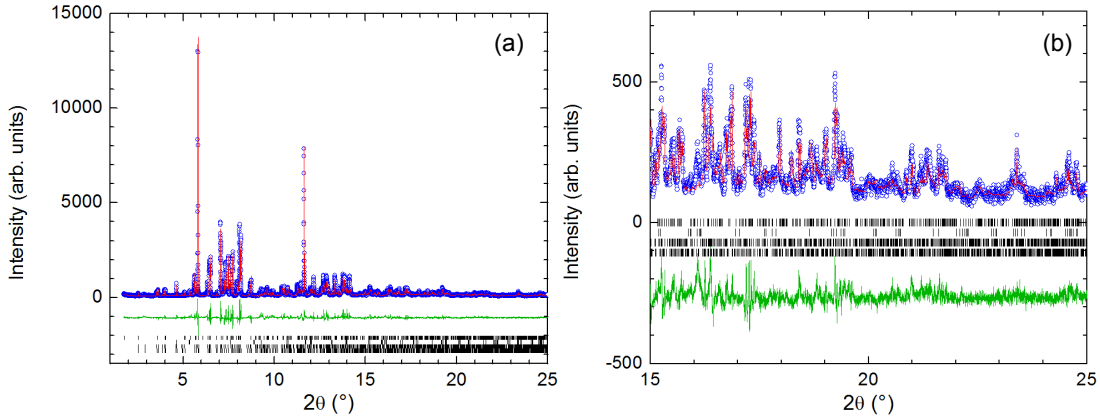

Figure 5.19: (a) Observed (open blue circles), calculated (red line) and difference (green line) synchrotron powder diffraction Rietveld profile of $K_{0.6}CrF_3$ after t = 236 min at T = 150 K, collected at ID31, λ = 0.39992 Å. Tick marks indicate reflection positions of *Pba*2 phase (I and II), K_2CrF_4 impurity phase and *Cmm*2 phase (from bottom to top). (b) Magnification of the high 2θ region.

The time dependence of the lattice constants, the volume and the refined weight fractions for *Cmm*2, *Pba*2-I and *Pba*2-II phases are plotted in Figure 5.17. The lattice parameters and fractions were refined without constraints. The weight fraction of the *Cmm*2 phase drops significantly to approximately 10 % after 130 min, at the same time its *c*-lattice parameter decreases. In trial refinements the lattice parameters of *Cmm*2 phase were fixed to the values obtained at t ~ 100 min; in that case the weight fraction of *Cmm*2 phase refined to ~ 1 %.

Rietveld refinement of the diffraction profile collected after t = 15 min and t = 236 min are shown in Figure 5.18 and Figure 5.19, respectively. The lattice constants after t = 236 min are a = 12.8620(4) Å, b = 12.6121(2) Å, c = 7.8873(1) Å and a = 12.9019(3) Å, b = 12.6453(4) Å, c = 7.8896(7) Å for *Pba*2-I and *Pba*2-II, respectively. The weight-fractions of phase I and II are comparable (~ 40 % and ~ 50 %). On further heating to T = 200 K, only a single *Pba*2 phase is observed, with a = 13.0588(2) Å, b = 12.5375(1) Å, c = 7.86231(5) Å.

5.3.6 Pressure Dependence of Structure

Powder diffraction profiles were collected at room temperature at the high-pressure beamline BL10XU (SPring-8, Japan) up to p = 18.5 GPa to study the influence of pressure on the structure. The small superlattice peaks indicating the monoclinic *P*112 symmetry of the CO room temperature phase (that was established from high-resolution SXRD) are not observed in the high-pressure powder diffraction profiles and hence refinements were carried out using the *Pba*2 structure model.

Up to p = 6 GPa, the lattice constants contract smoothly on increasing pressure. The pressure evolution of the lattice metrics is shown in Figure 5.20, together with a least squares fit to the semi-empirical 3rd order Birch-Murnaghan (BM) equation of states. The data was fitted using the program Eosfit [14]. In the orthorhombic phase, the isothermal bulk modulus K_0 and its pressure derivative K' are K_0 = 40(5) GPa and $\partial K_0/\partial p = K'$ = 10(6). The pressure dependence of the lattice parameters was fitted using the same equation of states (3rd order BM) by substituting the cubed lattice parameter for the volume. The linear bulk moduli for the different cell directions are $K_0(a)$ = 34(3) GPa, $K_0(b)$ = 39(5) GPa, $K_0(c)$ = 46(9) GPa; whereas the axial compressibilities are $K''(a)$ = -1.049 GPa^{-1}, $K''(b)$ = -5.143 GPa^{-1} and $K''(c)$ = -0.696 GPa^{-1}.

Above p = 6 GPa an abrupt symmetry change occurs: the splitting of several reflections, indicative of an orthorhombic distortion disappears: e.g. the (200), (020); (310), (130); (311), (131) and (320), (230) reflection merge to a singlet, pointing towards tetragonal symmetry. A splitting of reflections indicating a change of centring – in analogy to the low temperature induced phase, i.e. P → C – was not observed. Hence, trial refinements were carried out considering the tetragonal supergroups of *Pba*2, i.e. *P*4*bm*, *P*4$_2$*bc* and $P\bar{4}b2$, as possible candidates for the high-pressure phase. No indications for symmetry lower than *P*4*bm* were found.

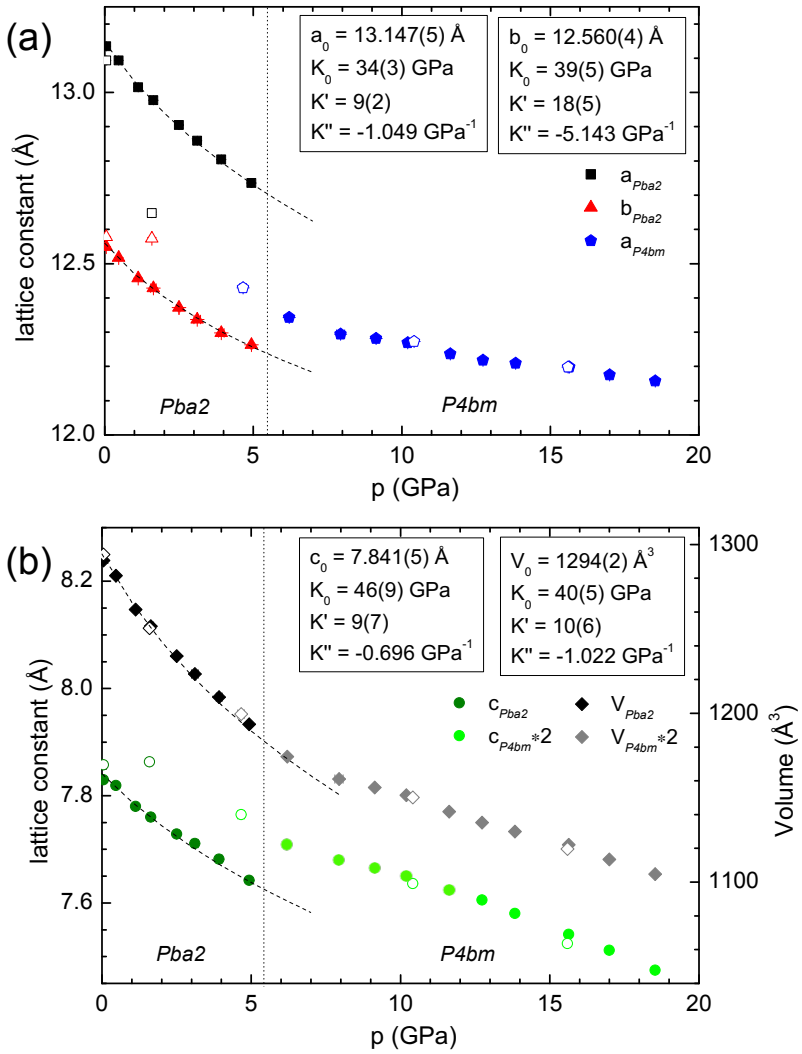

Figure 5.20: The pressure evolution (a) of the *a*- and *b*- lattice constant and (b) of the *c*-lattice constant and the unit cell volume *V* as deduced from Rietveld refinements of diffraction profiles collected at BL10XU, $T = 300$ K. The dashed line is a least-squares fit to a 3rd order Birch-Murnaghan equation of state. The lattice constants of the tetragonal phase were converted to the orthorhombic setting and open symbols represent data points collected on pressure release.

The reflections (*hkl*) with $l = 1$ have very small intensities and broaden further on increasing pressure. This makes it difficult to determine reliably whether the doubling of the *c*-axis is preserved in the high-pressure phase. Therefore, the simplest tetragonal cell (*P4bm*, $c \sim 4$ Å) was assumed for the pressure regime $p > 6$ GPa. Compared to the *Pba*2 phase, the tetragonal *P4bm* phase is stiffer and the contraction rate on pressurising decreases. Up to the highest pressure point collected ($p = 18.5$ GPa), the lattice constants contract almost linearly at a rate of $\Delta a_{P4bm} = -0.0157(1)$ Å GPa^{-1}, $\Delta c_{P4bm} = -0.0091(3)$ Å GPa^{-1} ($2{\cdot}\Delta c_{P4bm} = -0.0182(6)$ Å GPa^{-1})

and ΔV_{P4bm} = -2.80(7) Å^3 GPa^{-1} ($2{\cdot}\Delta V_{P4bm}$ = -5.6(1) Å^3 GPa^{-1}). In comparison, the lattice contractions in the *Pba*2 phase are Δa_{Pba2} =-0.084(3) Å GPa^{-1}, Δb_{Pba2} = -0.064(3) Å GPa^{-1}, Δc_{Pba2} = -0.039(2) Å GPa^{-1} and ΔV_{Pba2} = -20.8(9) Å^3 GPa^{-1}. On pressure release, the *Pba*2 structure is recovered below p = 5 GPa.

5.3.7 Magnetic Properties

The magnetic susceptibility measured in an applied field H increases steady with decreasing temperature. A weak cusp at T = 33 K followed by a kink at T = 6 K can be linked to an antiferromagnetic and ferromagnetic-like transition (Figure 5.21). The ZFC-FC branches bifurcate at the cusp at T = 33 K, and measurements in different applied fields show that the temperature of both magnetic transitions are field-independent (see Figure 5.21 and Figure 5.23). Further, the branching of ZFC-FC is robust and still observed in fields up to H = 10000 Oe.

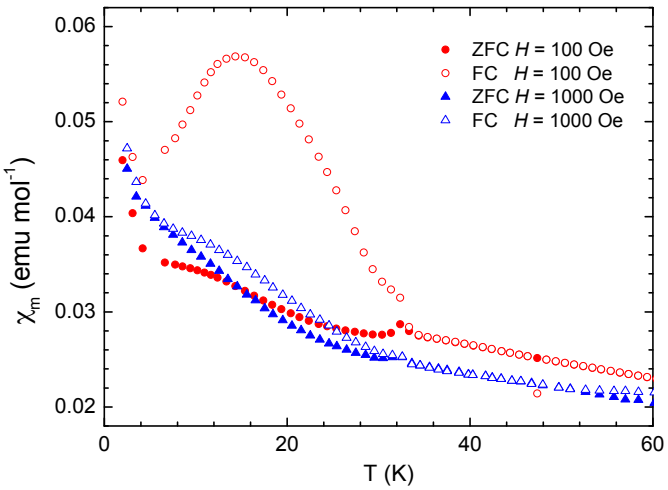

Figure 5.21: The ZFC-FC magnetic susceptibility of $K_{0.6}CrF_3$ (sample A) in different applied fields H = 100 and 1000 Oe. The bifurcation of ZFC and FC occurs independently of the applied field at T = 33 K, and is followed by an increase in magnetisation below T = 6 K.

The inverse susceptibility χ_m^{-1} (emu^{-1} mol) measured in H = 10000 Oe (see Figure 5.22) was fitted to a Curie-Weiss law in the temperature region between T = 150 K and 300 K. The obtained Curie and Weiss constants are C = 0.00193(7) mol emu^{-1} K^{-1} and θ = -49.9(2) K, respectively. The negative Weiss temperature and the cusp in susceptibility indicate antiferromagnetic behaviour.

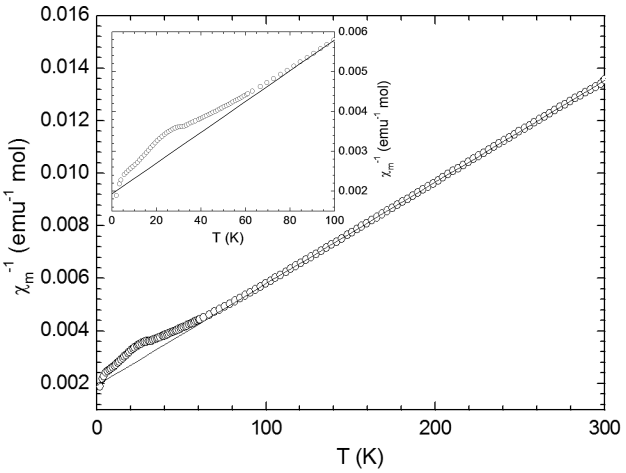

Figure 5.22: The inverse susceptibility χ_m^{-1} (emu^{-1} mol) measured in H = 10000 Oe. The line is a fit to the Curie-Weiss law for the high temperature region T = 150 K– 300 K.

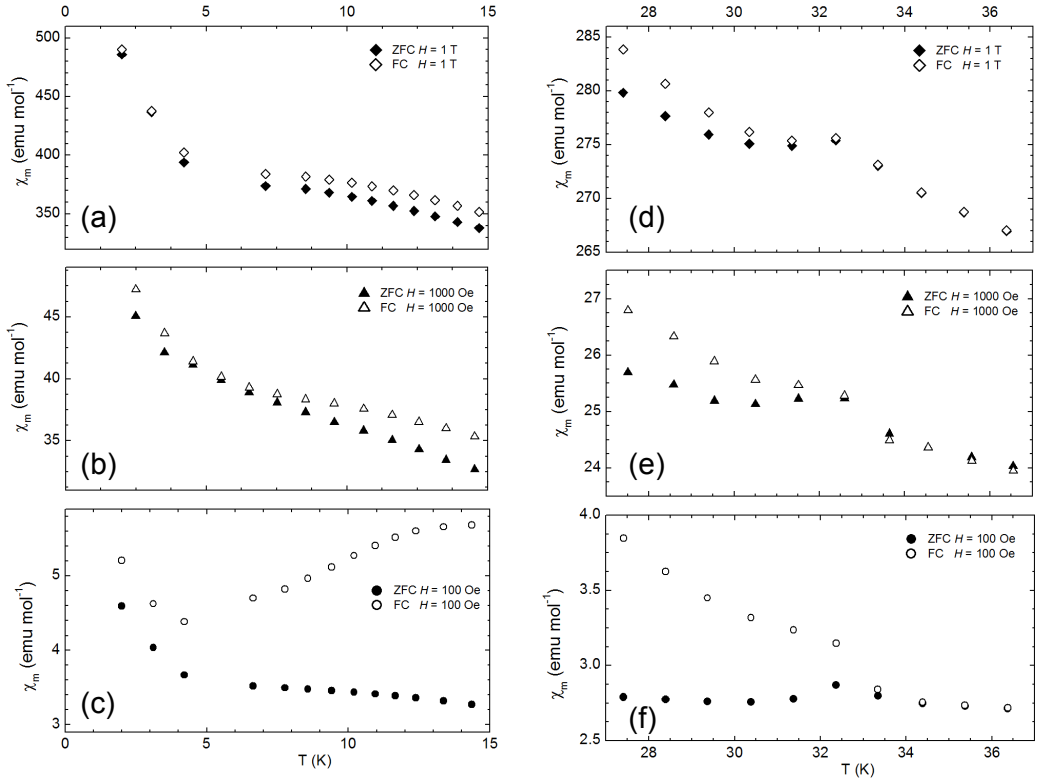

Figure 5.23: Magnification of selected temperature intervals of the ZFC-FC magnetic susceptibility of $K_{0.6}CrF_3$ (sample A) in different applied fields H = 100, 1000 and 10000 Oe. The transition temperatures T = 33 K and T = 6 K are field independent.

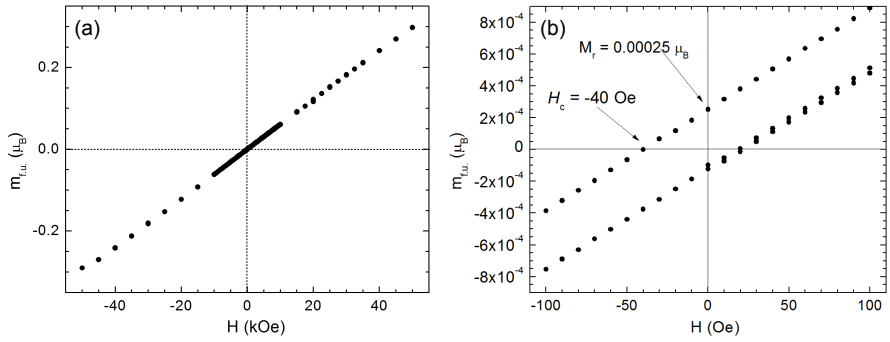

Figure 5.24: Magnetic hysteresis loop of $K_{0.6}CrF_3$ recorded at T = 15 K. H_{max} = ± 50000 Oe. (a) The magnetisation increases linearly with increasing field, and no saturation behaviour is observed up to maximum field strength. (b) The low field regime shows a small opening. The coercive field and remanescent magnetisation are small with H_c = -40 Oe and M_r = 0.00025 μ_B.

To further investigate the nature of magnetic ordering, a hysteresis loop was recorded at T = 15 K with maximum magnetic field strength of H = 50000 Oe (Figure 5.24). The magnetisation increases linearly with increasing field, and no saturation is observed. The hysteresis loop has a very small opening, which becomes increasingly small but does not vanish completely even in high fields. The coercive field is H_c = -40 Oe and the remanescent magnetisation is M_r = 0.00025 μ_B. The linear field-dependence and small opening of the hysteresis loop point towards a complex antiferromagnetic arrangement, with a small ferrimagnetic contribution possibly arising from small spin-canting and/ or Dzyaloshinskii-Moriya interaction as in related compounds [5].

5.4 Discussion

The results described in the previous paragraphs clearly demonstrate that the tetragonal tungsten bronze fluoride $K_{0.6}CrF_3$ has a very rich structural phase diagram. It shows a complex response to different external stimuli, such as temperature, pressure and X-ray illumination. A number of phase transitions are observed that can be linked to different CO schemes, which, in turn, have a strong influence on the electronic and magnetic behaviour. In the following section the results of the structural analysis and of the magnetic measurements will be discussed in the light of possible multiferroic behaviour.

5.4.1 The Room Temperature Structure

The diffraction profile of $K_{0.6}CrF_3$ ($K_{0.6}Cr^{II}_{0.6}Cr^{III}_{0.4}F_3$) collected at room temperature readily reveals the orthorhombic distorted tetragonal tungsten bronze (TTB) cell (space group *Pba*2) established previously [4]. The doubling of the unit-cell *c*-axis compared to the conventional TTB cell is confirmed by the presence of the (*hkl*, *l* = 1) reflections, such as e.g. (201), (021), (211) and (121). Doubling of the *c*-axis has been ascribed to the presence of ionic order ($KMnFeF_6$, $KMnCrF_6$) or CO ($K_{0.6}FeF_3$, K_xVF_3) in TTB-fluoride materials, but is also observed in the disordered material $K_{0.38}Mg_{0.38}In_{0.62}F_3$ where it was attributed to the octahedral tilting [15], [16], [17], [18], [19].

In $K_{0.6}CrF_3$, the doubled unit cell contains two layers of Cr ions, located at $z = 0.25$ and $z = 0.75$. There are three distinct Cr positions per layer: one extra-perovskite (2*b*) and two perovskite type (4*c*) sites. Each *Pba*2 unit cell has 12 Cr^{2+} (d^4) and 8 Cr^{3+} (d^3) ions, distributed over two 2*b* and four 4*c* sites. The different ionic size ($r(Cr^{2+}$, HS) = 0.94 Å and $r(Cr^{3+})$ = 0.755 Å) as well as the Jahn-Teller distortion of Cr^{2+} are likely to result in a CO and/or OO pattern, in order to minimise structural strain, similarly to what has been observed in related compounds [15], [17].

In principle, full CO can be realised in *Pba*2 symmetry if Cr^{2+} and Cr^{3+} occupy two of the perovskite-type (4*c*) sites each, and Cr^{2+} occupies the extra-perovskite (2*b*) site. However, this CO pattern would imply that the larger Cr^{2+} ions occupy exclusively the extra-perovskite site, thus maximising the structural strain. Bond-valence calculations of the refined room temperature *Pba*2 structure of $K_{0.6}CrF_3$ show that only a partially CO pattern is adopted: at $z = 0.25$, the extra-perovskite site (2*b*, Cr1)

is occupied by Cr^{2+}, whilst Cr^{2+} and Cr^{3+} alternate around perovskite cage (4*c*, Cr3 and Cr5, respectively) (see Figure 5.3). At $z = 0.75$, the extra-perovskite site (2*b*, Cr2) is occupied by Cr^{3+}, whereas $Cr^{2.5+}$ and Cr^{2+} occupy the perovskite sites (4*c*, Cr4 and Cr6, respectively). The same partially CO pattern is also observed in $K_{0.6}FeF_3$ [5]. The presence of a mixed-valence site (Cr4) was not convincing considering the electronic and size differences between Cr^{3+} and JT active Cr^{2+}. In order to split – and hence order – the Cr4 site, the space group symmetry has to be lower than orthorhombic. As a consequence, additional reflections should be present in the diffraction pattern. Indeed, small superlattice peaks are observed after prolonged data collection at room temperature (see Figure 5.4), clearly suggesting that the true crystal structure is not orthorhombic *Pba*2.

The observed superlattice peaks in the powder diffraction data collected at room temperature on $K_{0.6}CrF_3$ could all be indexed considering a small monoclinic distortion of the primitive orthorhombic cell. It is worth noticing that the presence of such peaks could also indicate a doubling or tripling of the lattice vectors, which would be characteristic of the FES (*Bbm*2) superstructure arising from octahedral tilt modulations as in K_xFeF_3 and $Ba_2NaNb_5O_{15}$ (BNN) [5], [17], [12]. However, the signature of these modulations has so far only been observed in electron diffraction patterns. This is because of the large unit cell dimensions of such superstructures ($a \sim 37.19$ Å, $b \sim 17.76$ Å, $c \sim 7.84$ Å calculated considering a *Bbm*2 symmetry for $K_{0.6}CrF_3$) and their frequently incommensurate nature. Our data do not show the presence of FES modulations and all reflection could be accounted for considering a primitive monoclinic cell. Therefore, the search for possible symmetries was limited to the three monoclinic subgroups of *Pba*2 that are *P*1*a*1, *Pb*11 and *P*112, each leading to a different fully CO pattern shown in Figure 5.5.

The CO pattern that we have determined for $K_{0.6}CrF_3$ has never been observed experimentally before in any related TTB structure, but was predicted theoretically to explain the ferroelectric behaviour. DFT calculations on $K_{0.6}FeF_3$ have shown that a fully CO pattern is the prerequisite for ferroelectricity to emerge[‡‡‡] [6]. In addition, full CO is intimately coupled to the ferroelasticity and may explain the presence of FES modulation satellites observed in the ED patterns of $K_{0.6}FeF_3$ [6].

[‡‡‡] It has been shown an insulating state in $K_{0.6}FeF_3$ can only be obtained for a fully CO structure. Insulating behaviour is required to maintain charge separation and electrical polarisation. Any mixed-valence site would lead to metallic behaviour, contradicting the ferroelectricity observed experimentally.

5.4.2 The High Temperature Phase

The two structural transitions ($P112 \rightarrow Pba2 \rightarrow P4_2/mbc$) occurring on heating are connected to the stepwise loss of CO. The transition from monoclinic (full CO) to orthorhombic (Cr4 site disordered) symmetry is marked by the loss of the superlattice peaks, a change in slope of the *c*-axis and the gradual increase in monoclinic angle γ towards 90°. Between $T = 423$ K and 650 K, the *Pba*2 phase expands smoothly with increasing temperature. Then the tilt modulation along the *c*-direction starts to straighten out (expansivity along *c*-axis increases) and the orthorhombic distortion $P = (a-b)/(a+b)$ gradually decreases. In addition, the off-centring of the Cr-ions from the centre of the fluorine octahedra diminishes continuously on heating, whilst preserving the acentric *Pba*2 structure. With the transformation to tetragonal symmetry, the remaining CO of the *Pba*2 phase and displacive character of the Cr atoms is lost.

The tetragonal phase emerging at $T < 823$ K is likely to be centric $P4_2/mbc$ based on the small differences in atomic positions between the acentric $P4_2bc$ and centric $P4_2/mbc$ setting. The space group $P4_2/mbc$ contains two crystallographic sites for Cr, the extra-perovskite (4*b*) site and the perovskite (16*i*) site. An ordering of Cr^{3+} and Cr^{2+} is not possible in this setting, as the combination of a 4-fold and 16-fold site is not compatible with the Cr^{2+}: Cr^{3+} ratio of 12:8. The acentric space group variant $P4_2bc$ allows in principle an ordered pattern with Cr^{3+} on one 8*c* site and Cr^{2+} on the 4*b* and the second 8*c* site. But the analysis of the bond distances (based on the $P4_2bc$ structure) showed that the average Cr-F bond distances on the two Cr-sites (8*c*) are very similar: $d_{Cr1\text{-}F} = 2.05(2)$ Å and $d_{Cr2\text{-}F} = 2.03(3)$ Å. The assignment of the centro-symmetric space group variant is further supported by the results of this bond-valence analysis, which point towards a mixed occupation of the Cr-sites (Table 5.9).

Although the CO is lost at high temperatures, the *c*-axis remains doubled (presence of (021) and (211) reflections, $c = 2c_{TTB}$). This is a consequence of the octahedral tilting, which is required if the halved *c*-axis is shorter than twice the average Cr-F bond length (height of a $[CrF_6]$ octahedron), $c/2 < 2 \cdot d_{Cr\text{-}F}$. Any tilt modulation along the *c*-direction leads to a multiplication (e.g. doubling) of the unit cell along the *c*-axis. It can be expected that the tilt modulation decreases continuously with increasing temperature (see Table 5.10) and a loss of the (021) and (211) reflections may be observed above $T > 823$ K. Hypothetically the prototypical *P*4/*mbm* structure ($a \approx b \approx 12$ Å, $c \approx 4$ Å) should be observed at sufficiently high temperatures. It

remains an open question, if such transition occurs below the melting temperature $T \approx 1150$ K [20].

5.4.3 The Low Temperature X-ray Induced Phase

Below room temperature, no structural phase transitions are observed down to $T = 5$ K. The superlattice peaks indicating the fully CO *P*112 structure cannot be monitored at low temperatures, as the cryostat used cuts the diffraction range obtainable. Hence, the structure has been refined using the *Pba*2 model. On cooling, the lattice contracts smoothly with decreasing temperature (Figure 5.25). However, the diffraction profiles collected below room temperature show a striking feature: although at first glance the phase remained orthorhombic *Pba*2, the Bragg peaks started to shift continuously with increasing X-ray exposure time. For consecutive scans (smaller half filled symbols) the orthorhombic splitting is reduced and the *c*-axis expands. The induced peak shift and change in lattice parameters is faster as the temperature is lowered.

To establish the nature and radiation dependence of the low temperature phase, the sample was cooled to $T = 5$ K with closed X-ray shutter, before data collection was started. The *Pba*2 structure – including the *c*-axis doubling – is retained down to $T = 5$ K. The influence of X-rays on the structure is very fast at this temperature, and even after $t = 90$ sec, the effect on the lattice parameters is noticeable, making it difficult to obtain the pristine cell parameters. A linear extrapolation of the high-temperature *a*- and *b*- lattice constants (indicated by the dashed line in Figure 5.25) gives an estimate of the unperturbed lattice parameters at $T = 5$ K ($a \approx 13.6$ Å, $b \approx 12.47$ Å).

To unravel the structural details of the X-ray induced phase, the sample was continuously irradiated at $T = 5$ K and the diffraction profiles were followed as a function of exposure time. The Bragg reflections shift continuously, and after one hour, the new 'induced phase' is stabilised, which can be indexed in space group *Cmm*2. Its *a*- and *b*- lattice vector lie along the base diagonal of the *Pba*2 phase, whereas the doubling of the *c*-axis is lost. Very interestingly, some *Cmm*2 phase (~ 20 wt%) is already present in the first diffraction profile collected ($t = 90$ sec). This indicates that the initial step of the structural conversion is extremely fast and occurs immediately after the X-rays are switched on.

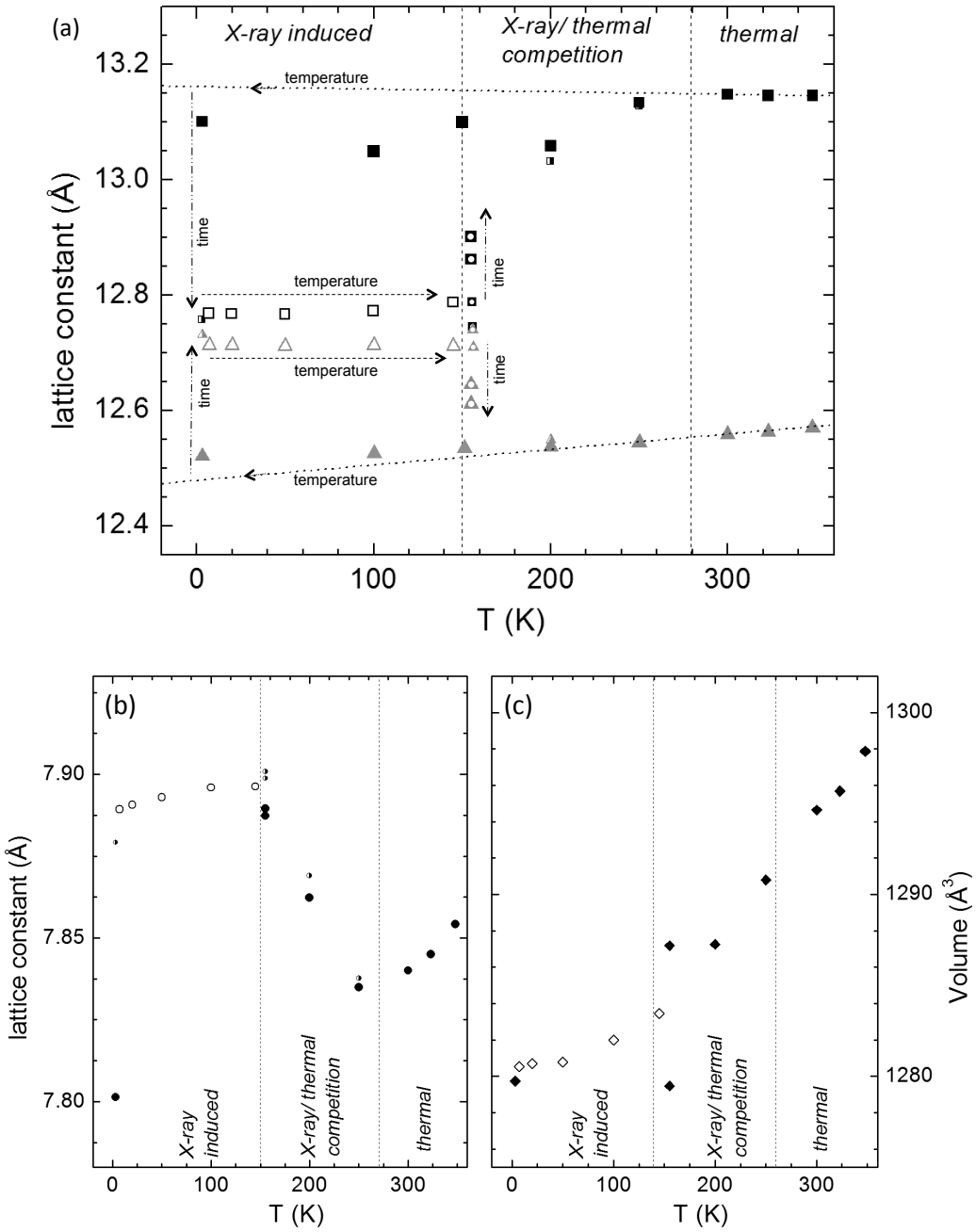

Figure 5.25: The behaviour of the lattice constants and unit cell volume below T = 350 K. The black and grey symbols were collected on cooling of the pristine *Pba*2 phase; the open symbols correspond to the lattice parameters of the induced *Cmm*2 phase (converted to *Pba*2 setting). The smaller symbols indicate the time-dependent behaviour at constant temperature with continuous X-ray irradiation (half-filled and symbols with dot were collected during cooling an heating cycle, respectively). Between T = 300 K and 100 K, data was collected at the same sample position on cooling, leading to the observed increase in lattice parameters between T = 250 and 100 K. At T = 5 K and on heating, diffraction profiles were collected on a new sample. Data points at T = 5 and 150 K are slightly offset for clarity.

The phase transition from *Pba*2 → *Cmm*2 is rather complex and develops in time through three well-defined steps: (i) an incubation time, (ii) a transition period and (iii) completed transition/ steady state. During the first ~1500 seconds, the incubation period (i), the phase fractions of *Pba*2 and *Cmm*2 phase remain constant whilst all lattice parameters of *Pba*2 change towards the values of the induced phase, i.e. the *b*- and *c*-axis increase whilst the *a*-axis decreases. Between t = 1500 sec and 3500 sec ('transition period' ii) the value of the *c*-axis remains constant whilst the *a*- and *b*-parameter continue to converge. The weight fraction of *Pba*2 starts to decrease, whilst the *Cmm*2 phase grows at the same rate. Following the incubation time, the percolation threshold is reached and the cooperative phase transition is triggered. After *t* = 3500 sec ('steady state', iii), the transfer from *Pba*2 to *Cmm*2 reaches a constant state as the *a*- and *b*- parameter of the *Pba*2 phase approach the values of the induced phase. Throughout the measurement, the lattice parameters of the induced *Cmm2* phase remain approximately constant.

The presence of ca. 20 wt% of *Cmm*2 phase in the first diffraction profile collected (*t* = 90 sec) implies that the transition from *Pba*2 to *Cmm*2 occurs very rapidly in part of the sample. The remaining *Pba*2 phase appears to transform more slowly to *Cmm*2, and the almost full conversion is only observed after an incubation time of ~25 minutes. This is consistent with a progressive generation of islands of charge-disordered phase with increasing X-ray illumination time. The X-rays remove localized electrons from the Cr atoms and instantaneously destroy the charge order locally, leading to the observed shift in lattice parameters. The increase of the c-axis is in line with an excitation of Cr by X-rays, because excited states are connected to larger ionic radii. Following the incubation time, the percolation threshold is reached and the cooperative phase transformation is triggered.

It is worth to stress that a constant fraction of *Pba*2 phase (20 wt%) is retained even after prolonged X-ray irradiation[§§§]. This observation could indicate that the excitation from *Pba*2 to *Cmm*2 occurs at the same rate as the relaxation from *Cmm*2 to *Pba*2*:* a steady state is reached. This is in agreement with the observed short-lived *Cmm*2 phase (see Figure 5.13). Alternatively, it could be explained by considering that the X-rays remove localized electrons from the Cr atoms. While the de-

[§§§] The diffraction profile collected after the induced phase has been stabilised, can be fitted with the *Cmm*2 phase only. However, the fit improves considerably when a secondary *Pba*2 phase is introduced: not only can the asymmetric peak-shape be accounted for, but also some 'missing' intensity is taken care of.

excitation of these states occurs preferentially into a fully charge disordered state (*Cmm*2), some relaxation occurs to restore the original CO pattern (*Pba*2). It is feasible to think that both pathways are involved, i.e. relaxation from the excited state to *Cmm*2 and then to *Pba*2, or relaxation from the excited state to *Pba*2.

Time-resolved X-ray diffraction experiments may further clarify the kinetics involved. Also standard angle-resolved diffraction experiments exploiting the tuneability of synchrotron radiation may be employed to determine the threshold value of photons per time required to obtain the *Cmm*2 phase and to further elucidate the mechanism of the X-ray induced phase transformation.

As mentioned above, the phase transition involves the loss of *c*-axis doubling and a change in tilt-pattern of the CrF_6 octahedra. It was observed that the structural crossover (i.e. weight fraction of *Pba*2 decreases whilst *Cmm*2 increases) occurs when $c_{Pba2} = 2 \cdot c_{Cmm2}$. Therefore, it would be interesting to determine if the loss of *c*-axis doubling and the change in tilt modulation occurs in consecutive steps or simultaneously at the phase transition. The diffraction profile collected within $t = 90$ sec shows that the doubling of the *c*-axis (*Pba*2) is preserved down to $T = 5$ K (presence of (201) reflection), and consequently refinements of the low temperature *Pba*2 phase were carried out assuming $c = 2 \cdot c_{TTB}$. But the doubling of the *c*-axis cannot be reliably established from the diffraction patterns after $t = 90$ sec, because the intensities of reflections indication a doubling of *c* (i.e. *hkl*, $l = 1$) become very small, and are further smeared out by the continuous shift. Hence we cannot determine whether the *c*-axis doubling is lost before the structural changeover (ii) occurs.

The unit cell of the induced phase is related to the ambient temperature structure by a 45° rotation of the *a*- and *b*-vector along the *c*-direction, doubling the base of the unit cell. In addition, the *c*-axis is halved in *Cmm*2. The CO pattern established at room temperature cannot be maintained: the *Cmm*2 unit cell contains two 2-fold and two 8-fold sites does not allow for full CO (the Cr^{2+} to Cr^{3+} ratio is 12:8). Analysis of the Cr-F distances revealed that all bond-lengths fall within $d = 1.96(3) - 2.03(2)$ Å (see Table 5.12). The mean Cr-F bond length in *Cmm*2 ($d_{avg} = 2.01(2)$ Å) is shorter than for Cr^{2+} (e.g. $d = 2.10(1)$ Å in $KCrF_3$) and longer than for Cr^{3+} (e.g. $d = 1.91(1)$ Å in Rb_2KCrF_6), indicating that CO and/or charge localisation is lost [1], [21].

A similar 'melting' of CO has been observed in the magnetoresistive manganite $Pr_{0.7}Ca_{0.3}MnO_3$ and the spinel $CuIr_2S_4$. The CO (antiferromagnetic) insulating state in

the manganites is lifted by X-ray influence, which induces a charge delocalised (ferromagnetic) metallic state. The photoinduced state is stabilised by structural changes and lattice relaxations but can be annealed out by thermal cycling [22]. In the spinel $CuIr_2S_4$, the ordering pattern of Ir-spin dimers is lost upon X-ray illumination, and a structural transition from triclinic – tetragonal symmetry occurs, liked to a reduction in electrical resistivity [23].

From the changes in bond-distances we can deduce that the X-ray induced phase of $K_{0.6}CrF_3$ is charge-disordered. As mentioned above, a disordered phase is likely to result in increase electrical conductivity and may be monitored by appropriate experimental setups, such as in the case of $CuIr_2S_4$ [23]. The melting of the CO leads to structural relaxations stabilising the induced phase (i.e. tilting along the *c*-direction is removed, whereas the tilt pattern of the [CrF_6] octahedra in the *ab* plane rearranges). Gradual evolution of the lattice constants of the photoinduced phase were linked to inhomogeneous character of the structural transition not only in the manganites and spinels, but also in molecular prussian-blue based systems [24]. Differently from these systems, the volume changes involved in the transition of $K_{0.6}CrF_3$ are comparably small: the differences in volume of the initial *Pba*2 and the final *Cmm*2 are $\Delta V = 0.08\ \%$. Small changes in the lattice can relax fast, which might explain the short-lived character of the induced phase (partial of *Pba*2 recovery within one hour at $T = 5$ K).

5.4.4 The Structure at High Pressures

The ambient temperature, high-pressure phase diagram of $K_{0.6}CrF_3$ was studied at beamline BL10XU. The relatively high background arising from the experimental setup and the resolution of the area detector prevent the observation of the superlattice peaks of the fully CO *P*112 structure. Hence, the structure will be referred to as *Pba*2.

Very little is known about the high-pressure behaviour of TTB materials; and the closest materials for comparisons are fluorides of perovskite type with which the TTBs share their basic building blocks, the MX_6 octahedra. However, this comparison suffers from the differences in connectivity of these octahedra, which dictates the geometric constraints for each crystallographic direction. The pressure induced volume reduction can be most easily compensated for along the *c*-axis, where the cooperative tilting of CrF_6 units is least constrained by the octahedron's connectivity. As a result of the TTB geometry, the unit cell *c*-axis is softest ($K_0(c)$ =

46(9) GPa) as compared to the in plane *a*- and *b*- directions ($K_0(a)$ = 34(3) GPa and $K_0(b)$ = 39(5) GPa). The isothermal bulk modulus of $K_{0.6}CrF_3$ (K_0 = 40(5) GPa), is smaller compared to perovskite type $KMnF_3$ (K_0 = 64(1) GPa) and the TTB $KMnCrF_6$ (K_0 = 48.8(8) GPa) [25].

The orthorhombic *Pba*2 phase is stable up to p = 6 GPa, where a symmetry change to tetragonal *P*4*bm* occurs, accompanied by the halving of the *c*-axis. Hydrostatic pressure is generally known to change the geometry of the coordination polyhedra and the hybridisation; therefore we can expect changes in crystal symmetry and CO pattern. A reliable discrimination of atomic positions and bond-distances at high-pressures is hampered by the width of the diffraction peaks, however changes in CO can be discussed qualitatively. The number and multiplicity of crystallographic sites changes: the four (4*c*) positions (*Pba*2) merge into a single eightfold (8*d*) site (*P*4*bm*), and the two (2*b*) sites (*Pba*2) correspond to one (2*b*) site (*P*4*bm*). From the stoichiometry, the ratio of Cr^{2+} to Cr^{3+} per unit cell is 6:4. Therefore both sites of *P*4*bm* must either be occupied statistically by a disordered array of Cr^{2+} and Cr^{3+}, or by Cr in an intermediate valence state.

Pressure-induced melting of CO has been observed in the halide perovskite $Cs_2Au_2I_6$: the charge disproportionation of Au^+ and Au^{3+} vanishes at p = 5.5 GPa and is accompanied by a change from insulating to semiconducting state [26]. Similar in perovskite type $YNiO_3$ the pressure induces melting of CO at p = 14 GPa; marked by a structural transition from monoclinic to orthorhombic symmetry [27]. Upon CO melting, the electronic structure changes as electrons are transferred to the conduction band; an effect which could be monitored by high-pressure electrical conductivity measurements (e.g. in a PPMS system). The possibility for pressure-induced metallisation is particularly appealing, as the suppression of CO could possibly lead to superconductivity. Further characterisation of the high-pressure phase by extended X-ray absorption fine structure (EXAFS) measurements might differentiate between a spatially disordered, but charge-localised and a charge-disordered arrangement.

5.4.5 Magnetic Properties

Very little is known about the magnetic structure of TTB fluorides, except for $KMnFeF_6$ and $K_{0.6}FeF_3$, which magnetic structures have been solved (or approximated) with a star-like spin arrangement in space group *Pb'a*2' [28],[29]. Generally speaking, the magnetic properties in transition metal fluorides are

dependent on correlation superexchange mechanisms between the magnetically active ions via the linking fluorine ligand. The magnetic interactions of 180° metal-ligand-metal arrangements can be analysed with the Goodenough-Kanamori-Anderson (GKA) rules [30], [31], [32]. The GKA rules give an estimate of the different orbital contributions towards the overall magnetic interactions and are illustrated in Figure 4.18. The *d*-orbitals in Cr^{2+} and Cr^{3+} are less than half filled with electron configurations of (d^4, e_g^2 t_{2g}^1) and (d^3, t^{2g2} e_g^0), respectively. There are three possible interaction pathways in $K_{0.6}CrF_3$, namely Cr^{2+} – Cr^{2+} (d^4 – d^4), Cr^{3+} – Cr^{3+} (d^3 – d^3) and Cr^{2+} – Cr^{3+} (d^4 – d^3). Each pair has three contributions, one σ (d_{x2-y2}) and two π (d_{xy}, d_{xz}; if x-axis is bond axis). The resulting interactions for the Cr^{2+}–Cr^{2+}, Cr^{3+}–Cr^{3+} and Cr^{2+}–Cr^{3+} pairs are expected to be moderately FM, weakly AFM and quasi-static FM, respectively, see also Figure 5.26.

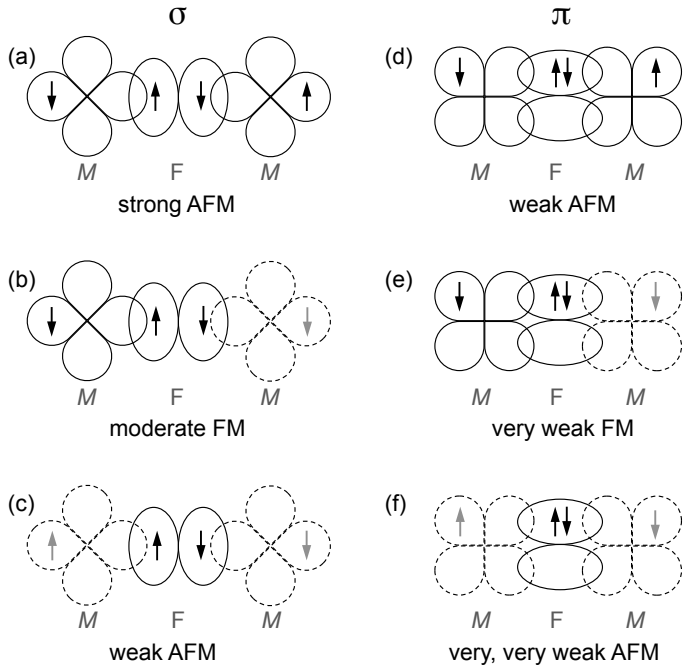

Figure 5.26 (a-f) The magnetic interactions according to the GKA rules (filled orbital: solid line, empty orbital: dashed line). (a – c) The three possible σ interactions strongly antiferromagnetic (AFM) [$d(e_g^2) - p - d(e_g^2)$], moderate ferromagnetic (FM) [$d(e_g^2) - p - d(e_g^0)$] and weak AFM [$d(e_g^0) - p - d(e_g^0)$]. (d – f) The exchange expected for the π interactions are weak AFM [$d(t_{2g}^2) - p - d(t_{2g}^2)$], very weak FM [$d(t_{2g}^2) - p - d(t_{2g}^0)$] and very, very weak AFM [$d(t_{2g}^0) - p - d(t_{2g}^0)$].

There are 60 Cr-F-Cr′ bonds in each unit cell of $K_{0.6}CrF_3$, two of which are Cr^{3+} - F - Cr^{3+} interactions (AFM coupling). All other interactions present (Cr^{2+} - F - Cr^{2+} and Cr^{2+} - F - Cr^{3+}) are expected to be FM. A hypothetical FM model e.g. with all

moments aligned parallel to the c-axis, would leave only two of 60 bond-conditions unsatisfied, but such a simple FM model would give rise to an appreciable spontaneous magnetisation, and is not supported by the magnetic susceptibility measurements. Although superexchange may play a dominant role in the correlation between Cr-centres, which can be approximated using the GKA rules, the TTB structure imposes strong geometric constraints on the system. One possible result of the geometric frustration is the lower ordering temperature of $K_{0.6}CrF_3$ (T_N = 33 K) as compared to the perovskite type $KCrF_3$, which contains only 180° Cr-F-Cr interactions and shows AFM coupling of FM planes at T_N = 46 K [1].

In the fluoride TTBs $K_{0.6}FeF_3$ and $KMnFeF_6$, the triangular spin alignment is predominantly confined to the *ab* plane and coupled AFM between adjacent planes. A similar arrangement may be proposed for $K_{0.6}CrF_3$. The magnetic moments arising from the Cr^{2+} and Cr^{3+} sublattices, and/or the two consecutive layers will be unequal, and if coupled AFM they will not cancel each other out completely, and hence may give rise to the small magnetic hysteresis observed.

The small value of magnetic susceptibility observed in the ZFC branch, and the increasing magnetisation with decreasing temperature in the FC branch both indicate highly anisotropic behaviour. In ZFC mode, small applied fields are not sufficient to reorient the spins in an anisotropic material, and give small values of magnetisation. Similarly, in FC mode, the spins are locked in a particular direction with respect to the external field. In isotropic materials the FC magnetisation remains almost constant with decreasing temperature, whilst the magnetisation increases with decreasing temperature in strongly anisotropic systems. The low symmetry of the crystal structure and the large anisotropy imply an important role played by the Dzyaloshinskii-Moriya interaction for the understanding of the magnetic behaviour of $K_{0.6}CrF_3$.

In summary, the geometric constrains imposed by the TTB structure gives magnetic frustration and anisotropy in $K_{0.6}CrF_3$. Unsurprisingly, a simple FM model based on the GKA rules, is not satisfactory to explain the experimental results. The small magnetic hysteresis and lack of saturation in high fields (H = 50000 Oe) observed, point towards ferrimagnetic behaviour between T = 33 K and 7 K. The sharp increase in susceptibility below T = 6 K is the signature of a FM type transition. Further magnetisation measurements (i.e. hysteresis loop at T < 5 K) and neutron diffraction experiments (at 33 K < T < 7 K and below T = 5 K) would be beneficial to

clarify the nature of the second transition at T = 6 K and the spin-ordering pattern(s) below T = 33 K.

5.4.6 $K_{0.6}CrF_6$ – a Potential Ferroelectric

Although the polarisability of $K_{0.6}CrF_3$ has not yet been measured experimentally, some predictions on ferroelectric properties can be made based on crystal structure considerations and the similarity to $K_{0.6}FeF_3$ [33], [34]. Generally, ferroelectricity can occur as the result of cooperative ionic displacements along a polar axis (displacive ferroelectricity) or as a consequence of electronic effects where the CO pattern determines the direction and magnitude of the polarisation [6], [35]. The results of our analysis have shown that $K_{0.6}CrF_3$ adopts a monoclinic superstructure arising from a specific Cr^{2+}/ Cr^{3+} ordering pattern. Such a distortion was predicted theoretically for $K_{0.6}FeF_3$, but never observed experimentally [6].

Let us firstly focus on the displacive features of the structure, which can be fully described considering only *Pba*2 symmetry. The average displacements of Cr with respect to the plane of the fluorine coordination octahedra is $d(z)$ = 0.213 Å. This value is larger compared to the displacements calculated for the most recently published *Pba*2 structure[****] of $K_{0.6}FeF_3$ [5]. A sizeable displacement (in positive *c*-direction – polarisation axis) of the Cr ions with respect to the plane of the fluorine coordination octahedra could support displacive ferroelectricity.

In addition to the polar crystal structure, also insulating properties are a prerequisite for ferroelectricity. An insulating state would only be stabilised is full charge ordering is present. As in the case of $K_{0.6}FeF_3$, full CO should give rise to monoclinic. Superlattice peaks indicating *P*112 symmetry are observed in the diffraction pattern of $K_{0.6}CrF_3$ and lead us to the deduction of a CO model. The symmetry of the observed CO differs from the *Pb*11 symmetry that was suggested for $K_{0.6}FeF_3$ [6]. One explanation might be that there is only a small energy difference between the different monoclinic models tested in reference [6]. It can also be related to the different chemical species. Nevertheless, the signature of full CO in the crystal structure is clearly appreciable from the high-resolution powder diffraction data presented. It would be extremely important to confirm these findings with theoretical calculations of different ordering models to clarify the nature of CO in $K_{0.6}CrF_3$.

[****] Structure was determined from a single crystal.

The transitions from full CO to partial CO (i.e. *P*112 to *Pba*2) and from acentric to centric (i.e. *Pba*2 to $P4_2/mbc$) occur at distinct and well-separated temperatures. Unless full CO is maintained in the *Pba*2 phase (which in this case would be of pseudo-orthorhombic character), it should be possible to differentiate between electronic and displacive contributions to the proposed ferroelectric properties of $K_{0.6}FeF_3$. With CO as the driving force, the potential ferroelectric properties are expected to be lost at the monoclinic – orthorhombic structural phase transition at T = 423 K, whereas displacive ferroelectricity should vanish with the transition from orthorhombic to tetragonal at T = 823 K.

With a melting of CO in the X-ray induced phase (and the connected increase of electrical conductivity) also potential ferroelectric properties are likely to be reduced or lost. Despite this, the atomic displacement of Cr from the basal plane of the fluorine coordination is still present (mean displacement d = 0.18(1) Å), and several fluorine atoms show a sizeable displacement from a hypothetical centric *Cmmm* structure, showing that the description in acentric *Cmm*2 is justified.

In summary, $K_{0.6}CrF_3$ can be regarded as a promising candidate for novel ferroelectric materials, both from its atomic- and charge arrangement. In addition, $K_{0.6}CrF_3$ is orders magnetically at T = 33 K, and we may expect coupling of ferroelectric and magnetic properties, as both arise from the same Cr-sublattice. Being fully CO and magnetic at low temperatures, $K_{0.6}CrF_3$ is suggested as an improper multiferroic material.

5.5 Summary

The room temperature structure of $K_{0.6}CrF_3$ was previously reported as orthorhombic *Pba*2, $c = c_{TTB}$ [4]. We find that the *c*-axis is doubled compared to the conventional TTB cell, so that a unit cell contains two layers of CrF_6 octahedra, located at $z = 0.25$ and 0.75. As in the case of $K_{0.6}FeF_3$, the *Pba*2 model for $K_{0.6}CrF_3$ implies partial CO. The ordering pattern is such that Cr^{2+} and Cr^{3+} are alternating along the *c*-axis on the extra-perovskite site (2-fold sites), whereas the perovskite site is ordered at $z = 0.25$, but partially disordered at $z = 0.75$ (4-fold perovskite sites). In analogy to $K_{0.6}FeF_3$, the symmetry has to be lowered to monoclinic in order to obtain a fully CO model [6]. Indeed, after prolonged data collection[††††] on the high-resolution powder diffraction beamline ID31, small superlattice peaks emerged at low 2θ, clearly indicating a symmetry lower than orthorhombic. Rietveld refinements of different monoclinic models (corresponding to different CO patterns) indicated that the structure is likely monoclinic *P*112.

The monoclinic cell is preserved on cooling and no further structural phase transitions are observed. However, continuous X-ray irradiation below $T = 150$ K leads to the stabilisation of a new metastable phase, which can be indexed with an orthorhombic *Cmm*2 cell. Compared to the *Pba*2 structure, the *a*- and *b*-lattice vectors rotate by 45° to lie along the base diagonal of the TTB cell, i.e. $a_{Cmm2} \approx a_{TTB} \cdot \sqrt{2}$, $b_{Cmm2} \approx b_{TTB} \cdot \sqrt{2}$ and the doubling of the *c*-axis is lost. This new orthorhombic phase is characterised by complete charge disorder where all sites are statistically occupied by Cr^{2+} and Cr^{3+}. The X-ray induced phase is stable up to $T = 150$ K, where the effect of X-ray irradiation starts to compete with thermal effects. The ambient temperature phase is observed after 2 hours at $T = 150$ K.

On further heating, two consecutive phase transitions are observed at $T = 423$ K and $T = 823$ K. These correspond to a transition from full CO monoclinic *P*112 to partially CO orthorhombic *Pba*2 and to charge-disordered and centric tetragonal $P4_2/mbc$ symmetry. Under applied hydrostatic pressure at room temperature, $K_{0.6}CrF_3$ undergoes a structural transition to tetragonal symmetry (space group *P4bm*) at $p = 6$ GPa, which remains stable up to the highest pressure point collected ($p = 18.5$ GPa).

[††††] Data was collected over 4 hours as compared to 20 minutes for a typical room temperature diffraction pattern.

In addition to the structural investigation, the magnetic properties were assessed by means of magnetic susceptibility measurements at variable temperatures (T = 300 K - 5 K). An antiferromagnetic and ferromagnetic transition at T = 33 K and 6 K, respectively, and the almost linear H-M dependence at T = 15 K, point towards a complex magnetic behaviour.

5.6 References

[1] S. Margadonna, G. Karotsis, *Journal of the American Chemical* Society 128 (2006) 16436.

[2] S. Margadonna, G. Karotsis, *Journal of Materials Chemistry* 17 (2007) 2013.

[3] S. Margadonna, Structural investigation of $K_{0.9}CrF_3$ at variable temperature and pressure, in preparation.

[4] Y. Hong, K. Baker, A. Shah, R. Williamson, W. Boo, *Inorganic Chemistry* 29 (1990) 3037.

[5] F. Mezzadri, S. Fabbrici, E. Montanari, L. Righi, G. Calestani, E. Gilioli, F. Bolzoni, A. Migliori, *Physical Review B: Condensed Matter and Materials Physics* 78 (2008) 064111.

[6] K. Yamauchi, S. Picozzi, *Physical Review Letters* 105 (2010) 107202.

[7] R.D. Shannon, *Acta Crystallographica Section A: Foundations of Crystallography* 32 (1976) 751.

[8] H. Fujihisa, *Review of High Pressure Science and Technology* 1 (2005) 29.

[9] A.C. Larson, R.B.V. Dreele, Los Alamos National Laboratory Report LAUR 86-748 (2004) 1.

[10] B. Toby, *Journal of Applied Crystallography* 34 (2001) 210.

[11] A. Wills, VaList, Program for Bond Valence Calculations. [Program available from www.ccp14.ac.uk]

[12] P. Labbe, H. Leligny, B. Raveau, J. Schneck, J.C. Toledano, *Journal of Physics: Condensed Matter* 2 (1990) 25.

[13] C. Capillas, E. Sururi Tasci, G. De La Flor, D. Orobengoa, J. Manuel Perez-Mato, M. Ilia Aroyo, *Zeitschrift für Kristallographie* 226 (2011) 186.

[14] R. Angel, *Reviews in Mineralogy and Geochemistry* 41 (2000) 35.

[15] E. Banks, S. Nakajima, G.J.B. Williams, *Acta Crystallographica, Section B: Structural Science* 35 (1979) 46.

[16] E. Banks, M. Shone, Y. Hong, R. Williamson, W. Boo, *Inorganic Chemistry* 21 (1982) 3894.

[17] S. Fabbrici, E. Montanari, L. Righi, G. Calestani, A. Migliori, *Chemistry of Materials* 16 (2004) 3007.

[18] Y. Hong, R. Williamson, W. Boo, *Inorganic Chemistry* 19 (1980) 2229.

[19] A. Caramanian, N. Dupont, P. Gredin, A. De Kozak, *Zeitschrift für Anorganische und Allgemeine Chemie* 625 (1999) 933.

[20] Y. Yeh, Y. Hong, W. Boo, D. Mattern, *Journal of Solid State Chemistry* 178 (2005) 2191.

[21] R.H. G. Siebert, *Zeitschrift für Anorganische und Allgemeine Chemie* 391 (1972) 117.

[22] V. Kiryukhin, D. Casa, J.P. Hill, B. Keimer, A. Vigliante, Y. Tomioka, Y. Tokura, *Nature* 386 (1997) 813.

[23] H. Ishibashi, T. Koo, Y. Hor, A. Borissov, P. Radaelli, Y. Horibe, S.-W. Cheong, V. Kiryukhin, *Physical Review B: Condensed Matter and Materials Physics* 66 (2002) 144424.

[24] S. Margadonna, K. Prassides, A.N. Fitch, *Angewandte Chemie International Edition* 43 (2004) 6316.

[25] M. Guennou, P. Bouvier, G. Garbarino, J. Kreisel, E.K.H. Salje, *Journal of Physics: Condensed Matter* 23 (2011) 485901.

[26] A.F. Kusmartseva, M. Yang, A.M. Arevalo-Lopez, K.V. Kamenev, J.P. Attfield, *Chemical Communications* 46 (2010) 6681.

[27] J. García-Muñoz, M. Amboage, M. Hanfland, J. Alonso, M. Martínez-Lope, R. Mortimer, *Physical Review B: Condensed Matter and Materials Physics* 69 (2004) 094106.

[28] P. Lacorre, J. Pannetier, G. Ferey, *Journal of Magnetism and Magnetic Materials* 94 (1991) 331.

[29] F. Mezzadri, G. Calestani, C. Pernechele, M. Solzi, G. Spina, L. Cianchi, F. Del Giallo, M. Lantieri, M. Buzzi, E. Gilioli, *Physical Review B: Condensed Matter and Materials Physics* 84 (2011) 104418.

[30] C. Wang, L. Li, S. Chi, Z. Zhu, Z. Ren, Y. Li, Y. Wang, X. Lin, Y. Luo, S. Jiang, X. Xu, G. Cao, Z.A. Xu, *EPL (Europhysics Letters)* 83 (2008) 67006.

[31] J. Kanamori, *Journal of Physics and Chemistry of Solids* 10 (1959) 87.

[32] P.W. Anderson (1963) *Magnetism*. New York: Academic New York.

[33] S.C. Abrahams, *Acta Crystallographica, Section B: Structural Science* 45 (1989) 228.

[34] E. Kroumova, M. Aroyo, J. Perez-Mato, *Acta Crystallographica, Section B: Structural Science* 58 (2002) 921.

[35] S. Picozzi, C. Ederer, *Journal of Physics: Condensed Matter* 21 (2009) 303201.

Chapter 6

Conclusions

6.1 Overview

Two centuries ago, in 1811, A. Lavoisier predicted fluorine to be an element, but it was not until 1886 that H. Moissan succeeded in its isolation. It took another 50 years before fluorine production reach industrial scale. Despite the availability of fluorine chemicals, their demand remained low initially, because appropriate equipment and training for their handling was lacking. Nevertheless, these problems were overcome and nowadays fluorine-containing materials are used constantly in everyday life.

In particular the field of organofluorine chemistry grows steadily, making use of the remarkable reactivity of fluorine and its compounds. On the other hand, the area of solid-state complex fluorides is relatively small, although many transition metals are now commercially produced and the handling of hydrofluoric acid or fluorine gas has become possible both in the industrial and laboratory environments. Yet still the synthesis of inorganic fluorides requires more precautions compared to their solid-state oxide relatives. Conventional solid-state reactions have to be carried out under strict exclusion of air and moisture, and in many cases inside sealed gold or platinum containers. It may be those synthetic challenges that have made solid-state fluorine-chemistry a less thoroughly and systematically developed area of research. Nevertheless, a number of fluoride-based materials of varying structure types are known, and their fascinating properties have stimulated the work presented in here.

The aim of this thesis was to advance the chemistry and structural description of selected complex fluorine compounds. The materials were chosen for their interesting physical properties, ranging from superconductivity to mulitferroicity. Firstly, reproducible synthetic protocols were developed for all materials, which afforded in most cases single-phase products and could be scaled up to give sample volumes suitable for different experiments. Secondly, the structural descriptions available were re-examined and extended with the aid of (synchrotron) X-ray and neutron powder diffraction. Thirdly, the physical properties were assessed by means of magnetic susceptibility and electrical resistivity measurements. Lastly, external stimuli suach as temperature and pressure were used to unreavel their structural, electronic and magnetic phase diagrams.

6.2 Main Achievements of This Thesis

The materials studied are related to the layered iron pnictide superconductors and to multiferroic compounds adopting the tetragonal tungsten bronze structure. Although these systems have fluorine building blocks as their common denominator, they vary in structure and properties, and this leads to a wide range of phenomena.

6.2.1 The Layered Transition Metal Pnictide Fluorides

The discovery of superconductivity in fluorine-doped LaFeAsO in 2008 created big excitement among researchers around the globe: the critical temperature was relatively high to start with, and the layered structure was promising for chemical substitution. Furthermore, iron is usually associated with magnetic properties that are believed to oppose the formation of an itinerant state. The field expanded rapidly, and numerous parent compounds and doped derivatives of the *Re*FeAsO family (*Re* = La, Ce, Pr, Nd, Sm, Gd, Tb, Dy, Ho, Er, Y) were reported.

All parent compounds are poor metals and adopt the tetragonal *P*4/*nmm* structure at room temperature. On cooling, they undergo a structural transition to orthorhombic *Cmma* symmetry, which involves stretching of the iron net from square to rectangular. Research efforts clearly concentrated on the iron-based compounds, but also isostructural materials of other transition metals (e.g. Ni, Co, Mn, Ru) display interesting properties. The oxypnictides are superconductors for iron and nickel, itinerant ferromagnets for cobalt, semiconducting antiferromagnets that show magnetoresistance for manganese and metallic but non-magnetic (except *Re* magnetism) for ruthenium.

At the same time, it was found that the fluorine-based *Ae*FeAsF (*Ae* = alkaline earth metal) have similar properties as their analogous oxypnictides. These can be obtained by replacing the [*Re*O] slab with a [*Ae*F] layer. But only the Ca, Sr and Eu based parent materials were prepared, and just the Ca and Sr compounds are known to become superconducting upon doping.

a) Superconductivity in La-doped SrFeAsF

Prior to this project, our research group had synthesised and characterised the $Nd_{1-x}Sr_xFeAsO$ and the $FeSe_{1-x}$ superconductors and obtained fascinating results. It

was demonstrated that hole doping in $Nd_{1-x}Sr_xFeAsO$ firstly reduces the electron cylinders of the Fermi surface before additional charge carriers are introduced that push the system into the superconducting regime. The iron chalcogenide $FeSe_{1-x}$ was studied at high pressures, and a remarkable increase of the critical temperature to $T_c = 37$ K at $p \sim 7$ GPa was found.

The promising properties of the 1111-type oxypnictides inspired the investigation of the isostructural AeT_MPnF system (Ae = Sr, Ba; T_M = Mn, Fe; Pn = P, As, Sb) that are the topic of Chapter 3. The iron-arsenide SrFeAsF was found to undergo a tetragonal → orthorhombic ($P4/nmm \rightarrow Cmma$) structural transition at $T_S = 180$ K, accompanied by short-range magnetic correlations manifesting in a spin density wave. Between $T = 150$ K and 100 K, long range striped antiferromagnetic order occurs. The experimental magnetic moment of Fe in the ordered state is quite small ($\mu_{eff} = 0.6(2)\ \mu_B$). This can be related to the itinerant electrons. The structural and magnetic properties are in agreement with the results obtained by other groups on CaFeAsF and SrFeAsF. Similar to the oxy-arsenides, the spin density wave and structural transition is gradually suppressed upon electron-doping. Superconducting phases of $La_xSr_{1-x}FeAsF$ ($x = 0.1, 0.2$) were obtained with $T_c = 27$ K for $x = 0.2$, albeit with small superconducting fractions.

b) Structure-Property Dependencies in AeMnPnF

Materials containing transition metals other than iron have been investigated well before 2008, but receive renewed attention since then. Again, the fluoride analogues are scarce and only few are known to exist.

In this work we studied the systematic substitution of the constituent elements of the AeT_MPnF materials by replacement of Ae (Sr, Ba), T_M (Fe, Mn) and Pn (P, As, Sb). Within the elemental combinations explored we find that the materials adopt the $P4/nmm$ structure throughout the measured temperature range ($T = 2$ K – 480 K) and are G-type antiferromagnetic insulators below $T_N \sim 350$ K. The Mn network tolerates a range of pnictides (P → Sb) and is more flexible than the Fe network (forms for As only). The unit cell volume expands linearly with the ionic radii of the pnictide and alkaline-earth metal. On the other hand, the distortion of the tetrahedra – deemed important for the superconducting properties in the iron pnictides – is not only dependent on the radius ratio of T_M and Pn, but also on the lattice mismatch between the [AeF] and [T_MPn] layer. The local structure of the AeMnPnF compounds was found to be close to the long-range structure. Curiously,

SrMnPF and BaMnSbF that appeared to be most regular on average, showed the largest distortions of their local geometry. Surely, local structure investigations will become increasingly important for our understanding of the electronic structures and physical properties of this class of materials.

The manganese pnictides appear to be unlikely candidates for new superconducting materials. They are far from magnetic instabilities (T_N ~ 350 K, μ_{eff} ~ 3.5 μ_B for *Ae* = Sr) and very insulating. On the other hand, LaMnSeO was suggested as a potential superconductor, making the synthesis of such compounds worthwhile. Besides, other interesting phenomena such as magentoresistance were observed in the oxide manganese materials Re_xMnAsO (*Re* = La, Nd) and may be present in the fluorides too. Initial measurements of SrMn*Pn*F did not indicate magnetoresistance, but may emerge with small changes in stoichiometry as in the case of NdMnAsO. It may be worthwhile to carry out the same measurements for BaMn*Pn*F and to investigate the relationship between composition and electrical transport.

6.2.2 The Tetragonal Tungsten Bronze Fluorides

The family of tetragonal tungsten bronze fluorides has received renewed attention over the last years, mainly focussing on ferroelectric K_xFeF_3 and related iron containing compounds, for instance $KMnFeF_6$, $K_{0.6}Fe_{0.4}Cu_{0.6}F_3$ and $K_{0.6}Cr_{0.4}Fe_{0.6}F_3$. The ferroelectric properties of $K_{0.6}FeF_3$ were predicted as early as 1988 and quickly confirmed experimentally [1], [2]. These predictions were based on empirical relationships between the crystal structure and physical properties, and successfully employed to a number of compounds containing fluorine-octahedra [3]. Furthermore, the TTB fluorides are known to show chemical or charge order. It is clear that the stoichiometry dictates the M^{2+}/M^{3+} ratio, upon which the chemical and charge order pattern are dependent. The underlying order gives rise to different structural types and influences the physical properties.

Despite the potential of the TTB fluorides as ferroelectrics, very little accurate crystallographic information is available. Clearly, it is absolutely necessary to carefully characterise the structure and composition of these materials to advance the field and to generalise the structure-property relationships of the TTB fluorides. For this reason, the compounds $KMnCrF_6$ and $K_{0.6}CrF_3$ were choosen as examples of ferroelectric fluorides and their complex behaviour was studied.

a) Chemical Order in Multiferroic $KMnCrF_6$

The phase diagram of the tetragonal tungsten bronze fluoride $KMnCrF_6$ was established in the temperature range of T = 5 K – 823 K, and at ambient temperature in the high-pressure regime up to 18 GPa. The previously suggested alternating order between Mn^{2+} and Cr^{3+} on the perovskite site was confirmed [4]. $KMnCrF_6$ was originally described crystallise in space group $P4_2bc$ at room temperature, but we found a subtle distortion to orthorhombic $Ccc2$ symmetry [4]. The lower symmetry could imply additional cationic order on the extra-perovskite site.

On heating to T ~ 350 K, a structural transition from orthorhombic $Ccc2$ to tetragonal $P4_2/mbc$ takes place. At the phase transition, the off-centring of Mn and Cr from the centre of their octahedral fluorine cages diminishes, and the cations approach the higher symmetry positions of centrosymmetric $P4_2/mbc$. Further, the structural transition is marked by a distinct change of slope in the temperature dependence of the c-axis, which is coupled to the cooperative tilting of MF_6 octahedra. Similar behaviour is observed in ferroelectric $K_{0.6}FeF_3$ [5]. The change from polar orthorhombic to apolar tetragonal symmetry is likely connected to a ferroelectric – paraelectric phase transition. Based on structural criteria that were previously applied to the prediction of $K_{0.6}FeF_3$ as a ferroelectric material, the temperature of ferroelectric – paraelectric transition was estimated to be T_C ~ 350 K. Below T_N = 23 K, $KMnCrF_6$ behaves as a weak ferromagnet and possible coupling of ferroelectric and ferromagnetic properties could lead to multiferroic properties. The high-pressure work shows that the orthorhombic structure established at ambient conditions is robust up to p = 18 GPa, but the axial compressibilities are anisotropic.

The results of the structural investigation can be transferred to other mixed metal TTB fluoride systems. The chemical order found in $KMnCrF_6$ is probably driven by the size difference of the Mn^{2+} (r = 0.83 Å) and Cr^{3+} (r = 0.62 Å) ion, as was already suggested for the iron-based system [6]. In the mixed metal TTB systems (e.g. $KMnCrF_6$) the ordering of M^{2+} and M^{3+} is bound to the chemical species Mn and Cr. It is probable that chemical ordering occurs in the known systems $KMnFeF_6$ (r_{Mn2+} = 0.83 Å, r_{Fe3+} = 0.55 Å) and $K_{1.2}Cu_{1.2}Fe_{0.8}F_6$ (r_{Cu2+} = 0.73 Å, r_{Fe3+} = 0.55 Å) but perhaps not in $K_{1.2}Fe_{1.2}Cr_{0.8}F_6$ (r_{Fe2+} = 0.61 Å, r_{Cr3+} = 0.62 Å). The latter two systems were described as disordered materials adopting the tetragonal space group $P4/mbm$ at room temperature (a ~ 12.59 Å, c ~ 3.94 Å) [7], [8]. Details of their structure were not reported. It may be worthwhile to reinvestigate their structure, and also those of $KFeCuF_6$ and $KFeCrF_6$ if they can be isolated.

b) The Intriguing Properties of Charge-Ordered $K_{0.6}CrF_3$

The fascinating properties of both $KCrF_3$ and $K_{0.6}FeF_3$ have initiated the study of $K_{0.6}CrF_3$. Preliminary diffraction experiments on $K_{0.6}CrF_3$ had already indicated a rich but complicated structural phase diagram. The delicate balance that stabilises a particular charge order pattern of Cr^{2+}/Cr^{3+} can be perturbed through changes in temperature, pressure and X-ray irradiation, in each case leading to different crystal structures.

At room temperature, $K_{0.6}CrF_3$ was reported to crystallise in the orthorhombic space group *Pba*2. This structural description involves a mixed valence site $Cr^{2.5+}$, which is not convincing considering that Cr^{2+} and Cr^{3+} are electronically different (JT active/ non-active) and have different ionic radii; hence they are likely to order. A detailed investigation of the room temperature phase revealed that the structure is distorted to monoclinic *P*112 symmetry, which is a clear signature of full charge ordering.

On heating to T = 350 K and 773 K, this charge order is gradually lost and the lattice changes to *Pba*2 and $P4_2/mbc$ symmetry, respectively. The latter transition is to a fully disordered system. On cooling below room temperature, the monoclinic *P*112 symmetry is preserved. Below T = 150 K, prolonged X-ray irradiation triggers a fully reversible phase transition. The X-ray induced phase is orthorhombic with space group *Cmm*2, and is completely charge disordered. High-pressure diffraction experiments at room temperature revealed a structural transition to tetragonal *P*4*bm* symmetry at p = 6 GPa, which corresponds to a disordered structure. The phase transition is reversible and the ambient pressure *Pba*2 (*P*112) phase is recovered on pressure release.

Two magnetic transitions are observed at T = 33 K and 6 K in magnetic susceptibility measurements. The magnetic hysteresis loop recorded at T = 15 K reveals only a very small ferromagnetic contribution. The multiferroic potential of $K_{0.6}CrF_3$ can be evaluated based on its similarities to ferroelectric $K_{0.6}FeF_3$. Both materials have comparable structures close to *Pba*2 symmetry and contain transition metal ions in different oxidation states. The ferroelectric properties of $K_{0.6}FeF_3$ were related to (i) the orthorhombic distortion of the structure, (ii) the off-centring of the Fe-ions from the centre of their fluorine octahedra and (iii) to the full Fe^{2+}/Fe^{3+} order. Although the underlying driving force of the ferroelectric transition is not yet fully understood for $K_{0.6}FeF_3$, it is apparent that $K_{0.6}CrF_3$ fulfils all the listed criteria.

Therefore, we can describe $K_{0.6}CrF_3$ as a ferroelectric charge ordered material and predict its possible mulitferroic behaviour below $T_N = 33$ K.

Charge ordering is observed in a number of transition metal (T_M) oxides and has receives increasing attention, because it may be related to the superconducting properties of the cuprates, or the magentoresistance of the manganites [9], [10], [11]. The CO of the TTB fluoride $K_{0.6}CrF_3$ shares important similarities with the well-studied oxide counterparts.: (i) Charge order is the long-range order of the two T_M oxidations states and evokes a subtle distortion to lower (i.e. monoclinic) crystal symmetry. (ii) A higher temperature structure variation exists, in which the charge order is lost. (iii) Electron-lattice coupling allows to switch or melt CO states, for instance through hydrostatic pressure or electromagnetic radiation. (iv) CO is likely connected to physical properties, i.e. ferroelectricity [11], [12], [13].

In the TTB fluorides, the CO pattern is dependent on the A-site cation content that determines the M^{2+}/M^{3+} ratio. For instance, in the $K_{0.6}FeF_3$ one perovskite site is disordered, whilst in $K_{0.5}FeF_3$ the extra-perovskite site is disordered [5], [6]. The observation of a disordered site in the iron-based TTB fluorides may indicate that (commensurate) CO only establishes for specific ratios of the transition metals, and that incommensurate charge ordering would be adapted by intermediate ratios. It may also be that the subtle lattice distortion associated with full (commensurate) CO is not sizeable enough to be observed experimentally with the resolution of current the diffractometers.

In the TM oxides, the transition from a charge disordered to a CO (charge localised) state is in general associated with a change in the electronic structure. This typically opens a gap in the electronic structure and leads to a change from conducting to insulating properties. This is observed for instance in the TTB fluoride $K_{0.6}FeF_3$, which shows a decrease in electrical conduction at the disorder-order transition temperature [14]. A similar change in physical properties is also expected for $K_{0.6}CrF_3$ at the *Pba*2 to $P4_2/mbc$ transition. The results of our structural investigation of $K_{0.6}CrF_3$, combined with the reported properties measurements of its close relative, $K_{0.6}FeF_3$, demonstrate that CO in the TTB fluorides is connected to interesting phenomena, such as ferroelectricity. In the T_M oxides, CO may be linked to superconductivity or magnetoresistance. Similar properties may be found in T_M fluorides, suggesting that this class of materials should be included in the search of new functional materials.

c) Chemical and Charge Order in Transition Metal Fluorides

The ordering mechanisms of $KMnCrF_6$ and $K_{0.6}CrF_6$ are fundamentally different. Whilst ordering in $KMnCrF_6$ occurs probably during synthesis at high temperatures and involves positional exchange of atoms, the ordering in the mixed-valence system $K_{0.6}CrF_3$ can occur through electron exchange via the bridging fluorine ligand, and is more likely to occur after the formation of the crystal lattice. This difference in ordering mechanism is not limited to the TTB fluorides, but is also observed in the fluoride-based pyrochlores.

In these materials charge order is in general observed for mix-valence compounds, such as $CsFe^{2+}Fe^{3+}F_6$ [15], $RbFe^{2+}Fe^{3+}F_6$ [16] or $(NH_4)Fe^{2+}Fe^{3+}F_6$ [17], where it involves a symmetry lowering transition. For instance, $CsFe^{2+}Fe^{3+}F_6$ was studied to evaluate the ordering mechanism. It was prepared using $^{57}Fe^{3+}F_3$ as a starting material and quenched from synthesis temperature [15]. Using Mössbauer spectroscopy, ^{57}Fe was found to be present in both its 2+ and 3+ oxidation state, demonstrating that charge exchange can occur at low temperatures [15]. The mixed metal $AM^{2+}M^{3+}F_6$ pyrochlores tend to be disordered, [15], except for M^{2+}/M^{3+} combinations with sufficiently different cation radii. It was shown that $(NH_4)CoAlF_6$ exists both in its cation ordered and disordered form, and that the metastable disordered form becomes ordered after appropriate heat treatment [18]. This suggests that cation order may not only be dependent on the radius difference, but also on the synthetic conditions [18], [15].

6.3 Outlook and Future Work

6.3.1 Transition Metal Pnictide Fluorides

Differently to the oxypnictides, which have been substituted in many variations, similar systematic exploration of the fluoride materials is still to be carried out. This is not limited to doping (i.e. isoelectronic replacement on the pnictide site or by oxygen doping on the fluorine site, in analogy to $LaFeAsO_{1-x}F_x$) but also to the exploration of new structural motives (i.e. replacing the [*Ae*F] layer with [$Ae_3M_2F_5$] or [$Ae_4M_2F_6$] slabs, and in the oxide analogues). The formation of some phases might not be favourable, for instance BaFeAsF, which competes with $BaFe_2As_2$. However, the sublattices of other compositions such as BaMnSbF or MgFePF may be more suited to form the 1111-type structure.

Doping has proven a powerful tool to tune material properties, and in particular the $CaFe_{1-x}Co_xAsF$ series has shown that high T_C's can be obtained from non-oxide compounds. Again, the synthesis of pure doping series comes first and is extremely important if one wants to firmly establish links between composition, structure and properties. The $La_xSr_{1-x}FeAsF$ materials presented in this work suffer from the presence of impurities, making it difficult to draw a composition dependent phase diagram. Other researchers also encountered difficulties in the preparation of single-phase $Re_xAe_{1-x}FeAsF$ materials. It is clear that higher doping levels ($x > 0.2$) are required to fully supress the $T \rightarrow O$ transition, but the solubility limit of *Re* in *Ae*FeAsF obtainable under ambient conditions seems to be reached. In this respect it would be desirable to explore alternative synthetic routes, for instance the use of high-pressure techniques to make doping more effective. High-pressure is known to stabilise phases not obtainable under ambient conditions, and it has been used as an effective synthetic tool to incorporate the smaller lanthanides *Re*FeAsO (*Re* = Tb, Dy, Ho).

6.3.2 Tetragonal Tungsten Bronze Fluorides

Throughout this work, it was outlined that the complex fluorides are in general more scarce compared to the corresponding oxide materials. This applies in particular to the TTB fluorides. Therefore, it is easy to find a number of elemental combinations or doping series that have not yet been prepared. On the other hand it might be a more useful approach to continue the systematic investigation of the K_xCrF_3 ($x < 0.6$) and the $K_xMn_xCr_{1-x}F_3$ ($x \neq 0.5$) series. In this respect, the importance of high-resolution diffraction studies coupled to analytic determination of the stoichiometry is stressed.

In this work, $KMnCrF_6$ and $K_{0.6}CrF_3$ were studied as representative members of the two classes of multiferroic TTB-fluorides. Our work highlights the presence of subtle structural distortions and CO phenomena that have a fundamental role on their physical properties. Further information on these materials could be obtainable is single crystals were available. For instance, the anisotropy of the physical properties (i.e. magnetism) could be determined and additional information about tilt-modulated superstructures (as e.g. the FES in $K_{0.6}FeF_3$ [6]) could be gained from electron diffraction. Powder samples can be image with this method, but the challenge is to select a grain representative of the bulk sample. The use of a single crystal would avoid this problem.

Nevertheless, the currently available polycrystalline specimens are suitable for a number of experiments that will contribute to our understanding of this exciting class of materials. For $KMnCrF_6$ and $K_{0.6}CrF_3$ we plan:

Firstly, to perform variable temperature neutron powder diffraction measurements. Low temperature data will help to gain insight into the complex magnetic spin arrangement, while room temperature data will allow (i) more precise determination of the K-content, (ii) confirmation of the position of fluorine anions and the tilt modulation of the MF_6 units and (iii) for $KMnCrF_6$ differentiation between different Mn/Cr ordering patterns. In fact, neutron diffractions experiments of $KMnCrF_6$ at ambient and low temperature are in progress. The Mn/Cr ordering pattern may also be clarified using element specific spectroscopy (e.g. electron energy loss spectroscopy) coupled to imaging techniques (e.g. scanning transmission electron microscopy). It would also be important to collect diffraction data of the pristine, i.e. non-X-ray induced low temperature phase of $K_{0.6}CrF_3$, and determine the atomic arrangement in the multiferroic region.

Diffractometers operating with lower energy synchrotron X-ray or neutron radiation are suited for this. The drawback of the latter technique is the larger quantity of material required, but it has the advantage that the magnetic spin structure can be probed simultaneously. Lastly, to verify the (centro)symmetry of the different structures using, for instance, spectroscopic techniques such as Raman. Raman measurements can distinguish between polar and apolar space groups, because the character of the crystals' point group symmetry gives rise to different modes. In fact, coupled Raman and low-energy diffraction measurements of both compounds will be carried out in the near future.

The ordering concepts established in this work should be tested and extended to the two best-known TTB fluoride systems, $KMnFeF_6$ and $K_{0.6}FeF_3$. It is likely that $KMnFeF_6$ shows a similar orthorhombic distortion (*Ccc*2) as chemically ordered $KMnCrF_6$. The suggested order is dependent on the 1:1 Mn/Cr ratio, but of course, other ordering patters could be adopted for different compositions. In any case high-resolution synchrotron diffraction is required to resolve the subtle splitting. $K_{0.6}CrF_3$ is fully charge ordered, and the diffraction profile of the corresponding iron system $K_{0.6}FeF_3$ system should be re-examined towards the presence of superlattice peaks arising from monoclinic symmetry. The possibility such a distortion is supported by theoretical calculations that have described $K_{0.6}FeF_3$ as an improper electric ferroelectric, in which complete charge order gives rise to the electrical polarisation and a monoclinic cell [19]. The difficulty in these experiments is that the monoclinic distortion may not be sizeable enough to be detectable from standard diffraction data. Preliminary high-resolution diffraction data have hinted that also $K_{0.6}FeF_3$ may be distorted to monoclinic symmetry, indicating that full charge-order is not limited to the Cr compound.

The charge-order of $K_{0.6}CrF_3$ melts upon X-ray irradiation, comparable to effects seen in the charge ordered manganites. It is highly probable that $K_{0.6}FeF_3$ will undergo similar transitions at low temperatures. A recent diffraction study of K_xFeF_3 reported a (conventional) structural transition below room temperature [20]. The emerging structure was related to *Cmmm* symmetry, but because the sample investigated contained several phases, the authors did not determine the space group and fractional coordinates more closely [20]. The reported *Cmmm* space group is closely related to the *Cmm*2 phase of the X-ray induced phase of $K_{0.6}CrF_3$. Considering that the synchrotron powder diffraction beamline used for the reported measurements has a comparable photonflux to beamline ID31 and the behaviour of the width of the $(660)_T$ reflection at $T = 100$ K, it is very likely that the structural

transition is photoinduced. The preliminary results of a low temperature diffraction study carried out in our group show that $K_{0.6}FeF_3$ is indeed affected by X-rays, making the melting of charge order a generic feature of the TTB fluorides K_xMF_3.

The ferroelectric properties of the TTB fluorides have not yet been measured, except for $K_{0.6}FeF_3$. The experimental assessment of the dielectric properties is crucial to firmly establish the TTB fluorides as ferroelectric. Yet only few laboratories have the instruments available to measure dielectric properties. It may be easier to determine the electrical conductivity as a function of temperature. As in the case of $K_{0.6}FeF_3$, an increase of electrical conductivity is expected at the transitions from charge ordered to disordered phases, i.e. from *P*112 to *Pba*2 and to $P4_2/mbc$. The combination of X-ray diffraction and electrical characterisation (e.g. conductivity or polarisability) in a single experimental setup would be an extremely powerful tool to understand the interplay of the multiple (electronic) ordering parameters and to shed further light on the ferroelectric mechanism in this class of materials.

6.4 Concluding Remarks

The most important point arising from this work is that transition metal fluorides represent an intriguing class of materials. Their unique combination of structural, electronic and magnetic features imply that these systems could represent an attractive alternative to the widely studied oxide analogues. Both classes of materials show phenomena such as metal-insulator transitions, ferroelectricity, multiferroism, magnetoresistance and superconductivity. Revealing the electronic and magnetic behaviour and determining the performance limits of different families of transition metal fluorides will greatly enhance our current understanding of the underlaying mechanisms behind the occurrence of these important phenomena. The fine tuning of the interplay of the charge, lattice, orbital and spin degrees of freedom in these systems should hold unforeseen surprises. Further research into these systems would be of key importance for the expansion of properties exhibited by existing solids.

6.5 References

[1] S.C.M. Abrahams, K.; Nielson, R.M., *Acta Crystallographica, Section B: Structural Science* 52 (1996) 4.

[2] J.A. Ravez, S.C.; De Pape, R., *Journal of Applied Physics* 65 (1989) 4.

[3] S.C. Abrahams, J. Ravex, *Ferroelectrics* 135 (1992) 21.

[4] E. Banks, M. Shone, Y. Hong, R. Williamson, W. Boo, *Inorganic Chemistry* 21 (1982) 3894.

[5] F. Mezzadri, S. Fabbrici, E. Montanari, L. Righi, G. Calestani, E. Gilioli, F. Bolzoni, A. Migliori, *Physical Review B: Condensed Matter and Materials Physics* 78 (2008) 064111.

[6] S. Fabbrici, E. Montanari, L. Righi, G. Calestani, A. Migliori, *Chemistry of Materials* 16 (2004) 3007.

[7] R. Blinc, P. Cevc, A. Potocnik, B. Zemva, E. Goreshnik, D. Hanzel, A. Gregorovic, Z. Trontelj, Z. Jaglicic, V. Laguta, *Journal of Applied Physics* 107 (2010) 043511.

[8] R. Blinc, G. Tavcar, B. Zemva, E. Goreshnik, D. Hanzel, P. Cevc, A. Potocnik, V. Laguta, Z. Trontelj, Z. Jaglicic, *Journal of Applied Physics* 106 (2009) 023924.

[9] N. Kumar, C. Rao, *ChemPhysChem* 4 (2003) 439.

[10] C. Rao, A. Arulraj, A. Cheetham, B. Raveau, *Journal of Physics: Condensed Matter* 12 (2000) R83.

[11] J.P. Attfield, *Solid State Sciences* 8 (2006) 861.

[12] J. Van Den Brink, D.I. Khomskii, *Journal of Physics: Condensed Matter* 20 (2008) 434217.

[13] S. Ishihara, *Journal of the Physical Society of Japan* 79 (2010) 011010.

[14] J. Ravez, S. Abrahams, R. De Pape, *Journal of Applied Physics* 65 (1989) 3987.

[15] E. Baum, P. Dahlke, V. Kaiser, M. Molinier, R.E. Schmidt, J. Pebler, W. Massa, D. Babel, *Zeitschrift für Anorganische und Allgemeine Chemie* 632 (2006) 2244.

[16] S.W. Kim, S.-H. Kim, P.S. Halasyamani, M.A. Green, K.P. Bhatti, C. Leighton, H. Das, C.J. Fennie, *Chemical Science* 3 (2012) 741.

[17] G. Ferey, M. Leblanc, R. Depape, *Journal of Solid State Chemistry* 40 (1981) 1.

[18] M. Subramanian, W. Marshall, R. Harlow, *Materials Research Bulletin* 31 (1996) 585.

[19] K. Yamauchi, S. Picozzi, *Physical Review Letters* 105 (2010) 107202.

[20] S.A. Reisinger, M. Leblanc, A.-M. Mercier, C.C. Tang, J.E. Parker, F.D. Morrison, P. Lightfoot, *Chemistry of Materials* 23 (2011) 5440.

Appendix

List of Publications and Presentations

- C. Drathen, T. Nakagawa, W. Crichton, A. Hill, Y. Ohishi and S. Margadonna; Structural transition in $KMnCrF_6$ – a chemically ordered magnetic ferroelectric. Submitted to Chemistry of Materials, 2012.
- C. Drathen, T. Nakagawa, A. Hill, Y. Ohishi and S. Margadonna; Multiple phase transitions in the charge-ordered multiferroic K_xCrF_3. In preparation.
- C. Drathen, A. Fitch, T. Hansen, L. Malavasi and S. Margadonna, Magnetism and structure of manganese pnictide *Ae*Mn*Pn*F (*Ae* = Sr, Ba; *Pn* = P, As, Sb). In preparation.
- C. Drathen, S. Margadonna, Chemical and charge order in multiferroic tetragonal tungsten bronze fluorides. Contributed talk, European Powder Diffraction conference – EPDIC 13, 28th – 31st October 2012, Grenoble, France.
- C. Drathen, S. Margadonna, The tetragonal tungsten bronze $KMnCrF_6$ – full ionic order in a potential multiferroic. Poster, Norwegian Synchrotron- and Neutron User Meeting, 30th – 31st January 2012, Stavanger, Norway.
- C. Drathen, Synthesis and characterization of manganese pnictides. Invited talk. Seminar of the Physical Chemistry Section, 13th April 2011, Department of Chemistry, University of Pavia, Italy.
- B. Maroni, D. Di Castro, M. Hanfland, J. Boby, C. Vercesi, M.C. Mozzati, S. Weyeneth, H. Keller, R. Khasanov, C. Drathen, P. Dore, P. Postorino and L. Malavasi; Pressure effects in the isoelectronic *Re*$Fe_{0.85}Ir_{0.15}$AsO System, Journal of the American Chemical Society, 2011, 133 (10), 3252-3255.
- C. Drathen, Structure – property relationships in the quaternary manganese pnictides *Ae*Mn*Pn*F (*Ae* = Ba, Sr; *Pn* = P, As, Sb). Contributed talk. 30th group meeting of the Royal Society Chemistry Solid State Group, 20th – 21th December 2010, UCL London, UK.
- C. Drathen, Magnetism and structure of manganese pnictides SrMn*Pn*F (*Pn* = P, As, Sb). Contributed talk. Jülich Centre for Neutron Science workshop, Trends and Perspectives in Neutron Scattering: Magnetism and Correlated Electron Systems, 04th- 07th October, 2010, Bernried, Germany.
- C. Drathen, S. Margadonna, Structural and electronic properties response upon rare-earth doping in SrFeAsF. Poster, 42nd IUPAC Congress, 02nd – 07th August 2009, Glasgow, UK.